

Karlsruher Institut für Technologie

Schriftenreihe

Kontinuumsmechanik im Maschinenbau

26

Felix Ernesti

A computational multi-scale approach
for brittle materials

Felix Ernesti

**A computational multi-scale approach
for brittle materials**

Schriftenreihe
Kontinuumsmechanik im Maschinenbau
Band 26

Karlsruher Institut für Technologie (KIT)
Institut für Technische Mechanik
Bereich Kontinuumsmechanik

Hrsg. Prof. Dr.-Ing. habil. Thomas Böhlke

Eine Übersicht aller bisher in dieser Schriftenreihe erschienenen Bände
finden Sie am Ende des Buchs.

A computational multi-scale approach for brittle materials

by
Felix Ernesti

Karlsruher Institut für Technologie
Institut für Technische Mechanik
Bereich Kontinuumsmechanik

A computational multi-scale approach for brittle materials

Zur Erlangung des akademischen Grades eines Doktors der Ingenieurwissenschaften (Dr.-Ing.) von der KIT-Fakultät für Maschinenbau des Karlsruher Instituts für Technologie (KIT) genehmigte Dissertation

von Felix Ernesti, M.Sc.

Tag der mündlichen Prüfung: 24. Januar 2023

Hauptreferent: Jun.-Prof. Dr. rer. nat. Matti Schneider

Korreferent: Prof. Dr.-Ing. Ralf Müller

Impressum



Scientific
Publishing

Karlsruher Institut für Technologie (KIT)
KIT Scientific Publishing
Straße am Forum 2
D-76131 Karlsruhe

KIT Scientific Publishing is a registered trademark
of Karlsruhe Institute of Technology.

Reprint using the book cover is not allowed.

www.ksp.kit.edu



This document – excluding parts marked otherwise, the cover, pictures and graphs – is licensed under a Creative Commons Attribution-Share Alike 4.0 International License (CC BY-SA 4.0): <https://creativecommons.org/licenses/by-sa/4.0/deed.en>



The cover page is licensed under a Creative Commons Attribution-No Derivatives 4.0 International License (CC BY-ND 4.0): <https://creativecommons.org/licenses/by-nd/4.0/deed.en>

Print on Demand 2023 – Gedruckt auf FSC-zertifiziertem Papier

ISSN 2192-693X

ISBN 978-3-7315-1285-1

DOI 10.5445/KSP/1000156458

Zusammenfassung

Materialien von industrieller Relevanz weisen oft eine komplexe Mikrostruktur auf, welche einen direkten Einfluss auf das makroskopische Materialverhalten hat. Um diese Mikrostrukturinformationen bei Simulationen auf der Bauteilebene zu verwenden, haben sich Multiskalenmethoden etabliert. Insbesondere Homogenisierungsmethoden werden häufig eingesetzt, da sie auf bewiesenen mathematischen Resultaten basieren.

Der erste Abschnitt dieser Arbeit konzentriert sich auf die Charakterisierung komplexer Mikrostrukturen. Es wird die Anwendbarkeit von Minkowskitensoren, welche ihren Ursprung in der stochastischen Geometrie haben, untersucht. Hierbei wird insbesondere ein normalisierter Tensor als geeigneter Charakterisierer für Mikrostrukturen identifiziert. Als Grundlage der darauffolgenden Kapitel dient ein Homogenisierungsergebnis für das Mumford-Shah Funktional mit periodischen Parametern, welches für Funktionen mit beschränkter Variation definiert ist. Diese Funktionen bilden auch die mathematische Grundlage für das Sprödbruch Modell von Francfort und Marigo. Das Homogenisierungsergebnis ist für den Fall einer Scherung senkrecht zur Ebene sowie unter Vernachlässigung der Irreversibilität auf das Francfort-Marigo Modell anwendbar. Erweiterungen des Homogenisierungsergebnisses lösen diese beiden Beschränkungen individuell auf und übertragen das Resultat auf stochastische Mikrostrukturen. Das resultierende homogenisierte Modell weist eine ähnliche Struktur zum ursprünglichen Francfort-Marigo Modell auf, allerdings mit potentiell anisotroper effektiver Steifigkeit und richtungsabhängiger effektiver Rissenergie. Zudem beinhaltet das

Homogenisierungsergebnis spezifische Zellformeln für die effektiven Materialparameter, welche voneinander entkoppelt sind.

Der zweite Teil dieser Arbeit widmet sich der Entwicklung numerischer Verfahren zur Berechnung der effektiven Rissenergie heterogener Materialien. Die Zellformel zur Berechnung dieser lässt sich als konvexes, jedoch nicht streng konvexes Optimierungsproblem aufstellen, welches den (periodischen) minimalen Schnitt durch eine Mikrostruktur bestimmt. Zur Lösung dieses Problems werden eine neue Diskretisierung sowie FFT-basierte Lösungsverfahren mit adaptiver Parameterwahl entwickelt. Mithilfe dieser Strategie können Materialien von industrieller Komplexität untersucht werden.

Im darauffolgenden Abschnitt wird der Fokus auf lokal anisotrope Mikrostrukturen gelegt. Diese erfordern eine Umformulierung des Zellproblems in eine anisotrope Form sowie eine Modifizierung des Lösungsverfahrens. Mithilfe dieser Erweiterungen können polykristalline Materialien sowie Faserstrukturen mit anisotropen Fasern untersucht werden.

Der letzte Abschnitt ist Untersuchungen zu verschiedenen Randbedingungen gewidmet. Die ursprünglich hergeleitete Zellformel verwendet Dirichlet-Randbedingungen. Untersuchungen zur Homogenisierung von Elastizitäts- oder Wärmeleitungsproblemen zeigen jedoch, dass die Verwendung periodischer Randbedingungen zu einem geringeren Fehler der approximierten effektiven Eigenschaften führt. Basierend auf diesen Ergebnissen wird untersucht, ob diese Verbesserung auf die Berechnung der effektiven Rissenergie übertragbar ist.

Summary

Materials used in an industrial context often exhibit a complex microstructure which directly influences the macroscopic material behavior. For simulations on the component scale, multi-scale methods may exploit the microstructural information. In particular homogenization methods are often used due to their well formulated mathematical background.

In a first step we focus on the characterization of complex microstructures. We investigate the applicability of Minkowski tensors, which originate from stochastic geometry, to characterize microstructures. We identify in particular a normalized tensor, the quadratic normal tensor, as a suitable characterizer.

The foundation of the subsequent chapters is laid by a periodic homogenization result for free discontinuity problems. These free discontinuity problems form the mathematical basis of the variational approach to fracture, known in the fracture community as the Francfort-Marigo model of brittle fracture. The homogenization result is directly applicable to a single loading step of the Francfort-Marigo model in the special case of anti-plane shear and without an irreversibility constraint. Furthermore, recent extensions lift these restrictions individually and provide extensions to random ergodic media, indicating that the homogenization result holds for the general Francfort-Marigo model and non-periodic microstructures. The homogenized model has a similar structure as the original Francfort-Marigo model but with homogeneous, possibly anisotropic material parameters, namely an effective stiffness and an effective crack energy. The homogenization result includes specific cell

formulas for both effective properties which decouple upon homogenization. The second part of this thesis is devoted to establish numerical tools to compute the effective crack energy of heterogeneous materials. The cell formula to compute the effective crack energy may be formulated as a convex, but not strictly convex, optimization problem to compute the (periodic) minimum cut through a given microstructure. To solve this problem we investigate novel discretization methods and FFT-based solvers with an adaptive parameter choice. With this strategy we investigate microstructures of industrial complexity.

Subsequently, we focus on locally anisotropic microstructures. This requires an anisotropic formulation of the governing cell formula and a modification of the solver. These alterations at hand, we investigate polycrystalline materials and fibrous structures with a distinct anisotropy of the fibers.

The last section is devoted to investigating the influence of different boundary conditions. The original cell formula for the effective crack energy is formulated using Dirichlet boundary conditions. Investigations on the homogenization of linear elasticity or heat conductivity show an advantage of periodic boundary conditions over the Dirichlet kind in the convergence rate of the apparent properties. Based on these results we investigate if this advantage translates to the computation of the effective crack energy.

Acknowledgments

First of all, I would like to thank my supervisor Jun.-Prof. Matti Schneider. I had a great time working with him for the last four years - four fruitful years in which I have probably learned more than in any other stage of my life.

Furthermore, I would like to thank Prof. Ralf Müller who took on the position of the second assessor of my thesis.

I am grateful to Prof. Thomas Böhlke, whose lectures have accompanied my studies ever since my first semester at KIT and who introduced me to the field of continuum mechanics.

I would like to thank Prof. Britta Nestler for chairing the doctoral exam and taking the time to answer my questions on organizational issues.

I am grateful to all my colleagues at the ITM for fruitful discussions on each of our research topics as well as lively debates on books, cinema or other current topics during our coffee break - thank you very much. Special thanks go to Max, Loredana, Andi, Tobias, Sebastian, Johannes, Hannes, Jonas, Lennart, Benedikt, Alok and Alex for the wonderful time I spent with you over the past four years.

In particular, I would like to thank Daniel who always had an open door for me and my questions and with whom I always had hilarious conversations. Furthermore, I would like to thank Jannick who has accompanied me since our third semester as a friend and a colleague. Special thanks goes to Ute Schlumberger-Maas, without who the ITM would not be the institute that it is, as well as Tom Langhoff for his advice and support. Additionally I would like to thank Ariane van Elst and Helga Betsarkis for their ongoing support.

Writing this thesis would not have been possible without the support of my family, to who I am very grateful.

Most of all, I would like to thank my wife Isabel, who supported and encouraged me to pursue my goals. I do not know where I would be without you.

Last but not least, I gratefully acknowledge funding by the Deutsche Forschungsgemeinschaft (DFG, German Research Foundation) for the project 426323259, as well as funding by the KIT center *MathSEE* (Mathematics in Sciences, Engineering, and Economics).

Karlsruhe, March 2023

Felix Ernesti

Contents

Zusammenfassung	i
Summary	iii
Acknowledgments	v
1 Introduction	1
1.1 Motivation and objectives	1
1.2 Outline and originality	3
2 Fundamental concepts	7
2.1 Basic concepts of brittle fracture mechanics	7
2.1.1 Linear elastic fracture mechanics	7
2.1.2 The variational approach to fracture	11
2.1.3 Phase-field fracture	13
2.2 Characterization of digital microstructures	18
2.2.1 Objectives	18
2.2.2 State of the art	19
2.3 Phase-field fracture on heterogeneous microstructures	21
2.3.1 Continuous model under investigation	22
2.3.2 Numerical setup	29
2.3.3 Phase-field fracture for a continuous-fiber reinforced brittle composite	31
2.3.4 Phase-field fracture for a short-fiber reinforced brittle composite	34
2.3.5 Conclusions	37

2.4	Homogenization methods for brittle fracture	38
2.4.1	Objectives	38
2.4.2	Homogenization of the Francfort-Marigo model . . .	40
2.4.3	The cell formula for periodic minimum cut/maximum flow	48
2.4.4	Discussion on the terminology "effective crack resistance"	51
3	Characterizing digital microstructures by the Minkowski-based QNT	55
3.1	Introduction	55
3.2	Using Minkowski tensors for describing microstructures .	59
3.2.1	Minkowski tensors	59
3.2.2	Minkowski-tensor based microstructure characterization	63
3.3	Efficient implementation for 3D image data	67
3.3.1	Algorithmic overview	67
3.3.2	Smoothing by image filters	69
3.3.3	Approximating the surface normal by finite differences	71
3.3.4	Computing Minkowski tensors	74
3.4	Numerical examples	75
3.4.1	Setup	75
3.4.2	Parameter selection and multigrid convergence . . .	75
3.4.3	A short-fiber reinforced composite	80
3.4.4	Sand grains and sand-binder composites	91
3.5	Conclusion and Outlook	95
4	Computing the effective crack energy on a combinatorially consistent grid	99
4.1	Introduction	99

4.2	The effective crack energy of a heterogeneous material . . .	105
4.2.1	Cell formulas for the minimum cut and the maximum flow	105
4.2.2	The combinatorial continuous maximum flow discretization	108
4.3	An FFT-based solver for the CCMF discretization	112
4.3.1	The primal formulation for the CCMF discretization	112
4.3.2	An FFT-based ADMM solver	115
4.4	Computational experiments	120
4.4.1	Setup	120
4.4.2	A single spherical inclusion	122
4.4.3	A continuous-fibe reinforced composite	123
4.4.4	A fiber-reinforced composite	127
4.4.5	Microstructures with a monodisperse pore distribution	131
4.4.6	Sand-binder composite	132
4.5	Conclusions	135
5	The effective crack energy of heterogeneous and locally anisotropic microstructures	137
5.1	Introduction	137
5.2	Minimum cut/maximum flow with anisotropic crack resistance	142
5.2.1	Cell formula for an anisotropic minimum cut	142
5.2.2	Anisotropic maximum flow formulation	144
5.3	Numerical treatment	146
5.3.1	The CCMF discretization for anisotropic maximum flow	146
5.3.2	The alternating direction method of multipliers	148
5.3.3	The anisotropic projector problem	150
5.4	Numerical examples	152
5.4.1	Setup	152
5.4.2	A polycrystalline microstructure	153

5.4.3	A carbon fiber reinforced polymer	159
5.5	Conclusion	161
6	On the influence of the boundary conditions when computing the effective crack energy	163
6.1	Introduction	163
6.2	The effective crack energy of heterogeneous random media	167
6.3	Finding the minimum cut with the fast marching method	170
6.3.1	From minimum cut to shortest path problems	170
6.3.2	Finding shortest paths by the fast marching method	172
6.4	Numerical investigations	177
6.4.1	Setup	177
6.4.2	A single rotated square inclusion	178
6.4.3	Comparison with minimum cut/maximum flow . .	180
6.4.4	The influence of boundary conditions	183
6.5	Conclusion	188
7	Summary and conclusions	191
A	Minkowski tensors for specific shapes	201
A.1	Minkowski tensor of a ball	201
A.2	Minkowski tensor of a cylinder	202
B	Performance of additional penalty factor choices for ADMM	205
	Bibliography	207

Chapter 1

Introduction

1.1 Motivation and objectives

With fracture, we denote a separation of a previously coherent material due to breakage of bonds between the molecules of the material. This breakage may occur due to crack initiation, the propagation of a pre-existing crack through the material or a complete failure of the structure. Fracture mechanics describes these different cracking behaviors of materials from various perspectives. The field of research may be broadly categorized into two principal cases, namely *brittle* fracture and *ductile* fracture. Brittle fracture describes a sudden crack propagation with almost no energy dissipation before the fracture. For ductile fracture on the other hand, a noticeable amount of energy has been dissipated before the crack propagates in the form of damage and plasticity. Furthermore, one distinguishes the dynamic case and the quasi-static case.

The actual mechanisms of fracture and crack propagation take place over a broad range of length scales. On the atomic scale, the separation of a previously intact material is described by breakage of inter-atomic bonds. On the component scale, a continuum mechanical perspective is typically taken. However, the classical continuum mechanical toolkit faces difficulties in the presence of cracks, which make in the displacement field discontinuous. Additional difficulties arise in the presence of

propagating cracks where the newly formed crack surface provides an additional unknown.

One particular question of interest in the field of brittle fracture is *when* cracks propagate, which is the basic motivation for failure criteria. Failure criteria play a crucial role in the engineering design of components to ensure their safety and reliability. Typical failure criteria involve either a stress-based approach, are energy based or focus on stress intensity factors. To equip failure criteria with necessary parameters, crack-related material properties are required. Of particular interest in brittle fracture are the critical energy release rate, the fracture toughness, as well as the ultimate tensile strength.

The theoretical strength of materials, derived from the strength of the atomic bonds in a hypothetically perfect arrangement, typically overestimates the actual strength measured in real-world experiments. This deviation is caused by a non-perfect arrangement of atoms on a small length scale mainly in the form of micro cracks and defects.

In addition to flaws and micro cracks, industrial materials often exhibit a random microstructure due to their manufacturing process. From fiber reinforced composites to polycrystalline materials or porous media, several intended or unintended production factors influence the microstructure. This makes a fully experimental characterization rather expensive. An effective tool to incorporate microstructure information into material models is given by multi-scale simulation methods and, in particular, homogenization methods. Assuming a distinct scale separation, the aim of homogenization methods is to treat the material on the component scale as homogeneous, where effective mechanical quantities and material coefficients arise from a separate field problem on a microstructure cell.

This thesis is devoted to the characterization of microstructures and the investigation of a homogenization result for variational brittle fracture (Francfort and Marigo, 1998). For the characterization of microstructures we rely on an approach originated in stochastic geom-

etry, the Minkowski tensors. In order to characterize microstructures of different sizes we establish the quadratic normal tensor as our primary characterizer.

For the homogenization of brittle fracture we pursue an approach based on a periodic homogenization result (Braides et al., 1996) for the Mumford-Shah functional (Mumford and Shah, 1989), as well as several extensions including irreversibility (Giacomini and Ponsiglione, 2006), random, ergodic media (Cagnetti et al., 2019) and the full Francfort-Marigo functional (Friedrich et al., 2022). Based on these theoretical works we consider a cell formula defining the effective crack energy. We aim to provide numerical tools to compute the effective crack energy building on an initial work of Schneider (2020).

1.2 Outline and originality

Chapter 2 is devoted to the concepts which form the basis of this work. We first give an overview on brittle fracture mechanics. We discuss the variational approach to fracture and the typical numerical treatment of the latter via phase-field fracture models. A second fundamental concept is given by microstructure characterization which is required to distinguish different microstructures using simple quantities. Based on these characteristics, homogenization methods may be applied. Thirdly, we discuss phase-field fracture on complex microstructures. The governing equations require careful treatment and we propose an implicit solver strategy. Lastly, we discuss a homogenization result (Braides et al., 1996) for the Mumford-Shah functional (Mumford and Shah, 1989) which shares various properties with the Francfort-Marigo model of brittle fracture (Francfort and Marigo, 1998). We discuss the requirements for this homogenization result to be applicable to the Francfort-Marigo model. We define the effective crack energy based on a cell formula derived by Braides et al. (1996). Extending Schneider (2020) we identify this formula

as the minimum cut problem and derive an equivalent form based on the minimum cut/maximum flow duality derived by Strang (1983).

In **chapter 3** we focus on the characterization of digital microstructures. We propose the use of Minkowski tensors, which originate in stochastic geometry, as a tool to characterize microstructures. These tensors are applicable to a wide range of different shapes. In particular, we introduce the quadratic normal tensor as a normalized Minkowski tensor which provides a measure of the anisotropy of a microstructure. We introduce a numerical method to compute the quadratic normal tensor on large digital microstructures. We compare the accuracy of our approach for fiber reinforced composites with the usual tool to determine the fiber orientation tensor based on a structure tensor approach. A final investigation on sand grain structures demonstrates the wide range of applicability of the quadratic normal tensor.

Chapter 4 is concerned with efficient algorithms to compute the effective crack energy on heterogeneous random microstructures. In order to find solutions of the cell problem derived in chapter 2, suitable discretizations and solvers are required. We provide extensions to the approach of Schneider (2020) who derived FFT-based solvers and discretizations. We discuss an implementation of a discretization based on a combinatorially consistent grid, which was introduced by Couprie et al. (2011), into the context of FFT-based solvers. Furthermore we rely on the alternating direction method of multipliers to solve the discretized problem using an adaptive parameter strategy.

In **chapter 5** we use both solvers and discretizations provided in the previous chapter and propose an extension to the anisotropic case. We discuss the anisotropic minimum cut/maximum flow problem and apply it to study anisotropic materials.

Chapter 6 is devoted to explore the influence of the boundary conditions when computing the effective crack energy on random microstructure cells of finite size. For this purpose we use fast marching methods to

compute the effective crack energy in two dimensional structures which allows us to choose the boundary conditions freely.

Finally, we summarize the novelties of our approach and give a final conclusion in **chapter 7** .

Chapter 2

Fundamental concepts

2.1 Basic concepts of brittle fracture mechanics¹

2.1.1 Linear elastic fracture mechanics

Modern fracture mechanics (Gross and Seelig, 2017) originated from the pioneering work of Griffith (1921), who postulated an energetic criterion for the quasi-static growth of a pre-existing crack in a brittle, isotropic, and elastic solid. He considered the change of the potential energy Π with the crack area A and postulated that a crack can only grow whenever the energy release rate $-d\Pi/dA$ reaches a critical value γ . Put differently, the crack grows whenever it is energetically more favorable to increase the surface energy of the crack than to increase the elastic energy stored in the body.

For the case of three-dimensional isotropic elasticity and a semi-infinite planar pre-existing crack in an infinite medium, Irwin (1957) investigated the stress state at the crack tip, which has an $r^{-\frac{1}{2}}$ -singularity where r denotes the Euclidean distance to the crack tip. He distinguished three different modes which quantify the degree of singularity of the

¹ This section is based on the introductory sections of Ernesti and Schneider (2021; 2022) and Ernesti et al. (2023) and provides an extension thereof.

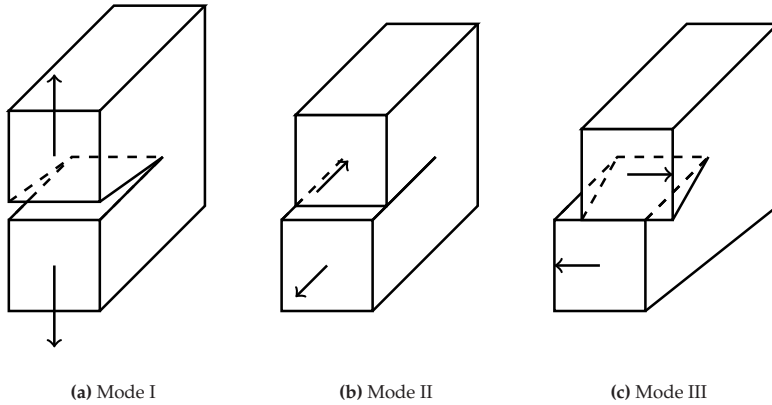


Figure 2.1: Schematic illustration of mode I, mode II and mode III loading.

normal, the in-plane and the out-of-plane shear stresses, respectively, see Fig. 2.1 for a graphic illustration. He associated a stress-intensity factor to each mode and postulated that the pre-existing crack has to grow provided a combination of the stress intensity factors reaches a critical value, the so-called fracture toughness. Expressing the energy-release rate in terms of these stress-intensity factors, Irwin converted Griffith's criterion into an investigation of the associated stress concentration at the crack tip (Irwin, 1962). Thus, in the case of linear elastic, isotropic and homogeneous brittle materials both Griffith's energy criterion and Irwin's notion of stress intensity factors coincide. In the literature, *fracture toughness* and *critical energy release rate* or *crack resistance* are often used interchangeably (Gross and Seelig, 2017). This work is focused on Griffith's point of view and we call the energy related quantity the crack resistance, avoiding the term fracture toughness altogether.

Independently, Cherepanov (1967) and Rice (1968) proposed a way to compute the local energy-release rate at a crack tip in terms of a contour integral around the crack tip, the so-called J-integral. This J-integral

offers an elegant way to deal with the stress singularity at the crack tip numerically, as it is independent of the chosen path of integration.

Following the first concept of Irwin (1957), the stress is infinitely large at the crack tip. This motivated a refinement of the model to account for small plastic effects close to the crack tip since atomic bonds cannot withstand an infinite load. These small-scale plastic effects are even considered for macroscopic brittle material behavior. The small plastic region around the crack is called the plastic zone (Irwin, 1968).

All three aforementioned pillars - Griffith's energy release rate, Irwin's stress intensity factors and techniques based on the J-integral - may be extended to (homogeneous) anisotropic brittle solids (Sih et al., 1965; Wu, 1967; Saouma et al., 1987; Williams, 1989). In the anisotropic case, however, some care has to be taken, as the fracture modes are not directly correlated to the normal and tangential jumps of the displacement field (Laubie, 2013).

Linear elastic fracture mechanics was also extended to account for elasto-plastic effects. Dugdale (1960) investigated mode I crack propagation, see Fig. 2.1a, with a perfectly plastic material behavior within the plastic zone. In his model, the plastic zone has an elongated shape in the anticipated crack direction. A generalization of this model is found in the form of cohesive zone models (Barenblatt, 1962; Elices et al., 2002), which express the correlation of the crack opening and the governing stresses explicitly via traction separation laws (Amidi and Wang, 2017). The concept of classical linear elastic fracture mechanics has also been extended to study fatigue (Rice, 1967). Additionally, leaving the quasi-static domain, dynamic effects like crack branching (Katzav et al., 2007) have been studied by accounting for dynamical stress intensity factors dependent on the speed of the crack. Creep and viscous effects have also been included (Hollstein and Kienzler, 1988).

Linear elastic fracture mechanics is first and foremost a tool to investigate *when* a pre-existing crack propagates, which is expressed via fracture criteria. Of additional interest is predicting *how* a crack grows and to

determine possible crack paths and surfaces (Chambolle et al., 2009). The question is whether the crack propagates in the same direction as before, kinks at a certain angle or, e.g., splits into several crack branches. The most common approaches to predict these kinking angles exploit the principle of local symmetry (Gol'dstein and Salganik, 1974) or follow the postulate of maximum energy-release (Hussain et al., 1974). In general, these two models yield different results for the kinking angle (Amestoy and Leblond, 1992). Of particular interest is the change of the crack direction at material interfaces in the context of a heterogeneous material. Early attempts study crack penetration at the interface (Cook and Erdogan, 1972; Erdogan and Biricikoglu, 1973) or whether the crack is deflected at the interface (Goree and Venezia, 1977; He and Hutchinson, 1989).

In addition to the aforementioned analytical methods, several contributions are concerned with computational fracture mechanics, see Sedmak (2018) for an overview. Equipped with numerical tools, these may either serve to investigate when a structure fails, or how a crack may propagate. In particular, in the absence of analytical solutions, discretization methods are required. Similar to other branches of mechanics, the most common technique for discretizing the involved equations are finite elements. Early attempts to compute stress-intensity factors numerically have been proposed by Chan et al. (1970) and Rice and Tracey (1973). However, it turns out to be difficult to resolve the singularity at the crack tip, since the error of a finite element solution correlates with the regularity of the approximated fields. For this purpose, enriched (Moës et al., 1999) or extended (Fries and Belytschko, 2010) finite-element discretizations were developed which account for the crack surface in cracked elements by adding special ansatz functions. An alternative approach form cohesive zone elements (Chowdhury and Narasimhan, 2000), which may be incorporated into the finite-element mesh. In these elements specific traction-separation laws (Wimmer et al., 2009) may be implemented to model the correlation of crack opening and

governing stresses. These traction separation laws are readily calibrated by experiments (Dastjerdi et al., 2013; Amidi and Wang, 2017). However, caution has to be taken, as cohesive zone elements may induce a mesh dependency (Rimoli and Rojas, 2015).

2.1.2 The variational approach to fracture

Francfort and Marigo (1998) revisited Griffiths energetic fracture criterion (Griffith, 1921) and introduced a variational approach to fracture. Consider a given domain $\Omega \subset \mathbb{R}^d$, $d \in \{2, 3\}$ with sufficiently smooth boundary, as well as a field of stiffness tensors $\mathbb{C} : \Omega \rightarrow L(\text{Sym}(d))$ a field of positive crack resistances $\gamma : \Omega \rightarrow \mathbb{R}_{>0}$. We denote by $L(\text{Sym}(d))$ the field of linear operators on symmetric $d \times d$ matrices and explicitly account for positive definite stiffnesses. The Francfort-Marigo model considers quasi-static crack growth. After a fixed discretization in (pseudo)-time, which discretizes an increasing external load, it seeks the displacement field $u : \Omega \rightarrow \mathbb{R}^d$ and the $d - 1$ dimensional crack surface $S \subset \Omega$ by minimizing the energy functional

$$FM(u, S) = \frac{1}{2} \int_{\Omega \setminus S} \nabla^s u(x) : \mathbb{C}(x) : \nabla^s u(x) dx + \int_S \gamma(x) dA \quad (2.1)$$

for each time step subjected to appropriate boundary conditions. The quantity $\nabla^s u$ denotes the strain field expressed via the symmetrized gradient operator ∇^s . A physical constraint is given by the irreversibility condition that the crack surface of the current time step must contain the crack surface of the previous time step. The Francfort-Marigo functional consists of the sum of two energies, a bulk energy and a surface energy. The bulk energy is quadratic in the strain field $\nabla^s u$ and describes the elastic deformation of the solid. The surface term is given by the γ -weighted surface area of the crack surface S . This additive decomposition into two energies allows the model to describe both

crack initiation and crack propagation within a single model. Upon an increased load, a global minimum may be found by either further elastic deformation of the solid, or via the formation of a crack surface. Notice, however, the differences compared to the formulation of Griffith (1921). His criterion for crack propagation is concerned with local stationary points. This specifically includes local minima, local maxima and saddle points. Solutions of the Francfort-Marigo model on the other hand rely on a global minimization of the functional (Chambolle and Crismale, 2019). This global minimization is, as mentioned by Francfort and Marigo (1998), "not dictated by any known thermodynamical argument," but merely a necessity for the mathematical treatment of the model. In contrast to the framework of linear elastic fracture mechanics based on Griffith (1921) and Irwin (1957), no preexisting crack is required in the Francfort-Marigo model.

The Francfort-Marigo functional (2.1) shows strong similarities with Mumford-Shah type functionals (Mumford and Shah, 1989) used in image segmentation. Consider a scalar variable $v : \Omega \rightarrow \mathbb{R}$ from the space of special functions of bounded variation (SBV) (Braides, 1998) with jump set S_v and the symmetric, positive definite tensor field A . A similar functional to (2.1) from the family of Mumford-Shah functionals is given by

$$MS(v) = \frac{1}{2} \int_{\Omega} \nabla v(x) \cdot A(x) \cdot \nabla v(x) dx + \int_{S_v} \gamma(x) dA. \quad (2.2)$$

Notice three main differences compared to the Francfort-Marigo model: The first difference regards the bulk energy. The Mumford-Shah functional considers a quadratic function of the gradient of v , whereas the Francfort-Marigo model considers a quadratic function of the symmetrized gradient of u . For the special case of anti-plane shear, for which the displacement field $u = (u_x, u_y, u_z)^T$ may be expressed using a scalar variable $v = u_z$, which only depends on the spatial dimensions

x and y , the bulk energies coincide. The second difference concerns the integral range of the surface part. The crack surface S serves as an additional objective variable, whereas the surface range in the Mumford-Shah functional is given by the jump set of v , namely S_v . The third difference between the models is given by the discretization in time. Within the Mumford-Shah functional there is no time stepping involved. The Francfort-Marigo model on the other hand explicitly accounts for changes in an external load and minimizes the Francfort-Marigo functional in each time step. Furthermore, the history of the previous steps is taken into account via the irreversibility constraint. To summarize, in the case of anti-plane shear, the Mumford-Shah functional describes the relaxed form of the Francfort-Marigo model in SBV where irreversibility is neglected. To prove the existence of weak solutions of the Francfort-Marigo model in the general case, i.e., including the symmetrized gradient instead of the gradient as well as accounting for irreversibility, the solution space of generalized special functions of bounded deformation (GSBD) (Dal Maso, 2013) is required (Chambolle and Crismale, 2021). In this function space the crack surface is identified with the jump set of u , namely S_u . The existence of strong solutions which treat the displacement field and the crack surface as two variables has been shown recently (Chambolle and Crismale, 2019). Various approaches to compute minimizers of the functional numerically have been proposed (Giacomini and Ponsiglione, 2003; Pandolfi et al., 2013; Schmidt et al., 2009). In particular, the Francfort-Marigo model has laid the foundation of the field of phase-field fracture (Bourdin et al., 2000) which enjoys great popularity, see Wu et al. (2020) for a recent review.

2.1.3 Phase-field fracture

The phase-field model of brittle fracture was introduced as a regularization of the Francfort-Marigo model, motivated by the Ambrosio-Tortorelli approximation (Ambrosio and Tortorelli, 1990) of the Mumford-

Shah functional (Mumford and Shah, 1989). Owing to their ability to nucleate cracks and to produce complex crack patterns, phase-field fracture models were subject to a flurry of activity (Ambati et al., 2015; Wu et al., 2020). The phase-field model introduces a damage variable $d : \Omega \rightarrow [0, 1]$ which takes values $d = 0$ when the material is fully intact and $d = 1$ within a crack. The range between these values is given by a smeared interface of phase-field width $l > 0$ which provides a regularization of the sharp interface which represents the crack in the Francfort-Marigo model. After a discretization in (pseudo-)time, the phase-field model in its original form is given by minimizing the functional

$$PF_l(u, d) = \int_{\Omega} \frac{1}{2} (1 - d)^2 \nabla^s u : \mathbb{C} : \nabla^s u + \gamma \left(\frac{\|d\|^2}{2l} + \frac{l}{2} \|\nabla d\|^2 \right) dx \quad (2.3)$$

in each time step for both u and d . To ensure the irreversibility of the phase-field model, these minimizers are sought under the constraint that $d^{i+1} \geq d^i$ almost everywhere, where the index i represents the time step. Chambolle (2004) showed that the phase-field functional Γ -converges to the Francfort-Marigo model as $l \rightarrow 0$. Similar to the solution theory for the Francfort-Marigo model, this convergence result relies on global minimizers.

Several methods have been established to enforce the irreversibility constraint, which is necessary for the physicality of the model since it prevents cracks from *healing*. Miehe et al. (2010a) introduced a formulation based on a history field which enjoys great popularity. Another approach (Bourdin et al., 2000; Burke et al., 2010) enforces the irreversibility constraint by fixing $d = 1$ in all points x where the damage field exceeds a certain threshold via Dirichlet boundary conditions. Alternatives rely on established methods for constrained optimization problems such as penalty methods (Gerasimov and De Lorenzis, 2019) or augmented Lagrangian methods (Wheeler et al., 2014).

of the strain field. Chambolle et al. (2018) proved that the approach of Amor et al. (2009) Γ -converges to the Francfort-Marigo model with the additional constraint that the crack faces do not interpenetrate as $l \rightarrow 0$. In the same work they showed that the method which uses the splitting of Miehe et al. (2010b) converges to a Francfort-Marigo type model which prevents crack propagation due to shear loading. Recent developments propose extensions to anisotropic stiffnesses (van Dijk et al., 2020) and multi-axial loading conditions (De Lorenzis and Maurini, 2021).

The phase-field model (2.3) is formulated within the context of brittle fracture and small strain elasticity. Extensions to finite deformations (Hesch and Weinberg, 2014; Miehe et al., 2016) and ductile fracture (Ambati et al., 2016; Kuhn et al., 2016) are, however, well established. Furthermore, applications of phase-field models to dynamic fracture problems were proposed (Borden et al., 2012; Mandal et al., 2020; Ren et al., 2019; Weinberg and Wieners, 2022) which rely on continuum wave equations instead of the quasi-static case. In these models, typically observed dynamical effects such as crack branching (Sun et al., 2021) can be modeled (Hofacker and Miehe, 2012).

Phase-field models may be used to simulate crack initiation and propagation on the component scale where the material properties are often modeled as isotropic and homogeneous. Moreover, models which specifically account for heterogeneities on the microscale were established (Kuhn et al., 2015; Chen et al., 2019; Ernesti et al., 2020).

Additionally, several extensions accounting for anisotropic crack resistances were proposed. Francfort and Marigo (1998) already proposed a way to incorporate a direction dependent crack resistance into their model. Focardi (2001) established a Γ -convergence result for an Ambrosio-Tortorelli approximation (Ambrosio and Tortorelli, 1990) of a Mumford-Shah functional with a direction dependent surface term. This result may be applied to the weak form of the Francfort-Marigo problem in case of anti-plane shear, neglecting irreversibility. Implementations of phase-field models with an anisotropic crack resistance were proposed

by Clayton and Knap (2014; 2015), who introduced a geometrically nonlinear phase-field model and expressed the anisotropy of the crack resistance via a second order tensor. Na and Sun (2018) and Bryant and Sun (2018) proposed a method coupling crystal plasticity with an anisotropic phase field fracture model. Expressing a general, anisotropic crack resistance via a second order tensor allows for only one weak direction within the plane. Nguyen et al. (2017) proposed a multi phase-field approach to consider more complex forms of anisotropy. Other approaches rely on a higher order phase-field model which accounts for second derivatives of the damage variable d . In this case, a fourth order crack resistance tensor may account for a more general case (Li et al., 2015; Teichtmeister et al., 2017; Kakouris and Triantafyllou, 2019; Ma and Sun, 2020).

Kuhn et al. (2015) investigated the use of different degradation functions within phase-field fracture models. Furthermore, different approximations of the crack energy, which establish a different interpretation of phase-field models were proposed (Pham et al., 2011). Phase-field models exhibit similarities to non-local damage models (Jirasek, 1998) and may be treated as such, instead of as the regularization of a free-discontinuity problem. In this interpretation, the phase-field width l serves as a material parameter (Kuhn, 2013) which influences the ultimate tensile strength of the material based on a one-dimensional analysis of the model. Additionally, length-scale insensitive methods were proposed (Wu and Nguyen, 2018) which are referred to as cohesive phase-field fracture.

2.2 Characterization of digital microstructures²

2.2.1 Objectives

Materials of industrial interest often display a heterogeneous underlying microstructure which influences the macroscopic material behavior. Let us consider an injection molded structural component made from a polymer material. For improving the stiffness of the component while keeping its lightweight potential, filler materials, such as glass fibers, are commonly added to the polymer melt before being modeled. As a result, the component's material is given by a fiber reinforced polymer which has a complex microstructure determined by the arrangement of the fibers. Often, both polymer and glass are considered isotropic. However, the macroscopic material behavior is strongly dependent on the fiber arrangement on the microscale which may induce a distinctly anisotropic material behavior on the component scale.

Due to the infinite number of possible arrangements on the microscale, an exhaustive experimental characterization of a composite's microstructure dependent anisotropic behavior may prove challenging. Hence, homogenization-based multi-scale methods have been developed to simulate the material behavior by explicitly taking the microstructural information into account, see Matouš et al. (2017) for a recent overview. These homogenization techniques compute the effective response of the heterogeneous material, taking the material behavior of the constituents and the microstructure into account. Therefore, the microstructure has to be quantified in terms of suitable data, which is where microstructure characterization comes into play.

² This section is based on the introduction of Ernesti et al. (2022). Changes to the text have been made in order to include it into the structure of this work.

2.2.2 State of the art

A common image-based microstructure-characterization method is scanning a material sample via micro-computed tomography (μ -CT) (Schladitz et al., 2017; Cnudde et al., 2009). After tomographic reconstruction, the local mass density of a material is determined and stored as 3D voxel data. In case of a two-phase material and after some processing, this voxel data may be interpreted as the characteristic function of the microstructure, i.e., the function which attains the value 1 for one phase, and the value 0 for the complementary phase. Correctly segmenting μ -CT scans requires a certain contrast in the absorption rates of the constituents to be applicable, for instance for porous media or for a variety of composite materials.

The mechanical behavior of composite and porous materials is strongly influenced by the volume fractions of the phases. If the characteristic function is accurately resolved by the μ CT-scan, the volume fraction can be computed accurately by numerical integration. With the volume fraction at hand, bounds that predict the possible range of effective elastic and thermal material properties may be established, see Voigt (1889) and Reuss (1929). However, for a high material contrast, these bounds span a wide range and hence provide limited information.

For higher accuracy, additional information is required, see Torquato (2002) for an overview. For instance, n -point correlation functions (Brown, 1955; Torquato and Stell, 1982) provide suitable additional information. Their applicability for anisotropic materials, however, is limited due to the high associated computational effort, see Eriksen et al. (2004).

For the class of fiber-reinforced composites, specific microstructure-characterization techniques have been established. In addition to the fiber volume-fraction, common characteristics include the fiber aspect-ratio and fiber-orientation tensors of second and fourth order (Kanatani, 1984; Advani and Tucker, 1987), see for instance Müller and Böhlke (2016). A variety of methods for computing fiber-orientation tensors

based on volumetric images has been established (Robb et al., 2007; Daniels et al., 2007). A common approach is based on the so-called structure tensor (Krause et al., 2010).

For porous structures, different microstructure characteristics are of interest. For instance, the tortuosity (Neumann et al., 2019) and chord-length distribution (Matheron, 1975; Torquato, 2002), as well as the pore-size distribution (Kate and Gokhale, 2006) are investigated. These measures are primarily responsible for the effective (isotropic) permeability of the porous medium in question.

Polycrystalline materials require a different approach. Typically, the grains differ only in their crystalline orientation, but have identical absorption rates. Hence, μ -CT scans are of limited use. Instead, for reconstructing the 3D-microstructure of polycrystalline materials, focused ion beam - scanning electron microscopy (FIB-SEM) (Bansal et al., 2006; Groeber et al., 2006; Zaefferer et al., 2008) or electron back-scattering diffraction (EBSD) (Korte et al., 2011; Adams and Olson, 1998; Larsen et al., 2002) are preferred. Primary microstructure characteristics of polycrystalline materials are the grain-size distribution (morphological texture) (Döbrich et al., 2004) and the orientation distribution (crystallographic texture) (Bunge, 1982; Böhlke, 2006; Böhlke and Lobos, 2014; Junk et al., 2012; Böhlke et al., 2010).

From a theoretical point of view, most materials undergoing a manufacturing process are influenced by stochastic factors, for instance due to slight variations in the composition or the seemingly chaotic behavior of the processing condition as a result of a high sensitivity to initial and boundary conditions. Still, the experimentally determined effective properties of such composites are often surprisingly deterministic. These observations may be formalized by the theory of stochastic homogenization (Kozlov, 1979; Papanicolaou and Varadhan, 1981) which forms the basis for modern computational multi-scale methods. We refer to section 2.4.2 where we discuss these homogenization methods in the context of brittle fracture.

2.3 Phase-field fracture on heterogeneous microstructures³

In this section, we investigate the classical phase-field fracture problem on heterogeneous microstructures. Classical here means that the phase-field functional we consider uses both a quadratic damage degradation function and a quadratic damage penalty term. We derive the governing equations in section 2.3.1. We introduce several energy splittings from the literature (Amor et al., 2009; Miehe et al., 2010b). Additionally, we follow Boeff et al. (2015) to adjust the phase-field model for heterogeneous material properties.

To solve the governing equations we rely on FFT-based solvers and discretizations on regular voxel grids, as well as a fully implicit scheme which is first order in time. To be more precise, we use a fast gradient-method for the staggered treatment of the fully-coupled nonlinear phase-field fracture system. Fast gradient-methods add an inertial term to classical gradient schemes, dramatically accelerating the latter, and exhibit good performance also for non-convex problems of interest, with recent research triggered by machine learning applications. The theoretical reasons are still under investigation (Jin et al., 2018), but it is commonly believed that the inertial term helps navigating through non-convex energy landscapes more rapidly, ignoring local stationary points and flat ravines. Here, we rely on the heavy-ball method, first introduced by Polyak (1964).

We investigate phase-field fracture on the complex microstructures of fiber reinforced composites in sections 2.3.3 and 2.3.4.

³ This section is based on Ernesti et al. (2020) which introduces a novel solver for phase-field fracture on heterogeneous microstructures. This solver was first presented in my masters thesis (Ernesti, 2018) and the publication (Ernesti et al., 2020) provides an extension thereof. We exclude the detailed discussion on the solver and its performance and provide only a selected choice of numerical examples which serve our purpose here.

2.3.1 Continuous model under investigation

Let $Y = [0, L_1] \times [0, L_2] \times [0, L_3]$ be a rectangular unit cell. Suppose two heterogeneous elastic strain energy potentials $\psi^+, \psi^- : Y \times \text{Sym}(3) \rightarrow \mathbb{R}$ are given, where $\text{Sym}(3)$ denotes the space of symmetric two-tensors in \mathbb{R}^3 . ψ^- measures the stored elastic energy per unit volume which is not degraded, whereas ψ^+ is responsible for the part which degrades as a result of damage. These potentials shall sum to the total (local) stored elastic energy density $\psi : Y \times \text{Sym}(3) \rightarrow \mathbb{R}$, i.e., the equation

$$\psi(x, \varepsilon) = \psi^+(x, \varepsilon) + \psi^-(x, \varepsilon) \quad (2.4)$$

shall hold for all $x \in Y$ and $\varepsilon \in \text{Sym}(3)$. For the present manuscript, we set $\psi(x, \varepsilon) = \frac{1}{2}\varepsilon : \mathbb{C}(x) : \varepsilon$ with a heterogeneous linear elastic tensor field \mathbb{C} .

Let furthermore a subvolume $\tilde{Y} \subseteq Y$ be given, containing all microscopic points where the material can be damaged. (In particular, \tilde{Y} may be equal to Y .) Denote by χ the characteristic function of \tilde{Y} , i.e., the function which equals unity on \tilde{Y} and vanishes elsewhere.

For a given macroscopic strain $E \in \text{Sym}(3)$, the functional under consideration reads

$$F(u, d) = \int_Y f(x, d(x))\psi^+(x, \varepsilon) + \psi^-(x, \varepsilon) + G_c \left(\frac{d^2}{2l} + \frac{l}{2} \|\nabla d\|^2 \right) dx, \quad (2.5)$$

a function of the periodic displacement fluctuation field $u : Y \rightarrow \mathbb{R}^3$ and the periodic damage field $d : Y \rightarrow \mathbb{R}$. Here, $\varepsilon = E + \nabla^s u$ denotes the total strain involving the symmetrized gradient operator ∇^s ,

$$f(x, d) = k_0 + (1 - k_0)(1 - \chi(x)d)^2 \quad (2.6)$$

is the damage degradation function involving a relative residual stiffness $k_0 > 0$ and $G_c > 0$ stands for the critical energy release rate according

to Griffith (1921). The latter is assumed to be homogeneous for now as we specify the material points that may damage via the characteristic function χ . The length parameter $l > 0$ describes the width of the transition zone between broken and intact material, and is decisive for crack nucleation. Before continuing, we discuss the types of splittings (2.4) we will consider in this section, where we assume \mathbb{C} to be isotropic, i.e., its application may be written as

$$\begin{aligned} \mathbb{C}(x) : \varepsilon &= 2\mu(x)\varepsilon + \lambda(x) \operatorname{tr}(\varepsilon) \operatorname{Id} = 2\mu(x)\varepsilon' + K(x) \operatorname{tr}(\varepsilon) \operatorname{Id}, \\ \varepsilon &\in \operatorname{Sym}(3), \quad x \in Y, \end{aligned} \quad (2.7)$$

for positive functions $\lambda, \mu, K : Y \rightarrow \mathbb{R}$, which encode the heterogeneous Lamé's constants and the compression modulus, and the deviatoric strain $\varepsilon' = \varepsilon - \frac{1}{3} \operatorname{tr}(\varepsilon) \operatorname{Id}$. In this isotropic case we distinguish three different energy splittings:

1. Trivial splitting: no distinction between tension and compression

$$\psi^+(x, \varepsilon) = \frac{1}{2} \varepsilon : \mathbb{C}(x) : \varepsilon, \quad \psi^-(x, \varepsilon) \equiv 0, \quad x \in Y, \quad \varepsilon \in \operatorname{Sym}(3). \quad (2.8)$$

2. The spherical splitting of Amor et al. (2009)

$$\begin{aligned} \psi^+(x, \varepsilon) &= \mu(x) \|\varepsilon'\|^2 + 2\lambda(x) \langle \operatorname{tr}(\varepsilon) \rangle_+^2, \\ \psi^-(x, \varepsilon) &= 2\lambda(x) \langle \operatorname{tr}(\varepsilon) \rangle_-^2, \\ x &\in Y, \quad \varepsilon \in \operatorname{Sym}(3), \end{aligned} \quad (2.9)$$

where $\langle \cdot \rangle_{\pm}$ denote the McCauley brackets

$$\langle \cdot \rangle_+ = \max(0, \cdot) \quad \text{and} \quad \langle \cdot \rangle_- = \min(0, \cdot).$$

3. The eigenvalue splitting of Miehe et al. (2010b)

$$\begin{aligned} \psi^\pm(x, \varepsilon) &= \mu(x)(\langle \varepsilon_1 \rangle_\pm^2 + \langle \varepsilon_2 \rangle_\pm^2 + \langle \varepsilon_3 \rangle_\pm^2) + \lambda(x)\langle \text{tr}(\varepsilon) \rangle_\pm^2, \\ x \in Y, \quad \varepsilon &\in \text{Sym}(3), \end{aligned} \quad (2.10)$$

where ε_i ($i = 1, 2, 3$) denote the eigenvalues of the symmetric tensor ε . The last two splittings enable the model to distinguish tensile and compressive loading. More precisely, Chambolle et al. (2018) proved that the phase-field model using Amor's splitting Γ -converges for $l \rightarrow 0$ to the Francfort–Marigo model with a constraint of non-interpenetration. In the same paper it was shown that the splitting of Miehe et al. (2010b) converges to a Francfort-Marigo model which restricts crack opening to shear loading, which is typical, for instance, for concrete.

Suppose that μ and λ are essentially bounded from above. Then, for all three splittings considered, the phase-field functional (2.5) is well-defined on the product Banach space $V \times Z$, where V contains all periodic H^1 displacement vector fields with mean zero and Z is the intersection of periodic scalar-valued H^1 damage fields with $L^\infty(Y)$. The restriction to essentially bounded damage fields ensures that the first term in (2.5) is integrable.

It can be shown, see Burke et al. (2013), that F is Gâteaux-differentiable on $V \times Z$ with directional derivative

$$DF(u, d)[v, z] = D_u F(u, d)[v] + D_d F(u, d)[z] \quad (2.11)$$

for $u, v \in V, d, z \in Z$. The directional derivatives are given by

$$D_u F(u, d)[v] = \int_Y \left[f(d) \frac{\partial \psi^+}{\partial \varepsilon}(\varepsilon) + \frac{\partial \psi^-}{\partial \varepsilon}(\varepsilon) \right] : \nabla^s v \, dx, \quad \varepsilon \equiv E + \nabla^s u, \quad (2.12)$$

where we, for simplicity of notation, suppress the x -dependence, and

$$D_d F(u, d)[z] = \int_Y \frac{\partial f}{\partial d}(d) \psi^+(\varepsilon) z + G_c \left[\frac{dz}{l} + l \nabla d \cdot \nabla z \right] dx. \quad (2.13)$$

We say that (u, d) is a critical point of F if both $D_u F(u, d) = 0$ in V' and $D_d F(u, d) = 0$ in Z' hold. Integrating by parts, it is readily seen that such a critical point (u, d) satisfies both the balance of linear momentum

$$\operatorname{div}(\sigma)(\varepsilon, d) = 0 \quad (2.14)$$

with the stress

$$\sigma(\varepsilon, d) = f(d) \frac{\partial \psi^+}{\partial \varepsilon}(\varepsilon) + \frac{\partial \psi^-}{\partial \varepsilon}(\varepsilon), \quad \varepsilon \equiv E + \nabla^s u, \quad (2.15)$$

and an advection-diffusion-type equation for the damage variable

$$0 = \frac{\partial f}{\partial d}(\cdot, d) \psi^+(\varepsilon) + G_c \left[\frac{d}{l} - l \Delta d \right],$$

which can, for later reference, be equivalently rewritten in the form

$$(1 + \alpha)d - l^2 \Delta d = \alpha \quad (2.16)$$

involving the function $\alpha : Y \rightarrow \mathbb{R}$ determined by the equation

$$\alpha(x) = \frac{2l}{G_c} (1 - k_0) \chi(x) \psi^+(x, \varepsilon(x)). \quad (2.17)$$

To conclude the discussion of the continuous model, several remarks are in order.

1. The model we presented does not account for irreversibility, i.e., it is purely elastic. Such a model may be reasonable for monotonic loading, where, in addition, no local unloading occurs. To account for irreversibility, several strategies have been developed. Classically, the

constraint $\dot{d} \geq 0$ is enforced, and solved by, for instance, augmented Lagrangian methods (Wheeler et al., 2014), primal-dual active-set methods (Heister et al., 2015) or penalty formulations (Gerasimov and De Lorenzis, 2019).

An alternative approach is based on the usage of a suitable history-field, as pioneered by Miehe et al. (2010a). More precisely, for a given (pseudo-)time-dependent strain loading

$$E : [t_0, t_1] \rightarrow \text{Sym}(3),$$

the history-field based model seeks the displacement field and the damage field

$$u : [t_0, t_1] \times Y \rightarrow \mathbb{R}^3 \quad \text{and} \quad d : [t_0, t_1] \times Y \rightarrow \mathbb{R},$$

s.t. the balance of linear momentum (2.14) is satisfied, for

$$\varepsilon(t, x) = E(t) + \nabla^s u(t, x),$$

together with the advection-diffusion-type equation (2.16) for the damage variable with the forcing term

$$\alpha(t, x) = \frac{2l}{G_c} (1 - k_0) \chi(x) \sup_{t_0 \leq \tau \leq t} \psi^+(x, \varepsilon(\tau, x)). \quad (2.18)$$

Thus, the entire history of the elastic energy density is taken into account, in contrast to equation (2.17). From an implementation point of view, using either (2.17) or (2.18) does not make much of a difference, because equation (2.16) needs to be solved in both cases. However, the resulting models are different, see (Ernesti et al., 2020, section 4.3.6).

2. The model we presented is quasi-static, and allows for brutal fracture. However, some care has to be taken, as brutal fracture involves cracks

propagating with infinite speed. This violates physical experience, where cracks propagate with finite speed. To account for finite-speed crack-propagation, Ginzburg-Landau-type equations (Miehe et al., 2010b; Kuhn, 2013) replacing (2.16) may be used. More precisely, a multiple of \dot{d} is added to the equation (2.16). Upon a backwards Euler time-discretization, the resulting equation is of similar type as equation (2.16) and may be treated by the same techniques, see Chen et al. (2019), section 2. However, for the sake of brevity, we will consider the unregularized form (2.16). Investigating this choice has the added benefit that our computational techniques do not deteriorate for vanishing viscous regularization (or, equivalently, infinite phase-field mobility parameter).

3. The reader may wonder about the particular form of the energy functional (2.5) that we consider. In particular, the appearance of the set $\tilde{Y} \subseteq Y$ (and its associated characteristic function) are non-standard.

Most of the models and computational strategies for phase-field fracture have been developed with homogeneous materials in mind. Consider, for the sake of exposition and $l > 0$, the functional

$$G(u, d) = \int_Y g(x, d) \psi^+(x, \varepsilon) + \psi^-(x, \varepsilon) + \gamma \left[\frac{d^2}{2l} + \frac{l}{2} \|\nabla d\|^2 \right] dx \quad (2.19)$$

with $g(x, d) = k_0 + (1 - k_0)(1 - d)^2$ and a heterogeneous crack resistance $\gamma : Y \rightarrow (0, \infty)$. The corresponding Euler-Lagrange equations consist of the balance of linear momentum (2.14) (with g replacing f in (2.15)) and the phase-field equation

$$0 = \frac{\partial g}{\partial d}(\cdot, d) \psi^+(\varepsilon) + \frac{d}{l} - l \operatorname{div}(\gamma \nabla d). \quad (2.20)$$

Thus, in contrast to the phase-field equation used in this work (2.16), equation (2.20) involves gradients of the crack resistance γ , compli-

cating the numerical treatment.

Instead, we chose to work with a homogeneous crack resistance G_c , but restrict the domain, where cracks may occur, to the subset $\tilde{Y} \subseteq Y$. Thus, we consider \tilde{Y} as a homogeneous elastic-brittle material with internal variable field d , whose evolution is governed by the non-local PDE (2.17).

Clearly, our framework can be extended to heterogeneous crack resistances as follows. Suppose γ is piece-wise constant, i.e., might be written as $\gamma = \sum_{k=1}^K G_{c,k} \chi_k$, where the $G_{c,k}$ are positive and the sets corresponding to χ_k form a non-overlapping partition of Y . Then, the natural extension of (2.5) is the functional

$$F^K(u, d_1, \dots, d_K) = \int_Y f^K(x, d_1, \dots, d_k) \psi^+(x, \varepsilon) + \psi^-(x, \varepsilon) \\ + \sum_{k=1}^K G_{c,k} \left[\frac{d_k^2}{2l} + \frac{l}{2} \|\nabla d_k\|^2 \right] dx,$$

involving K distinct periodic damage variables d_1, \dots, d_K , and f^K reads

$$f^K(x, d_1, \dots, d_K) = k_0 + (1 - k_0) \left(1 - \sum_{k=1}^K \chi_k(x) d_k(x) \right)^2.$$

Thus, also K different phase-field equations need to be solved for this approach. For this section, we restrict to a single brittle phase \tilde{Y} , characterized by a single crack resistance G_c , and consider the complement of \tilde{Y} in Y to deform elastically.

The principal advantage of our approach is that, for the phase-field equation (2.16), the coefficients in front of the derivatives are homogeneous, implicating a simplified treatment by FFT-based methods compared to the formula (2.20).

4. Due to the χ -term in (2.17) and (2.18), α is concentrated on the chosen region \tilde{Y} . Similarly, $f(x, d) = 1$ for $x \notin \tilde{Y}$. Thus, d has no direct effect on the mechanical behavior of the composite outside of \tilde{Y} .

Formally setting $l = 0$ in (2.16) shows that d vanishes outside of \tilde{Y} . For positive l , the damage field may also be positive in $Y \setminus \tilde{Y}$. However, for small l , d will be small in $Y \setminus \tilde{Y}$, as well. Rather, this phenomenon is closely tied to computing the energy dissipated by creating a crack,

$$\int_Y G_c \left[\frac{d^2}{2l} + \frac{l}{2} \|\nabla d\|^2 \right] dx,$$

as a part of the functional (2.5), correctly. We have learned this approach from Boeff et al. (2015), who call it "non-local phase damage".

2.3.2 Numerical setup

In order to solve the governing equations (2.14) and (2.16), suitable discretizations and solvers are required. In the work at hand we rely on an FFT-based solver framework and discretization methods on regular voxel grids. We integrated this into an in-house FFT-based computational micromechanics solver, based on Python 3.7 with Cython extensions. This in-house code is strain-based, i.e., the primary variable is the (compatible) strain field instead of the displacement field. Furthermore, we consider periodic boundary conditions. Thus, we seek a periodic strain field with prescribed mean value E . We rely on a staggered grid discretization (Schneider et al., 2016) to discretize the strain field. For the damage variable we rely on the original Moulinec–Suquet discretization (Moulinec and Suquet, 1994; 1998).

In each load step we solve the balance of linear momentum using an accelerated gradient descent method, namely the heavy-ball method, first introduced by Polyak (1964). In each iteration we solve the advection-diffusion type equation for the phase-field variable using gradient descent. I introduced this approach in my master thesis Ernesti (2018) and

for a detailed discussion I refer to (Ernesti et al., 2020, section 3).

To change between load steps, affine extrapolation is used for the strain, as described by Moulinec and Suquet (1998), and the last converged damage field is taken as initial guess for the succeeding step.

For the mechanical sub-problem, we use the convergence criterion provided in (Ernesti et al., 2020, equation (3.4)), with a prescribed tolerance tol . In section 2.3.3 we chose $\text{tol} = 10^{-5}$ and in section 2.3.4 we chose $\text{tol} = 10^{-4}$. The damage sub-problem is terminated upon satisfying the criterion in (Ernesti et al., 2020, equation(3.17)) with $\text{tol} = 10^{-6}$, similar to Chen et al. (2019).

The average stress Σ is computed by volume averaging

$$\Sigma := \langle \sigma \rangle_Y \equiv \frac{1}{|Y|} \int_Y \sigma \, dx$$

of the individual components of the stress tensor.

All computations were performed on a desktop computer with a 6-core Intel i7 CPU and 32GB RAM.

	E in GPa	ν	G_c in N/mm
Polyamide	3.45	0.39	0.1
E-glass	72.00	0.22	-

Table 2.1: Material parameters of polyamide and E-glass (Ernesti, 2018)

h in μm	l in μm	k_0
2	6	10^{-4}

Table 2.2: Numerical parameters

2.3.3 Phase-field fracture for a continuous-fiber reinforced brittle composite

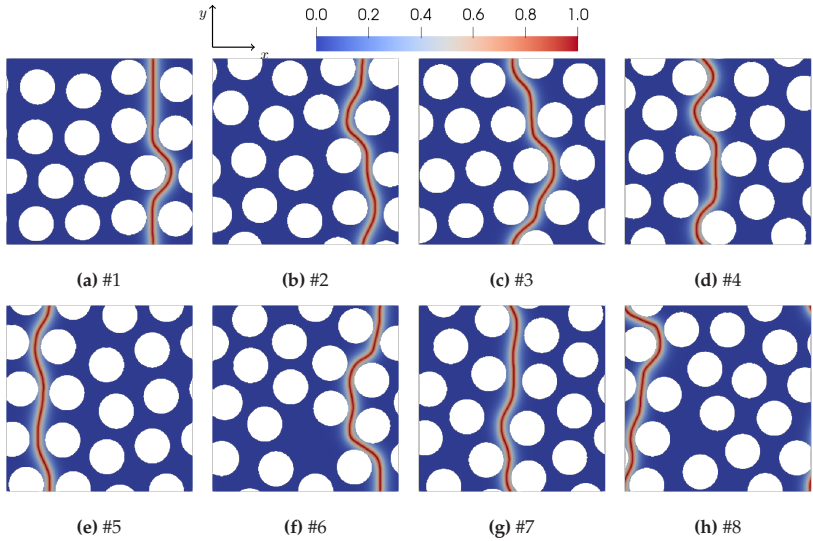


Figure 2.3: Damage fields and crack paths upon final failure for eight different microstructures. (Ernesti et al., 2020)

In this section, we investigate the phase-field fracture behavior of continuous-fiber reinforced composites. This allows us to rely on 2D structures. We consider the inclusions linear elastic and the matrix material brittle, see Tab. 2.1 for the material parameters. The numerical parameters, i.e., the pixel length h , the phase-field width l and the remaining stiffness k_0 are listed in Tab. 2.2. These parameters have been selected carefully in (Ernesti et al., 2020, section 4). We consider a stochastic arrangement of the fillers. The fiber volume-fraction is chosen as 45%, with 16 fibers placed within the volume, using the Torquato-Jiao

algorithm (Torquato and Jiao, 2010). We rely upon images of a resolution of 256×256 pixels.

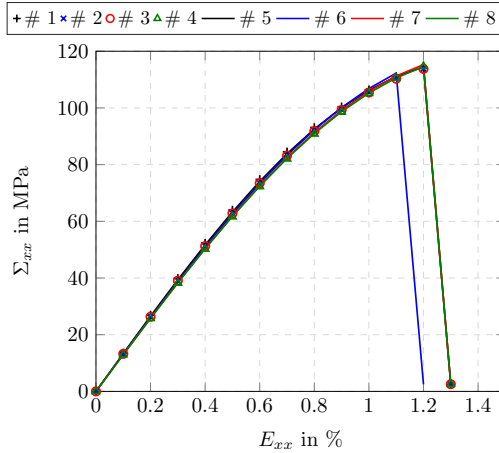


Figure 2.4: Stress-strain diagram upon uni-axial extension, on 8 different microstructures, see Fig. 2.3. (Ernesti et al., 2020)

Eight different microstructures were generated, see Fig. 2.3. These microstructures were subjected to uni-axial strain loading in x -direction and 0.1%-steps until complete failure of the structure. The resulting stress-strain diagrams for the stresses perpendicular to the fiber direction are shown in Fig. 2.4. Only small scatter is observed prior to failing. Also, the post-critical stresses are identical for the different microstructures.

structure	E_{xx}^{crit} in %	Σ_{xx}^{max} in MPa
#1	1.3	114.10
#2	1.3	113.82
#3	1.3	113.76
#4	1.3	114.66
#5	1.3	114.44
#6	1.2	112.27
#7	1.3	115.27
#8	1.3	114.58
$\mu \pm \sigma$	1.29 ± 0.03	114.11 ± 0.83

Table 2.3: Strain and stress at failure on the 8 microstructure realizations, see Fig. 2.3.

Seven of the eight microstructures fail at 1.3% axial strain, see Tab. 2.3. Also, the maximum effective axial-stresses are very similar, at about 114MPa and a standard deviation below 1MPa. Taking into account the differences in the resulting crack paths, see Fig. 2.3, this may be surprising.

2.3.4 Phase-field fracture for a short-fiber reinforced brittle composite

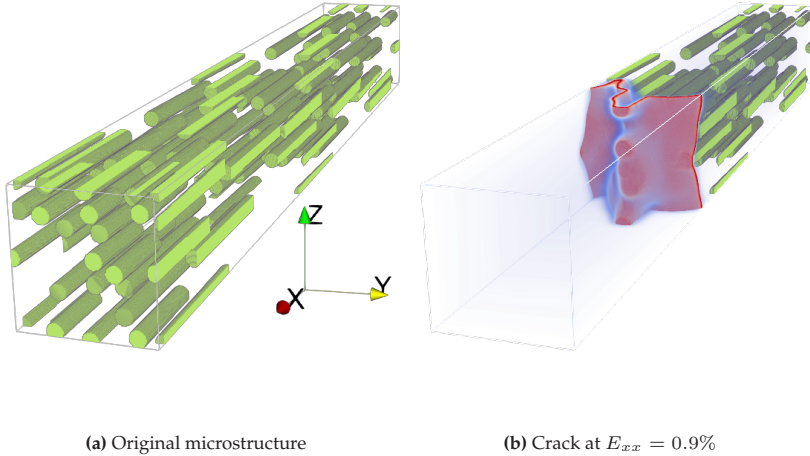


Figure 2.5: Microstructure and crack surface for uni-axial strain loading in x -direction. (Ernesti et al., 2020)

As our final example for phase-field fracture, we consider a short-fiber reinforced composite with distributed fibers. The material parameters are identical to the previous section, listed in Tab. 2.1.

Aligned fibers with a length of $320\mu\text{m}$ and a diameter of $32\mu\text{m}$ were dispersed in a periodic unit cell with dimensions $256 \times 256 \times 2048\mu\text{m}^3$, up to a fiber volume fraction of 18%. Both the fiber diameter and the cell dimensions were chosen carefully to ensure that the numerical parameters in Tab. 2.2 can be used, as well.

The resulting microstructure, see Fig. 2.5a, was generated by the Sequential Addition and Migration algorithm (Schneider, 2017) and discretized by $128 \times 128 \times 1024$ voxels.

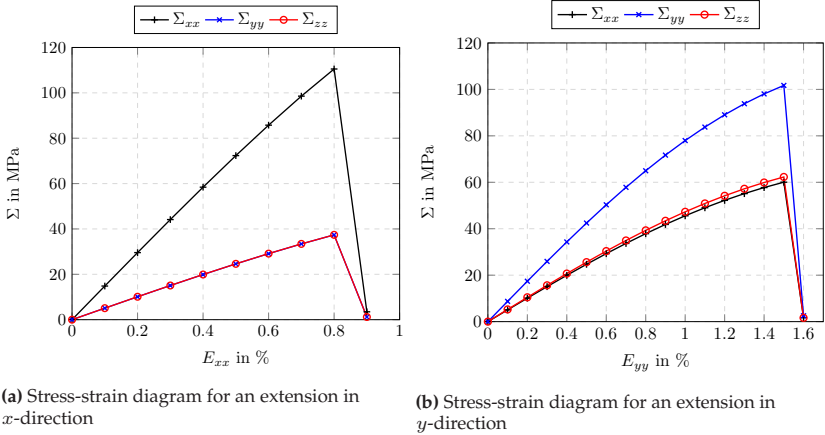
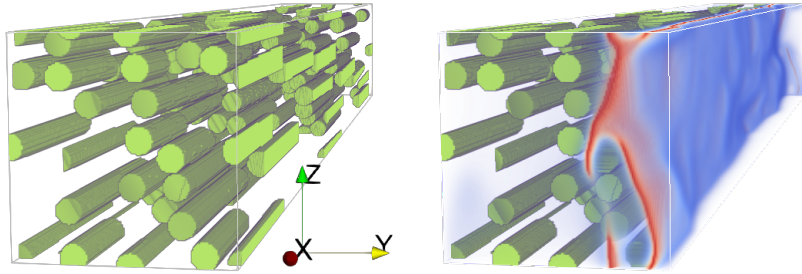


Figure 2.6: Stress-strain diagrams for extensions in x - and y -directions. (Ernesti et al., 2020)

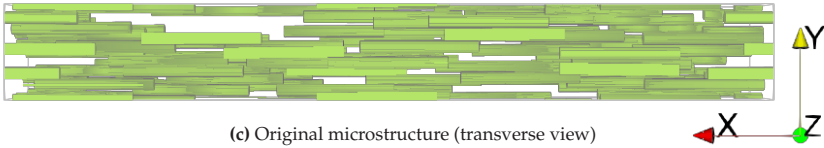
The structure was subjected to uni-axial strain loading, successively increasing the level by 0.1% per steps. The structure failed at $E_{xx} = 0.9\%$, and the corresponding stress-strain diagrams are shown in Fig. 2.6a. The stress-strain diagram is linear elastic prior to failure. Also, in the diagram, the stresses transversal to the fiber directions are indistinguishable.

The crack upon failure is shown in Fig. 2.5b. The crack surface forms around the fibers, showing matrix cracking and fiber pull-out. Furthermore, we conducted a similar experiment as before, but with loading in E_{yy} -direction. The structure failed after 16 0.1% steps. The stress-strain diagram is shown in Fig. 2.6b. In contrast to loading in fiber direction, a damaging effect is seen in the stress-strain curves. Furthermore, upon loading, the symmetry between Σ_{xx} and Σ_{zz} is slightly broken. The crack upon failure is shown in Fig. 2.7b and runs entirely through the matrix. A transverse view of the crack is shown in Fig. 2.7d. The crack is straight in the x - z -plane, but avoids the individual fibers.

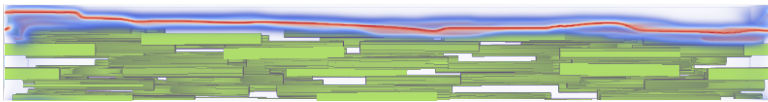


(a) Original microstructure

(b) Crack at $E_{yy} = 1.6\%$



(c) Original microstructure (transverse view)



(d) Crack at $E_{yy} = 1.6\%$ (transverse view)

Figure 2.7: Crack surface and stress-strain diagram for uni-axial strain loading in y -direction. (Ernesti et al., 2020)

2.3.5 Conclusions

In this section, we presented an approach to compute phase-field fracture on heterogeneous microstructures. We discussed the governing equations which rely on a strategy by Boeff et al. (2015) to deal with heterogeneous material parameters. We solved these equations using FFT-based fast gradient solvers and discretizations on a regular grid. Finally, we investigated phase-field fracture on complex microstructures of fiber reinforced composites.

The strategy presented here follows an approach often conducted in FFT-based micromechanics for the homogenization of complex materials, see Schneider (2021a) for an overview: A cell formula for the balance of linear momentum on a stochastic microstructure cell is conducted. This cell is considered large enough in order to be *representative* for the microstructure of the considered material. Using FFT-based solvers for this cell problem and extracting the local fields allows to compute the effective stress-strain relation via averaging. For linear elastic materials this allows to compute an effective stiffness which may then be used for simulations on the component scale. For hardening type materials, upscaling approaches may be conducted (Gajek et al., 2021). For softening type materials, however, which includes phase-field fracture, this relation of effective stresses and strains provides limited information (Gitman et al., 2007). Hence, the question remains how to extract *effective* properties in the context of fracture mechanics which result from a homogenization result.

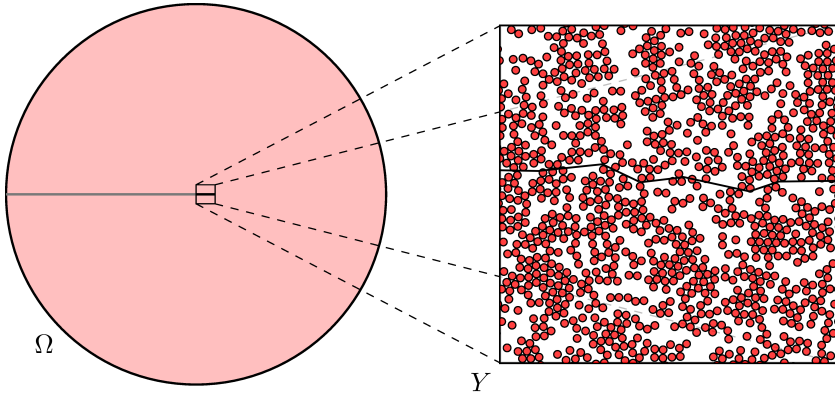


Figure 2.8: Schematic of a crack increment in a microstructured material (Ernesti and Schneider, 2021, Fig. 2).

2.4 Homogenization methods for brittle fracture⁴

2.4.1 Objectives

As we pointed out in section 2.2, materials of industrial interest often exhibit a stochastic microstructure which strongly influences the macroscopic material behavior. To perform mechanical simulations on the component scale by taking the microstructure into account, multi-scale methods are often conducted. These multi-scale methods are well established for hardening material behavior, i.e., a monotone stress-strain relation, see Matouš et al. (2017) for an overview. In this context, homogenization methods (Papanicolaou and Varadhan, 1981; Kozlov, 1978) play a key role. Building upon a well-defined

⁴ This section is based on the introductory sections of Ernesti and Schneider (2021; 2022) as well as section 1 and 2 of Ernesti et al. (2023) and provides an extension thereof.

mathematical foundation, these methods aim to establish *effective* models based on the arrangement of the microstructure and the governing material behavior of the different phases on the microscale. Computational approaches typically rely on simulations on finite cells which represent the underlying microstructure. If these are chosen sufficiently large, these are called representative volume elements (RVEs) (Drugan and Willis, 1996; Kanit et al., 2003).

These well established homogenization and multi-scale methods face difficulties when leaving the realm of hardening-type materials. In the presence of a propagating crack the stress-strain relation is no longer monotonic and thus softening of the material occurs. One example is given by Gitman et al. (2007) who performed numerical simulations using a non-local damage model. They showed that in the post-peak loading regime, the average stress response tends to zero as the size of the volume element goes to infinity. In particular, the strategy of computing effective quantities via simulations on representative volume elements – which works well for hardening-type materials – leads to impractical results in case of softening.

Classically, homogenization relies on a distinct scale separation. More precisely, the macroscopic displacement or stress fields should vary slowly compared to the local fields on the microscale. In the classical linear elastic fracture mechanics setting and for an evolving crack, the stress singularity at the crack tip typically prohibits such a scale separation. Indeed, in classical linear elastic homogenization, the displacement field is split into a smooth macroscopic and a highly-oscillating microscopic part. Upon homogenization, the relationship between the macroscopic and the microscopic displacement fields is simplified to a one-way coupling. This permits the transfer of information from the microscale to the macro scale via the effective stiffness. In the case of an evolving crack, the displacement field is no longer smooth at the crack tip, even for a homogeneous medium. In particular, the classical macro-micro decomposition, which was

successful for linear elastic homogenization, loses its promise. Moreover, the evolution of the crack needs to be accounted for at both scales.

From another perspective, let us consider a non-local damage model. The non-locality is necessary to obtain mesh-independent results for a corresponding finite-element model. Thus, two scales are present in such a multi-scale non-local damage model, the typical scale of heterogeneity and the length scale of the nonlocality. In upscaling, the scale of heterogeneity is small, and we wish to pass to the limit of vanishing heterogeneity size. On the one hand, if we fix the non-local length scale, the nonlocality would exceed the size of the heterogeneities upon homogenization. On the other hand, tying the non-local length scale to the size of the heterogeneities would recover the mesh-dependence of the model upon homogenization, and thus rendering the procedure illegitimate. Nevertheless, computations of phase-field fracture on microstructures may be pursued, see section 2.3. Furthermore using non-local damage models (Boeff et al., 2015; Berthier et al., 2014) to simulate crack propagation on microstructures are well established. Unfortunately, connecting these results to macroscopic material properties appears challenging as the apparent stresses for softening materials are inherently size-dependent, see Gitman et al. (2007).

The actual question is: Which model is suitable for the macroscopic modeling of fracture mechanics that results from the homogenization limit of a model on the microscale? An illustration of this procedure is given in Fig. 2.8. In the following section we identify the Francfort-Marigo model of brittle fracture (Francfort and Marigo, 1998) as a suitable candidate.

2.4.2 Homogenization of the Francfort-Marigo model

The strategy pursued in this thesis to homogenizing brittle fracture has been proposed by Schneider (2020) and is based on a homogenization

result by Braides et al. (1996) for free discontinuity problems. For a given domain $\Omega \subset \mathbb{R}^d$ we consider periodic functions $f : \Omega \times \mathbb{R}^d \rightarrow [0, \infty)$ and $g : \Omega \times \mathbb{R} \times S^{d-1} \rightarrow [0, \infty)$ which, for constants $c_1, c_2, c_3, c_4 > 0$ satisfy the growth conditions

$$\begin{aligned} c_1 \|\xi\|^2 &\leq f(x, \xi) \leq c_2(1 + \|\xi\|^2) \quad \forall \xi \in \mathbb{R}^d \quad \text{and} \\ c_3(1 + |z|) &\leq g(x, z, n) \leq c_4(1 + |z|) \quad \forall n \in S^{d-1} \forall z \in \mathbb{R}. \end{aligned} \quad (2.21)$$

Furthermore, we consider the family of functionals

$$B_\eta(v) = \int_\Omega f\left(\frac{x}{\eta}, \nabla v\right) dx + \int_{S_v} g\left(\frac{x}{\eta}, [v], n_v\right) dA. \quad (2.22)$$

Here, $[v] = v^+ - v^-$ denotes the jump of v and n_v denotes the unit normal to the jump set of v , S_v . The length parameter η represents the periodicity of the functions f and g , see Fig. 2.9a for an illustration. We signify f as the bulk term of the energy functional (2.22) and g as the surface term of the functional. Braides et al. (1996) proved that this series of functionals converges to the homogeneous functional

$$B^{\text{hom}}(v) = \int_\Omega f^{\text{hom}}(\nabla v) dx + \int_{S_v} g^{\text{hom}}([v], n_v) dA \quad (2.23)$$

as $\eta \rightarrow 0$ in the sense of Γ -convergence. The expressions f^{hom} and g^{hom} denote the homogeneous bulk and surface terms. Notice that the heterogeneous and the homogeneous functionals are very similar in their structure.

Additionally, Braides et al. (1996) provide specific cell formulas for both effective terms. Consider the infinite periodic continuation of the domain Ω and a finite cuboid cell $[0, L]^d$ within this infinite domain. For the effective bulk function the governing cell formula, equipped with zero

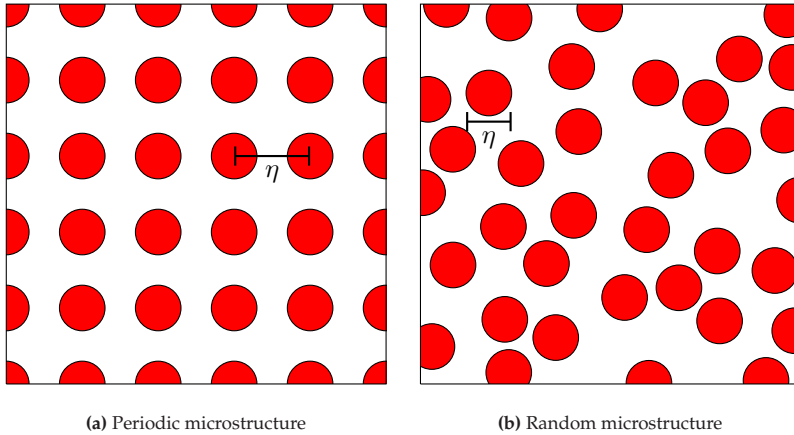


Figure 2.9: Schematic illustration of a periodic microstructure with period η and a stochastic microstructure with characteristic length η .

Dirichlet boundary conditions on the boundary of the cube, reads

$$f^{\text{hom}}(\bar{\xi}) = \lim_{L \rightarrow \infty} \inf_{v \in H_0^1} \frac{1}{L^d} \int_{[0, L]^d} f(x, \nabla v + \bar{\xi}) dx. \quad (2.24)$$

This is a classic formula for the homogenization of bulk energies. Suppose, for instance, $f(x, \xi) = \xi^T A(x) \xi$ for some symmetric, positive definite matrix field A . In this case, the cell formula (2.24) may be interpreted as the homogenization of the static heat equation with A denoting a heterogeneous heat conductivity tensor and ξ denoting the gradient of the temperature field. The resulting effective bulk term provides a formula for the effective heat conductivity A^{eff} (Jikov et al., 1994; Bakhvalov and Panasenko, 1989). Alternatively to the Dirichlet boundary conditions used in (2.24), periodic boundary conditions are also suitable since the effective bulk energy does not depend on the boundary conditions (Sab, 1992). Furthermore, using periodic boundary conditions for a periodic homogenization problem permits to rely on a

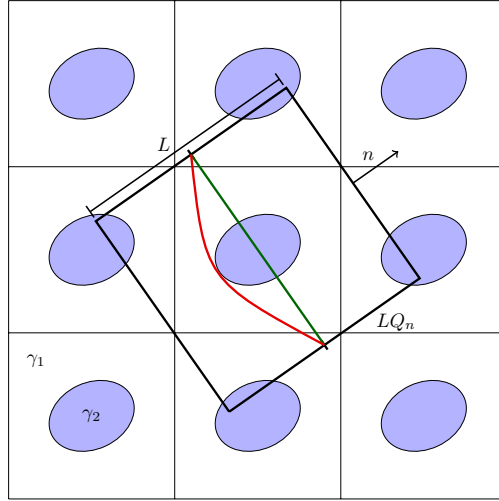


Figure 2.10: Visualization of the computation of the effective crack energy. The cube LQ_n is placed into the periodic structure. Depending on the material contrast γ_2/γ_1 either the green or the red path is favored. The image is a slight modification of Fig. 1 in Ernesti et al. (2023).

single period of the structure. For this case, well established tools for solving the periodic cell problem are available (Moulinec and Suquet, 1994; 1998; Dorn and Schneider, 2019).

For the effective surface term, Braides et al. (1996) proceed as follows. Consider a rotated cuboid LQ_n with its e_1 axis aligned with the normal n and edge length L placed in the infinite periodic continuation of our domain Ω , see Fig. 2.10. The formula for the effective surface term reads

$$g^{\text{hom}}(z, n) = \lim_{L \rightarrow \infty} \inf_{v \in \mathcal{V}} \frac{1}{L^{d-1}} \int_{LQ_n \cap S_v} g(x, [v], n_v) dA \quad (2.25)$$

with the solution space

$$\mathcal{V} = \left\{ v \in \text{SBV}(LQ_n), \nabla v = 0 \text{ a. e.}, \right. \\ \left. v = \begin{cases} z, x \cdot n > 0 \\ 0, x \cdot n \leq 0 \end{cases} \text{ on } \partial LQ_n \right\}. \quad (2.26)$$

and $z \in \mathbb{R}$ quantifying the jump of v at the boundary. This minimization problem is fundamentally different to the problem associated with the bulk term. In (2.25) we seek a function in the space of SBV with minimal g -weighted integral over its jump set. In other words, we seek a g -weighted minimum surface cutting through the rotated cube LQ_n with mean normal n fulfilling the boundary conditions specified in the set \mathcal{V} . Thus, we refer to (2.25) as the minimum cut problem. A visualization of this procedure for a periodic structure of inclusions is shown in Fig. 2.10, where we set $g(\cdot, x, \cdot) = \gamma_2$ in the inclusion and $g(\cdot, x, \cdot) = \gamma_1$ in the surrounding area. In this example we distinguish two cases, depending on the material contrast γ_2/γ_1 . For a large contrast, the minimum surface will avoid the inclusion, illustrated by the red curve, for a small contrast it will cut the inclusion in a straight line. Similar to the bulk term, formula (2.25) is expressed via an infinite volume limit. However, using periodic boundary conditions instead of Dirichlet boundary conditions allows us to rely on a single periodic cell (Braides and Piat, 1995; Chambolle and Thouroude, 2009) via the following procedure. Let $Y \subset \mathbb{R}^d$ be the cuboid cell describing a single period of the periodic functions f and g . Using periodic boundary conditions, the effective crack energy may be computed via

$$g^{\text{hom}}(z, n) = \inf_{v \in \text{SBV, periodic}} \frac{1}{|Y|} \int_Y g(x, [v], n + \nabla v) dx. \quad (2.27)$$

Notice that the two formulas for f^{hom} and g^{hom} are fully decoupled, i.e., the formula (2.24) does not depend on g and (2.25) does not depend on f . This decoupling results from the different scaling of the surface and the bulk term within the functional (2.22), as well as the condition (2.21). If this condition is not fulfilled due to a certain scaling of f or g with the length scale η , a coupling of the two terms may be observed (Pellet et al., 2019).

The work of Braides et al. (1996) on periodic homogenization has recently been extended to the case of stochastic homogenization by Cagnetti et al. (2019). This is of particular importance for the application to industrial materials, which often exhibit a randomness in their microstructure. Cagnetti et al. (2019) investigated the functional (2.22) with the same assumptions (2.21) but considered non-periodic, random and ergodic functions f and g . The parameter η in (2.22) serves as a length parameter of the microstructure indicating a scale separation in a random medium, see Fig. 2.9b for a schematic illustration. In their work, they showed that both the homogenized functional (2.23) and the cell formulas (2.24) and (2.25) are the same as in the periodic case. Hence, the decoupling of the two formulas holds upon stochastic homogenization as well. For the stochastic homogenization result the infinite volume limit for both the bulk term and the surface term is indispensable.

Let us now consider the Francfort-Marigo model (Francfort and Marigo, 1998) and discuss how the homogenization results of Braides et al. (1996) and Cagnetti et al. (2019) apply for this model. For heterogeneous \mathbb{C} and γ with characteristic length η , the weak form of the Francfort-Marigo functional reads

$$FM_\eta(u) = \frac{1}{2} \int_{\Omega} \nabla^s u : \mathbb{C} \left(\frac{x}{\eta} \right) : \nabla^s u \, dx + \int_{S_u} \gamma \left(\frac{x}{\eta} \right) \, dA. \quad (2.28)$$

For a given discretization in (pseudo-)time this functional is to be minimized in each time step with the constraint that the jump set S_u must contain the jump set of the previous time step. The weak solution of this

minimization problem is found in the function space SBD (Chambolle and Crismale, 2021). This functional is very similar to the functional (2.22). In particular, $g(x, [v], n) = \gamma(x)$ is a suitable option, since γ is strictly positive. Furthermore, \mathbb{C} is positive definite and thus a similar growth condition as (2.21) holds. However, we notice two deviations between the models. Firstly, the bulk energy of Braides et al. (1996) depends on the gradient of v , whereas in (2.28) the bulk term depends on the symmetrized gradient of u . Thus, instead of SBV in case of Braides et al. (1996), the function space SBD (Chambolle and Crismale, 2021) is required. Only in the case of anti-plane shear these two terms coincide. Lifting this restriction, however, is subject of current research. In a recent preprint, Friedrich et al. (2022) investigated the case $u \in SBD$ for $d = 2$, i.e., lifting the restriction to anti-plane shear. For the 3D case they considered a homogeneous crack resistance. In their preprint they showed a periodic homogenization result of the Francfort-Marigo functional to the homogeneous functional

$$FM^{\text{hom}} \frac{1}{2} \int_{\Omega} \nabla^s u : \mathbb{C}^{\text{eff}} : \nabla^s u \, dx + \int_{S_u} \gamma^{\text{eff}}(n_u) \, dA. \quad (2.29)$$

The second deviation between the Francfort-Marigo model and the functional (2.22) is given in the presence of a time stepping. The Francfort-Marigo model explicitly considers discrete time steps and introduces an irreversibility constraint. In the functional of Braides et al. (1996) on the other hand, no time stepping scheme is present. Without the irreversibility constraint, the results of Braides et al. (1996) and Friedrich et al. (2022) may be applied in each step separately providing a homogenization result for the Francfort-Marigo model. This holds in particular for the initial time step if no pre-existing crack is present, i.e., S_u is initially empty. The consideration of a time-stepping scheme and an irreversibility constraint in the homogenization result of Braides et al. (1996) has been provided by Giacomini and Ponsiglione (2006).

They showed a periodic homogenization result and found the same cell formulas as Braides et al. (1996). Therefore, in case of anti-plane shear, a periodic homogenization result for the Francfort-Marigo model is available. A proof for the general case, i.e., a stochastic homogenization result of the Francfort-Marigo model under any loading case including the irreversibility constraint, is, however, still pending, as the restrictions are only lifted individually.

All aforementioned extensions of the homogenization result of Braides et al. (1996) show the same formulas for the effective properties and a decoupling upon homogenization. In order to compute the effective stiffness \mathbb{C}^{eff} in case of periodic homogenization, one may rely on the cell formula (Bakhvalov and Panasenko, 1989), defined on a single periodic cell Y equipped with periodic boundary conditions. For a macroscopic strain field $E \in \text{Sym}(d)$ the cell formula reads

$$E : \mathbb{C}^{\text{eff}} : E = \inf_{u, \text{periodic}} \frac{1}{|Y|} \int_Y (E + \nabla^s u) : \mathbb{C}(x) : (E + \nabla^s u) dx. \quad (2.30)$$

Additionally, the case of computing effective stiffnesses in stochastic homogenization is well-studied and any boundary conditions may be conducted. Upon an infinite-volume limit, the effects of the boundary conditions vanish (Sab, 1992; Bourgeat and Piatnitski, 2004; Owhadi, 2003). However, for cells of finite size, the chosen type of boundary conditions *does* have an influence on the approximation quality of the "true" effective⁵ stiffness, see the works (Sab, 1992; Kanit et al., 2003) among numerous others. It can be shown – both theoretically and

⁵ A part of the mechanics community distinguishes apparent and effective properties. The former correspond to cells of finite size, whereas the latter emerge only upon an infinite volume limit (for stationary and ergodic media). Alternatively, apparent properties may be interpreted as approximations of the effective properties, in the same way as the displacement computed in a Galerkin discretization approximates the displacement of the continuous solution. In this work, we follow the second paradigm and use the terminology *effective* for quantities computed on cells of finite size, as well, tacitly assuming their approximative character.

numerically – that optimal convergence rates are reached when using periodic boundary conditions and *periodized* ensembles of microstructures, see Schneider et al. (2022) for a thorough discussion.

The cell formula for the effective crack energy is – in all aforementioned cases – given by the formula (2.25). In the periodic case, the equivalent formula (2.27) applies. Thus, computing the effective crack energy breaks down to computing a γ -weighted minimal surface, the minimum cut.

Computing minimal surfaces in the context of fracture has been considered for predicting crack propagation on two-dimensional micrographs even before the homogenization result of Braides et al. (1996) by Jeulin (1988; 1994a;b). In fact, in two spatial dimensions, the problem of computing the effective crack energy simplifies drastically. Indeed, it reduces to the problem of computing minimum (weighted) geodesics, for which efficient algorithms are available (Sethian, 1999; Osher and Fedkiw, 2002). Based on the homogenization result by Braides et al. (1996), Schneider (2020) established numerical tools to solve the cell formula for the effective crack energy on complex, three-dimensional microstructures.

2.4.3 The cell formula for periodic minimum cut/maximum flow

Consider the unit cell $Y = [0, L_1] \times [0, L_2] \times [0, L_3]$ and the field of crack resistances $\gamma : Y \rightarrow \mathbb{R}_{\geq 0}$ which satisfies for positive constants $\gamma_1, \gamma_2 > 0$ the condition

$$\gamma_1 \leq \gamma(x) \leq \gamma_2 \quad \forall x \in Y.$$

Based on the homogenization result of Braides et al. (1996) and following contributions (Cagnetti et al., 2019; Friedrich et al., 2022; Giacomini and Ponsiglione, 2006) we define the effective crack energy via the cell

formula

$$\gamma^{\text{eff}}(n) = \inf_{\phi \text{ periodic}} \frac{1}{|Y|} \int_Y \gamma(x) \|n + \nabla \phi\| dx \quad n \in S^2 \quad (2.31)$$

using periodic boundary conditions. This minimization problem seeks the periodic minimum cut through the cell Y with mean normal n . For a periodic cell Y this cell formula is equivalent to (2.25). A detailed discussion on the preferred boundary conditions in stochastic homogenization is given in chapter 6.

A question of particular mathematical interest relates to whether a minimizer exists, i.e., if the infimum is actually attained, and if so, in which function space? Following Hintermüller et al. (2018) this is the case if γ is lower semicontinuous. We are mainly interested in heterogeneous materials for which γ is a piecewise constant function and describes for instance inclusions of higher crack resistance within a matrix. To fulfill lower semicontinuity we set the value of γ at the interface of the inclusions to the lower value. Under this assumption the minimizer is attained in BV. Notice, however, that the functional is convex but not strictly convex. Hence, any minimizer is a global minimizer but no uniqueness is guaranteed. Nevertheless, the resulting effective crack energy, i.e., the minimum value, is attained for any minimizer. The objective function of the minimization problem (2.31) is, for any normal n , given by

$$f(\xi) = \frac{1}{|Y|} \int_Y \gamma(x) \|\xi\| dx.$$

This objective function is homogeneous of degree one in its argument, i.e., $f(\lambda\xi) = \lambda f(\xi) \forall \lambda > 0$, and thus non-differentiable. Due to this non-differentiability of the objective function, gradient based methods to solve the minimization problem may not be applied directly. As a remedy we follow the strategy proposed by Schneider (2020). We

consider the constrained optimization problem

$$\frac{1}{|Y|} \int_Y \gamma \|\xi\| dx \rightarrow \min_{\xi \in \mathcal{K}_{\bar{\xi}}} \text{ with} \quad (2.32)$$

$$\mathcal{K}_{\bar{\xi}} = \{\xi : Y \rightarrow \mathbb{R}^3 \mid \xi = \bar{\xi} + \nabla \phi, \bar{\xi} \in \mathbb{R}^3, \phi \text{ periodic}\}.$$

If the direction $\bar{\xi}$ has length unity, the minimum value of this optimization problem is the effective crack energy for unit normal $n = \bar{\xi}$ given in (2.31). The problem (2.32) seeks the minimum cut ξ which satisfies the compatibility constraint specified via the set $\mathcal{K}_{\bar{\xi}}$. This constrained form permits a dualization of the problem, as suggested by (Schneider, 2020). The formal dual problem to (2.32) is given by the *maximum flow* problem. This duality was first described by Strang (1983) who found that minimum cut is dual to maximum flow. The maximum flow problem seeks the periodic flow field $v : Y \rightarrow \mathbb{R}^3$, solving

$$\frac{1}{|Y|} \int_Y \bar{\xi} \cdot v(x) dx \rightarrow \max_{\substack{\text{div } v=0, \\ \|v(x)\| \leq \gamma(x)}}. \quad (2.33)$$

This problem may be interpreted as a linear program with two constraints. The first constraint is linear and enforces that the flow field is divergence free. This is the dual constraint to the compatibility of the cut field ξ . The second constrained bounds the local norm of the flow field v with the local crack resistance γ . Both optimization problems, the minimum cut and the maximum flow problem are equivalent. Hence, for $\|\bar{\xi}\| = 1$ both problems compute the effective crack energy with $n = \bar{\xi}$. To solve (2.33) numerically, suitable discretizations and solvers are required. Schneider (2020) used an FFT-based solution framework with a trigonometric collocation discretization (Moulinec and Suquet, 1994; 1998) and a finite element discretization with reduced integration (Willot, 2015a). He solved the governing equations with a primal dual hybrid gradient method (Esser et al., 2010; Pock et al., 2009). A similar approach has been proposed by Willot (2020) who investigated

the related problem of finding the effective conductivity of resistor networks. Michel and Suquet (2022) proposed a different approach to computing the effective crack energy. For the discretization of the governing formulas they conducted a discretization method based on trigonometric collocation (Moulinec and Suquet, 1994; 1998). In their work (Michel and Suquet, 2022) they pointed out similarities of the governing equations with the problem of computing limit loads of structures (Christiansen, 1981). For their similar problem they conducted classical optimization methods.

Finding novel discretization methods and solvers to compute the effective crack energy via minimum cut/maximum flow is the main goal of chapter 4.

2.4.4 Discussion on the terminology "effective crack resistance"

Independent of the homogenization result for fracture, discussed in section 2.4.2 several approaches concerning effective properties in fracture mechanics are found in the literature. These methods define the *effective crack resistance* or the *effective toughness* using computations on heterogeneous materials and classical linear elastic fracture mechanics or phase-field fracture. Their approaches differ from our definition of the effective crack energy and we wish to put our approach into perspective. In particular, this difference gave reasons for naming the effective surface term when homogenizing the Francfort-Marigo model the *effective crack energy* instead of effective crack resistance.

Bower and Ortiz (1991) provided a perturbative solution for a semi-infinite crack passing through a single, tough inclusion in a matrix. They relied on methods from classical linear elastic fracture mechanics and defined an effective toughness by either averaging or taking the maximum value of evaluated stress intensity factors during crack propagation.

Roux et al. (2003) discussed an emerging effective crack resistance

for a material with isotropic and homogeneous elastic properties and a heterogeneous crack resistance. In this context, a self-consistent method for estimating the effective fracture toughness of a planar crack propagating through inclusions is established. For a medium with randomly distributed heterogeneities, they identified regions of weak pinning, where the fracture toughness is given by the arithmetic mean of the local toughness, and strong pinning, where a much higher toughness emerges, see also Démerly et al. (2014) for a related study. Lebihain (2019) and Lebihain et al. (2021) extended the mentioned studies by accounting for cracks which bypass an inclusion, based on a perturbative, coplanar approach (Rice, 1985).

To account for heterogeneity in the elastic properties, Hossain et al. (2014) performed phase-field fracture computations on heterogeneous microstructures with specific, so-called "surfing" boundary conditions. The emerging effective crack resistance equals the maximum in time of the J-integral evaluated along the crack tip, see also Kuhn and Müller (2016) and Brach et al. (2019).

Let us compare these approaches to compute the effective crack resistance with our approach based on the homogenization result (Braides et al., 1996; Giacomini and Ponsiglione, 2006; Cagnetti et al., 2019; Friedrich et al., 2022) for the Francfort-Marigo model of brittle fracture (Francfort and Marigo, 1998). The problem of heterogeneous fracture mechanics in general involves two prominent length scales: the correlation length of the heterogeneities and the typical size of a displacement increment. Typically, in a quasi-static framework, the size of the displacement increment is assumed to be infinitesimal. In this framework, when we consider a crack propagating through a microstructure, its progress may be hindered by various factors, like being pinned to an interface or avoiding an inclusion. This interpretation is implicit in Hossain et al. (2014) as well as Lebihain et al. (2021), for example, who consider crack propagation through microstructures of a fixed size and in continuous time, which is only discretized to enable a

numerical treatment.

In practical applications however, the displacement increment is typically of the order of magnitude of the macroscopic scale. In particular, in a homogeneous macro-model, the size of the heterogeneities has vanished due to a distinct scale separation and an incrementally discretized load is considered. This is the point of view considered when homogenizing the Francfort-Marigo model. The displacement increment is fixed, once and for all, as the limit of infinitesimally small heterogeneities is considered. Therefore, in this setting, the crack passes a microstructure cell within a single (macroscopic) increment.

Another difference is the understanding of the emerging *effective* properties. As Hossain et al. (2014) always consider a time-continuous problem, their crack resistance is defined as the maximum in time of the local J-integral. Similarly, Lebihain et al. (2021) define the effective crack resistance by either the average in time or the maximum evaluated energy release rate. Notice that these definitions are neither related, nor motivated by mathematical homogenization results. Hence, in their case, a macroscopic material model has to be postulated. This macroscopic model then requires a discretization in time for numerical purposes.

In contrast, the homogenization result for the Francfort-Marigo model practically works with an energy equivalence between the macroscopic and the microscopic fracture energy, as a result of the energetic framework. In particular, no time step is present in evaluating the cell formula since the time step has been fixed once and for all on the macroscale. A detailed discussion on this difference is also found in Michel and Suquet (2022).

Finally, let us remark that Γ -convergence implies the convergence of *absolute* minimizers, but does not predict what happens to *local* minimizers. Although an energy equivalence between the microscopic fracture energy and the macroscopic fracture energy appears in a natural way, the (absolutely) minimal surface in the cell problem is be a byproduct of Γ -convergence. From a physical point of view, it

might be more appropriate to work with crack surfaces that are just local minima of the weighted area. Still, keeping the assessment of the safety of microstructured components in mind, the absolutely minimal surface serves as a lower bound for the (real) effective crack energy, and is furthermore robust w.r.t. stochastic fluctuations in the microstructure.

Chapter 3

Characterizing digital microstructures by the Minkowski-based quadratic normal tensor¹

3.1 Introduction

For material modeling of microstructured media, an accurate characterization of the underlying microstructure is indispensable. The overall goal is to find simple quantities that describe the geometric shape as well as the composition of the microstructure under consideration. Once a microstructured material is characterized in these terms, correlations between microstructure characteristics and effective material parameters may be investigated via multi-scale methods, see Matouš et al. (2017). For microstructures of different material classes, different characteristics have been established. Particle reinforced composites may be characterized by the size(-distribution) of the particles and the volume fraction of the latter. The special case of fiber-reinforced composites additionally takes the fiber-orientation distribution, expressed via fiber orientation

¹ This chapter is based on Ernesti et al. (2022). In order to include this paper into the structure of this work I shortened the introduction and made minor changes to the manuscript.

tensors (Kanatani, 1984; Advani and Tucker, 1987) into account. For porous media, in addition to the porosity, i.e., the volume fraction of the porous space, the pore-size distribution (Kate and Gokhale, 2006), the turtosity (Neumann et al., 2019) and the chord-length distribution (Mathéron, 1975) are the typical quantities of interest. Polycrystalline materials are typically characterized in terms of a grain-size distribution (Döbrich et al., 2004) and an orientation distribution (Bunge, 1982; Böhlke, 2006). Since microstructures are often stochastic, a mathematical investigation of microstructure and their characterization is strongly related to the field of stochastic geometry. One basic tool in stochastic geometry to describe geometrical shapes and sizes is given by Minkowski functionals (Schneider and Weil, 2008; Hadwiger, 1951), also known as intrinsic volumes. They are defined for wide classes of shapes, including all convex sets and their finite unions as well as all bounded sets with smooth boundary. A Minkowski functional associates to any such shape a scalar quantity. If one requires such a functional to be invariant with respect to Euclidean motions, additive and to satisfy a certain continuity property, then it can be shown, see Hadwiger (1951), that in 3D it can be written as linear combination of only four *basic* functionals, the Minkowski functionals. Among them are the total volume, the total surface area, the Euler characteristic and one further functional, which for convex shapes may be interpreted as the mean width, or in the context of smooth boundaries as the integral of mean curvature. Approaches for computing Minkowski functionals are based, for instance, on marching squares (Mantz et al., 2008) or on Steiner's formula (Klenk et al., 2006; Guderlei et al., 2007). Being scalar-valued and rotation invariant, Minkowski-functionals are intrinsically insensitive to anisotropic features of the shape in question. Therefore, tensor-valued analogs of Minkowski functionals, the so-called Minkowski tensors (Alesker, 1999; Hug et al., 2008a;b; Jensen and Kiderlen, 2017), were introduced and studied. In addition to additivity and continuity, Minkowski tensors are required to be equivariant w.r.t. Euclidean transformations. This means, for instance, that rotating a

shape first and computing its Minkowski tensor afterwards leads to the same result as computing the Minkowski tensor first and rotating the tensor afterwards. A direct consequence of this property is that Minkowski tensors preserve axes of symmetry of structures, i.e., if a shape is rotationally invariant w.r.t. an axis \mathbf{p} , the Minkowski tensor will be rotationally invariant w.r.t. \mathbf{p} as well.

Minkowski tensors may be computed for general microstructures with distinct interfaces, such as porous media, foams, bones or granular structures (Schröder-Turk et al., 2011). For porous media, Klatt et al. (2017) conducted a comparison between the common chord-length analysis and a Minkowski-tensor based approach. Schröder-Turk et al. (2011; 2013) evaluated Minkowski tensors for a given triangulation of the interface via explicitly known expressions for polytopes. Their ansatz was successfully used for characterizing the anisotropy of granular matter and metal foams, as well as identifying defects in molecular dynamics simulations of metal phases. For 3D gray-value images, Svane (2014; 2015) introduced approximation formulas for Minkowski functionals and tensors, also establishing convergence upon mesh refinement, called multigrid convergence in this context. Unfortunately, the cited works (Svane, 2014; 2015) did not include numerical examples. For finite point samples, Voronoi-based estimators Hug et al. (2017) may be used for approximating Minkowski tensors.

Contributions

We present an applied approach for characterizing digital microstructures of industrial complexity in terms of the quadratic normal tensor, a tensor-valued quantity based on Minkowski tensors, bringing these concepts to the attention of the engineering community.

For phenomenological continuum theories, which use microstructure information as state or microstructure variables to model the influence of microstructure on macroscopic material behavior, the Minkowski

tensors are promising quantities, because they are in principle observable and can be effectively calculated from three-dimensional image data. The Minkowski tensors complement, e.g., the already widely used fiber-orientation tensors (Advani and Tucker, 1987; Kanatani, 1984), which approximate the tangent distribution of the fiber centerline, and tensorial texture coefficients (Böhlke, 2006; Böhlke et al., 2010), which describe the distribution of crystal orientations.

We introduce the relevant Minkowski functionals and tensors in section 3.2 and isolate among them those suitable for microstructure characterization. In section 3.3, we present a novel algorithm for computing the quadratic normal tensor. For large microstructures with complex geometry, finding triangulations of the interface may be a challenging task, in particular if the microstructure is described by voxel data. Therefore, we present here an alternative to triangulation-based algorithms (Schröder-Turk et al., 2011) that works directly with gray-value images as input. The outward-pointing unit normals on the materials interface are approximated by finite-difference gradients of the discretized characteristic function.

We investigate multigrid convergence of our approach by numerical studies in section 3.4. For fiber-reinforced composites, we compare the quadratic normal tensor to the more conventional fiber-orientation tensor of second order (Kanatani, 1984; Advani and Tucker, 1987). We compare the accuracy of our approach to the commonly used structure-tensor based algorithm (Krause et al., 2010) for computing fiber-orientation tensors. Last but not least, we study the anisotropy of sand grains and porous sand-binder aggregates based on the quadratic normal tensor.

3.2 Using Minkowski tensors for describing microstructures

3.2.1 Minkowski tensors

We briefly introduce Minkowski functionals and Minkowski tensors in a form suitable for our purposes and restrict to the 3D case. We refer to Schröder-Turk et al. (2013; 2011) or the lecture notes by Jensen and Kiderlen (2017) for the general case.

Consider a solid body, by which we mean a bounded, not necessarily connected set K in \mathbb{R}^3 with sufficiently regular boundary ∂K . Here regularity can mean smoothness or convexity of some form. For our purposes it will be completely sufficient to assume that K is polyconvex, i.e., K can be represented as a finite union of (not necessarily disjoint) convex sets. To gain insight into the morphology of K , a shape index φ associates to any such set K a scalar value. If one requires the shape index φ to satisfy some natural basic properties, namely invariance with respect to rigid motions, additivity (meaning that $\varphi(K \cup L) = \varphi(K) + \varphi(L) - \varphi(K \cap L)$ for solid bodies K, L) and a certain continuity (for convex sets, and w.r.t. the Hausdorff distance, see e.g. (Schneider and Weil, 2008, §12.3)), then it is a well-known fact due to Hadwiger (1951) that φ may be represented as a linear combination of only four basic functionals V_0, \dots, V_3 , known as Minkowski functionals or intrinsic volumes. The Minkowski functionals encompass the volume $V = V_3$, the surface area $S = 2V_2$, and two further functionals, V_1 and V_0 , which in special situations can be interpreted as the total mean curvature and the total Gaussian curvature of the body K . The latter is proportional to the Euler characteristic of K , i.e., the genus of the surface ∂K , which is a topological invariant. Volume and surface area are computed by

$$V(K) = \int_K dV \quad \text{and} \quad S(K) = \int_{\partial K} dS. \quad (3.1)$$

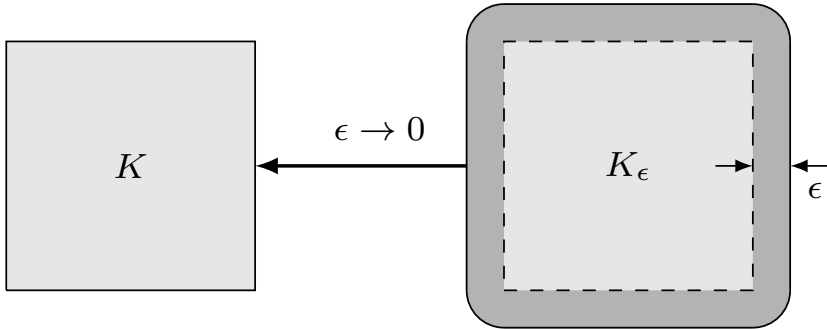


Figure 3.1: Illustration of the ε -parallel expansion K_ε of the shape $K \subseteq \mathbb{R}^3$. (Ernesti et al., 2022)

If the boundary ∂K is sufficiently smooth, then the local mean curvature H and the Gaussian curvature G (i.e. the average and the product of the principal curvatures) are well-defined at each boundary point and the total curvatures may be computed via

$$V_1(K) = \frac{1}{\pi} \int_{\partial K} H dS \quad \text{and} \quad V_0(K) = \frac{1}{4\pi} \int_{\partial K} G dS. \quad (3.2)$$

Such integral representations are also available for non-smooth bodies when one replaces ∂K by an integration over the normal bundle of K (Zähle, 1986). For practical computations, the additivity property is essential, allowing to decompose complex structures into simple convex pieces and to treat these pieces individually. For convex shapes, the Steiner formula provides another way to characterize the Minkowski functionals and another idea how to compute them.

Consider, for a convex body K and $\varepsilon > 0$, the ε -approximation

$$K_\varepsilon = \{ \mathbf{x} \in \mathbb{R}^3 : \|\mathbf{x} - \mathbf{y}\| \leq \varepsilon \text{ for some } \mathbf{y} \in K \},$$

see Fig. 3.1 for a schematic illustration. The Steiner formula (Schneider, 2014) states that the volume of K_ε is a polynomial in ε , whose coefficients are (up to some normalization constants) the Minkowski functionals of K :

$$V(K_\varepsilon) = V(K) + \varepsilon S(K) + \pi \varepsilon^2 V_1(K) + \frac{4\pi}{3} \varepsilon^3 V_0(K). \quad (3.3)$$

This allows to recover the Minkowski functionals of K by computing volumes of a number of ε -approximations and inverting the above formula, see Klenk et al. (2006). One can also use the fact that the ε -approximations K_ε are smooth even if K is not, allowing to determine the Minkowski functionals V_1 and V_0 by means of the limit procedure

$$V_1(K) = \lim_{\varepsilon \rightarrow 0} V_1(K_\varepsilon) \quad \text{and} \quad V_0(K) = \lim_{\varepsilon \rightarrow 0} V_0(K_\varepsilon).$$

While these approximation results follow from the continuity of the Minkowski functionals, ε -approximation properties of more general classes of sets are discussed in Rataj (2006). For more background to our informal discussion, we refer to Schröder-Turk et al. (2013) and the references therein.

Since Minkowski functionals are, by definition, invariant w.r.t. Euclidean motions or change of frame, they are insensitive to directional and positional information. Hence, they are inappropriate for detecting anisotropies in a shape K . For this latter purpose and other applications, a more general theory of tensor-valued shape indices has been developed, which are covariant w.r.t. Euclidean motions, see Schröder-Turk et al. (2013). In analogy to Hadwiger's theorem (Hadwiger, 1951) and restricting to $\mathbb{R}^3 \otimes_{\text{sym}} \mathbb{R}^3 \cong \mathbb{R}_{\text{sym}}^{3 \times 3}$ tensors, there are only six linearly independent shape indices (in addition to the Minkowski functionals multiplied by the identity), see Alesker (1999) and in particular (Hug et al., 2008b, §4). For a (convex) body K with sufficiently smooth

boundary, these may be expressed as

$$\begin{aligned}
 W_0^{2,0}(K) &= \int_K \mathbf{x} \otimes \mathbf{x} dV, & W_1^{2,0}(K) &= \frac{1}{3} \int_{\partial K} \mathbf{x} \otimes \mathbf{x} dS, \\
 W_2^{2,0}(K) &= \frac{1}{3} \int_{\partial K} H(\mathbf{x}) \mathbf{x} \otimes \mathbf{x} dS, & W_3^{2,0}(K) &= \frac{1}{3} \int_{\partial K} G(\mathbf{x}) \mathbf{x} \otimes \mathbf{x} dS, \\
 W_1^{0,2}(K) &= \frac{1}{3} \int_{\partial K} \mathbf{n} \otimes \mathbf{n} dS, & W_2^{0,2}(K) &= \frac{1}{3} \int_{\partial K} H(\mathbf{x}) \mathbf{n} \otimes \mathbf{n} dS.
 \end{aligned} \tag{3.4}$$

Here, \mathbf{x} denotes the position vector of a point in K (or ∂K) and \mathbf{n} stands for the field of outward-pointing unit-normal vectors on ∂K . For Minkowski tensors, Steiner-type formulas based on support measures have been established, see Schneider (2000). Note that some Minkowski functionals can be recovered from Minkowski tensors. For instance, the surface area is given by the formula $S(K) = 3\text{tr}(W_1^{0,2}(K))$.

Based on these Minkowski tensors, Schröder-Turk et al. (2011) introduce the eigenvalue ratios

$$\beta(W) = \frac{\min_{\lambda \in E(W)} |\lambda|}{\max_{\lambda \in E(W)} |\lambda|}, \tag{3.5}$$

as scalar measures of anisotropy. Here W stands for any of the six Minkowski tensors defined in (3.4) and $E(W)$ is the set of eigenvalues of the symmetric matrix W . Clearly, $\beta(W) \in [0, 1]$. For $W = W_0^{2,0}$, $W_1^{2,0}$ and $W_1^{0,2}$, the matrix $W(K)$ is positive semi-definite in general (and this is also true for the other Minkowski tensors if K is a convex body), implying that all eigenvalues of W are nonnegative. In this case, $\beta(W) = 1$ if and only if all eigenvalues are equal, i.e., if the tensor is a multiple of the identity. Note that smaller values of $\beta(W)$ correspond to a higher degree of anisotropy.

3.2.2 Minkowski-tensor based microstructure characterization

Heterogeneous materials often exhibit random variations in their microstructure, but a resulting deterministic material behavior (Torquato, 2002). For characterizing microstructures, we are interested in singling out a small number of tensor-valued descriptors that may in turn be used as input for homogenization schemes, see Klusemann and Svendsen (2010) for an overview. These microstructure identifiers should preferably exhibit certain natural properties:

1. **Respect for symmetries:** We seek microstructure identifiers that preserve symmetry information. If a microstructure possesses some symmetry, then this is typically reflected in the macroscopic material behavior. Therefore, identifiers should capture such symmetry.
2. **Robustness:** To be of practical use, small changes in the microstructure should only result in small changes in the descriptor.
3. **Translation invariance:** For homogenization, statistical homogeneity is essential (Torquato, 2002). Thus, our identifiers should be invariant with respect to translations of the shape K . Furthermore, we want to explicitly include periodic structures, as periodic homogenization is often used for studying random microstructures (Kanit et al., 2003).
4. **Universal applicability:** Minimal assumptions on the geometry of the structure allow for general application on a variety of different microstructures.

In the light of these criteria, Minkowski tensors are promising candidates for microstructure characteristics.

1. Their covariant tensorial nature reflects the anisotropy and direction dependence of the structure in question.
2. They are robust due to their continuity properties w.r.t. the Hausdorff distance. For example, if a sequence of convex bodies K_n converges

to a convex body K , as $n \rightarrow \infty$, then all their Minkowski functionals and Minkowski tensors converge as well. Similar results hold e.g. if a polyconvex set K is approximated by its parallel sets K_ε , see Schneider (2014) and Rataj (2006). There are also stability results showing Hölder continuity with exponent at least $1/2$, see Hug and Schneider (2015).

3. If translation invariance is required, then beside the Minkowski functionals among the above mentioned Minkowski tensors precisely $W_1^{0,2}$ and $W_2^{0,2}$ are suitable. As computing the curvature of interfaces of 3D voxel images is not straightforward (Lenoir, 1997; Monga et al., 1991), we restrict in this article to the volume V , the surface area S and the Minkowski tensor $W_1^{0,2}$.
4. The Minkowski tensors are not restricted to specific shape assumptions on K . Indeed, only minimal assumptions on K are required (Schröder-Turk et al., 2011). For any practical application it is probably sufficient to note that any set (however complex) can be approximated arbitrarily well by a polyconvex set on which Minkowski tensors are defined. The tensor $W_1^{0,2}$ under consideration can in fact be defined under much weaker regularity assumptions, e.g. for sets with piecewise smooth boundaries. This flexibility distinguishes them from other approaches, where geometric priors are required for characterizing microstructures. For instance, for fiber-reinforced composites, fibers are often assumed to be (locally) cylindrical. Such geometrical priors run into problems for fibrous microstructure where the fibers deviate from their original cylindrical shape. For instance, during injection molding, fibers may be bent or twisted (Heinecke and Willberg, 2019). As they are independent of priors, Minkowski tensors may be suitable for characterizing fibers with distinct curvature.

In the field of microstructure characterization, K is often the set union of a multitude of bodies, for instance inclusions within a surround-

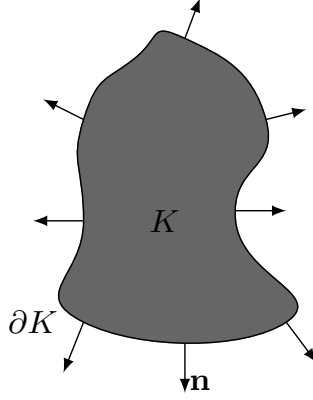


Figure 3.2: Body K with outward-pointing unit-normal field \mathbf{n} . (Ernesti et al., 2022)

ing matrix material. In this context, we are interested in a tensorial anisotropy-measure, which is stable w.r.t. an infinite-volume limit, where the number of inclusions tends to infinity. Thus, we normalize $W_1^{0,2}$ to obtain the quadratic normal tensor (QNT)

$$\text{QNT}(K) = \frac{W_1^{0,2}(K)}{\text{tr}(W_1^{0,2}(K))}, \quad (3.6)$$

which, for a single body or microstructure K with sufficiently smooth boundary, may be written in the form

$$\text{QNT}(K) = \frac{1}{S(K)} \int_{\partial K} \mathbf{n} \otimes \mathbf{n} \, dS,$$

where again $\mathbf{n} = \mathbf{n}(\mathbf{x})$ is the field of normal vectors on ∂K , see Fig. 3.2. For a geometric interpretation of the QNT, observe that for any vector $\boldsymbol{\xi} \in \mathbb{R}^3$ the expression

$$(\mathbf{n} \otimes \mathbf{n})\boldsymbol{\xi} = \mathbf{n}(\mathbf{n} \cdot \boldsymbol{\xi})$$

describes the orthogonal projection of ξ onto the line spanned by the normal direction \mathbf{n} at \mathbf{x} . In this sense, $\text{QNT}(K)$ may be interpreted as an average over the normal projections computed w.r.t. the uniform probability measure concentrated on the surface ∂K . (Note that the resulting average matrix is still symmetric and positive definite but does not represent a projection anymore.)

The $\text{QNT}(K)$ admits an additional interpretation from a mechanical point of view. Suppose the structure K deforms with a homogeneous stress σ . Then, contracting the stress tensor with the QNT

$$\text{QNT}(K) : \sigma = \frac{1}{S(K)} \int_{\partial K} \mathbf{n} \cdot (\sigma \mathbf{n}) dS$$

computes the mean normal stress on the surface ∂K .

By construction, the QNT is symmetric, positive semi-definite and has trace 1. In particular, $\text{QNT}(K)$ admits an eigenvalue decomposition with real-valued, non-negative eigenvalues λ_1, λ_2 and λ_3 , which sum to 1. In case of a convex K , certain eigenvalue combinations can directly be interpreted in terms of the resulting shape of K : $\lambda_1 \gg \lambda_2 = \lambda_3$, for instance, indicates a rather flat shape within the plane perpendicular to the eigenvector corresponding to λ_1 . For $\lambda_1 = \lambda_2 \gg \lambda_3$ we expect K to be a needle expanded in the direction of the eigenvector associated with λ_3 , see also Appendix A.2, where the QNT is computed for a cylinder, and the sand grain experiments in section 3.4.4.

Another advantage of Minkowski tensors is that they are locally defined and therefore locally computable. Complex polyconvex shapes can be cut into simple pieces and each piece can be treated separately. Then the additivity allows to recover the Minkowski tensor of the whole body from the Minkowski tensors of the pieces, allowing for efficient computation and parallelization.

3.3 Efficient implementation for 3D image data

3.3.1 Algorithmic overview

Consider a (periodic) heterogeneous two-phase material on the domain $Y = [0, L_x] \times [0, L_y] \times [0, L_z]$. The microstructure of the material is described by its characteristic function $\chi : Y \rightarrow \{0, 1\}$, defining the two phases Ω_0 and Ω_1 via $\Omega_0 = \{\mathbf{x} \in Y : \chi(\mathbf{x}) = 0\}$ and $\Omega_1 = Y \setminus \Omega_0$, respectively. Our aim is to describe phase Ω_1 using the Minkowski functionals and tensors $V(\Omega_1)$, $S(\Omega_1)$, $W_1^{0,2}(\Omega_1)$ and $\text{QNT}(\Omega_1)$.

Note that Ω_1 is unknown in practice, only CT images of Ω_1 can be observed. μ -CT data is typically stored as 3D gray-value voxel data. We interpret the voxel data as a mapping $\chi_h : Y_h \rightarrow [0, 1]$ from the discrete set Y_h , comprising the centers of a regular voxel grid with voxel length h , to the unit interval representing gray values. The gray value $\chi_h(\mathbf{y})$ associated to a point $\mathbf{y} \in Y_h$ stands for the volume fraction of Ω_1 in the voxel centered at \mathbf{y} . The relation between χ and its discretization χ_h is demonstrated in Fig. 3.3. Fig. 3.3a shows the characteristic function χ of a ball. Fig. 3.3b shows the non-discretized ball with the regular grid Y_h in the background. In Fig. 3.3c, we see the discrete characteristic function χ_h of this ball as a gray-value image. Note that, in general, the input data χ_h does not allow to recover the phases Ω_0 and Ω_1 exactly as the interface is blurred. Only in the limit as $h \rightarrow 0$ the correct characteristic function and, therefore, the correct sets are recovered. For determining $W_1^{0,2}$ and S , in addition the normal directions are needed. In a weak sense, the unit normal \mathbf{n} of the set Ω_1 at a boundary point is recovered by $\mathbf{n} = -\nabla\chi$, whereas $-\nabla\chi = 0$ away from the boundary. This statement may be formalized in terms of functions of bounded variation (Ambrosio et al., 2000). Therefore, we will compute the gradient numerically and establish formulas for $W_1^{0,2}$ and S based on

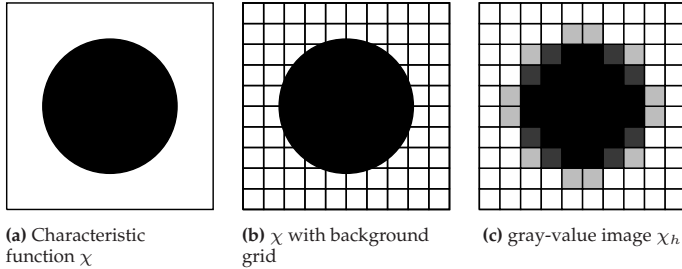


Figure 3.3: Characteristic function of a ball and its discrete representation by a gray-value image on a regular voxel grid. (Ernesti et al., 2022)

volume averaging, see section 3.3.4. To improve the gradient estimation, a smoothing of the characteristic function χ_h is applied beforehand. The algorithm for computing the Minkowski quantities from a given voxel image is summarized in Alg. 1. First, we apply an image filter \mathcal{F}_σ to the characteristic function χ_h . Secondly, we estimate the outward-pointing normal vector by computing the gradient \mathbf{g} from the resulting smoothed image \mathcal{I}_h^σ . Finally, the desired quantities $V, S, W_1^{0,2}$ and QNT are estimated.

Algorithm 1 Computation of Minkowski quantities

- | | |
|---|---|
| <p>1: $\mathcal{I}_h^\sigma \leftarrow \mathcal{F}_\sigma * \chi_h$</p> <p>2: $\mathbf{g}(\mathbf{x}) \leftarrow \nabla_h \mathcal{I}_h^\sigma(\mathbf{x})$</p> <p>3: Compute V by (3.7)</p> <p>4: Compute S by (3.8)</p> <p>5: Compute $W_1^{0,2}$ by (3.9)</p> <p>6: Compute QNT by $W_1^{0,2} / \text{tr}(W_1^{0,2})$</p> <p>7: return $(V, S, W_1^{0,2}, \text{QNT})$</p> | <p>▷ Blur image with image filter</p> <p>▷ Compute gradient</p> |
|---|---|
-

3.3.2 Smoothing by image filters

Due to the reconstruction procedure, μ -CT scans often exhibit artifacts and impurities. Furthermore, binary voxel-based images do not allow reconstructing interfaces accurately (Mantz et al., 2008). To deal with these issues, we apply an image filter to the discrete characteristic function (prior to computing the gradient). As different filters (and different choices of parameters) are available, we will also address choosing an appropriate filter. Applying the filter is realized by convolving the image with a specific filter kernel \mathcal{F}_σ . The filter parameter σ controls the width of filtering, and the result is the filtered image \mathcal{I}_h^σ , given as the convolution

$$\mathcal{I}_h^\sigma = \mathcal{F}_\sigma * \chi_h.$$

In our implementation, the convolution with \mathcal{F}_σ is implemented via fast Fourier transform (FFT) (Cooley and Turkey, 1965), see Alg.2. Notice that in some cases the Fourier-transformed filter kernel may be computed efficiently without using the FFT.

Algorithm 2 FFT-based filter application

- 1: $\widehat{\chi}_h \leftarrow \text{FFT}(\chi_h)$ ▷ Transformation of the characteristic function
 - 2: $\widehat{\mathcal{F}}_\sigma \leftarrow \text{FFT}(\mathcal{F}_\sigma)$ ▷ Transformation of the filter kernel
 - 3: $\widehat{\mathcal{I}}_h^\sigma(\xi) \leftarrow \widehat{\chi}_h(\xi)\widehat{\mathcal{F}}_\sigma(\xi)$ ▷ Multiplication in Fourier space for all frequencies ξ
 - 4: $\mathcal{I}_h^\sigma \leftarrow \text{IFFT}(\widehat{\mathcal{I}}_h^\sigma)$ ▷ Inverse transformation
-

We shall consider a dimensionless filter parameter σ and scale it by the voxel length h . As filter kernels, we consider a Gaussian

kernel (Bredies and Lorenz, 2018)

$$\mathcal{G}_\sigma(\mathbf{x}) = \frac{1}{(h\sigma)^3(2\pi)^{\frac{3}{2}}} \exp\left(-\frac{\|\mathbf{x}\|^2}{2(h\sigma)^2}\right)$$

and the characteristic function of the unit ball, scaled to integrate to unity,

$$\mathcal{B}_\sigma(\mathbf{x}) = \begin{cases} \frac{3}{4\pi(h\sigma)^3} & \text{if } \|\mathbf{x}\| \leq h\sigma, \\ 0 & \text{otherwise.} \end{cases}$$

In Fig. 3.4, the effect of filtering by a Gaussian and a ball kernel, respectively, is shown for a 1D laminate structure discretized with a voxel length of $h = 2 \mu\text{m}$ for three different filter parameters σ . The red curve illustrates the impact of the Gaussian filter, whereas the blue line represents the ball-filtered image. In the Gaussian case, the resulting image is smooth across the laminate's interface. However, for larger σ , not only the interface is blurred, but no region of black or white remains. In fact, due to its global support, this even holds for small σ .

The impact of the ball filter is completely different. The piecewise constant indicator function with jumps at the interfaces is transformed into a piecewise linear function with slopes $\pm\frac{1}{2h\sigma}$. Therefore, when applying the ball filter to a structure with diameter larger than $2h\sigma$, some region with $\mathcal{I}_h^\sigma = 1$ will remain.

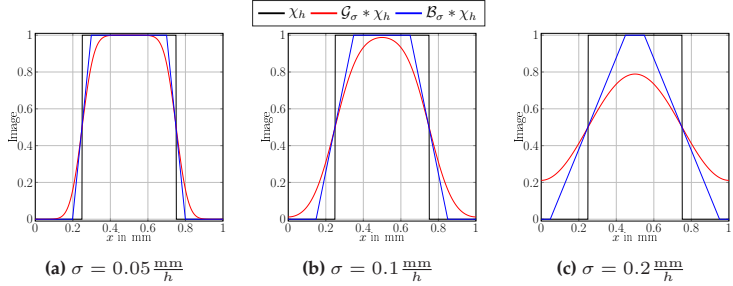


Figure 3.4: Influence of filtering with different kernels and widths σ . (Ernesti et al., 2022)

3.3.3 Approximating the surface normal by finite differences

Computing the Minkowski tensor $W_1^{0,2}(\Omega_1)$ requires determining the (unit) normal vector field \mathbf{n} on the surface $\partial\Omega_1$. We approximate the normal field \mathbf{n} by computing the gradient vector field

$$\mathbf{g} = \nabla_h \mathcal{I}_h^\sigma$$

of the filtered image \mathcal{I}_h^σ numerically. Notice that \mathbf{g} is dependent on the voxel length h . At boundary points, we consider $\mathbf{n} \approx -\mathbf{g}/\|\mathbf{g}\|$ as the outward pointing unit normal, provided $\mathbf{g} \neq 0$. We briefly discuss the choice of the numerical gradient-approximation method. Finite-difference approximations are a simple way for approximating the gradient of a function given on a regular voxel grid numerically. Suppose a function $f : Y \rightarrow \mathbb{R}$, $\mathbf{x} \mapsto f(\mathbf{x})$ is given. We consider three finite-difference discretization schemes for the partial derivative in e_i -direction ($i = 1, 2, 3$):

1. first-order approximation by forward differences, i.e.,

$$\partial_i^h f(\mathbf{x}) \approx \frac{f(\mathbf{x} + h\mathbf{e}_i) - f(\mathbf{x})}{h};$$

2. first-order approximation by backward differences, i.e.,

$$\partial_i^h f(\mathbf{x}) \approx \frac{f(\mathbf{x}) - f(\mathbf{x} - h\mathbf{e}_i)}{h};$$

3. second-order approximation by central differences, i.e.,

$$\partial_i^h f(\mathbf{x}) \approx \frac{f(\mathbf{x} + h\mathbf{e}_i) - f(\mathbf{x} - h\mathbf{e}_i)}{2h}.$$

Since our numerical experiments are performed on periodic structures, we treat the boundary in a periodic fashion. Under certain regularity assumptions on the function to differentiate, the first-order approximations converge linearly in h to the exact gradient, whereas the second order approximation converges quadratically as $h \rightarrow 0$, see Olver (2014). However, some further differences arise, which we demonstrate by example, see Fig. 3.5.

Consider the filtered gray-value image of a ball, shown in Fig. 3.5a. When computing the gradient via central differences, the symmetry of the structure is recovered in the symmetry of the gradient field, since $\mathcal{I}_h^\sigma(\mathbf{x})$ and $\mathbf{n}(\mathbf{x})$ are evaluated at the same position, see Fig. 3.5d. However, if we compute the gradient via forward or backward differences, respectively, this will not be the case. The forward or backward partial derivatives in direction \mathbf{e}_i are not evaluated at \mathbf{x} , but at $\mathbf{x} \pm h/2\mathbf{e}_i$, respectively, the faces of the cell. In particular, the partial derivatives in different directions will also be located on different faces. The resulting gradient fields are shown in Fig. 3.5c and Fig. 3.5b, respectively. Both appear deformed and uneven compared to the central-differences approach. Furthermore, a diagonal offset is noticeable. Numerical tests show that, in our present

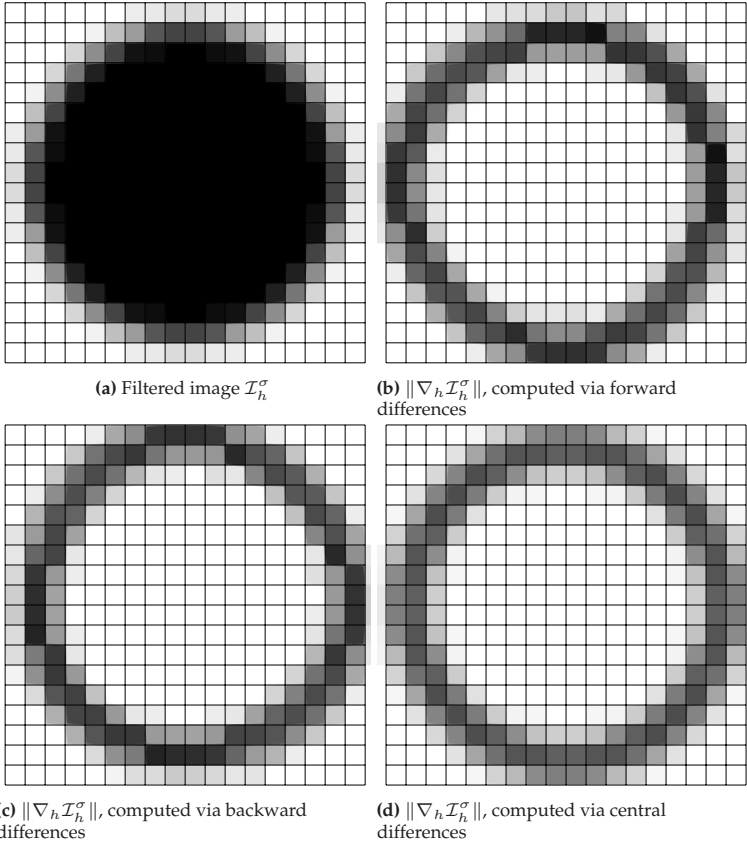


Figure 3.5: Filtered gray-value image of a ball (a) and norm of the gradient computed via the three different finite-difference approximations (b)-(d). (Ernesti et al., 2022)

setting, the gradient approximation based on central differences is more accurate than the other approaches and will therefore be preferred, see also Section 3.4.2.

3.3.4 Computing Minkowski tensors

In this section, we propose formulas for computing the volume (fraction) of Ω_1 , the surface area of $\partial\Omega_1$ and the Minkowski tensor $W_1^{0,2}(\Omega_1)$. Their accuracy and multigrid convergence will be investigated by numerical means in Section 3.4.2.

The volume is approximated by quadrature, more precisely, by the trapezoidal rule, via

$$V(\Omega_1) \approx \sum_{\mathbf{x} \in Y_h} \chi_h(\mathbf{x}) h^3. \quad (3.7)$$

Motivated by results from geometric measure theory, see Giusti (1984) (Definition 1.6, Theorem 1.24 and Definition 3.3) and Maggi (2012) (Proposition 12.20), we approximate the surface area via

$$S(\Omega_1) \approx \sum_{\mathbf{x} \in Y_h} \|\mathbf{g}(\mathbf{x})\| h^3, \quad (3.8)$$

where the gradient $\mathbf{g}(\mathbf{x})$ is computed by finite differences and $\|\cdot\|$ denotes the Euclidean norm. Due to the relation $S(\Omega_1) = 3\text{tr}(W_1^{0,2}(\Omega_1))$, we approximate the Minkowski tensor $W_1^{0,2}$ by

$$W_1^{0,2}(\Omega_1) \approx \frac{1}{3} \sum_{\mathbf{x} \in Y_h} \mathbf{g}(\mathbf{x}) \otimes \mathbf{g}(\mathbf{x}) \frac{h^3}{\|\mathbf{g}(\mathbf{x})\| + \epsilon}, \quad (3.9)$$

where $\epsilon > 0$ is a small constant used to avoid division by zero. The approximation of the quadratic normal tensor QNT is computed from the approximation of $W_1^{0,2}$ by dividing by the trace, as in its definition (3.6).

3.4 Numerical examples

3.4.1 Setup

The algorithms 1 and 2 (as well as algorithm 3 discussed in Section 3.4.3 below) were implemented in Python 3.7 with Cython (Behnel et al., 2011) extensions. Critical operations were parallelized using OpenMP. For the eigenvalue decomposition of the structure tensor, discussed in Section 3.4.3 below, we rely on LAPACK (Anderson et al., 1999). The computations were performed on a desktop computer with a 6-core Intel i7 CPU and 32GB RAM.

3.4.2 Parameter selection and multigrid convergence

The proposed algorithm depends on several basic parameters including the grid size, the gray scale depth, the type and width of the applied filter and the choice of the gradient approximation, which we are free to choose in order to tune the algorithm. In this section, we investigate the influence of these parameters and propose suitable choices.

In practical applications, the continuous range $[0, 1]$ of gray values is replaced by a set of discrete colors

$$\mathcal{C}^p = \begin{cases} \{0, 1\} & \text{if } p = 1, \\ \{0, \frac{1}{p^3-1}, \frac{2}{p^3-1}, \dots, 1\} & \text{if } p \geq 2 \end{cases}$$

of depth $p \geq 1$. In this context, we consider the discrete characteristic function as the mapping $\chi_h : Y_h \rightarrow \mathcal{C}^p$. For $p = 1$, we voxelize the object under consideration in a binary manner, by coloring a voxel if its center lies inside the object. For $p > 1$, we compute the binary image on the finer grid $h' = h/p$ and determine the gray-value of a voxel of size h as the mean value of its p^3 sub-voxels, resulting in a gray-value image of depth p . We investigate a ball B_R of radius $R > 0$ for different p . The

Minkowski quantities of B_R are known exactly and given by

$$\begin{aligned} V(B_R) &= \frac{4\pi R^3}{3}, & S(B_R) &= 4\pi R^2, \\ W_1^{0,2}(B_R) &= \frac{4\pi R^2}{9} \text{Id}, & \text{QNT}(B_R) &= \frac{1}{3} \text{Id}, \end{aligned}$$

see Appendix A.1 for a derivation of the expressions for $W_1^{0,2}$ and QNT. Hence these quantities can be compared to the corresponding numerically determined quantities V^\approx , S^\approx , $W^\approx = W_1^{0,2,\approx}$ and QNT^\approx . For $W = W_1^{0,2}$ and QNT, we define error measures by

$$E = \frac{\|W(B_R) - W^\approx(B_R)\|}{\|W(B_R)\|} \quad \text{and} \quad \bar{E} = \frac{\|\text{QNT}(B_R) - \text{QNT}^\approx(B_R)\|}{\|\text{QNT}(B_R)\|},$$

where $\|\cdot\|$ denotes the Frobenius norm. Since W is connected to the surface area via $S = 3\text{tr}(W)$, the error E is directly affected by an error in computing S . In contrast, this latter error does not necessarily affect \bar{E} , as both QNT and QNT^\approx have trace 1.

We investigate the influence of the different gradient approximations, filter kernels and filter widths σ , as well as that of the depth p of the initial gray-value image, and we examine multigrid convergence as $h \rightarrow 0$ numerically. The effect of the filters on the initial gray-value image, depending on the image depth, is exemplified in Fig. 3.6. In Fig. 3.6a, we see a slice through the characteristic function of a ball with a regular grid in the background. In Fig. 3.6b and 3.6c, we see slices of the discrete characteristic functions of the ball for depths 1 and 4. The center of the ball does not lie in the center of a voxel, but was chosen with a slight displacement, which results in a more uneven representation of the ball in the discrete images compared to Fig. 3.3.

Apparently, images with a higher depth give rise to a more accurate representation of a ball than binary images do. Fig. 3.6d and 3.6e show the image after applying a ball-filter with $\sigma = 1.2$. We see that the

difference between depth 1 and 4 has become smaller, but remains visible. The filtered binary image ($p = 1$) seems more uneven than the filtered gray-scale image ($p = 4$).

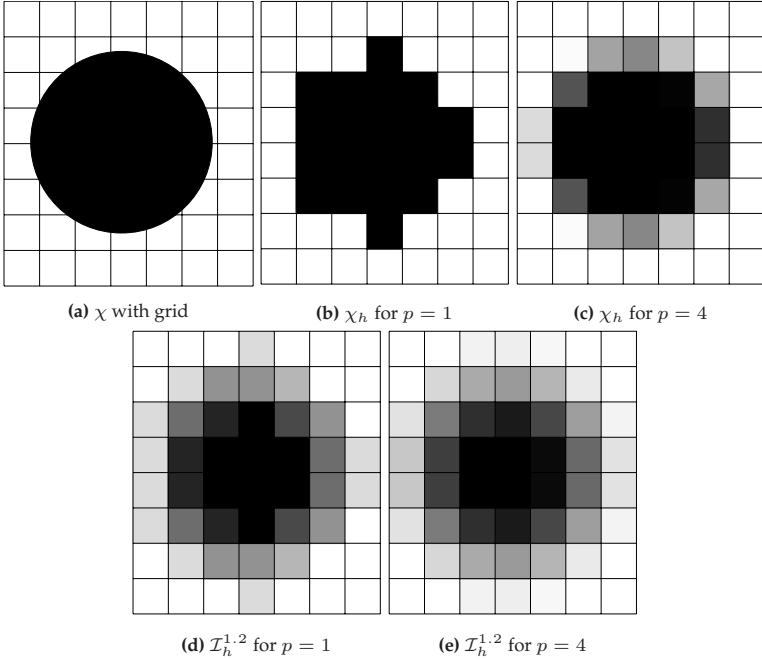


Figure 3.6: Characteristic function χ , discrete characteristic function χ_h and filtered image $\mathcal{I}_h^{1,2}$ for a single ball using depth 1 and 4. (Ernesti et al., 2022)

First, we study the influence of the gray-value depth p of the initial voxel image for different spatial resolutions. The structure under consideration contains a single ball of diameter $16\mu\text{m}$ in a box of edge length $24\mu\text{m}$, i.e., the material has a volume fraction of 15.5%. For this first study, we omit using a filter and rely on central differences for the gradient estimation. Fig. 3.7a shows the computed volume fraction vs. D/h , the diameter of

the ball per voxel length, for several gray-value depths p . The binary image, i.e., $p = 1$, exhibits the largest error and oscillates around the correct value. Only for a high resolution above $D/h = 10$, the error is within reasonable bounds. For a higher depth, the volume fraction is accurate even for the lowest resolution.

The computed surface area vs. D/h is shown in Fig. 3.7b. Using the binary image without any filter overestimates the surface area significantly and does not converge. For $p \geq 2$, we see that the error is reasonable for a resolution of 4 voxels per diameter and higher. For higher resolution and higher depth, the surface-area computation is rather accurate, but systematically overestimates the correct value by about 2% and does not converge. The error E of the Minkowski tensor is shown in Fig. 3.7c. For $p \geq 2$, it is below 6% even for the second-coarsest resolution of $D/h = 4$ and stays below 3% at higher resolutions. Finally, the quadratic normal tensor QNT is the one among the computed characteristics which is computed most accurately, see Fig. 3.7d. For $p \geq 2$, the error is below 5% for all spatial resolutions. Additionally, for all image depths, multigrid convergence is visible. This suggests that, to some degree, the error of computing the Minkowski tensor results from the mentioned overestimation of the surface area. Indeed, since QNT differs from $W_1^{0,2}$ by its trace and $\text{tr}(W_1^{0,2}) = S/3$, the error of computing the surface area present in $W_1^{0,2}$ cancels out to some extent in QNT.

In a second series of numerical experiments we repeated large parts of the above tests using first-order gradient approximations, as described in Section 3.3.3, instead of central differences. Compared to the latter, both first-order gradient approximations induce much larger errors, exceeding 20%. Therefore, we will restrict to central differences for the remainder of the article.

Finally, we examine the influence of different filter kernels. Fig. 3.8 shows the surface area as well as the two tensor-error measures vs. D/h for gray-value depth $p = 1$ (binary) on the left and $p = 3$ on the right.

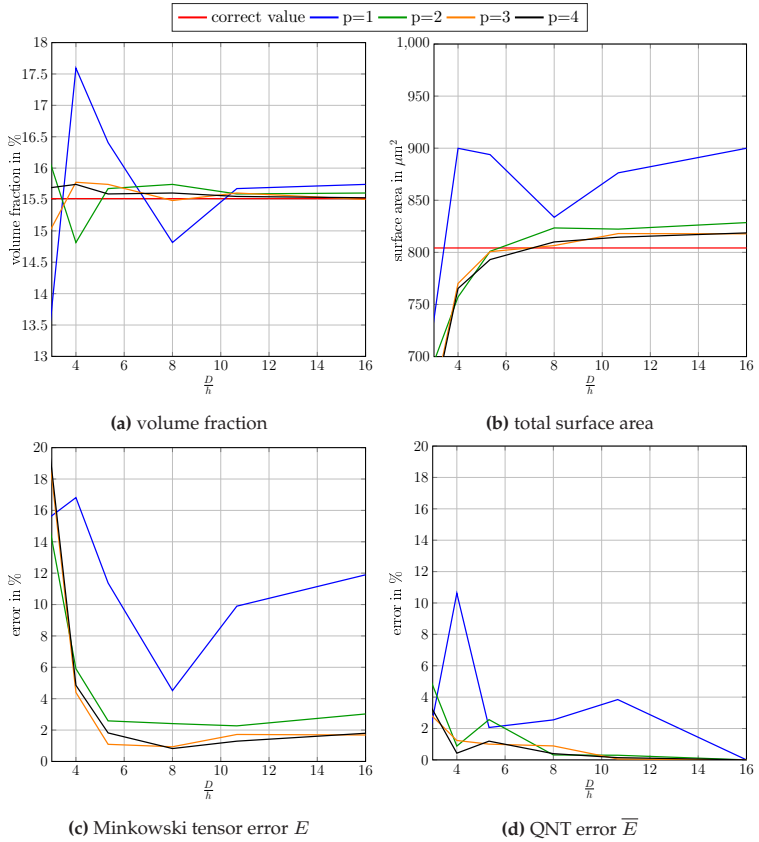


Figure 3.7: Volume fraction, total surface area and tensor errors E and \bar{E} for the unfiltered image, i.e., $\sigma = 0$. The gradient was computed via central differences. (Ernesti et al., 2022)

We consider the ball filter \mathcal{B}_σ and the Gaussian filter \mathcal{G}_σ , both with filter parameters $\sigma = 1.2$ and $\sigma = 2$, i.e., for a filter width slightly larger than a single voxel and a filter width of 2 voxels.

In general, the errors for the gray-value image are smaller compared to the binary image. Focusing on the surface-area computation, i.e., Fig. 3.8a and Fig. 3.8b, we notice that applying no filter is actually most beneficial for a low spatial resolution. For $p = 3$, this even holds up to $D/h = 10$. For $p = 1$, the surface area is strongly overestimated for higher resolution. Even for $p = 3$, no multigrid convergence is achieved, if the filtering step is skipped. To achieve convergence, the ball filter with $\sigma = 1.2$ is the most accurate. For $p = 1$, the ball filter with $\sigma = 1.2$ appears to be the best choice for resolutions up to $D/h = 10$. Above that threshold, the choice $\sigma = 2$ exhibits the smallest error. Nevertheless, the ball filter with $\sigma = 1.2$ serves as a good compromise. For both gray-image depths, applying the ball filter leads to better results than applying the Gaussian filter for computing the surface area of the structure.

Investigating the error E , see Fig. 3.8c and Fig. 3.8d, permits us to draw similar conclusions. Fig. 3.8e and Fig. 3.8f show that the filter choice plays a subordinate role compared to the image depth for the error \bar{E} . For the binary image, the Gaussian filter with $\sigma = 2$ exhibits the lowest error, staying below the threshold of 2% for all resolutions. For gray-value images, however, the error of computing the quadratic normal tensor is below 3% for all resolutions and filters, which is accurate enough for most applications.

3.4.3 A short-fiber reinforced composite

Characterization of fiber-reinforced composites

Short-fiber reinforced composites enjoy great popularity owing to their high (mass-)specific stiffness (Jones, 1998). The local fiber alignment is strongly dependent on the manufacturing process (Chung and Kwon, 1995). The effective material behavior of short-fiber reinforced com-

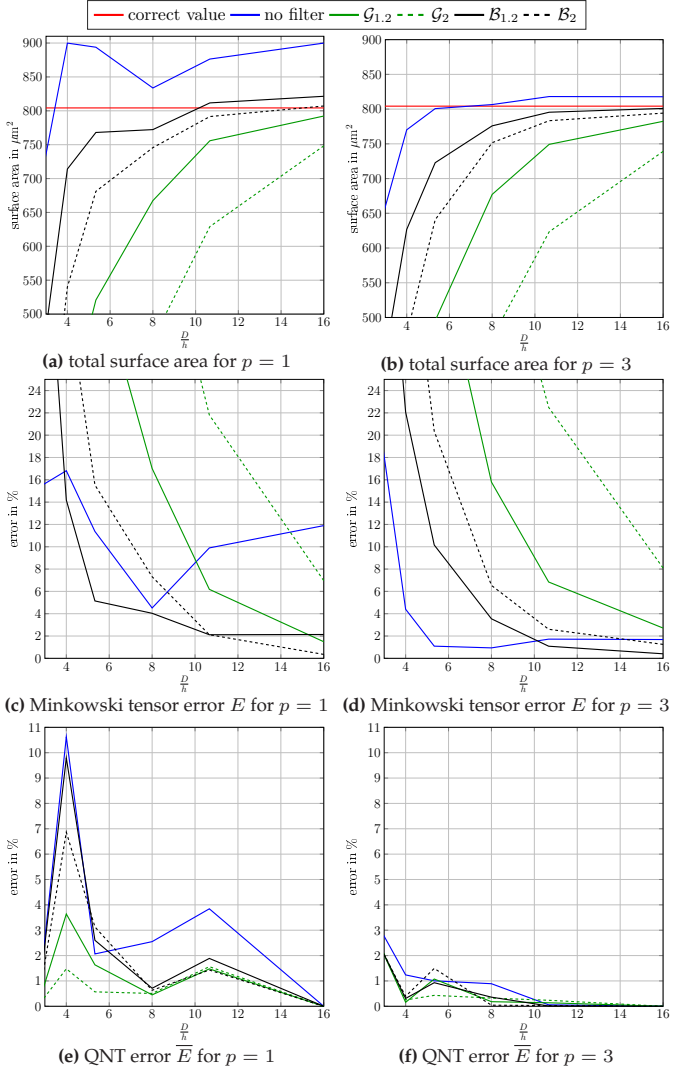


Figure 3.8: Surface area and tensor errors E and \bar{E} for depths $p = 1$ and $p = 3$ comparing the filter choice. (Ernesti et al., 2022)

posites is anisotropic, in general, and strongly dependent on the local fiber orientation. Each fiber is interpreted as a straight spherical cylinder of length L and diameter D , axis-aligned with unit vector \mathbf{p} . Frequently used microstructure characteristics for fiber-reinforced composite materials are the volume fraction, the aspect ratio L/D and the fiber-orientation tensors of second or fourth order (Kanatani, 1984; Advani and Tucker, 1987). For fibers of equal length and equal diameter, the resulting fiber-orientation tensors (of order 2 and 4) of a structure with N fibers and orientation vectors $\mathbf{p}_1, \dots, \mathbf{p}_N$ are defined by

$$A = \frac{1}{N} \sum_{i=1}^N \mathbf{p}_i \otimes \mathbf{p}_i \quad \text{and} \quad \mathbb{A} = \frac{1}{N} \sum_{i=1}^N \mathbf{p}_i \otimes \mathbf{p}_i \otimes \mathbf{p}_i \otimes \mathbf{p}_i.$$

For varying fiber length and diameter, similar expressions have been proposed in Bay and Tucker III (1992) based on length- or volume-weighted averaging.

For a gray-value μ -CT image, the fiber-orientation tensors of second and fourth order may be computed by a variety of methods, see Pinter et al. (2018). A popular approach uses the structure tensor (Krause et al., 2010), see Alg. 3. Alternatively, fibers may be segmented individually, see Hessman et al. (2019) for recent work.

To gain insight into the relation between the fiber-orientation tensor A and the Minkowski tensor $W_1^{0,2}$, we compare their expressions for a single fiber of length L and diameter D , oriented in direction \mathbf{p} , see Appendix A.2 for the detailed computation:

$$A = \mathbf{p} \otimes \mathbf{p}, \tag{3.10}$$

$$W_1^{0,2} = \frac{\pi D^2}{6} \left[\mathbf{p} \otimes \mathbf{p} + \frac{L}{D} \left(\text{Id} - \mathbf{p} \otimes \mathbf{p} \right) \right] \quad \text{and} \tag{3.11}$$

$$\text{QNT} = \frac{1}{1 + 2\frac{L}{D}} \left[\mathbf{p} \otimes \mathbf{p} + \frac{L}{D} \left(\text{Id} - \mathbf{p} \otimes \mathbf{p} \right) \right]. \tag{3.12}$$

For microstructures containing N fibers, A is computed by averaging the single-fiber expression (3.10). $W_1^{0,2}$ is computed by summing (3.11) over all fibers. The resulting quadratic normal tensor QNT may be computed as a surface-area weighted average of expression (3.12).

The fiber-orientation tensor and the quadratic normal tensor need to be interpreted differently:

- For a single fiber K , the fiber-orientation tensor of second order is a singular matrix (of rank 1) describing the projection onto the fiber axis. In contrast, the Minkowski tensor $W_1^{0,2}(K)$ of a single fiber K is a full rank matrix, which arises as a weighted sum of the orthogonal projection onto the fiber axis and the complementary projection onto the plane perpendicular to this axis.
- For high aspect ratios, i.e., for $L \gg D$, for the QNT, the prefactor in front of the complementary projection is much larger than the other prefactor.
- Using the fiber-orientation tensor as a descriptor of a microstructure rests upon specific assumptions that are often not satisfied for real structures. Typically, fibers are not of equal length, because they break during the manufacturing process (Inceoglu et al., 2011). Furthermore, the assumption that fibers are straight cylinders is not met in most of the cases, as longer fibers bend during manufacturing and therefore exhibit curvature (Heinecke and Willberg, 2019). In such situations, the structure-tensor based computation of the fiber-orientation tensor still gives *some* tensorial quantity as output. However, interpreting this result as a fiber-orientation tensor may not be justified.

The Minkowski tensors, on the other hand, are not restricted to specific geometric assumptions such as particular shapes. Therefore, for structures containing curved fibers of different lengths or mixtures of fibers with other objects etc., $W_1^{0,2}$ is still a geometrically well-defined quantity. As Minkowski tensors are integrals of locally computable quantities, see (3.4), they are even well-defined locally on any piece of

	A	QNT for $\frac{L}{D} = 10$	QNT for $\frac{L}{D} = 25$	QNT for $\frac{L}{D} = 50$
#1	$\begin{pmatrix} 1 & 0 & 0 \\ 0 & 0 & 0 \\ 0 & 0 & 0 \end{pmatrix}$	$\begin{pmatrix} 0.048 & 0 & 0 \\ 0 & 0.476 & 0 \\ 0 & 0 & 0.476 \end{pmatrix}$	$\begin{pmatrix} 0.025 & 0 & 0 \\ 0 & 0.4875 & 0 \\ 0 & 0 & 0.4875 \end{pmatrix}$	$\begin{pmatrix} 0.012 & 0 & 0 \\ 0 & 0.494 & 0 \\ 0 & 0 & 0.494 \end{pmatrix}$
#2	$\begin{pmatrix} 0.79 & 0 & 0 \\ 0 & 0.19 & 0 \\ 0 & 0 & 0.02 \end{pmatrix}$	$\begin{pmatrix} 0.1379 & 0 & 0 \\ 0 & 0.3946 & 0 \\ 0 & 0 & 0.4675 \end{pmatrix}$	$\begin{pmatrix} 0.1219 & 0 & 0 \\ 0 & 0.3996 & 0 \\ 0 & 0 & 0.4785 \end{pmatrix}$	$\begin{pmatrix} 0.1131 & 0 & 0 \\ 0 & 0.4024 & 0 \\ 0 & 0 & 0.4845 \end{pmatrix}$
#3	$\begin{pmatrix} 0.49 & 0 & 0 \\ 0 & 0.49 & 0 \\ 0 & 0 & 0.02 \end{pmatrix}$	$\begin{pmatrix} 0.266 & 0 & 0 \\ 0 & 0.266 & 0 \\ 0 & 0 & 0.468 \end{pmatrix}$	$\begin{pmatrix} 0.2607 & 0 & 0 \\ 0 & 0.2607 & 0 \\ 0 & 0 & 0.4785 \end{pmatrix}$	$\begin{pmatrix} 0.258 & 0 & 0 \\ 0 & 0.258 & 0 \\ 0 & 0 & 0.484 \end{pmatrix}$
#4	$\begin{pmatrix} 0.6 & 0 & 0 \\ 0 & 0.3 & 0 \\ 0 & 0 & 0.1 \end{pmatrix}$	$\begin{pmatrix} 0.219 & 0 & 0 \\ 0 & 0.348 & 0 \\ 0 & 0 & 0.433 \end{pmatrix}$	$\begin{pmatrix} 0.21 & 0 & 0 \\ 0 & 0.349 & 0 \\ 0 & 0 & 0.441 \end{pmatrix}$	$\begin{pmatrix} 0.205 & 0 & 0 \\ 0 & 0.349 & 0 \\ 0 & 0 & 0.446 \end{pmatrix}$
#5	$\begin{pmatrix} 0.33 & 0 & 0 \\ 0 & 0.33 & 0 \\ 0 & 0 & 0.33 \end{pmatrix}$	$\begin{pmatrix} 0.333 & 0 & 0 \\ 0 & 0.335 & 0 \\ 0 & 0 & 0.332 \end{pmatrix}$	$\begin{pmatrix} 0.333 & 0 & 0 \\ 0 & 0.335 & 0 \\ 0 & 0 & 0.332 \end{pmatrix}$	$\begin{pmatrix} 0.333 & 0 & 0 \\ 0 & 0.335 & 0 \\ 0 & 0 & 0.332 \end{pmatrix}$

Table 3.1: Comparison of fiber-orientation tensor A and quadratic normal tensor QNT for microstructures of different orientation and aspect ratio.

a complex geometric structure. In contrast, the fiber orientation tensor is a non-local quantity intrinsically tied to cylindrical shapes.

An overview of how the fiber-orientation tensor compares with the quadratic normal tensor for varying aspect ratios is given in Tab. 3.1. For this study, we generated 5×3 different microstructures, each containing 20% fibers of equal length and diameter, using the sequential addition and migration algorithm (Schneider, 2017). This algorithm draws fibers from an angular central Gaussian distributions on the two-dimensional sphere (Tyler, 1987). Indeed, the set of possible angular central Gaussian distributions may be parameterized by the second-order fiber-orientation tensors, see Montgomery-Smith et al. (2011). Across the microstructures we varied the orientation distribution (5 different ones #1 – #5) and the aspect ratio (3 different choices: $L/D = 10, 25$ and 50). For convenience, all matrices are chosen to be diagonal w.r.t. the standard basis $\{e_1, e_2, e_3\}$.

Microstructure #1 is composed of aligned fibers in e_1 -direction. The second microstructure lies almost entirely within the $e_1 - e_2$ -plane, with preferred direction e_1 . The almost planar-isotropic case in the $e_1 - e_2$ -plane is realized via microstructure #3. A general anisotropic case with preferred direction e_1 and least preferred direction e_3 is given in case #4. And, finally, microstructure #5 shows the isotropic case. For

the isotropic orientation (#5), all tensors are nearly equal. The QNT for the almost planar orientation (#3) results in one larger (corresponding to the normal vector of the plane) and two equal smaller eigenvalues, indicating no preferred direction within the plane. The QNT of structure #2 exhibits three different eigenvalues. The largest is equal to the largest eigenvalue of #3. Of the two smaller eigenvalues, the smallest indicates a preferred direction. The same interpretation holds for structure #4. For the uni-directional case (#1), the largest eigenvalue appears twice, which indicates a planar symmetry in both planes normal to the corresponding eigenvectors. By the smallest eigenvalue, again a preferred direction is indicated.

In contrast to the fiber orientation tensor A , the quadratic normal tensor varies also with the aspect ratio L/D of the fibers. This may also be seen from the eigenvalue ratio β of QNT, see (3.5), listed in Tab. 3.2. This scalar measure of anisotropy is smallest in case of a unidirectional orientation distribution (#1) and almost 1 in the isotropic case #5. The degree of anisotropy is amplified for higher aspect ratios, which results in a lower β .

	β for $\frac{L}{D} = 10$	β for $\frac{L}{D} = 25$	β for $\frac{L}{D} = 50$
#1	0.1003	0.0503	0.0250
#2	0.2943	0.2544	0.2343
#3	0.5690	0.5448	0.5327
#4	0.5055	0.4751	0.4598
#5	0.991	0.9903	0.9899

Table 3.2: The degree of anisotropy of the different structures considered in Tab. 3.1 measured by means of the eigenvalue ratio $\beta(\text{QNT})$ of the quadratic normal tensor, see equation (3.5). Apparently, the anisotropy does not only depend on the fiber-orientation distribution, but is also sensitive to the aspect ratio L/D of the fibers

Sensitivity w.r.t. inter-fiber spacing

A well-known challenge when computing fiber-orientation measures on μ -CT scans is the sensitivity w.r.t. spatial resolution, as well as overlapping or touching fibers (Wirjadi et al., 2009). In the following study, we investigate the influence of the inter-fiber distance. Using the sequential addition and migration algorithm (Schneider, 2017), we generated structures with 20% fibers of aspect ratio 25, containing a total of 1336 inclusions. The fiber-orientation tensor was chosen almost planar isotropic with $A = \text{diag}(0.49, 0.49, 0.02)$. The minimum distance between the fibers compared to their diameter can be chosen as an input for the microstructure generator. We generated 6 microstructures with minimum relative distance varying from 1% to 50%. Volumetric views and transverse slices of three of these structures are shown in Fig. 3.9. For 1% relative distance, several bundles of touching or almost touching fibers are visible, whereas, for 50%, each fiber is comfortably surrounded by matrix material. All structures were voxelized with gray-value depth $p = 2$ and for three spatial resolutions of $D/h = 4, D/h = 8$ and $D/h = 12$, resulting in volume images with $256^3, 512^3$ and 768^3 voxels, respectively.

For this data set, we compare the surface-area computation and the errors for the tensors $W_1^{0,2}$ and QNT. As processing options, we compare no filter and the ball filter \mathcal{B}_σ with filter parameter $\sigma = 1.2$. The central-difference approximation is used for the gradient. Fig. 3.10a shows the computed total surface area vs. the minimum fiber distance relative to the diameter for the three spatial resolutions under consideration, using the ball filter with $\sigma = 1.2$. We observe two trends. Firstly, the surface area is generally underestimated for all spatial resolutions. However, we clearly see multigrid convergence. Furthermore, the error is smaller for the larger minimum distance. This observation conforms to our expectations, as the surface area of touching or almost touching fibers is not computed accurately enough by a gradient-based approximation.

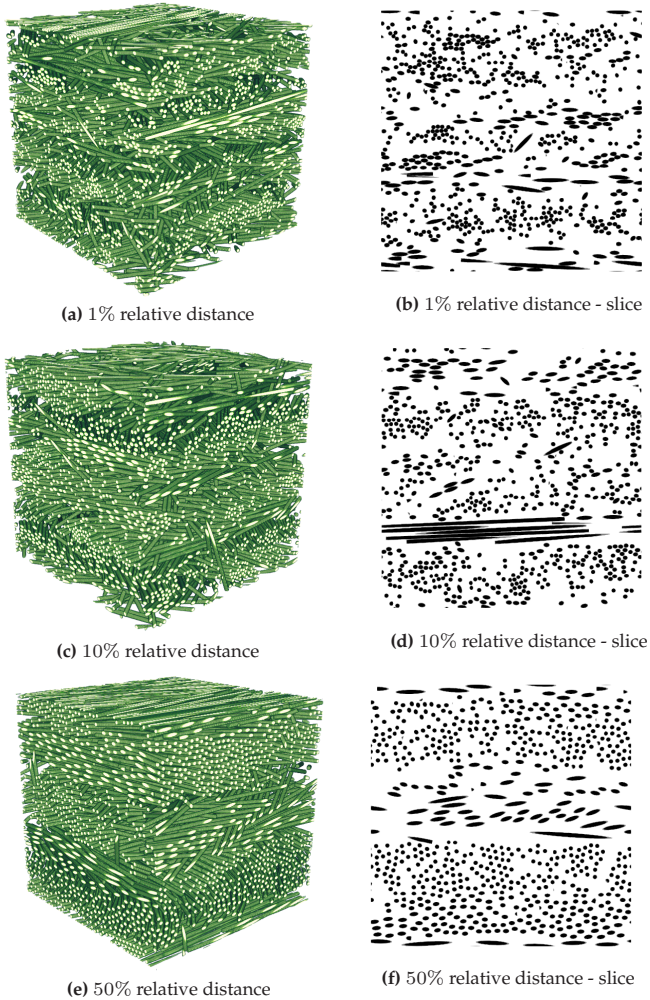


Figure 3.9: Fiber-reinforced composite containing 1336 fibers of equal length and varying inter-fiber spacing. The structures were generated synthetically using the sequential addition and migration algorithm (Schneider, 2017). (Ernesti et al., 2022)

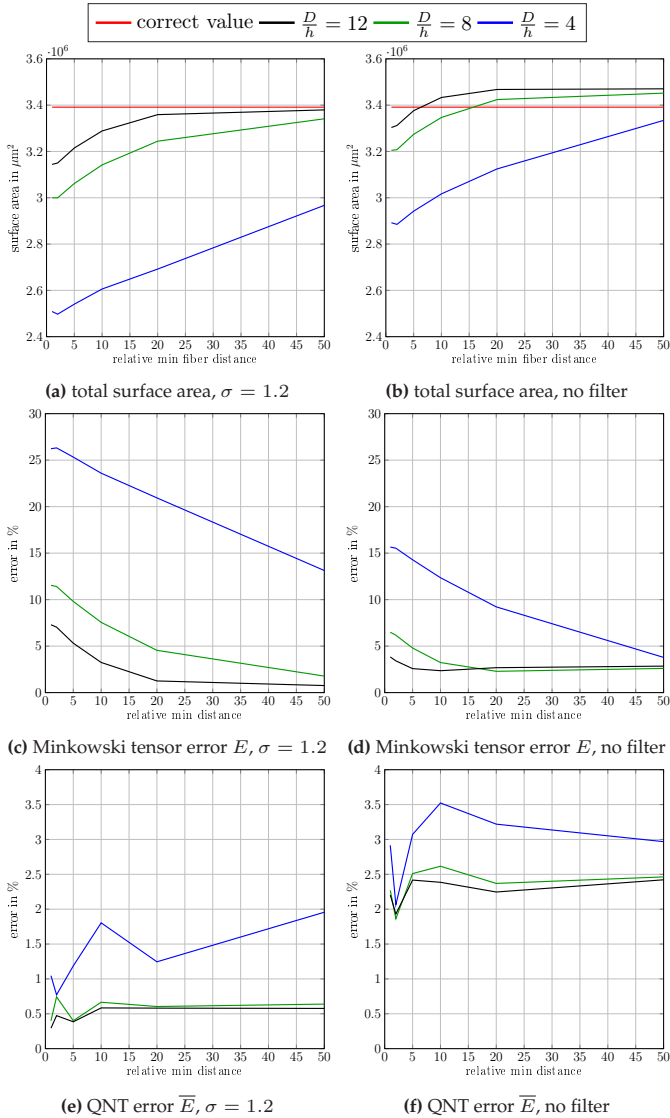


Figure 3.10: total surface area and the errors E and \bar{E} plotted vs. the minimum relative distance between fibers. (Ernesti et al., 2022)

In Fig. 3.10b, we see the results of the surface area computation without applying any filter. The errors are, in general, lower than in the case of $\sigma = 1.2$. However, neither multigrid convergence, nor a convergence as the minimum fiber distance increases is observed. Fig. 3.10c and Fig. 3.10d show the error E for both filter choices. Again, the results reflect the relative error of the surface area estimation. Fig. 3.10e and Fig. 3.10f contain the errors of the quadratic normal tensor for both filter choices. For no filter application, the error is below 4%, and for $\sigma = 1.2$, it is even below 2% for all spatial resolutions and minimum inter-fiber distances. No clear trend w.r.t. the inter-fiber spacing is visible. Hence, the quadratic normal tensor QNT may serve as a microstructure descriptor that is robust w.r.t. small inter-fiber spacing.

We compare our approach with the well-established structure-tensor method, see Algorithm 3, which we implemented into our code. Com-

Algorithm 3 Computing the fiber-orientation tensor via the structure-tensor method (Krause et al., 2010)

- | | |
|---|--|
| 1: $\mathcal{I}_h^\sigma \leftarrow \mathcal{F}_\sigma * \chi_h$ | ▷ Blur image with image filter |
| 2: $\mathbf{g}(\mathbf{x}) \leftarrow \nabla_h \mathcal{I}_h^\sigma$ | ▷ Apply discrete gradient |
| 3: $I(\mathbf{x}) \leftarrow \mathbf{g}(\mathbf{x}) \otimes \mathbf{g}(\mathbf{x})$ | ▷ Compute local tensor |
| 4: $I_\mu \leftarrow \mathcal{F}_\mu * I$ | ▷ Blur local tensor with second filter |
| 5: $\{\lambda_i(\mathbf{x}), \mathbf{v}_i(\mathbf{x})\} \leftarrow \text{Eig}(I_\mu(\mathbf{x}))$
(sorted, smallest first) | ▷ Local eigenvalue decomposition |
| 6: $A^\approx = \sum_{\mathbf{x} \in Y_h} \mathbf{v}_1(\mathbf{x}) \otimes \mathbf{v}_1(\mathbf{x})$ | ▷ Extract local orientation tensor |
| 7: return $A^\approx / \text{tr}(A^\approx)$ | |
-

puting the fiber-orientation tensor numerically via the structure-tensor algorithm requires applying a second filter \mathcal{F}_μ with filter parameter μ to the tensor field $\mathbf{n}(\mathbf{x}) \otimes \mathbf{n}(\mathbf{x})$ (component-wise, this tensor field denotes said ‘structure tensor’). Pinter et al. (2018) recommend that for the filter parameter for the second filter should be larger than for the first filter, which should be rather small. In our case, this is best recovered by

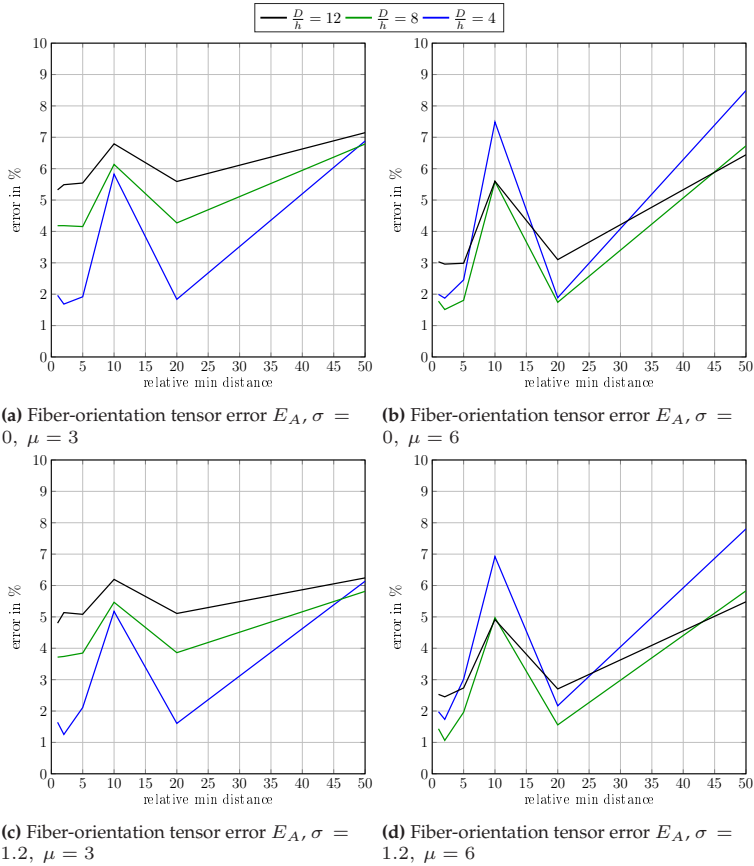


Figure 3.11: Error of the structure-tensor based fiber orientation tensor computation using different filter parameters for the first and second filter. (Ernesti et al., 2022)

choosing the ball filter with small filter parameter (i.e., $\sigma = 1.2$) or no filter (i.e., $\sigma = 0$) as the first filter. For the second filter, we choose a Gaussian kernel \mathcal{G}_μ with $\mu = 3$ and $\mu = 6$. To evaluate the accuracy of the method, we introduce the fiber-orientation tensor error measure (similar to \overline{E})

$$E_A = \frac{\|A - A^\approx\|}{\|A\|},$$

where A^\approx is the approximated fiber-orientation tensor computed by the structure tensor approach.

Fig. 3.11 shows the error of this method for the four filter combinations $\sigma = 0, 1.2$; $\mu = 3, 6$. The error is below 9% for all structures and resolutions. The first filter width $\sigma = 1.2$ results in a lower error than for $\sigma = 0$. This holds for all spatial resolutions and fiber-distance thresholds. For the second filter, however, the optimal choice depends on the spatial resolution. The two finer resolutions benefit from a larger second filter and even exhibit a larger error for the smaller μ than for the coarse resolution. With respect to the relative minimum distance of fibers, no clear trend is visible. The error fluctuates between 1% and 8% for the different microstructures. The error of the quadratic normal tensor QNT, on the other hand, was below 2% for all spatial resolutions and hence provides a reliable option for characterizing fiber-reinforced composites. All computations were performed in a matter of minutes.

3.4.4 Sand grains and sand-binder composites

For manufacturing parts with complex geometry, casting is often the preferred choice (Rao, 2003). For casting, the mold enters a cavity of the specified shape. This cavity, in turn, is realized as a sand core, which has to be destroyed after the casting process. Such sand cores are composed of sand grains which are held together by an organic or inorganic binder. These constituents, their proportion and shape,

strongly influence the overall material behavior of the sand-binder aggregate (Schneider et al., 2018). Loosely speaking, if the strength of the aggregate is too low, the part will not survive the casting process. On the other hand, excessive strength may prevent the part to be extracted unscathed from the sand core.

In this section, we compute the quadratic normal tensors of sand cores to study their anisotropy and to demonstrate the wide range of applicability of quadratic normal tensors. We consider six different sand-grain shapes which were obtained from fitting cleaned up and binarized μ -CT scans (Schneider et al., 2018). The individual grains are shown in Fig. 3.12.

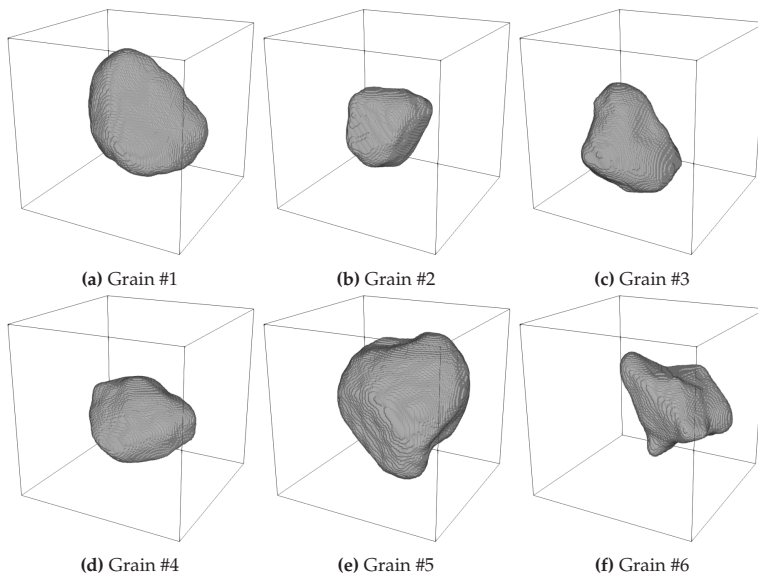


Figure 3.12: Six different sand grains whose shapes are analyzed using QNT, see Tab. 3.3. (Ernesti et al., 2022)

Grain	QNT	β	Grain	QNT	β
#1	$\begin{pmatrix} 0.2743 & 0.0518 & 0.0722 \\ 0.0518 & 0.2486 & 0.0179 \\ 0.0722 & 0.0179 & 0.4772 \end{pmatrix}$	0.4044	#2	$\begin{pmatrix} 0.3669 & -0.0428 & 0.0405 \\ -0.0428 & 0.2949 & -0.0204 \\ 0.0405 & -0.0204 & 0.3382 \end{pmatrix}$	0.6643
#3	$\begin{pmatrix} 0.382 & 0.0405 & 0.0055 \\ 0.0405 & 0.2945 & -0.0462 \\ 0.0055 & -0.0462 & 0.3235 \end{pmatrix}$	0.626	#4	$\begin{pmatrix} 0.2195 & 0.0407 & 0.0319 \\ 0.0407 & 0.3979 & 0.0936 \\ 0.0319 & 0.0936 & 0.3826 \end{pmatrix}$	0.4244
#5	$\begin{pmatrix} 0.28 & 0.0092 & 0.0013 \\ 0.0092 & 0.2875 & 0.07 \\ 0.0013 & 0.07 & 0.4325 \end{pmatrix}$	0.5564	#6	$\begin{pmatrix} 0.3123 & 0.07 & 0.0428 \\ 0.07 & 0.3202 & -0.023 \\ 0.0428 & -0.023 & 0.3674 \end{pmatrix}$	0.5795

Table 3.3: Quadratic normal tensor QNT and eigenvalue ratio β of the six grains in Fig. 3.12.

These sand grains are non-convex and anisotropic. The computed quadratic normal tensors QNT are listed in Tab. 3.3. For the computation, we chose the ball filter \mathcal{B}_σ with $\sigma = 1.2$ voxels and used central differences for the gradient-approximation. In addition to the quadratic normal tensor, we quantify the degree of anisotropy by listing the eigenvalue ratios (3.5) of QNT. We observe that all sand grains have a distinct degree of anisotropy, varying between $\beta = 0.4$ and $\beta = 0.63$. To gain further insight into the anisotropy of the grains, we compute the eigenvalue decomposition of QNT for grain #1. The eigensystem reads

$$\lambda_1 = 0.5046, \mathbf{v}_1 = \begin{pmatrix} -0.3233 \\ -0.1308 \\ -0.9372 \end{pmatrix}; \quad \lambda_2 = 0.2914, \mathbf{v}_2 = \begin{pmatrix} -0.6666 \\ -0.6715 \\ 0.3236 \end{pmatrix};$$

$$\lambda_3 = 0.204, \mathbf{v}_3 = \begin{pmatrix} -0.6717 \\ 0.7294 \\ 0.1299 \end{pmatrix}.$$

The largest eigenvalue indicates a somewhat disc-like shape within the plane normal to \mathbf{v}_1 . The vectors \mathbf{v}_2 and \mathbf{v}_3 lie in that plane, the lower eigenvalue λ_3 indicates a slight extension in direction \mathbf{v}_3 . For a better understanding, we point at Tab. 3.1, where fiber-reinforced composites are analyzed and a ‘translation’ to well-known orientation tensors is provided.

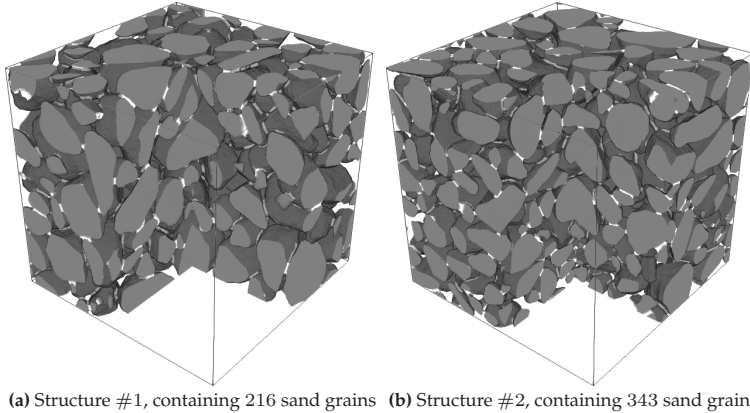


Figure 3.13: Sand core structures, containing 58.58% sand and 1.28% inorganic binder. The structures were generated by the mechanical contraction method (Schneider et al., 2018). (Ernesti et al., 2022)

These six sand grains of Fig. 3.12 were used for generating sand-binder composite microstructures, characteristic for casting applications, using the mechanical contraction method (Schneider et al., 2018). Two realizations, containing 216 and 343 sand grains, are shown in Fig. 3.13. Both structures consist of 58.58% sand grains and 1.28% inorganic binder. In contrast to particle-filled composites, these microstructures involve an interpenetrating porous phase.

On μ -CT images of sand-binder composites, the binder phase cannot be distinguished from the sand phase, see Schneider et al. (2018). Therefore, we investigate how the presence of the binder phase affects the Minkowski tensors. We compare the quadratic normal tensor QNT of the sand-binder composite to the one with only sand grains for both structures in Fig. 3.13. We chose the ball filter \mathcal{B}_σ with $\sigma = 1.2$ voxels and central differences for the gradient approximation. For all structures, the resulting tensor QNT, the degree of anisotropy β and the total surface area are listed in Tab. 3.4. The quadratic normal tensor is almost

	Sand grains alone			Sand-binder composite		
	QNT	β	$S[\text{mm}^2]$	QNT	β	$S[\text{mm}^2]$
Structure #1	$\begin{pmatrix} 0.3294 & -0.0002 & -0.0025 \\ -0.0002 & 0.3412 & -0.0094 \\ -0.0025 & -0.0094 & 0.3293 \end{pmatrix}$	0.9329	51.74	$\begin{pmatrix} 0.3292 & -0.0015 & -0.0006 \\ -0.0015 & 0.3396 & -0.0074 \\ -0.0006 & -0.0074 & 0.3312 \end{pmatrix}$	0.9485	47.26
Structure #2	$\begin{pmatrix} 0.3218 & -0.0004 & -0.0011 \\ -0.0004 & 0.3366 & -0.0028 \\ -0.0011 & -0.0028 & 0.3415 \end{pmatrix}$	0.9385	80.72	$\begin{pmatrix} 0.3233 & -0.001 & -0.0014 \\ -0.001 & 0.3362 & -0.0026 \\ -0.0014 & -0.0026 & 0.3405 \end{pmatrix}$	0.9451	73.96

Table 3.4: Quadratic normal tensor, degree of anisotropy and total surface area for grain structures #1 and #2 with and without binder.

isotropic in all four cases. Removing the binder phase leads to slightly more anisotropic quadratic normal tensors compared to the sand-binder composite. However, the change is marginal. Without the binder, the surface area of every grain is fully exposed, which results in a 9.5% larger total surface area in case of structure #1 and 9.1% larger surface area in case of structure #2. In general, we see that, although the grains within both structures are highly anisotropic, the resulting microstructure as a whole is almost isotropic. Hence, mechanical contraction of anisotropic shapes results in an overall isotropic microstructure. This conforms to the results of Schneider et al. (2018), where elastic homogenization studies on similar structures were performed. An isotropic approximation of the effective stiffness tensor was shown to be accurate.

3.5 Conclusion and Outlook

In this study, we proposed using Minkowski tensors, a tensor-valued generalization of the scalar-valued Minkowski functionals, for the analysis of microstructures given implicitly on voxel images. Due to their tensorial nature, Minkowski tensors naturally contain information about the anisotropy of geometric structures and can be incorporated into continuum mechanical or other physical modeling approaches. We provide an efficient and compact algorithm for computing the Minkowski tensor $W_1^{0,2}$ and the resulting quadratic normal tensor

(QNT) from 3D gray-value image data. This algorithm is based on image filtering and a numerical gradient computation. We demonstrated the multigrid convergence of our algorithm on a single-ball structure. Central differences and a ball filter with low filter parameter turned out to be the most accurate for binary images. For gray-value images of low resolution, skipping the filtering step may be beneficial. Furthermore, we demonstrated that the quadratic normal tensor is rather insensitive to errors in the surface area computation, thus providing a robust measure of microstructure anisotropy.

For fiber-reinforced composites, we compared characterizations based on the QNT to the well-established fiber-orientation tensors. We compared our approach to the common structure-tensor approach and demonstrated the accuracy and robustness of the quadratic normal tensor.

Finally, we studied the QNT of sand-core microstructures. Its applicability to complex grain geometries demonstrates the versatility of the Minkowski-tensor approach.

In future applications, further Minkowski tensors may be used for describing and characterizing a variety of microstructures, including curved fibers, fibers of different length and diameter, mixtures of several different shapes within a matrix, or polycrystalline structures. For a robust curvature-approximation technique based on voxel-image data, for instance, the curvature-dependent Minkowski tensor $W_2^{0,2}$ may be computed, providing additional information on the microstructure.

The Minkowski tensors of the second rank may reflect only three types of material symmetries: isotropy, transverse isotropy and orthotropy. To detect finer material symmetries, working with higher-order Minkowski tensors is necessary. Mickel et al. (2013) suggested using irreducible Minkowski tensors for anisotropy characterization, a decomposition of the surface-normal density into those of some basic shapes in the spirit of Fourier analysis. This approach may also be beneficial for fiber-orientation analysis. Moreover, the concept of Minkowski maps (Klatt et al., 2012; Göring et al., 2013) may allow studying the local

differences of the fiber orientation across an inhomogeneous medium. Last but not least, Minkowski tensors may serve as input for further studies. Similar to fiber-orientation tensor based mean-field models (Benveniste, 1987; Kehler et al., 2018), models based on Minkowski tensors may be developed. The quadratic normal tensor is able to provide insights for structures containing curved fibers and may serve as a tool for investigating their mechanical behavior.

Chapter 4

An FFT-based method for computing the effective crack energy of a heterogeneous material on a combinatorially consistent grid¹

4.1 Introduction

Francfort and Marigo (1998) revisited Griffith's original proposition (Griffith, 1921) in a quasi-static setting in order to include crack nucleation and crack branching, utilizing a variational formulation. More precisely, for a given body Ω and after a discretization in pseudo-time, they seek the displacement u and the crack surface S as minimizers of the Francfort-Marigo functional

$$FM(u, S) = \frac{1}{2} \int_{\Omega \setminus S} \nabla^s u(x) : \mathbb{C}(x) : \nabla^s u(x) dx + \int_S \gamma(x) dA \quad (4.1)$$

¹ This chapter is based on Ernesti and Schneider (2021). In order to include this paper into the structure of this work I shortened the introduction and made minor changes to the manuscript.

under the constraint of crack irreversibility, i.e., that the crack set S must contain the crack set of the previous time step. Here, $\nabla^s u$ denotes the symmetrized gradient of the displacement field, i.e., the strain tensor field, \mathbb{C} refers to the stiffness tensor and γ denotes the crack resistance. Some care has to be taken with the formulation (4.1), as Griffith's original proposal concerns only critical points of the functional (4.1) including local minima, local maxima and saddle points, whereas a rigorous mathematical treatment (Chambolle and Crismale, 2019) of the Francfort-Marigo model (4.1) appears to be limited to *global minimizers*. Please note that the formulation (4.1) accounts for heterogeneities in a natural way.

A pertinent numerical approach to minimize the Francfort-Marigo functional (4.1) was introduced by Bourdin et al. (2000), and founded what is now referred to as phase-field fracture, see Wu et al. (2020) for a recent review. In close analogy to the Ambrosio-Tortorelli approximation (Ambrosio and Tortorelli, 1990) of the Mumford-Shah functional (Mumford and Shah, 1989), the phase field model approximates the crack surface S via a smeared interface of width l and introduces a damage variable d . Owing to their ability to nucleate cracks and to produce complex crack patterns, phase-field fracture models were subject to a flurry of activity (Ambati et al., 2015). In particular, strategies to account for material anisotropy in the phase-field framework (Prajapati et al., 2020; Teichtmeister et al., 2017; Schreiber et al., 2009) were proposed. As for linear elastic fracture mechanics of anisotropic media, such models may require elaborate and expensive experimental techniques to identify the material parameters.

To alleviate this burden, multi-scale methods, in particular homogenization approaches, proved to be very effective for elastic and hardening-type inelastic material behavior. We refer to Matouš et al. (2017) for a recent overview. Relevant for this chapter is a mathematical homogenization result of Braides et al. (1996) for the Mumford-Shah functional (Mumford and Shah, 1989). In case of anti-plane shear and

neglecting the irreversibility constraint, this homogenization result is applicable to the Francfort-Marigo model of brittle fracture. More precisely, in a quasi-static setting and after a discretization in pseudo-time, we consider a fixed periodic microstructure (with non-degenerate stiffness and crack resistance). Following Braides et al. (1996) we identify the Γ -limit for vanishing period as the functional

$$FM_{\text{eff}}(u, S) = \frac{1}{2} \int_{\Omega \setminus S} \nabla^s u(x) : \mathbb{C}_{\text{eff}} : \nabla^s u(x) dx + \int_S \gamma_{\text{eff}}(n) dA, \quad (4.2)$$

where n denotes the unit normal to the crack surface S . Here, the (possibly anisotropic) effective stiffness tensor \mathbb{C}_{eff} arises from the usual elastic homogenization formula based on the classical cell problem (Milton, 2002). The integrand γ_{eff} of the surface term is a function of a unit vector, and may be computed by a corrector problem involving the local crack resistances only. This corrector problem may be interpreted as finding the γ -weighted minimal surface with average normal n cutting the microstructure (Schneider, 2020).

In particular, the volumetric and the surface energies decouple upon homogenization, as a result of the different scalings of these terms in the model (4.1). Please note that this volume-surface decoupling is a consequence of the assumed non-degeneracy of the integrands. In case of degeneracy, an interaction of the two terms is not excluded, see Barchiesi et al. (2016) and Pellet et al. (2019).

Recently, the homogenization statement was extended to the case of stationary and ergodic random materials (Cagnetti et al., 2019). Furthermore, Friedrich et al. (2022) showed the homogenization result (4.2) for linear elasticity (without the restriction to anti-plane shear). Let us also highlight that the effective model (4.2) also emerges when homogenizing the Ambrosio-Tortorelli approximation of the Francfort-Marigo model, i.e., phase-field fracture models, see Bach et al. (2021).

A method for computing the effective crack energy for three-dimensional

solids based on the homogenization result of Braides et al. (1996) and following contributions was proposed by Schneider (2020). The approach is based on a convex reformulation of the minimum-cut problem (Strang, 1983) in terms of maximum flow. More precisely, a primal-dual hybrid gradient method (Esser et al., 2010; Pock et al., 2009) was used, extending previous FFT-based computational homogenization methods for thermal conductivity and elasticity.

Contributions

This chapter is concerned with computing the effective crack energy via an appropriate cell formula (to be discussed in Section 4.2.1) corresponding to the mathematical homogenization results (Braides et al., 1996; Cagnetti et al., 2019; Friedrich et al., 2022). Please note that the computed effective crack energy may differ from the *effective crack resistance*, depending on the underlying length scales and loading scenarios (see Section 2.1, item 5, in Schneider (2020) for a discussion). Still, the computed effective crack energy gives rise to a lower bound for the effective crack resistance, and may thus be used for assessing the safety of components made of such composites.

Previous work (Schneider, 2020) provided a computational approach for computing the effective crack energy using an FFT-based primal-dual hybrid gradient solver and two discretization schemes, i.e., trigonometric collocation and the rotated staggered grid. The approach (Schneider, 2020) has two shortcomings. First, the solution fields are characterized by ringing or checkerboard artifacts, depending on the discretization. Moreover, the solver does not permit reaching a high accuracy for complex three-dimensional microstructures. Although the first shortcoming concerns the discretization and the second issue is related to the numerical resolution, both effects are actually related. Indeed, as computing the effective crack energy involves a pointwise constraint on a vector field, discretization-related artifacts may interfere with

solver performance.

The cell problem for computing the effective crack energy is closely related to the minimum-cut problem put forward by Strang (1983) in his analysis of the continuous maximum flow problem, see Section 4.2.1. To be more precise, the maximum flow problem is rooted in graph theory and seeks a feasible flow through a flow network that obtains the maximum possible flow rate under capacity constraints (Ford and Fulkerson, 1956). With the help of duality theory for linear programming, it may be shown that the maximum flow equals the minimum capacity of a cut disconnecting the source and the sink (Ford and Fulkerson, 1956; Elias et al., 1956). Strang (1983) proposed a continuum generalization of the graph-theoretic maximum flow problem, involving an incompressible flow field subject to a (continuous) capacity constraint. Similar to the graph-theoretic version, he established a duality result which equates the maximum flow rate with the capacity of a minimum cut. However, the continuous version is no longer based on *linear* duality theory, and requires more sophisticated mathematical tools. Previous work (Schneider, 2020) realized that the cell problem corresponding to the mathematical homogenization results (Braides et al., 1996; Cagnetti et al., 2019; Friedrich et al., 2022) may be interpreted as a minimum-cut problem, where the microscopic (heterogeneous) crack resistance is regarded as a (spatially varying) capacity. Then, the maximum flow–minimum cut duality, valid on a discrete level, is invoked to construct a suitable primal-dual solver.

For the graph-theoretic maximum flow problem, a variety of efficient solvers is available (Ford and Fulkerson, 1956; Dinic, 1970; Edmonds and Karp, 1972; Goldberg and Rao, 1998). Unfortunately, these solvers are unsuited for the continuous maximum flow problem. Indeed, working with a graph-theoretic discretization leads to so-called metrication artifacts, which do not vanish upon mesh refinement (Kolmogorov and Zabin, 2004). More precisely, for the graph-theoretic version, the capacity constraints are associated to the edges, whereas, when representing

the continuous maximum flow problem in terms of a finite difference discretization, the capacity constraints are associated to the nodes of the graph. As a remedy, Couprie et al. (2011) introduced the *combinatorial continuous maximum flow* (CCMF) discretization, whose node-based capacity constraints account for all adjacent edges in a suitable way. The CCMF discretization, to be discussed in Section 4.2.2, naturally avoids metrication errors, and may be implemented into standard convex optimization solvers (Boyd and Vandenberghe, 2004). However, as the authors remark themselves: "In 3D, our CCMF implementation is suffering from memory limitations in the direct solver we used, limiting its performances." (Couprie et al., 2011, Sec. 4.4.3)

Our contributions are threefold. For a start, we propose using the CCMF discretization for the effective crack energy associated to the mathematical homogenization results (Braides et al., 1996; Cagnetti et al., 2019; Friedrich et al., 2022), see Section 4.2 for details. In this way, the artifacts of the previously used discretizations (Schneider, 2020) are fully eliminated. Our second contribution concerns a novel FFT-based solver for the maximum flow problem in the CCMF discretization on regular periodic grids, filling the gap mentioned by Couprie et al. (2011). The proposed solver, see Section 6.4, is based on a doubling of the degrees of freedom per cell, which makes the nonlocal capacity constraint for the CCMF discretization *local*, at the expense of additional constraints enforcing compatibility of the flow field across the faces of the voxel grid. As a byproduct, we arrive at an expression for the minimum-cut problem that is much simpler than in Couprie et al. (2011), see Section 4.3.1. Then, the alternating direction method of multipliers (ADMM), pioneered by Michel et al. (2000; 2001) in conjunction with FFT-based methods, is used to extract the minimum cut, see Section 4.3.2. Last but not least, we study recently proposed (Schneider, 2021b), adaptive strategies for choosing the penalty parameter in the ADMM. Finally, we demonstrate the capabilities of our approach in applications of industrial size, see Section 4.4. We find that an adaptive parameter-selection strategy is

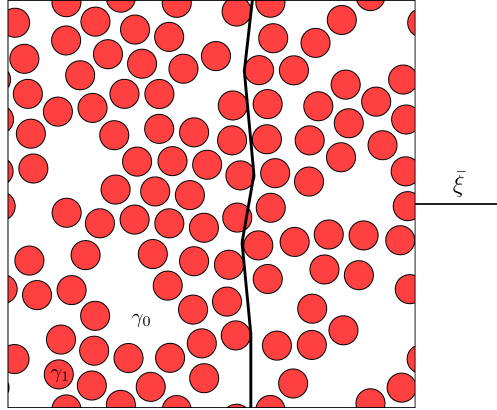


Figure 4.1: Schematic of a potentially minimal crack traversing a two-phase microstructure for prescribed normal $\bar{\xi}$. (Ernesti and Schneider, 2021)

critical for high performance and high accuracy, improving upon the standard ADMM used by Willot (2020), who treats the closely related graph-based maximum flow problem (not the continuous one).

4.2 The effective crack energy of a heterogeneous material

4.2.1 Cell formulas for the minimum cut and the maximum flow

Let us consider a cuboid cell $Y = [0, L_1] \times [0, L_2] \times [0, L_3]$, on which a heterogeneous field of crack resistances $\gamma : Y \rightarrow \mathbb{R}$ is given. For mathematical reasons, we suppose that there are positive constants γ_{\pm} , s.t. the inequalities

$$\gamma_- \leq \gamma(x) \leq \gamma_+ \quad \text{hold for all } x \in Y.$$

We define the effective crack energy γ_{eff} (Braides et al., 1996; Cagnetti et al., 2019; Schneider, 2020), a function on the unit sphere $S^2 \subseteq \mathbb{R}^3$, by

$$\gamma_{\text{eff}}(\bar{\xi}) = \inf_{\phi} \frac{1}{|Y|} \int_Y \gamma \|\bar{\xi} + \nabla\phi\| dx, \quad \bar{\xi} \in S^2, \quad (4.3)$$

see Fig. 4.1, where $|Y| = L_1 L_2 L_3$ denotes the volume of the cell and the infimum is evaluated over all smooth scalar fields $\phi : Y \rightarrow \mathbb{R}$ which are periodic, together with all their derivatives. This formula computes the (periodic) minimum cut through the cell Y with mean normal $\bar{\xi}$ as a γ -weighted minimal surface. The scalar ϕ plays the role of a characteristic function jumping across the cut. Please note that the integrand in the right hand side of equation (4.3) is a function which is homogeneous of degree one, i.e., it satisfies $f(\lambda\xi) = \lambda f(\xi)$ for all vectors $\xi \in \mathbb{R}^3$ and all scalars $\lambda > 0$. This contrasts with thermal conductivity (Milton, 2002), where a homogeneity of degree two leads to a linear Euler-Lagrange equation associated to the variational problem. For the problem at hand (4.3), additional complications arise. For a start, due to the one-homogeneity, the functional in the definition (4.3) is not differentiable. In particular, the first-order necessary conditions are (strongly) non-linear. Furthermore, the one-homogeneity permits *localization* to appear for minimizers of the variational problem (4.3). This localization is not unwarranted, as such minimizers actually represent minimum cuts through the microstructure (Strang, 1983), weighted by the crack resistance, and enables computing the effective crack energy by the local crack resistance averaged over the minimum cut. In fact, the minimum cut needs not be unique. However, the computed effective crack energy is unique as a consequence of the convexity of the functional to be minimized.

To circumvent the inherent lack of differentiability characterizing the functional (4.3), dual and primal-dual formulations may be exploited (Chambolle and Pock, 2016). As an example, the (formal)

dual to the variational problem is given by the maximum flow problem (Strang, 1983)

$$\frac{1}{|Y|} \int_Y v \cdot \bar{\xi} dx \longrightarrow \max_{\substack{\operatorname{div}(v)=0 \\ \|v\| \leq \gamma}}, \quad (4.4)$$

where the maximum is evaluated over all smooth and solenoidal vector fields $v : Y \rightarrow \mathbb{R}^3$ which satisfy the pointwise constraint

$$\|v(x)\| \leq \gamma(x) \quad \text{for (almost) all } x \in Y. \quad (4.5)$$

Due to the non-negativity of the terms involved, the latter condition may also be recast in the form

$$\|v(x)\|^2 \leq \gamma(x)^2 \quad \text{for (almost) all } x \in Y. \quad (4.6)$$

The dual problem (4.4) maximizes the total flow in direction $\bar{\xi}$ through the microstructure under the point-wise constraints (4.5). The advantage of the dual formulation (4.4) over the primal formulation (4.3) is that it represents a smooth (in fact linear) optimization problem with linear and quadratic constraints, for which powerful solution methods are available (Boyd and Vandenberghe, 2004). However, some caution is advised, as the primal (4.3) and the dual problem (4.4) are strongly dual in the continuous setting only for a *continuous* crack resistance γ (Strang, 1983). As soon as the crack resistance γ is discontinuous, explicit counterexamples (Nozawa, 1994) to strong duality are known, i.e., the maximum computed in the dual problem (4.4) is strictly less than the minimum computed for the primal problem (4.3).

For practical considerations, this delicacy does not play much of a role. Indeed, in finite dimensions, convex optimization problems with convex constraints *always* satisfy strong duality provided Slater's condition is satisfied (Boyd and Vandenberghe, 2004, Sec. 5.2). Slater's condition states that there is a strictly feasible point, i.e., a point where all inequality

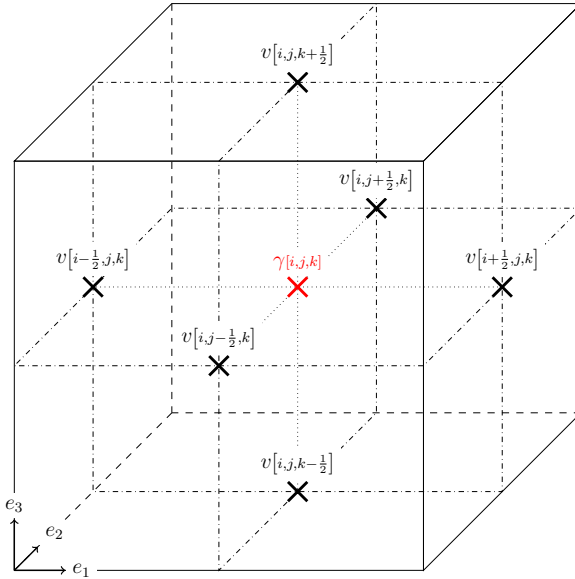


Figure 4.2: Consistent placement of the flow-field variables on a generic voxel cell. (Ernesti and Schneider, 2021)

constraints are satisfied as strict inequalities. Due to our prerequisite $\gamma \geq \gamma_- > 0$, the field $v \equiv 0$ is strictly feasible for the dual problem (4.4), and strong duality holds upon discretization. In particular, we may exploit the maximum flow formulation (4.4), as long as it arises by formal Lagrangian dualization (Boyd and Vandenberghe, 2004, Ch. 5) of a discretization of the cell problem (4.3).

4.2.2 The combinatorial continuous maximum flow discretization

In this section, we discuss the combinatorial continuous maximum flow discretization (CCMF) introduced by Couprie et al. (2011) for the special

case of regular grids and in the periodic setting. The discretization scheme naturally approximates the continuous maximum flow formulation (4.4), and we take it as our point of departure.

For this purpose, suppose that the unit cell $Y = [0, L_1] \times [0, L_2] \times [0, L_3]$ is discretized by a regular grid with N_i ($i = 1, 2, 3$) voxels for each coordinate direction. Each voxel is assumed to be cubic with edge length h , i.e., the conditions $h = L_i/N_i$ ($i = 1, 2, 3$) are assumed to hold. In a finite volume discretization, where each individual voxel serves as a control volume, the flow between adjacent cells is quantified by a flow field v , which is located at the voxel faces, see Fig. 4.2. The conservation of mass is encoded by the balance of in- and outflow

$$0 = v\left[i+\frac{1}{2}, j, k\right] - v\left[i-\frac{1}{2}, j, k\right] + v\left[i, j+\frac{1}{2}, k\right] - v\left[i, j-\frac{1}{2}, k\right] + v\left[i, j, k+\frac{1}{2}\right] - v\left[i, j, k-\frac{1}{2}\right], \quad (4.7)$$

where we tacitly assume the integer indices i, j, k to satisfy

$$0 \leq i < N_1, \quad 0 \leq j < N_2 \quad \text{and} \quad 0 \leq k < N_3,$$

and the equation (4.7) should be interpreted in a periodic fashion. Let us denote by

$$\gamma^{[i,j,k]} = \gamma\left(\left(i + \frac{1}{2}\right)h, \left(j + \frac{1}{2}\right)h, \left(k + \frac{1}{2}\right)h\right)$$

the evaluations of the crack resistance γ at the voxel centers, which we sample on a discrete grid Y_N . Then, for the CCMF-discretization, the constraint (4.5) is approximated by the $N_1 N_2 N_3$ constraints

$$2\gamma^{[i,j,k]^2} \geq v\left[i+\frac{1}{2}, j, k\right]^2 + v\left[i-\frac{1}{2}, j, k\right]^2 + v\left[i, j+\frac{1}{2}, k\right]^2 + v\left[i, j-\frac{1}{2}, k\right]^2 + v\left[i, j, k+\frac{1}{2}\right]^2 + v\left[i, j, k-\frac{1}{2}\right]^2. \quad (4.8)$$

Here, the constraint (4.8) is associated to each cell, and accounts for all six in- and outflow variables located on the corresponding adjacent

faces, see Fig. 4.2. Compared to the continuous formulation (4.6), which involves a vector of dimension three, twice the number of terms is considered. This is compensated by adding a factor two on the right hand side.

Then, for prescribed average crack normal $\bar{\xi} \in S^2$, the CCMF discretization approximates the maximum flow problem (4.4) by the maximization problem

$$\frac{1}{N_1 N_2 N_3} \sum_{i,j,k} \bar{\xi}_x v[i+\frac{1}{2},j,k] + \bar{\xi}_y v[i,j+\frac{1}{2},k] + \bar{\xi}_z v[i,j,k+\frac{1}{2}] \longrightarrow \max_{v \text{ satisfying (4.7) and (4.8)}} . \quad (4.9)$$

With FFT-based solution methods, to be discussed in Section 6.4, in mind, we transform the natural finite volume formulation into a more compact representation that is simpler to manipulate algebraically. For this purpose, we regard the flow field v as a vector field located at the voxel centers, with the identification

$$\begin{aligned} v_x[i,j,k] &= v[i+\frac{1}{2},j,k], \\ v_y[i,j,k] &= v[i,j+\frac{1}{2},k], \\ v_z[i,j,k] &= v[i,j,k+\frac{1}{2}]. \end{aligned}$$

We also introduce a (backwards) divergence-type operator div^- via

$$\begin{aligned} (\text{div}^- v)[i,j,k] &= v_x[i,j,k] - v_x[i-1,j,k] + v_y[i,j,k] \\ &\quad - v_y[i,j-1,k] + v_z[i,j,k] - v_z[i,j,k-1]. \end{aligned}$$

Then, the mass conservation (4.7) is satisfied precisely if $\text{div}^- v = 0$ holds. To encode the constraint (4.8), we introduce the backwards shift

operator S , which operates as follows

$$S(v)_{[i,j,k]} = \begin{bmatrix} v_x[i-1,j,k] \\ v_y[i,j-1,k] \\ v_z[i,j,k-1] \end{bmatrix}. \quad (4.10)$$

Then, the constraint (4.8) is equivalent to the condition

$$\|v_{[i,j,k]}\|^2 + \|S(v)_{[i,j,k]}\|^2 \leq 2\gamma_{[i,j,k]}^2, \quad (4.11)$$

expressed in terms of the Euclidean norm of the involved vectors. Last but not least, let us introduce the L^2 inner product on such vector fields

$$\langle v, \tilde{v} \rangle_{L^2} = \frac{1}{N_1 N_2 N_3} \sum_{i,j,k} (v_x[i,j,k] \tilde{v}_x[i,j,k] + v_y[i,j,k] \tilde{v}_y[i,j,k] + v_z[i,j,k] \tilde{v}_z[i,j,k]) \quad (4.12)$$

with corresponding norm $\|\cdot\|_{L^2}$. With this notation at hand, we may express the maximization problem (4.13) in the compact form

$$\langle \bar{\xi}, v \rangle_{L^2} \longrightarrow \max_{\substack{\text{div}^- v=0 \\ \|v\|^2 + \|Sv\|^2 \leq 2\gamma^2}}, \quad (4.13)$$

where we regard $\bar{\xi}$ as a constant vector field and the norm constraint is enforced at every voxel. In the latter formulation, the similarities (and differences) to the continuous formulation (4.4) become apparent. Indeed, both the objective function and the divergence constraint are discretized in the natural way. The norm constraint, however, is replaced by a "non-local" constraint which involves neighboring values of the flow field, as well. Please note that this is a feature rather than a bug, as the flow-field variables are naturally located on the voxel faces, whereas the crack resistance is associated to the voxel center. Instead of *interpolating* the flow-field variables, the CCMF discretization averages the squares

of the flow fields. Such an approach has its merits, as will become clear in Section 4.4.

4.3 An FFT-based solver for the CCMF discretization

4.3.1 The primal formulation for the CCMF discretization

On a voxel grid, we consider the maximum flow problem (4.13)

$$\langle \bar{\xi}, v \rangle_{L^2} \longrightarrow \max_{\substack{\text{div}^- v=0 \\ \|v\|^2 + \|Sv\|^2 \leq 2\gamma^2}} \quad (4.14)$$

in the combinatorial continuous maximum flow (CCMF) discretization. With FFT-based resolution in mind, we compute the corresponding Lagrangian dual, i.e., the associated minimum cut problem.

For later reference please notice that the adjoint of the backward shift operator S (5.14) w.r.t. the inner product (4.12) is given by the (periodized) *forward* shift operator

$$S^*(v)_{[i,j,k]} = \begin{bmatrix} v_x[i+1,j,k] \\ v_y[i,j+1,k] \\ v_z[i,j,k+1] \end{bmatrix}. \quad (4.15)$$

In particular, as backward and forward shifting are mutual inverses, the equation $S^*S = \text{Id}$ holds in terms of the identity operator Id .

The shift operator is non-local, which makes the inequality constraint in the maximum flow problem (4.14) non-local, as well. With computational resolution in mind, we seek a local formulation that relies upon a doubling of dimension. For this purpose, we introduce the linear

extension operator A , acting on vector fields v via

$$(Av) = \frac{1}{\sqrt{2}} \begin{bmatrix} v \\ Sv \end{bmatrix}, \quad (4.16)$$

and producing a vector field with six scalar components per voxel. Then, the problem (4.14) may be expressed in the equivalent form

$$\langle \bar{\xi}, v \rangle_{L^2} \longrightarrow \max_{\substack{\operatorname{div}^- v=0 \\ \|Av\| \leq \gamma}}, \quad (4.17)$$

where the factor two in front of the crack resistance (4.14) was transferred into the A -operator (4.16) and the norm in the constraint refers to the Euclidean norm of vectors with six components. For later reference, let us remark that the adjoint of the operator A (4.16) w.r.t. the six-component version of the L^2 inner product (4.12) is given by

$$A^* \begin{bmatrix} w_1 \\ w_2 \end{bmatrix} = \frac{1}{\sqrt{2}}(w_1 + S^* w_2) \quad (4.18)$$

in terms of the backward shift operator (4.15). In particular, it holds

$$A^* Av = \frac{1}{2}(v + S^* Sv) = v,$$

i.e., $A^*A = \operatorname{Id}$ and $\|A\| = 1$ in operator norm. Thus, the operator A is an isometric embedding, and the operator A^* is a left inverse to the operator A . In turn, the operator AA^* is the orthogonal projector onto the image of the operator A . To complete the necessary notation, we define the indicator function ι_T of a set T via

$$\iota_T(u) = \begin{cases} 0 & u \in T \\ +\infty, & \text{otherwise,} \end{cases}$$

which permits encoding a constraint to the set T in terms of an objective function.

With the necessary terminology at hand, we turn our attention to deriving the Lagrangian dual of the maximum flow problem (4.14) in the constrained form

$$\langle \bar{\xi}, v \rangle_{L^2} - \iota_{\{\text{div}^- v=0\}}(v) - \iota_{\mathcal{C}_\gamma}(w) \longrightarrow \max_{w+Av=0}, \quad (4.19)$$

where we denote by \mathcal{C}_γ the set

$$\mathcal{C}_\gamma = \{w : Y_N \rightarrow \mathbb{R}^6 \mid \|w_{[i,j,k]}\| \leq \gamma_{[i,j,k]} \text{ for all } i, j, k\}. \quad (4.20)$$

The associated Lagrangian function reads

$$L(v, w, \xi) = \langle \bar{\xi}, v \rangle_{L^2} - \iota_{\{\text{div}^- v=0\}}(v) - \iota_{\mathcal{C}_\gamma}(w) - \langle \xi, Av + w \rangle_{L^2} \quad (4.21)$$

in terms of the Lagrangian multiplier field $\xi : Y_N \rightarrow \mathbb{R}^6$. To evaluate the dual function

$$\varphi(\xi) = \sup_{v,w} L(v, w, \xi),$$

we rearrange the expression of the Lagrangian (4.21)

$$\begin{aligned} \varphi(\xi) &= \sup_v \langle \bar{\xi}, v \rangle_{L^2} - \iota_{\{\text{div}^- v=0\}}(v) - \underbrace{\langle \xi, Av \rangle_{L^2}}_{=\langle A^* \xi, v \rangle_{L^2}} + \sup_w \langle \xi, w \rangle_{L^2} - \iota_{\mathcal{C}_\gamma}(w) \\ &= \begin{cases} \frac{1}{N_1 N_2 N_3} \sum_{i,j,k} \gamma_{[i,j,k]} \|\xi_{[i,j,k]}\|, & \xi \in \mathcal{K}_{\bar{\xi}}, \\ +\infty, & \text{otherwise,} \end{cases} \end{aligned}$$

in terms of the set of compatible normal fields

$$\begin{aligned} \mathcal{K}_{\bar{\xi}} &= \{\xi : Y_N \rightarrow \mathbb{R}^6 \mid \text{there is some } \phi : Y_N \rightarrow \mathbb{R}, \\ &\text{s.t. } A^* \xi = \bar{\xi} + \nabla^+ \phi\}. \end{aligned} \quad (4.22)$$

This set may be interpreted as follows. Fields $\xi : Y_N \rightarrow \mathbb{R}^6$ associate to every voxel six scalar values. These values are assigned to each face of the voxel. Please note that any face of the voxel mesh is thus assigned with *two* values, one for each adjacent voxel. Up to a factor $\sqrt{2}$, $A^*\xi$ refers to the face-wise average of these two values. The set $\mathcal{K}_{\bar{\xi}}$ contains all fields, whose averages $A^*\xi$ are compatible in the sense that they arise as the sum of a constant vector (which is fixed beforehand) and the gradient of a scalar field (one scalar per voxel). Thus, up to face-wise averaging, the compatibility constraint is similar to thermal conductivity or elasticity. The final form

$$\frac{1}{N_1 N_2 N_3} \sum_{i,j,k} \gamma^{[i,j,k]} \|\xi^{[i,j,k]}\| \longrightarrow \min_{\xi \in \mathcal{K}_{\bar{\xi}}} \quad (4.23)$$

of the dual to the CCMF problem (4.14) is remarkably close to the original minimum cut formulation (4.3), cf. the more involved formulas in section 2.3 in Couprie et al. (2011).

4.3.2 An FFT-based ADMM solver

To proceed, we rewrite the optimization problem (4.23) as an equivalent convex program that is amenable to operator-splitting approaches

$$f(\xi) + g(\xi) \longrightarrow \min_{\xi} \quad (4.24)$$

in terms of the convex functions

$$f(\xi) = \iota_{\mathcal{K}_{\bar{\xi}}}(\xi) \quad \text{and} \quad g(\xi) = \frac{1}{N_1 N_2 N_3} \sum_{i,j,k} \gamma^{[i,j,k]} \|\xi^{[i,j,k]}\|.$$

The starting point of operator-splitting approaches is the rewriting of the unconstrained problem (5.21) in constrained form

$$f(\xi) + g(e) \longrightarrow \min_{\xi=e}. \quad (4.25)$$

For solving the problem (5.22), we utilize the alternating direction method of multipliers (ADMM) (Glowinski and Marrocco, 1975; Gabay and Mercier, 1976), which was pioneered in the context of FFT-based methods by Michel et al. (2000; 2001), and applied to non-smooth optimization by Willot (2020). For this purpose, we investigate the augmented Lagrangian function

$$L_\rho(\xi, e, v) = f(\xi) + g(e) + \langle v, \xi - e \rangle_{L^2} + \frac{\rho}{2} \|\xi - e\|_{L^2}^2, \quad (4.26)$$

involving a penalization factor $\rho > 0$ and the Lagrange multiplier $v : Y_N \rightarrow \mathbb{R}^6$. The ADMM is based on the three-term recursion

$$\begin{aligned} \xi^{k+1} &= \operatorname{argmin}_\xi L_\rho(\xi, e^k, v^k), \\ e^{k+1} &= \operatorname{argmin}_e L_\rho(\xi^{k+1}, e, v^k), \\ v^{k+1} &= v^k + \rho(\xi^{k+1} - e^{k+1}). \end{aligned} \quad (4.27)$$

Let us investigate the first line more explicitly,

$$\begin{aligned} \xi^{k+1} &= \operatorname{argmin}_\xi L_\rho(\xi, e^k, v^k) \\ &= \operatorname{argmin}_\xi f(\xi) + \langle v^k, \xi \rangle_{L^2} + \frac{\rho}{2} \|\xi - e^k\|_{L^2}^2 \\ &= \operatorname{argmin}_{\xi \in \mathcal{K}_{\bar{\xi}}} \left\| \xi - e^k + \frac{1}{\rho} v^k \right\|_{L^2}^2. \end{aligned}$$

Thus, ξ^{k+1} arises as the orthogonal projection of the point $e^k - v^k/\rho$ onto the set $\mathcal{K}_{\bar{\xi}}$,

$$\xi^{k+1} = \mathcal{P}_{\mathcal{K}_{\bar{\xi}}} \left(e^k - \frac{1}{\rho} v^k \right).$$

Let us write down an explicit expression for the projection operator $\mathcal{P}_{\mathcal{K}_{\bar{\xi}}}$. For given $w : Y_N \rightarrow \mathbb{R}^6$, we seek $\xi : Y_N \rightarrow \mathbb{R}^6$, s.t.

$$\xi = \mathcal{P}_{\mathcal{K}_{\bar{\xi}}}(w), \quad \text{i.e.,} \quad \xi = \operatorname{argmin}_{\xi \in \mathcal{K}_{\bar{\xi}}} \|\xi - w\|_{L^2}^2 \quad \text{holds.} \quad (4.28)$$

With the help of the orthogonal projector $P = AA^*$ and its orthogonal, complementary projector $Q = \operatorname{Id} - AA^*$, we may decompose the vector field ξ

$$\xi = \xi_P + \xi_Q \quad \text{with} \quad \xi_P = P\xi \quad \text{and} \quad \xi_Q = Q\xi, \quad (4.29)$$

s.t., by orthogonality,

$$\|\xi\|_{L^2}^2 = \|\xi_P\|_{L^2}^2 + \|\xi_Q\|_{L^2}^2 \quad (4.30)$$

holds. Then, we may express the set $\mathcal{K}_{\bar{\xi}}$ in the form

$$\begin{aligned} \mathcal{K}_{\bar{\xi}} = \{ \xi : Y_N \rightarrow \mathbb{R}^6 \mid \text{there are } \phi : Y_N \rightarrow \mathbb{R} \text{ and } \eta : Y_N \rightarrow \mathbb{R}^6, \\ \text{s.t. } \xi = A(\bar{\xi} + \nabla^+ \phi) + Q\eta \}. \end{aligned} \quad (4.31)$$

To show equivalence of definitions, let us take an element $\xi \in \mathcal{K}_{\bar{\xi}}$ according to the former definition (4.22), which was characterized by the defining constraint

$$A^* \xi = \bar{\xi} + \nabla^+ \phi.$$

Then, by definition of ξ_P , we observe

$$\xi_P \equiv P\xi = AA^* \xi = A(\bar{\xi} + \nabla^+ \phi),$$

and ξ is contained in the set (4.31). Conversely, applying A^* to an element ξ of the set (4.31) yields

$$A^* \xi = \underbrace{A^* A}_{=\operatorname{Id}} (\bar{\xi} + \nabla^+ \phi) + \underbrace{A^* Q}_{=0} \eta = \bar{\xi} + \nabla^+ \phi,$$

which shows that ξ lies in the original set (4.22). Returning to the projection problem (4.28)

$$\xi = \operatorname{argmin}_{\xi \in \mathcal{K}_{\bar{\xi}}} \|\xi - w\|_{L^2}^2,$$

we decompose $w = w_P + w_Q$ in the same form (4.29). Due to the Pythagorean theorem (4.30), we observe

$$\begin{aligned} \xi &= \operatorname{argmin}_{\xi \in \mathcal{K}_{\bar{\xi}}} \|\xi - w\|_{L^2}^2 \\ &= \operatorname{argmin}_{\xi \in \mathcal{K}_{\bar{\xi}}} \|\xi_P - w_P\|_{L^2}^2 + \|\xi_Q - w_Q\|_{L^2}^2 \\ &= \operatorname{argmin}_{\phi, \eta} \|A(\bar{\xi} + \nabla^+ \phi) - w_P\|_{L^2}^2 + \|Q\eta - w_Q\|_{L^2}^2, \end{aligned}$$

where we inserted the definition (4.31) in the last line. We observe that the optimization problems for the variables ϕ and η *decouple*. The problem for $Q\eta$ is particularly simple, and is solved by $Q\eta = w_Q \equiv Qw$. Using that A is an isometric embedding, the problem for ϕ becomes

$$\|\bar{\xi} + \nabla^+ \phi - A^*w\|_{L^2}^2 \longrightarrow \min_{\phi}.$$

The corresponding critical point satisfies

$$\operatorname{div}^- [\bar{\xi} + \nabla^+ \phi - A^*w] = 0 \quad \iff \quad \operatorname{div}^- \nabla^+ \phi = \operatorname{div}^- A^*w.$$

The latter equation may be solved formally to give

$$\phi = (\operatorname{div}^- \nabla^+)^{\dagger} \operatorname{div}^- A^*w,$$

where \dagger denotes the Moore-Penrose pseudo inverse. Reinserting the found expressions into the definition (4.31), we find

$$\xi = A\bar{\xi} + A\nabla^+(\operatorname{div}^- \nabla^+)^{\dagger} \operatorname{div}^- A^*w + (\operatorname{Id} - AA^*)w,$$

which we may also write in the more convenient form

$$\begin{aligned} \mathcal{P}_{\mathcal{K}_{\bar{\xi}}}(w) &= A\bar{\xi} + (\text{Id} - AA^* + A\Gamma A^*) w \\ &\text{with } \Gamma = \nabla^+(\text{div}^- \nabla^+)^{\dagger} \text{div}^-. \end{aligned} \quad (4.32)$$

The second line (5.24) can be rewritten using Moreau's identity (Chambolle and Pock, 2016, Eq. (3.8)) in the form

$$e^{k+1} = [v^k + \rho \xi^{k+1} - \mathcal{P}_{\mathcal{C}_{\gamma}}(v^k + \rho \xi^{k+1})] / \rho,$$

where $\mathcal{P}_{\mathcal{C}_{\gamma}}$ is the orthogonal projector

$$(\mathcal{P}_{\mathcal{C}_{\gamma}}(w))_{[i,j,k]} = \begin{cases} \gamma^{[i,j,k]} w_{[i,j,k]} / \|w_{[i,j,k]}\|, & \|w_{[i,j,k]}\| > \gamma^{[i,j,k]}, \\ w_{[i,j,k]}, & \text{otherwise,} \end{cases}$$

onto the constraint set \mathcal{C}_{γ} (4.20). Thus, we are led to the following scheme

$$\begin{aligned} \xi^{k+1} &= A\bar{\xi} - \frac{1}{\rho} (\text{Id} - AA^* + A\Gamma A^*) (v^k - \rho e^k), \\ e^{k+1} &= [v^k + \rho \xi^{k+1} - \mathcal{P}_{\mathcal{C}_{\gamma}}(v^k + \rho \xi^{k+1})] / \rho, \\ v^{k+1} &= v^k + \rho (\xi^{k+1} - e^{k+1}). \end{aligned} \quad (4.33)$$

A recent study (Schneider, 2021b) highlighted the importance of utilizing a damping factor and choosing the penalty factor ρ adaptively. For this purpose, we consider the modified scheme

$$\begin{aligned} \xi^{k+1/2} &= A\bar{\xi} - \frac{1}{\rho^k} (\text{Id} - AA^* + A\Gamma A^*) (v^k - \rho^k e^k), \\ \xi^{k+1} &= 2(1 - \delta)\xi^{k+1/2} - (1 - 2\delta)e^k, \\ e^{k+1} &= [v^k + \rho^k \xi^{k+1} - \mathcal{P}_{\mathcal{C}_{\gamma}}(v^k + \rho^k \xi^{k+1})] / \rho^k, \\ v^{k+1} &= v^k + \rho^k (\xi^{k+1} - e^{k+1}). \end{aligned} \quad (4.34)$$

with damping $\delta \in (0, 1)$ and adaptive penalty parameter ρ^k . In general, the over-relaxation $\delta = 1/4$ is recommended (Monchiet and Bonnet, 2012; Moulinec and Silva, 2014; Schneider, 2021b). Simple choices for the parameter ρ^k are based on the Lorenz-Tran-Dinh scaling (Lorenz and Tran-Dinh, 2019)

$$\rho^k = \frac{\|v^k\|_{L^2}}{\|e^k\|_{L^2}}$$

or the Barzilai-Borwein scaling (Xu et al., 2017)

$$\rho^k = \frac{\langle v^k - v^{k-1}, e^k - e^{k-1} \rangle_{L^2}}{\|e^k - e^{k-1}\|_{L^2}^2}$$

and an additional safeguard (Schneider, 2021b, Sec. 2.5). In our computational experiments, the latter two schemes outperform, both, constant penalty parameter ρ and residual balancing (He et al., 2000).

Last but not least, let us stress that the operator Γ has an explicit form in Fourier space, see (Willot et al., 2014, Eq. 18)

4.4 Computational experiments

4.4.1 Setup

The algorithm (4.34) was integrated into an existing FFT-based computational homogenization code for thermal conductivity (Dorn and Schneider, 2019), written in Python with Cython extensions (and OpenMP). In the context of small-strain inelasticity, the implementation of the ADMM (4.34) and the memory-efficient computation of the penalty factor is discussed in Schneider (2021b). In the same paper, the convergence criterion

$$\left\| e^k - \xi^{k+\frac{1}{2}} \right\|_{L^2} \leq \text{tol} \|\langle v \rangle_Y\|, \quad (4.35)$$

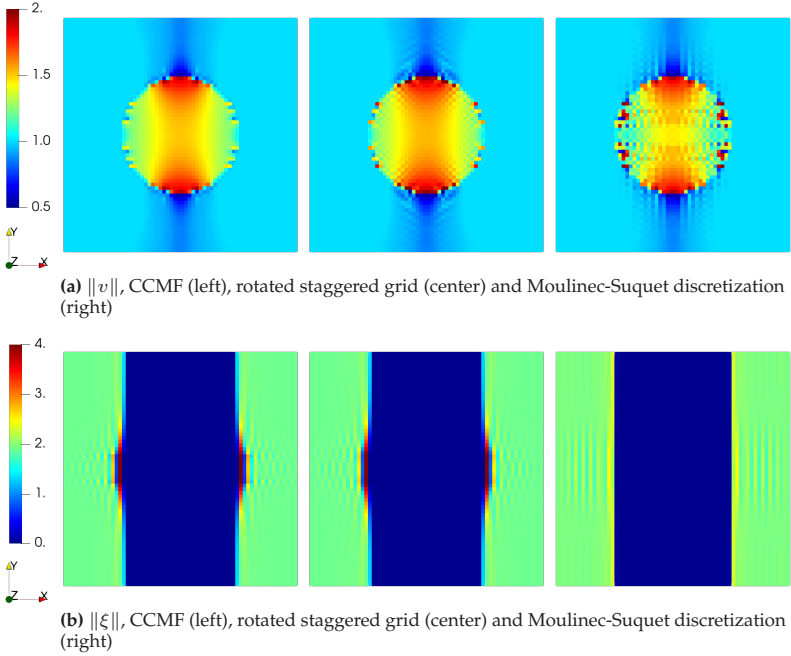


Figure 4.3: Flow v and normal ξ fields on a cross section through a 64^3 single-sphere microstructure for $\tilde{\xi} = e_x$, $\gamma_{\text{ball}} = 10 \gamma_{\text{matrix}}$ and different discretizations. (Ernesti and Schneider, 2021)

for prescribed tolerance tol , is identified as suitable. All computational experiments were run on a desktop computer with 32GB RAM and six 3.7GHz cores, and on a workstation with 512 GB RAM and two Intel Xeon(R) Gold 6146 processors (12×3.20 GHz), respectively. If not mentioned otherwise, we will use ADMM with damping factor $\delta = 0.25$ and the Barzilai-Borwein adaptive choice for the penalty factor. The default tolerance tol (5.33) was set to $\text{tol} = 10^{-4}$.

4.4.2 A single spherical inclusion

As a first example, we build upon previous numerical experiments (Schneider, 2020, Sec. 4.2.2) and compare the CCMF-discretization to previously investigated discretization schemes, namely the rotated staggered grid (Saenger et al., 2000; Saenger and Bohlen, 2004; Willot, 2015a) and the Moulinec-Suquet discretization (Moulinec and Suquet, 1994; 1998). We consider a 64^3 box containing a single spherical inclusion with a diameter of 32 voxels. The crack resistance of the inclusion is chosen as $\gamma_{\text{sphere}} = 10 \gamma_{\text{matrix}}$. We prescribe a unit vector $\bar{\xi} = e_x$ in x -direction as the crack normal. We solved the problem up to a tolerance of 10^{-4} using ADMM and chose the penalty factor as lower bound $\rho = \min\{\gamma_{\text{sphere}}, \gamma_{\text{matrix}}\}$, which was the preferred choice for the primal-dual hybrid gradient method (Schneider, 2020, Sec. 3). Solution fields on a central cross section are shown in Fig. 4.3.

The local flow fields v are shown in Fig. 4.3a. The Moulinec-Suquet discretization shows significant artifacts, which is characteristic for Fourier spectral discretizations. The rotated staggered grid discretization, on the other hand, features checkerboard artifacts, although at a lower degree. In contrast, the flow field corresponding to the CCMF-discretization is much smoother, similar to the explicit jump discretization in the context of thermal conductivity (Wiegmann and Zemitis, 2006; Dorn and Schneider, 2019). The differences in the local crack-normal field ξ for the CCMF and the rotated staggered grid discretization are negligible and differ from the Moulinec-Suquet discretization in the local maximum values close to the central inclusion, see Fig. 4.3b.

All discretization methods give rise to the same effective crack energy, i.e., $\gamma_{\text{eff}} = \gamma_{\text{matrix}}$, as the crack bypasses the inclusion in a plane. This is independent of the material contrast, as long as the crack resistance of the matrix exceeds the crack resistance of the single sphere (Schneider, 2020, Sec. 4.2.2).

As the Moulinec-Suquet discretization shows the strongest artifacts, we

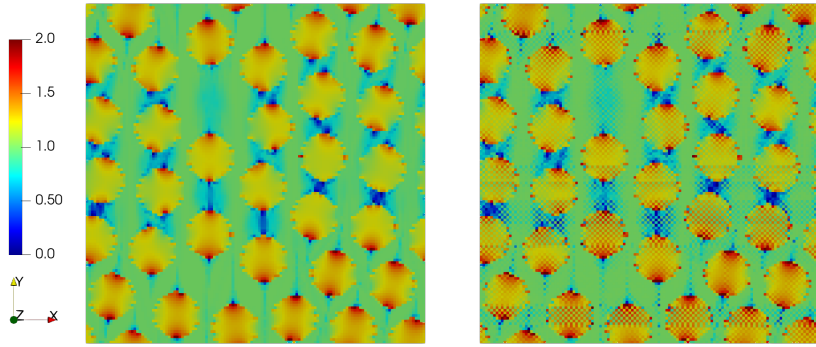
focus on the remaining two discretization methods for the remaining investigations.

4.4.3 A continuous-fiber reinforced composite

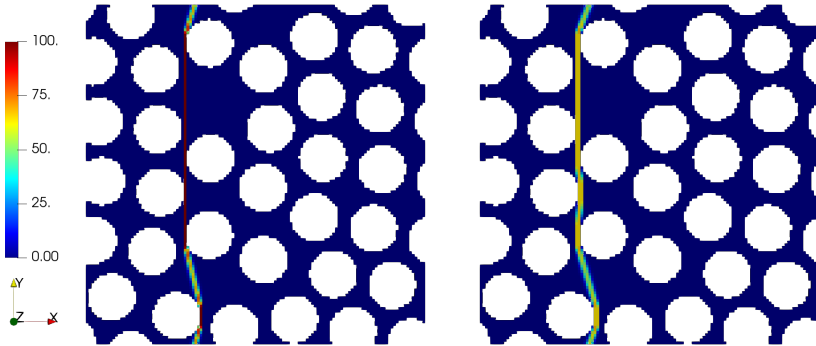
In this section, we wish to assess the performance of the ADMM solver introduced in Section 6.4. As a measure of verification, we choose a comparatively simple microstructure which enables us to employ a high-fidelity interior-point solver (Domahidi et al., 2013) for second-order cone programs (Ernesti et al., 2021). The latter produces high-precision solutions, but is limited in terms of problem size.

Accounting for this limitation, we consider a continuously fiber-reinforced composite with 50% filler content. The two-dimensional microstructure, containing 32 circular inclusions, was generated by the mechanical-contraction method (Williams and Philipse, 2003) and discretized on a 128^2 voxel grid. The inclusions were furnished by a crack resistance of $\gamma_{\text{fiber}} = 10 \gamma_{\text{matrix}}$. We investigate the effective crack energy in direction $\bar{\xi} = e_x$ and compare the CCMF discretization and the rotated staggered grid discretization, as well as different ADMM damping parameters δ , namely $\delta = 0.25$ and $\delta = 0.5$. Furthermore, we investigate different selection strategies for the ADMM penalty-factor, the lower bound $\rho = \min\{\gamma_{\text{fiber}}, \gamma_{\text{matrix}}\}$, preferred in Schneider (2020) and the Barzilai-Borwein scaling (Xu et al., 2017), as well as the scaling by Lorenz and Tran-Dinh (2019) and residual balancing (He et al., 2000). As announced earlier, we compare the effective crack energy to solutions obtained by the high-fidelity solver ECOS (Domahidi et al., 2013) applied to conic reformulations of the minimum-cut problem (4.23) for the CCMF scheme and the discretization on a rotated staggered grid. We assess the solver quality in terms of the relative error

$$\text{error} = \frac{|\gamma_{\text{eff}} - \gamma_{\text{eff}}^{\text{accurate}}|}{\gamma_{\text{eff}}^{\text{accurate}}} \quad (4.36)$$



(a) $\|v\|$, CCMF (left) and rotated staggered grid discretization (right)



(b) $\|\xi\|$, CCMF (left) and rotated staggered grid discretization (right)

Figure 4.4: Cross section through the solution fields v and ξ for a 128^2 microstructure, containing 32 circular inclusions for CCMF and rotated staggered grid discretization for $\tilde{\xi} = e_x$ and $\gamma_{\text{fiber}} = 10\gamma_{\text{matrix}}$. (Ernesti and Schneider, 2021)

in the effective crack energy, where $\gamma_{\text{eff}}^{\text{accurate}}$ is computed by the interior-point solver (Domahidi et al., 2013) with a residual of 10^{-10} .

Fig. 4.4a shows the local flow field for, both the CCMF discretization and the rotated staggered grid discretization. For the rotated staggered grid, the flow field exhibits significant checkerboard artifacts in the inclusions as well as the matrix. The CCMF solution, on the other hand, is devoid of such artifacts. The corresponding crack paths are shown in Fig. 4.4b. The cracks bypass the inclusions and look qualitatively similar for both discretizations. However, the rotated staggered grid discretization shows a wider crack path, whereas the CCMF crack path is sharper. This allows the CCMF crack path to avoid several inclusions in a straight line, whereas the rotated staggered grid crack path has to avoid them, resulting in a less straight crack path. This observation is also reflected in the resulting effective crack energy, i.e. $\gamma_{\text{eff}} = 1.021 \gamma_{\text{matrix}}$ for the rotated staggered grid and $\gamma_{\text{eff}} = 1.014 \gamma_{\text{matrix}}$ for the CCMF discretization.

Fig. 4.5a shows the residual of the solver vs the iteration count for the two strategies for selecting the penalty factor, two damping factors and the two discretizations under consideration. During the first 1000 iterations, all solvers behave similarly, with a slight advantage for the choice $\delta = 0.25$. After 2000 iterations, all solvers result in a residual below 10^{-3} . For the CCMF discretization, the ADMM solver with $\delta = 0.25$ and Barzilai-Borwein penalty-choice speeds up at 1600 iterations and reaches the required tolerance of 10^{-5} shortly thereafter. For $\delta = 0.5$ a similar acceleration occurs after slightly more than 8000 iterations. Selecting the lower bound for the penalty factor ρ does not reach the required tolerance within 10000 iterations.

For the rotated staggered grid discretization, the Barzilai-Borwein penalty-factor outperforms the constant choice, as well. For this discretization, the difference between the two damping factor choices is much smaller than for CCMF.

The investigations are supplemented by Fig. 4.5b, which records the associated relative error (4.36).

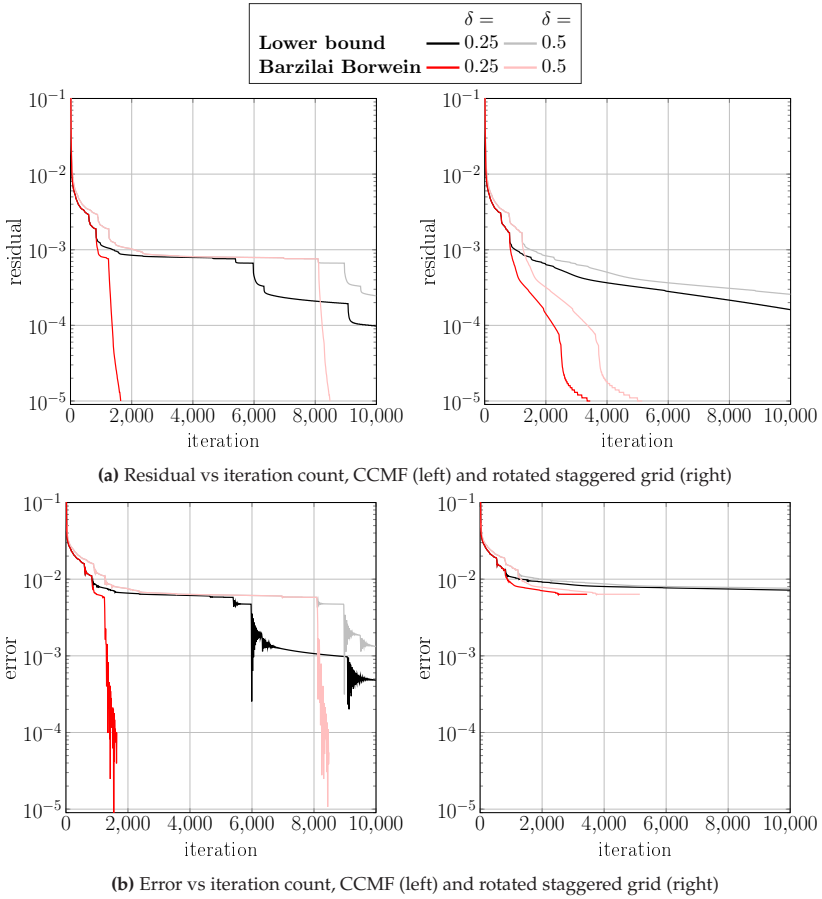


Figure 4.5: Residual and error measure (4.36) for CCMF and rotated staggered grid discretizations, comparing different solver parameters. (Ernesti and Schneider, 2021)

Indeed, the relation between the residual (5.33) and the error in the quantity of interest (4.36) is not directly apparent. Indeed, we know that convergence of effective properties is implied by convergence of the fields. However, the quantitative relation between these may only be determined by comparison to a ground truth. For the CCMF discretizations, the relative error (4.36) correlates with the residual rather well, reaching an accuracy below 10^{-4} at convergence. In contrast, the solution for the rotated staggered grid leads to an error of only 0.5%, i.e., hits a "stall".

In addition to the mentioned penalty-factor choices, we studied two further (less competitive) approaches, namely residual balancing (He et al., 2000), which is often recommended in the literature, as well as an the approach suggested by Lorenz and Tran-Dinh (2019), which proved to be promising in small-strain micromechanics (Schneider, 2021b). To increase readability, the residual and the error (4.36) were moved to Fig. B.1b of Appendix B.

With this validation at hand, we restrict to the CCMF discretization in combination with ADMM, damping factor $\delta = 0.25$ and the Barzilai-Borwein penalty-factor for the remainder of this chapter.

4.4.4 A fiber-reinforced composite

After the necessary verification steps, we turn our attention to problems with a higher degree of complexity. We consider a short-fiber reinforced composite with 18% filler content. The synthetic structure contains 376 fibers with an aspect ratio (length/diameter) of 20, and was generated by the sequential addition and migration algorithm (Schneider, 2017). The prescribed fiber-orientation tensor of second order (Kanatani, 1984; Advani and Tucker, 1987) was $\text{diag}(0.75, 0.19, 0.06)$, i.e., the fibers lie almost exclusively in the x - y -plane with a strong preference in x -direction. The fibers are discretized with eight voxels per diameter, resulting in a volume image with 256^3 voxels, see Fig. 4.6a. Since the computations

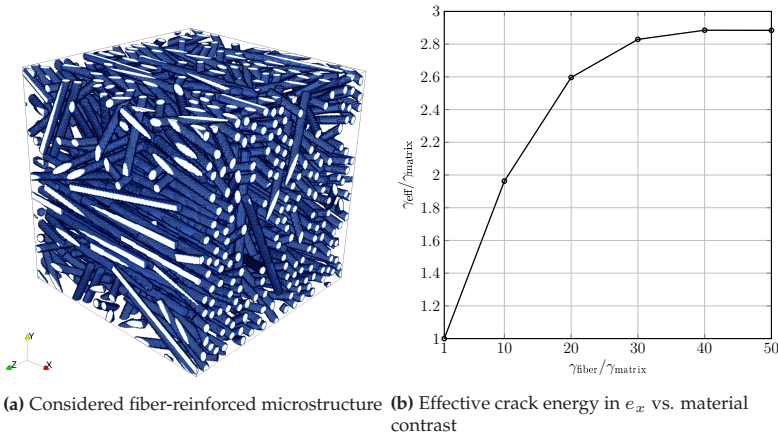


Figure 4.6: Microstructure and effective crack energy for the fiber-reinforced composite. (Ernesti and Schneider, 2021)

on such large structures are costly, we first investigate the influence of the tolerance entering the stopping criterion (5.33). For a configuration $\gamma_{\text{fiber}} = 50 \gamma_{\text{matrix}}$, we computed the effective crack energy in direction $\bar{\xi} = e_x$. After 1000, 2500, 5000, 7500, and 10000 iterations, we take a look at the corresponding residual and the computed effective crack energy, see Tab. 4.1. We observe that, after 1000 iterations we reach a residual of almost 10^{-3} with a relative deviation in effective crack energy about 2% compared to the prediction after 10000 iterations. After 2500 iterations, the relative error is below 1% with a residual at about $6 \cdot 10^{-4}$. For more than 5000 iterations, the effective crack energy does not change in the third significant digit, whereas the residual decreases only slowly.

To complement these numbers, we take a look at a cross section through the computed crack surface at different iteration counts, see Fig. 4.7. We observe an influence of the solver accuracy on the solution field ξ . Indeed, after 1000 iterations, several distinct crack paths are present in the vicinity of the solution. These different cracks, however, come with different "intensities", as well. This ambiguity is reduced after

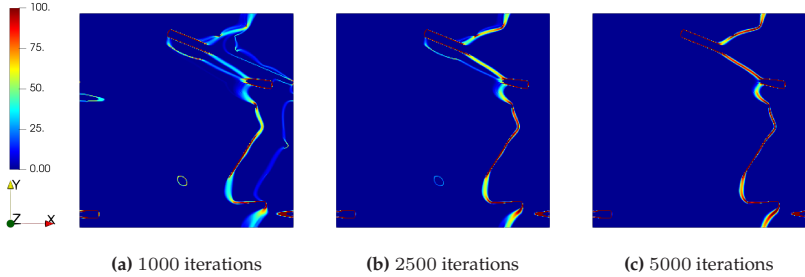


Figure 4.7: Cross section through crack surface for $\gamma_{\text{fiber}} = 50 \gamma_{\text{matrix}}$ at different ADMM iterations. (Ernesti and Schneider, 2021)

# iteration	residual	$\gamma_{\text{eff}}/\gamma_{\text{matrix}}$
1000	$1.7 \cdot 10^{-3}$	2.94
2500	$6.1 \cdot 10^{-4}$	2.89
5000	$1.9 \cdot 10^{-4}$	2.87
7500	$1.0 \cdot 10^{-4}$	2.87
10000	$5.5 \cdot 10^{-5}$	2.87

Table 4.1: Residual and computed effective crack energy with normal $\bar{\xi} = e_x$ depending on the number of ADMM iterations for a fiber-reinforced composite, see Fig. 4.6a, with material parameters $\gamma_{\text{fiber}} = 50 \gamma_{\text{matrix}}$

2500 iterations. Only after 5000 iterations, the solver finds a unique crack surface.

Please note that, in general, we do not expect the minimum-cut problem (4.3) to have a unique solution. Rather, for the problem at hand, a unique crack is formed and, at low levels of the residual, additional cracks appear, compare also Section 4.1.2 in Schneider (2020). These vanish, however, at high accuracy. To balance accuracy and ensuing computational costs, we fix the tolerance to $5 \cdot 10^{-4}$.

Next, we investigate the resulting crack surfaces and effective crack energies corresponding to different crack normals, see Fig. 4.8. In

$\gamma_{\text{fiber}}/\gamma_{\text{matrix}}$	# iterations
10	404
20	2701
30	2633
40	2626
50	2717

Table 4.2: Number of ADMM iterations for varying material contrast $\gamma_{\text{fiber}}/\gamma_{\text{matrix}}$

e_x -direction, the effective crack energy is highest. This is caused by a preferred fiber orientation in this direction, forcing the crack surface to bypass the numerous inclusions. In e_y -direction, see Fig. 4.8b, the crack surface looks roughly similar. However, the crack needs to avoid fewer fibers, resulting in a lower effective crack energy. In e_z -direction, the crack surface is almost straight, see Fig. 4.8b, resulting in the lowest effective crack energy.

Last but not least, we investigate the influence of the material contrast on the computed effective crack energy in $\bar{\xi} = e_x$ -direction, see Fig. 4.6b. This contrast is responsible for the allowed crack-inclusion interaction-mechanisms. Indeed, for high contrast, the inclusions can only be avoided, i.e., inclusion bypass is the only viable option. In general, the particles' anisotropy (encoded by the aspect ratio and the fiber orientation for the example at hand) and the filler content determine the threshold in contrast where only inclusion bypass is permitted. For the example at hand, Fig. 4.6b reveals that this threshold is roughly at a material contrast of 40. In Tab. 4.2, the influence of the material contrast on the ADMM iteration count is listed. For a contrast of 10, the solver requires 404 iterations to reach the desired tolerance. Above a contrast of 20, the iteration count stabilizes at approximately 2700. For lower contrast, it may be energetically more favorable to cross some of the inclusions. For decreasing material contrast, this inclusion-crossing mechanism occurs more frequently.

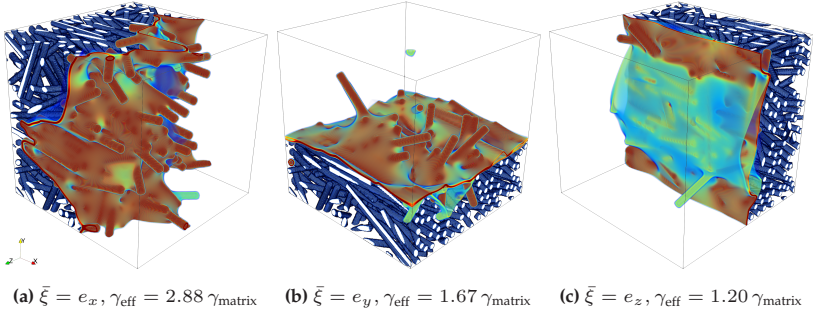


Figure 4.8: Crack surfaces for the Cartesian normals, material contrast $\gamma_{\text{fiber}}/\gamma_{\text{matrix}} = 50$ and the fiber-reinforced composite, see Fig. 4.6a. (Ernesti and Schneider, 2021)

4.4.5 Microstructures with a monodisperse pore distribution

As our next example, we consider microstructures with monodisperse, spherical pores and varying degrees of porosity. For a porosity between 5 and 50%, we generated microstructures with 200 spheres by the mechanical contraction method (Williams and Philipse, 2003), see Fig. 4.9. All structures were discretized on a 256^3 voxel grid. The solid material has crack resistance γ , and the spherical pores are furnished with a vanishing crack resistance, resulting in an infinite material contrast. Please note that in the previous study (Schneider, 2020, Sec. 4.1.1), the pores were furnished with a non-vanishing (yet small) crack resistance to ensure robust convergence of the utilized solution scheme. Such a restriction appears unnecessary for the improved solution method presented in this chapter.

The effective crack energy in direction $\bar{\xi} = e_x$ and the required ADMM iterations are listed in Tab. 4.3. Following physical intuition, the effective crack energy decreases for increasing porosity. If the crack were straight, its crack energy would be proportional to the in-plane porosity of the crack plane. For a curved crack, there is a competition between

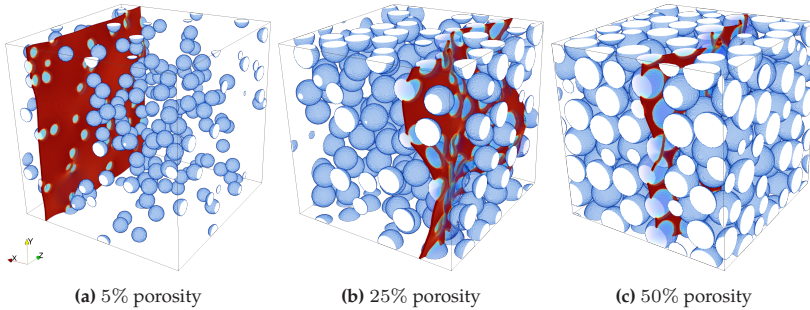


Figure 4.9: Crack surface through microstructures with varying porosity. (Ernesti and Schneider, 2021)

porosity in %	$\gamma_{\text{eff}}/\gamma$	iterations
5	0.871	4986
25	0.535	3300
40	0.412	3327
50	0.305	2358

Table 4.3: Influence of the porosity on the effective crack energy and solver performance for varying porosity

"maximizing the porosity" and remaining as straight as possible, see Fig. 4.9. The iteration count appears to be uncorrelated with the porosity. As a remark, we found the iteration count to be strongly dependent on the specific realization of the microstructure, in general. Thus, we expect that no such correlation may be inferred from a single sample, but would require a more elaborate study.

4.4.6 Sand-binder composite

In our final example, we examine the microstructure of a sand-binder aggregate which is characteristic for inorganically bound sand cores used in casting applications. The synthetic structure was generated by a

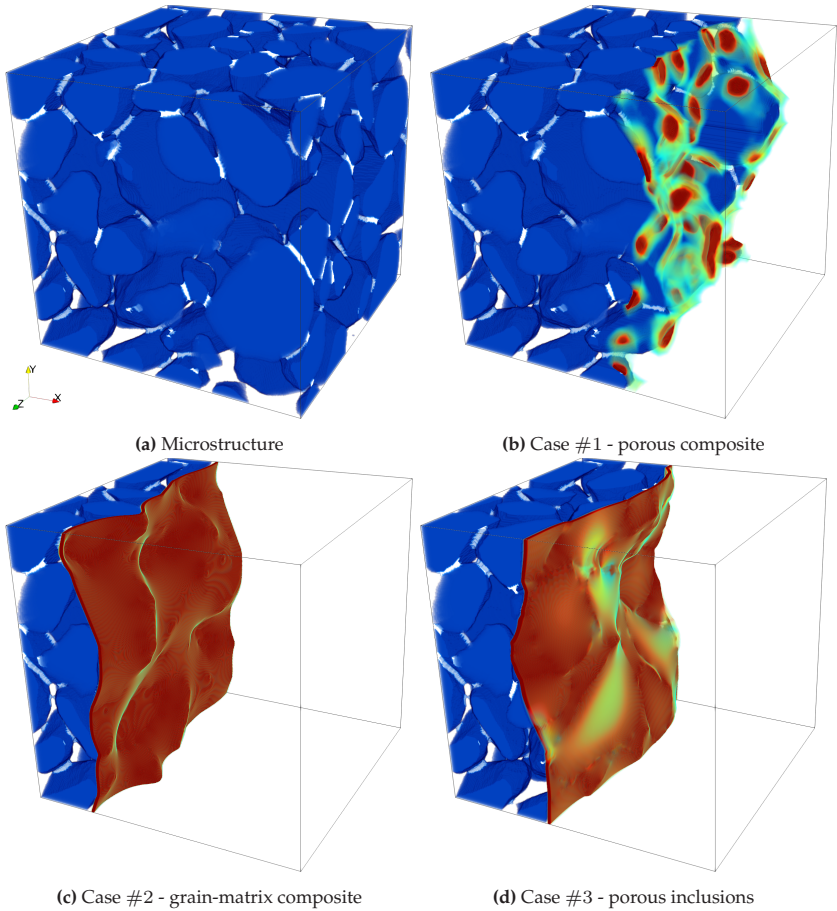


Figure 4.10: Bond sand-grain microstructure and Crack surfaces through the structure for three different combinations of crack resistances for matrix, inclusion and binder. (Ernesti and Schneider, 2021)

	γ_{matrix} in MPa $\cdot\mu\text{m}$	γ_{grain} in MPa $\cdot\mu\text{m}$	γ_{binder} in MPa $\cdot\mu\text{m}$
#1	0	1	1
#2	1	10	1
#3	10	1	10

Table 4.4: Material parameters for the three cases under consideration

	γ_{eff} in MPa $\cdot\mu\text{m}$	iterations
#1	0.074	3204
#2	1.133	1711
#3	3.246	3971

Table 4.5: Effective crack energies and iteration count for the three cases under consideration

mechanical-contraction type method (Schneider et al., 2018; Etemeyer et al., 2020), and is shown in Fig. 4.10a. The microstructure consists of three phases: The sand grains (58.6%), connected by a binder phase (1.3%), and a third phase (40.1%). In the physical applications, the latter phase represents the pore space. We wish to utilize the microstructure to get insights for a number of physical scenarios, and we will refer to the third phase more generally as the "matrix" for reasons that will become clear shortly.

The crack resistances associated to the phases are denoted by γ_{grain} , γ_{binder} and γ_{matrix} , respectively. To investigate the effective crack energy and possible crack surfaces through the microstructure, we consider three different parameter scenarios, where the single phases model different physical scenarios. The governing parameters for the three cases under consideration are listed in Tab. 4.4. The resulting effective crack energies, as well as the required iteration counts are listed in Tab. 4.5. In parameter case #1, the crack resistance of the grains and the binder are equal, and the matrix material corresponds to a pore space. The resulting

crack surface is shown in Fig. 4.10b. We notice that the crack is fully contained in the binder phase. The effective crack energy is reduced to 7.5% of the crack resistance which grain and binder share. The second parameter case models the structure as a matrix material with tougher sand-grain inclusions. The binder phase is treated as additional matrix material. Fig. 4.10c shows the crack surface avoiding the sand-grain shaped inclusions. The resulting effective crack energy of the composite is $1.133 \gamma_{\text{matrix}}$. The third case deals with the same contrast, i.e., the binder phase is once again treated as additional matrix. This time, however, the sand-grain shaped inclusions are weaker than the surrounding material. The effective crack energy is 32% of the matrix crack resistance. Fig. 4.10d shows the crack surface crossing several grains in order to avoid the matrix phase as much as possible.

4.5 Conclusions

In this chapter, we presented a powerful FFT-based solution method for computing the effective crack energy of industrial-scale composite microstructures. Based on a homogenization result for the Francfort-Marigo model of brittle fracture (Francfort and Marigo, 1998) in an anti-plane shear setting, see Braides et al. (1996), a cell formula for computing the effective crack energy was investigated. This cell formula may be interpreted as a minimum cut / maximum flow problem (Strang, 1983), which finds various applications, for instance in graph networks and image segmentation. Following Couprie et al. (2011), we considered the CCMF discretization on regular voxel data and integrated it into an FFT-based computational homogenization framework. In comparison to traditional spectral and finite-difference discretizations, we found the CCMF discretization to significantly reduce artifacts in the local fields. For solving the discretized equations, we investigated the alternating direction method of multipliers (ADMM) with various adaptive strate-

gies, and found a damping parameter $\delta = 0.25$ combined with the Barzilai-Borwein penalty-factor choice to be the most effective. We demonstrated the applicability of our approach to various large-scale problems, considering complex microstructures, as well as large or even infinite contrast in the local crack resistance. The presented framework was implemented into an existing homogenization code for thermal conductivity, and, although we ran some computations on a workstation, all presented computations could be done on a conventional desktop computer.

Chapter 5

Computing the effective crack energy of heterogeneous and anisotropic microstructures via anisotropic minimal surfaces¹

5.1 Introduction

Francfort and Marigo (1998) reformulated Griffith's theory of crack propagation (Griffith, 1921) as a variational problem, introducing the Francfort-Marigo model of fracture. For a fixed domain Ω and a fixed time discretization, they seek minimizers, i.e., the displacement field u and the crack surface S across which u may be discontinuous, of the energy functional

$$FM(u, S) = \frac{1}{2} \int_{\Omega \setminus S} \nabla^s u : \mathbb{C}(x) : \nabla^s u \, dx + \int_S \gamma(x) \, dA. \quad (5.1)$$

The energy consists of a volume-energy part accounting for elastic deformations, and a surface-energy part quantifying the crack-surface energy. Physical assumptions of their model include $S^t \subseteq S^{t+1}$ at all time

¹ This chapter is based on Ernesti and Schneider (2022). In order to include this paper into the structure of this work I shortened the introduction and made minor changes to the manuscript.

steps t , i.e., the crack surface may only grow. Notice that their formulation is based on global minimization for reasons of mathematical well-posedness, whereas Griffith seeks local critical points. The Francfort-Marigo model naturally includes heterogeneous material properties, as both crack resistance γ and the stiffness tensor \mathbb{C} may depend on the position. Furthermore, distinct material anisotropy may already be expressed in terms of an anisotropic stiffness tensor. Additionally, as noted by the authors themselves (Francfort and Marigo, 1998, eq. (17)) the surface energy may account for anisotropy by replacing the isotropic crack resistance in the surface energy by an anisotropic term $\gamma(x, n(x))$ depending on the unit normal n of the crack surface.

The prevailing tool for treating the Francfort-Marigo model computationally is the phase-field model of fracture. The method, introduced by Bourdin et al. (2000), is motivated by the Ambrosio-Tortorelli approximation (Ambrosio and Tortorelli, 1990) of the Mumford-Shah functional (Mumford and Shah, 1989), used in image segmentation. The phase-field model involves a length-scale parameter l and seeks minimizers u as well as d , namely the displacement field and the damage variable, of the functional

$$PF_l(u, d) = \frac{1}{2} \int_{\Omega} (1-d)^2 \nabla^s u : \mathbb{C}(x) : \nabla^s u + \frac{\gamma(x)}{2} \left[\frac{d^2}{l} + l \|\nabla d\|^2 \right] dx. \quad (5.2)$$

Chambolle (2004) showed that, for $l \rightarrow 0$, the phase-field model Γ -converges to the Francfort-Marigo model. Additionally, the phase-field model shows similarities to nonlocal damage models (Dimitrijevic and Hackl, 2008; Bažant, 1991) and may be treated as such as long as $l > 0$ is regarded as a material parameter (Kuhn, 2013).

The phase-field fracture model is rather popular in the scientific community, including a variety of contributions over the last decade, see Wu et al. (2020) for a recent overview. Of particular interest to

this chapter are contributions that account for material anisotropy. Investigations on modeling anisotropic fracture using an anisotropic stiffness but isotropic crack energy were carried out (Gmati et al., 2020; Shanthraj et al., 2017). An approach to incorporate tension-compression anisotropy into the context of an anisotropic stiffness was suggested by van Dijk et al. (2020). Clayton and Knap (2014) introduced a geometrically nonlinear phase-field model with an anisotropic crack resistance, which takes, in case of small deformation elasticity, the form

$$PF_l(u, d) = \int_{\Omega} \frac{1}{2} (1-d)^2 \nabla^s u : \mathbb{C}(x) : \nabla^s u + \frac{\gamma(x)}{2} \left[\frac{d^2}{l} + l \nabla d \cdot M^p \nabla d \right] dx \quad (5.3)$$

with $M^p(x) = p(x) \otimes p(x) + \beta(x)(\text{Id} - p(x) \otimes p(x))$ and a field of unit vectors p . They applied their model at small deformations to simulating cleavage in polycrystalline ceramics (Clayton and Knap, 2015). The positive cleavage parameter β is introduced to penalize crack propagation within the plane perpendicular to the unit vector p . Further extensions to incorporate crystal plasticity and ductile fracture were reported (Na and Sun, 2018; Bryant and Sun, 2018). The tensor M^p permits to model either one weak plane, or one tough direction. Introducing a general symmetric and positive definite tensor M , up to three different crack resistances, i.e, the eigenvalues of M , in the three eigendirections may be prescribed. More general approaches were proposed using a multi phase-field setting, see Nguyen et al. (2017), or a higher order phase-field method, using fourth order tensors (Teichtmeister et al., 2017; Kakouris and Triantafyllou, 2019; Ma and Sun, 2020; Li et al., 2015), to study polycrystalline materials. Pillai et al. (2020) proposed an anisotropic cohesive phase-field model to simulate the behavior of anisotropic fiber structures. Incorporating weak interfaces via cohesive elements was proposed by Rezaei et al. (2021).

To account for the influence of the microstructure of a material to its

macroscopic behavior, multi-scale methods may be used, see Matouš et al. (2017) for an overview. For hardening material behavior, those multi-scale approaches are well understood. Softening materials, in contrast, where distinct strain localization may occur, are more challenging (Gitman et al., 2007).

Braides et al. (1996) established a periodic homogenization result for the Mumford-Shah functional (Mumford and Shah, 1989) which is closely related to the Francfort-Marigo model of brittle fracture (Francfort and Marigo, 1998). Consider the Francfort-Marigo model with periodic material properties \mathbb{C} and γ with a fixed discretization in time, i.e., the quasi-static case. Furthermore, we neglect the irreversibility constraint and consider the loading case anti-plane shear. Subjected to these assumptions, the Francfort-Marigo model converges, as shown by Braides et al. (1996), to the effective functional

$$FM^{\text{eff}}(u, S) = \frac{1}{2} \int_{\Omega \setminus S} \nabla^s u : \mathbb{C}^{\text{eff}} : \nabla^s u \, dx + \int_S \gamma^{\text{eff}}(n) \, dA \quad (5.4)$$

with effective, possibly anisotropic stiffness tensor \mathbb{C}^{eff} and *effective crack energy* $\gamma^{\text{eff}}(n)$. Furthermore, they showed that the two effective quantities decouple, i.e., the local stiffness tensor has no influence on the effective crack energy and the local crack resistance does not influence the effective stiffness. A key ingredient for the homogenization result of Braides and coworkers was a formulation on a *single unknown*, namely the displacement field which is permitted to be discontinuous across specific crack surfaces. In this way, the headache concerning the distinction of a displacement field and the crack can be avoided. Indeed, the (possibly jumping) displacement field can be decomposed additively into a macroscopic and a microscopic part.

The work of Braides et al. (1996) was further extended to stochastic homogenization by Cagnetti et al. (2019), ensuring representative volume elements to exist for the Francfort-Marigo fracture model under

anti-plane shear. Recently, the restriction to anti-plane shear was lifted by Friedrich et al. (2022), so the homogenization result holds in general. To compute the effective quantities, Braides et al. (1996) provide specific formulas. Computing the effective stiffness reduces to classical linear elastic homogenization (Milton, 2002), whereas the effective crack energy $\gamma^{\text{eff}}(n)$ associated to a crack with normal n may be computed as a γ -weighted minimal surface cutting the microstructure. Note that the homogenization results are based on the notion of Γ -convergence. Thus, they only concern global minimizers of both the original and the effective functional.

Schneider (2020) proposed a method for computing the effective crack energy for heterogeneous, locally isotropic microstructures using a reformulation of the cell formula of Braides et al. (1996) into a convex optimization problem. The transformation of the cell formula relies on Strang's minimum cut/maximum flow duality (Strang, 1983). The established optimization problem was solved using FFT based algorithms. Recently, Ernesti and Schneider (2021) proposed a discretization on a combinatorially consistent grid, which improves the solution quality, introducing an associated adaptive ADMM solver, see also chapter 4.

Contributions

This chapter extends the approach presented in chapter 4 to account for a locally anisotropic crack resistance, enabling to treat matrix-inclusion composites with anisotropic phases or polycrystalline materials. In section 5.2.1, we introduce the cell formula for the effective anisotropic crack energy and anisotropic phases. We describe the anisotropy in terms of a tensor, similar to approaches applied in phase-field fracture (Clayton and Knap, 2014). We transform the anisotropic minimum cut problem into an anisotropic maximum flow problem in section 5.2.2, which gives rise to a convex optimization problem.

Powerful solution methods for maximum flow problems arose for

maximum-flow problems on graphs (Ford and Fulkerson, 1956). Due to metrication artifacts, these are not directly applicable to the continuous maximum flow problem at hand (Kolmogorov and Zabini, 2004). This may be overcome by a combinatorial continuous maximum flow (CCMF) discretization (Couprie et al., 2011), recently applied to computing the effective crack energy of solids (Ernesti and Schneider, 2021), see also chapter 4. We propose a way to account for anisotropic crack resistances within the CCMF discretization in section 5.3.1. As the anisotropy of the crack resistance is described in terms of a (symmetric positive definite) second-order tensor, the maximum-flow formulation involves the projection onto an ellipsoid. We express the governing projection operator as the solution of a constrained optimization problem in section 5.3.3. Finally, we apply our anisotropic minimum cut/maximum flow approach to brittle materials with a distinct anisotropy. In section 5.4.2 we investigate polycrystalline brittle materials, such as ceramics with distinct cleavage in each grain. Last but not least, we investigate fracture of carbon fiber reinforced composites, where each fiber itself shows strong anisotropy of transversely isotropic kind.

5.2 Minimum cut/maximum flow with anisotropic crack resistance

5.2.1 Cell formula for an anisotropic minimum cut

Consider a unit cell $Y = [0, L_1] \times [0, L_2] \times [0, L_3]$ and a given field of heterogeneous and direction-dependent crack resistances

$$\gamma : Y \times \mathbb{R}^3 \rightarrow \mathbb{R} \tag{5.5}$$

We assume that, for any microscopic point $x \in Y$, the association

$$\mathbb{R}^3 \ni \xi \mapsto \gamma(x, \xi)$$

defines a *norm* on the vector space \mathbb{R}^3 , i.e., it is one-homogeneous, satisfies the triangle inequality and is non-degenerate. Moreover, we assume that there are positive constants γ_-, γ_+ , s.t. the inequalities

$$\gamma_- \leq \gamma(x, \xi) \leq \gamma_+ \quad \text{hold for all } x \in Y \quad \text{and} \quad \xi \in \mathbb{R}^3 \text{ with } \|\xi\| = 1. \quad (5.6)$$

Under these assumptions, we define the effective crack energy as a function on the unit sphere S^2 via

$$\gamma_{\text{eff}}(\bar{\xi}) = \inf_{\phi} \frac{1}{|Y|} \int_Y \gamma(x, \bar{\xi} + \nabla\phi(x)) \, dx, \quad (5.7)$$

where the infimum is evaluated over all smooth periodic fields ϕ . Upon one-homogeneous extension, the effective crack energy γ_{eff} gives rise to a norm on \mathbb{R}^3 , as well.

In this article, we specialize the form of the microscopic crack resistances considered to those which describe an anisotropic Euclidean norm. More precisely, for a field $\mathbf{G} : Y \rightarrow \text{Sym}(3)$ of symmetric, positive definite *crack resistance tensors*, we consider the local crack resistance field

$$\gamma(x, \xi) = \|\mathbf{G}(x)[\xi]\|.$$

Then, equation (5.7) becomes

$$\gamma_{\text{eff}}(\bar{\xi}) = \inf_{\phi} \frac{1}{|Y|} \int_Y \|\mathbf{G}(x) [\bar{\xi} + \nabla\phi(x)]\| \, dx. \quad (5.8)$$

The isotropic case (Schneider, 2020; Ernesti and Schneider, 2021), also described in chapter 4, where we consider the isotropic crack resistance field $\gamma : Y \rightarrow \mathbb{R}$, is recovered via $\mathbf{G}(x) = \gamma(x) \text{Id}$.

5.2.2 Anisotropic maximum flow formulation

We define the energy functional

$$f(\xi) = \frac{1}{|Y|} \int_Y \|\mathbf{G} \xi\| dx \quad (5.9)$$

and, for fixed $\bar{\xi} \in \mathbb{R}^3$, the set of kinematic constraints

$$\mathcal{K}_{\bar{\xi}} = \{\xi : Y \rightarrow \mathbb{R}^3 \text{ periodic} \mid \xi = \bar{\xi} + \nabla \phi \\ \text{for some periodic } \phi : Y \rightarrow \mathbb{R}\}.$$

With the energy functional and the kinematic constraints at hand, we call

$$f(\xi) \rightarrow \min_{\xi \in \mathcal{K}_{\bar{\xi}}}, \quad (5.10)$$

the *anisotropic minimum cut* problem. For fixed normal $\bar{\xi}$, the minimum effective crack energy (5.8) computes as the minimum value of this minimization problem.

Treating this problem numerically is challenging, since the energy functional is homogeneous of degree one and thus non-differentiable. Extending the isotropic case (Schneider, 2020; Ernesti and Schneider, 2021), see also chapter 4, we introduce a dual formulation, i.e., a corresponding *anisotropic maximum flow* problem (Strang, 1983). The formal dual problem to the minimization problem (5.10) is given by

$$f^*(v) - \frac{1}{|Y|} \int_Y \bar{\xi} \cdot v dx \rightarrow \min_{\text{div } v=0}, \quad (5.11)$$

where f^* denotes the Legendre-Fenchel dual of f , given by

$$f^*(v) = \sup_{\xi} \frac{1}{|Y|} \int_Y \xi \cdot v dx - f(\xi) \equiv \sup_{\xi} \frac{1}{|Y|} \int_Y \xi \cdot v - \|\mathbf{G} \xi\| dx \quad (5.12)$$

and the minimum (5.11) is evaluated over all periodic solenoidal fields v . Since the tensor \mathbf{G} is symmetric and positive definite, and thus invertible, we transform the Legendre-Fenchel dual (5.12)

$$\begin{aligned} f^*(v) &= \sup_{\xi} \frac{1}{|Y|} \int_Y \xi \cdot v - \|\mathbf{G} \xi\| dx \\ &= \sup_{\tilde{\xi}=\mathbf{G} \xi} \frac{1}{|Y|} \int_Y \tilde{\xi} \cdot \mathbf{G}^{-1} v - \|\tilde{\xi}\| dx \\ &= \begin{cases} 0 & \|\mathbf{G}^{-1} v\| \leq 1, \\ +\infty & \text{otherwise.} \end{cases} \end{aligned}$$

Thus, the Legendre-Fenchel dual f^* equals the indicator function

$$\iota_{\mathcal{C}} = \begin{cases} 0 & v \in \mathcal{C}, \\ +\infty & \text{otherwise,} \end{cases}$$

of the closed set

$$\mathcal{C} = \{v : Y \rightarrow \mathbb{R}^3, \text{ periodic} \mid \|\mathbf{G}(x)^{-1}v(x)\| \leq 1 \text{ for almost all } x \in Y\}. \quad (5.13)$$

Since \mathbf{G} is symmetric and positive definite, the set \mathcal{C} is a convex domain. More precisely, the constraint in the definition of the set \mathcal{C} describes an ellipsoid centered at the origin, see Fig. 5.1. Combining (5.12) with this expression for \mathcal{C} , we arrive at the anisotropic maximum flow problem

$$\frac{1}{|Y|} \int_Y \bar{\xi} \cdot v dx \longrightarrow \max_{\text{div} v=0, \|\mathbf{G}^{-1} v\| \leq 1}.$$

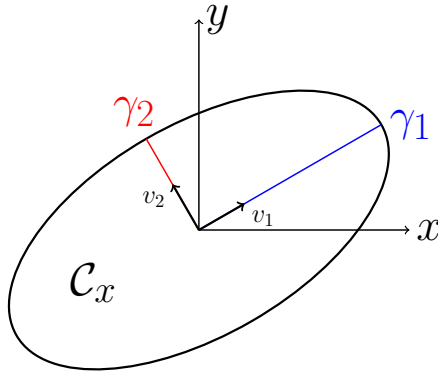


Figure 5.1: Schematic sketch of the ellipsoidal domain \mathcal{C}_x , i.e., all vectors satisfying $\|\mathbf{G}(x)^{-1}v(x)\| \leq 1$, with eigensystem $\{v_i\}$ and semi-axis γ_i . (Ernesti and Schneider, 2022)

5.3 Numerical treatment

Ernesti and Schneider (2021) proposed to solve the maximum flow problem in the combinatorial continuous maximum flow (CCMF) discretization (Couprie et al., 2011) by FFT-based methods (Schneider, 2021a). The formulation is based on doubling the degrees of freedom. We present an extension of this strategy to account for an anisotropic crack resistance expressed via a heterogeneous field of crack resistance tensors $\mathbf{G} : Y \rightarrow \text{Sym}(3)$. We refer to Ernesti and Schneider (2021), as well as chapter 4, as a general reference throughout this section.

5.3.1 The CCMF discretization for anisotropic maximum flow

We discretize the unit cell $Y = [0, L_1] \times [0, L_2] \times [0, L_3]$ on a regular cubic voxel grid Y_N with N_i , ($i = 1, 2, 3$) voxels in each direction under the assumption that each voxel is cubic with edge length $h = L_i/N_i$, ($i=1,2,3$).

We evaluate the crack resistance tensor at the voxel center, i.e.,

$$\mathbf{G}_{[i,j,k]} = \mathbf{G} \left(\left(i + \frac{1}{2} \right) h, \left(j + \frac{1}{2} \right) h, \left(k + \frac{1}{2} \right) h \right)$$

and the flow field $v : Y \rightarrow \mathbb{R}^3$ on the faces of each voxel

$$\begin{aligned} v_x[i,j,k] &= v_x \left(ih, \left(j + \frac{1}{2} \right) h, \left(k + \frac{1}{2} \right) h \right), \\ v_y[i,j,k] &= v_y \left(\left(i + \frac{1}{2} \right) h, jh, \left(k + \frac{1}{2} \right) h \right), \\ v_z[i,j,k] &= v_z \left(\left(i + \frac{1}{2} \right) h, \left(j + \frac{1}{2} \right) h, kh \right). \end{aligned}$$

This placement of the flow field enables to encode the conservation of mass via the discrete backwards divergence operator div^-

$$(\text{div}^- v)_{[i,j,k]} = v_x[i,j,k] - v_x[i-1,j,k] + v_y[i,j,k] - v_y[i,j-1,k] + v_z[i,j,k] - v_z[i,j,k-1].$$

To enforce the constraint $\|\mathbf{G}^{-1} v\| \leq 1$ in the context of the CCMF discretization, we introduce the nonlocal shift operator S

$$S(v)_{[i,j,k]} \equiv \begin{bmatrix} v_x[i-1,j,k] \\ v_y[i,j-1,k] \\ v_z[i,j,k-1] \end{bmatrix}. \quad (5.14)$$

The constraint is then enforced via the inequality

$$\|\mathbf{G}_{[i,j,k]}^{-1} v_{[i,j,k]}\|^2 + \|\mathbf{G}_{[i,j,k]}^{-1} S(v)_{[i,j,k]}\|^2 \leq 2. \quad (5.15)$$

To integrate the CCMF discretization of the anisotropic maximum flow problem into an FFT-based homogenization solver for heat conductivity, we introduce the extension operator A , given by

$$A(v) = \frac{1}{\sqrt{2}} \begin{bmatrix} v \\ S(v) \end{bmatrix}. \quad (5.16)$$

With this notation at hand, accompanied by the inner product

$$\langle v, w \rangle = \frac{1}{N_1 N_2 N_3} \sum_{i,j,k} v_x[i,j,k] w_x[i,j,k] + v_y[i,j,k] w_y[i,j,k] + v_w[i,j,k], v_z[i,j,k]$$

we may rewrite the discrete maximum flow problem as

$$\langle \bar{\xi}, v \rangle \longrightarrow \max_{\substack{\text{div}^- v=0, \\ \|\tilde{\mathbf{G}}^{-1} A(v)\| \leq 1}} \quad \text{with} \quad \tilde{\mathbf{G}} = \begin{bmatrix} \mathbf{G} & 0 \\ 0 & \mathbf{G} \end{bmatrix}. \quad (5.17)$$

For the CCMF discretization, the set \mathcal{C} from equation (5.13) reads

$$\mathcal{C}_{\mathbf{G}} = \left\{ w : Y_N \rightarrow \mathbb{R}^6, \quad \left\| \left\| \tilde{\mathbf{G}}[i,j,k]^{-1} w[i,j,k] \right\| \right\| \leq 1 \text{ for all } i, j, k \right\}. \quad (5.18)$$

The derivation of the associated discrete primal problem follows the same steps as the isotropic case, described in section 4.3.1. The discrete minimum cut problem with a tensorial crack resistance is given by

$$\frac{1}{N_1 N_2 N_3} \sum_{i,j,k} \left\| \left\| \tilde{\mathbf{G}}[i,j,k] \xi[i,j,k] \right\| \right\| \longrightarrow \min_{\xi \in \mathcal{K}_{\bar{\xi}}} \quad (5.19)$$

with set of discretely compatible fields

$$\begin{aligned} \mathcal{K}_{\bar{\xi}} = \{ \xi : Y_N \rightarrow \mathbb{R}^6 \mid & \text{there is some } \phi : Y_N \rightarrow \mathbb{R}, \\ & \text{s.t. } A^* \xi = \bar{\xi} + \nabla^+ \phi \}. \end{aligned} \quad (5.20)$$

The operator A^* denotes the left inverse of A , i.e., $A^* A = \text{Id}$ holds, and ∇^+ refers to the discrete forward gradient operator.

5.3.2 The alternating direction method of multipliers

To solve equation (5.19) with the alternating direction method of multipliers (ADMM), we rewrite the discrete minimum cut problem equivalently

as

$$f(\xi) + g(\xi) \longrightarrow \min_{\xi} \quad (5.21)$$

with the two convex functions

$$f(\xi) = \iota_{\mathcal{K}_{\bar{\xi}}}(\xi) \quad \text{and} \quad g(\xi) = \frac{1}{N_1 N_2 N_3} \sum_{i,j,k} \|\mathbf{G}^{[i,j,k]} \xi^{[i,j,k]}\|,$$

where $\iota_{\mathcal{K}_{\bar{\xi}}}$ is the indicator function of the set $\mathcal{K}_{\bar{\xi}}$ described in (5.20). The operator-splitting approach starts by rewriting the problem as a constrained optimization problem

$$f(\xi) + g(e) \longrightarrow \min_{\xi=e}. \quad (5.22)$$

The alternating direction method of multipliers (ADMM) (Glowinski and Marrocco, 1975; Gabay and Mercier, 1976) was introduced into the context of FFT-based methods by Michel et al. (2000; 2001), see also the application to non-smooth optimization by Willot (2020). Applied to our problem, we investigate the augmented Lagrangian function

$$L_{\rho}(\xi, e, v) = f(\xi) + g(e) + \langle v, \xi - e \rangle + \frac{\rho}{2} \|\xi - e\|^2, \quad (5.23)$$

involving a penalty factor $\rho > 0$ and the Lagrange multiplier, i.e., our flow field, $v : Y_N \rightarrow \mathbb{R}^6$. The damped ADMM recursion (4.34) with damping factor δ is given by

$$\begin{aligned} \xi^{k+1/2} &= \operatorname{argmin}_{\xi} L_{\rho}(\xi, e^k, v^k), \\ \xi^{k+1} &= 2(1 - \delta)\xi^{k+1/2} - (1 - 2\delta)e^k, \\ e^{k+1} &= \operatorname{argmin}_e L_{\rho}(\xi^{k+1}, e, v^k), \\ v^{k+1} &= v^k + \rho(\xi^{k+1} - e^{k+1}). \end{aligned} \quad (5.24)$$

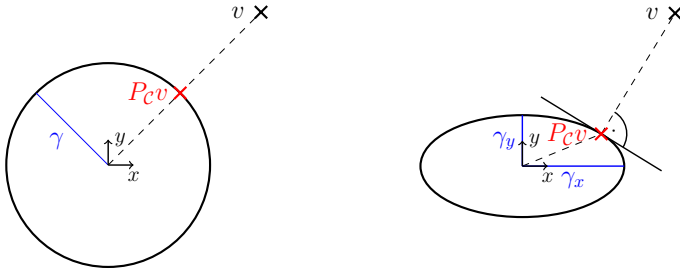


Figure 5.2: Schematic of the projection of the vector v onto the admissible set in the case of isotropic (left) and anisotropic (right) crack resistance. (Ernesti and Schneider, 2022)

More explicitly, the ADMM algorithm for anisotropic minimum cut/maximum flow with adaptive penalty factor ρ^k is given by

$$\begin{aligned}
 \xi^{k+1/2} &= \mathcal{P}_{\mathcal{K}_{\bar{\xi}}} \left(e^k - \frac{1}{\rho^k} v^k \right), \\
 \xi^{k+1} &= 2(1 - \delta)\xi^{k+1/2} - (1 - 2\delta)e^k, \\
 e^{k+1} &= [v^k + \rho^k \xi^{k+1} - \mathcal{P}_{\mathcal{C}_{\mathbf{G}}}(v^k + \rho^k \xi^{k+1})] / \rho^k, \\
 v^{k+1} &= v^k + \rho^k (\xi^{k+1} - e^{k+1}),
 \end{aligned} \tag{5.25}$$

where $\mathcal{P}_{\mathcal{K}_{\bar{\xi}}}$ and $\mathcal{P}_{\mathcal{C}_{\mathbf{G}}}$ denote the orthogonal projectors onto the sets $\mathcal{K}_{\bar{\xi}}$ and $\mathcal{C}_{\mathbf{G}}$, respectively.

5.3.3 The anisotropic projector problem

Within the ADMM iterations (5.25), evaluating two projection operators is required. The projection onto the compatible fields expressed via the projector $\mathcal{P}_{\mathcal{K}_{\bar{\xi}}}$ may be efficiently performed with the help of the FFT (4.32). Additionally, the orthogonal projection onto the set $\mathcal{C}_{\mathbf{G}}$ is required, expressed via the projection operator $\mathcal{P}_{\mathcal{C}_{\mathbf{G}}}$ and illustrated in Fig. 5.2. In the isotropic case, the set of constraints \mathcal{C} comprises a sphere

per voxel. Thus, the projection onto \mathcal{C} involves orthogonal projections onto a spheres with radii $\gamma(x)$ and is straightforward. In the anisotropic case, however, the set $\mathcal{C}_{\mathbf{G}}$ comprises an ellipsoid for each voxel, with the eigenvalues γ_i of \mathbf{G} as semi-axes. Following Kiseliiov (1994), we write this projection as an optimization problem.

Consider a vector $v \in \mathbb{R}^n$ and a symmetric, positive definite tensor \mathbf{Q} . We seek the projection $w \in \mathbb{R}^n$, such that

$$\|w - v\|^2 \rightarrow \min_{w^T \mathbf{Q} w \leq 1}. \quad (5.26)$$

Introducing the Lagrange parameter λ , the governing KKT-conditions, see for instance (Nocedal and Wright, 1999, Thm. 12.1), read

$$2(w - v) + 2\lambda \mathbf{Q} w = 0, \quad (5.27)$$

$$w^T \mathbf{Q} w - 1 \leq 0, \quad (5.28)$$

$$\lambda \geq 0 \quad \lambda(w^T \mathbf{Q} w - 1) = 0. \quad (5.29)$$

From conditions (5.27) we find

$$w = (\text{Id} + \lambda \mathbf{Q})^{-1} v. \quad (5.30)$$

If the vector v satisfies $v^T \mathbf{Q} v \leq 1$, the problem (5.26) is trivially solved for $w = v$ (and $\lambda = 0$). We therefore focus on the case $v^T \mathbf{Q} v > 0$. Since the tensor \mathbf{Q} is symmetric and positive definite, the inequality (5.28) describes a convex domain. Thus, the projection w lies on the boundary of the admissible set. Thus, the inequality (5.28) is satisfied as an equality. We insert the representation (5.30) into the conditions $w^T \mathbf{Q} w - 1 = 0$ and solve the resulting equation

$$v^T (\text{Id} + \lambda \mathbf{Q})^{-1} \mathbf{Q} (\text{Id} + \lambda \mathbf{Q})^{-1} v - 1 = 0 \quad (5.31)$$

for the scalar λ , using Newton's method and initial value $\lambda^0 = 0$, following Kisieliov (1994). In the mentioned reference, global convergence of this algorithm is proved.

For the application at hand, where $n = 6$, we set

$$\mathbf{Q} = \tilde{\mathbf{G}}(x)^{-2} \quad (5.32)$$

for each $x \in Y$. Therefore, the projection operator summarizes as

$$\mathcal{P}_{\mathcal{C}_{\mathbf{G}}} v(x) = \begin{cases} v(x), & \left\| \tilde{\mathbf{G}}(x)^{-1} v(x) \right\| \leq 1, \\ (\text{Id} + \lambda \mathbf{Q})^{-1} v(x), & \text{otherwise,} \end{cases}$$

with λ solving (5.31).

5.4 Numerical examples

5.4.1 Setup

The presented computational approach was integrated into an existing FFT-based code for computing effective crack energies on microstructures (Ernesti and Schneider, 2021), which is embedded into an FFT-based computational homogenization code for thermal conductivity (Dorn and Schneider, 2019). The software is written in Python with Cython extensions (and OpenMP). All computations were performed using the ADMM solver presented in chapter 4 with either the Barzilai-Borwein adaptivity or the averaging adaptivity, and a damping factor of 0.25. If not mentioned otherwise, the governing equations were solved for a prescribed tolerance $\text{tol} = 10^{-4}$ and the convergence criterion (Schneider, 2021b)

$$\left\| e^k - \xi^{k+\frac{1}{2}} \right\|_{L^2} \leq \text{tol} \|\langle v \rangle\|. \quad (5.33)$$

The computational experiments in this section were run on a desktop computer with 32GB RAM and six 3.7GHz cores and on a workstation with 512 GB RAM and two Intel Xeon(R) Gold 6146 processors (12×3.20 GHz), respectively.

5.4.2 A polycrystalline microstructure

As our first example, we consider a polycrystalline microstructure generated synthetically based on Laguerre tessellations and the algorithm described in Kuhn et al. (2020). Following a similar approach as Nguyen et al. (2017) within the context of phase-field fracture, we distinguish between 2D and 3D structures. In a 2D microstructure with distinct anisotropy, we identify one weak and one tough direction, whereas in 3D, we identify one weak and two tough directions, resulting in one weak plane. Since elastic deformation and thus elastic material constants do not play a role in our model, we normalize the crack resistance tensor to a value γ and consider a cleavage anisotropy factor $\beta \in [1, 100]$ as proposed in Clayton and Knap (2014; 2015) for polycrystalline silicon carbide. The crack resistance tensor for 2D and 3D structures is given by

$$\begin{aligned} \mathbf{G}^{2D} &= R_{\text{grain}}^T \begin{bmatrix} \gamma & 0 \\ 0 & \beta\gamma \end{bmatrix} R_{\text{grain}} \quad \text{and} \\ \mathbf{G}^{3D} &= R_{\text{grain}}^T \begin{bmatrix} \gamma & 0 & 0 \\ 0 & \beta\gamma & 0 \\ 0 & 0 & \beta\gamma \end{bmatrix} R_{\text{grain}}, \end{aligned} \tag{5.34}$$

respectively, where R_{grain} is a rotation matrix encoding the orientation of each grain.

Two-dimensional structures

We start with a 2D Laguerre tessellation and planar grain orientations. In our first study, we vary the number of grains as well as the cleavage anisotropy factor β . For each structure, we vary the loading angle

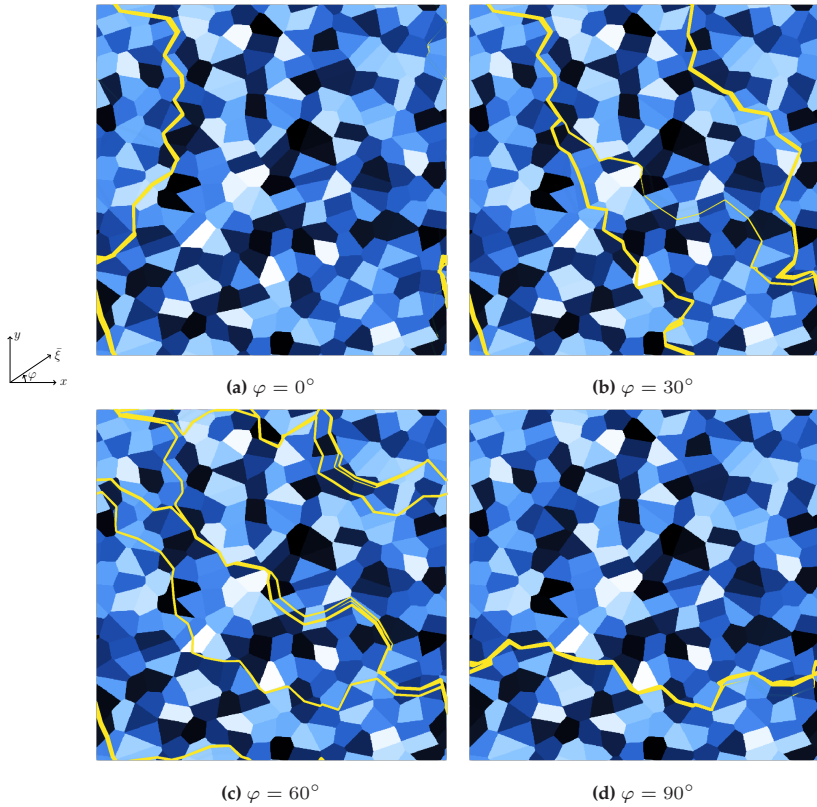


Figure 5.3: Crack path through a microstructure with 256 grains and a cleavage anisotropy factor $\beta = 10$ for prescribed normal $\xi = (\cos(\varphi), \sin(\varphi))$. (Ernesti and Schneider, 2022)

in seven equidistant steps from 0 to 90 degrees. For each loading angle, we additionally consider the case where each grain is rotated by 90 degrees. This results in 14 computations per structure. We used the Barzilai-Borwein adaptivity within the ADMM solver for most computations. For some cases, the averaging adaptivity converged faster and we switched to the latter solver choice in those cases. We extracted the mean value as well as the standard deviation of the 14 computations per structure. The crack path for various loading angles is shown in Fig. 5.3. We see that the crack changes its direction for each grain in order to minimize its surface energy. To close the crack path for a non-axis aligned normal, the crack has to pass the cell several times. Furthermore, we observe local similarities in the crack path for different loading angles.

Fig. 5.4a shows the influence of the number of grains on the effective crack energy. For a low number of grains, we observe a rather large standard deviation and no clear trend in the mean value. From 16^2 to 32^2 grains, the standard deviation decreases significantly. This trend continues for 64^2 grains, where the standard deviation decreases even further while the mean value remains within the same range, indicating representativity. We thus find a structure of 32^2 grains to be sufficiently large.

Secondly, we investigate the influence of the anisotropy factor on the effective crack energy for the structure containing 1024 grains, see Fig. 5.4b. Note that the case $\beta = 1$ gives rise to a homogeneous ξ -field, since no local differences arise in the crack resistance. In particular, the effective crack energy becomes $\gamma_{\text{eff}} \equiv \gamma$. The effective crack energy increases with an increasing anisotropy factor until a certain threshold is reached at $\beta = 50$, beyond this internal contrast, no significant increase is visible. At this threshold, the crack favors the weakest direction in each grain. This is also reflected in Fig. 5.5. Clear differences in the crack path may be observed between $\beta = 5$ and $\beta = 10$, see Fig. 5.5a and Fig. 5.5b, respectively. For increasing anisotropy, the differences become more

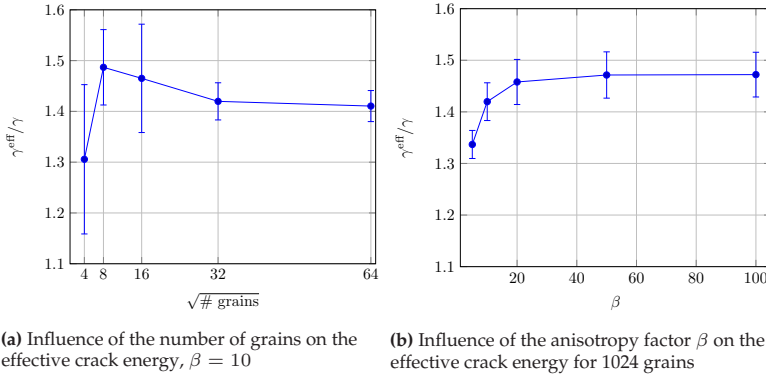


Figure 5.4: Influence of the number of grains and the cleavage factor on the effective crack energy in the two-dimensional case. (Ernesti and Schneider, 2022)

subtle, such that the crack paths for $\beta = 20$ and $\beta = 50$ are almost indistinguishable, see Fig. 5.5c and see Fig. 5.5d, respectively.

Three-dimensional structures

We consider generated 3D Laguerre tessellations (Kuhn et al., 2020) with random grain orientation in each grain. Similar to the 2D case, we vary both the number of grains and the anisotropy factor. Since 3D simulations are much more costly compared to 2D simulations, we perform only three simulations per microstructure for the size study by investigating a normals in e_x , e_y and e_z -direction, respectively, and only one simulation per cleavage anisotropy factor β for the internal contrast study. Fig. 5.6 shows two cracked microstructures with 216 and 1728 grains, respectively. Similar to the 2D case, the crack surface changes its orientation in each grain. Fig. 5.7a shows the results of the size study for an anisotropy factor $\beta = 10$. The effective crack energy increases for increasing number of grains. For a very small structure containing 27 grains, the deviation between the three loading directions is rather large. For an increasing number of grains, this standard deviation is

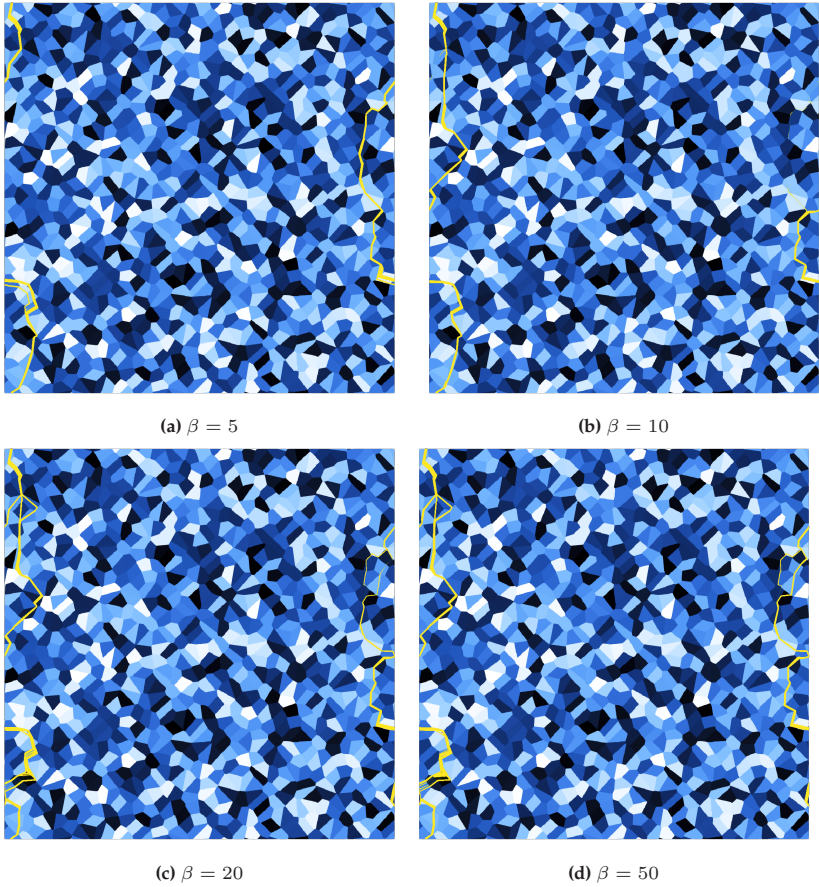


Figure 5.5: Crack path through a microstructure containing 1024 grains for $\bar{\xi} = e_x$ and varying cleavage anisotropy factors. (Ernesti and Schneider, 2022)

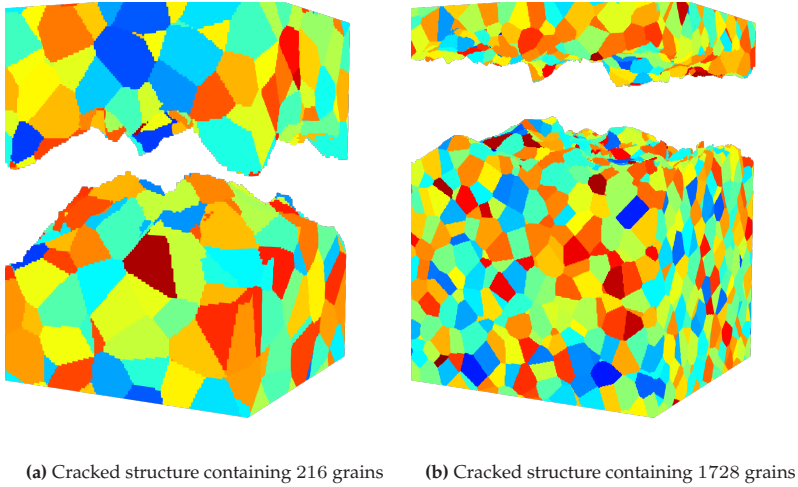


Figure 5.6: Cracked microstructure for different number of grains. (Ernesti and Schneider, 2022)

reduced to a negligible amount. Two main distinctions between the 2D and the 3D case emerge in case of the size study. Firstly, the range of the effective crack resistances differ significantly: In the 2D case the effective crack energy ranged around $\gamma^{\text{eff}} \simeq 1.4\gamma$, whereas for the 3D case we find $\gamma^{\text{eff}} \simeq 5.2\gamma$ for $\beta = 10$. Secondly, the effective crack energy increases with increasing number of grains in the 3D, at least within the range of our observation, whereas in the 2D case we observed saturation. This indicates that even more than the considered 13824 grains could be necessary to reach representative results.

Shifting our focus to the contrast study, see Fig. 5.7b, we observe a nearly linear correlation between the cleavage factor β and the effective crack energy. This clearly differs from the 2D case, which displayed a saturation. This effect has a geometric origin. In the 2D case, a continuous crack path can be found which passes each grain in the energetically most favorable direction. In 3D, this is not the case, as planar cracks within each grain cannot be combined into a continuous, global crack surface, in

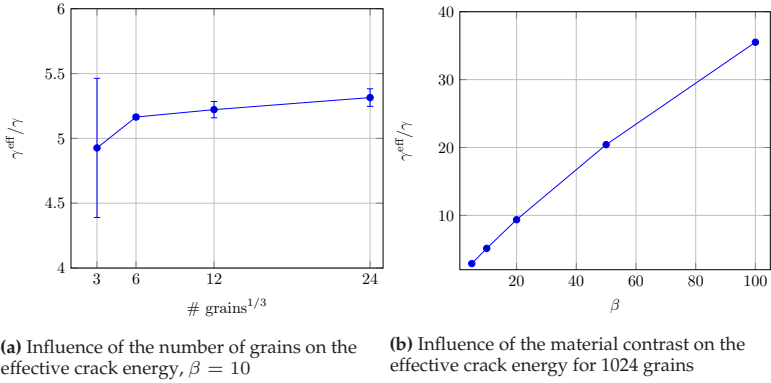
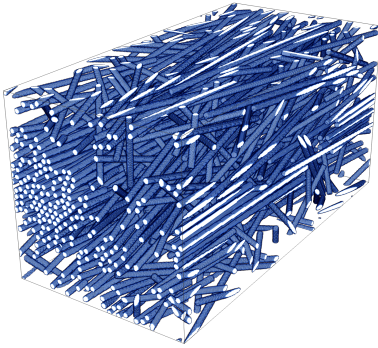


Figure 5.7: Influence of the number of grains and of the material contrast on the effective crack energy in the three-dimensional case. (Ernesti and Schneider, 2022)

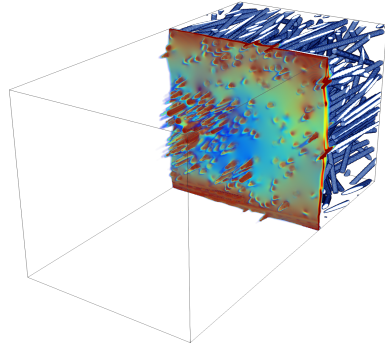
general. Hence, in the two- and three-dimensional context, the effective crack resistance of polycrystalline materials differs fundamentally in the context of anisotropic intergranular fracture, modeled with one cleavage parameter. In two spatial dimensions, the parameter β plays a subordinate role (at least if it is sufficiently large), in the three-dimensional case we see clearly that β is an important material parameter, which needs to be identified.

5.4.3 A carbon fiber reinforced polymer

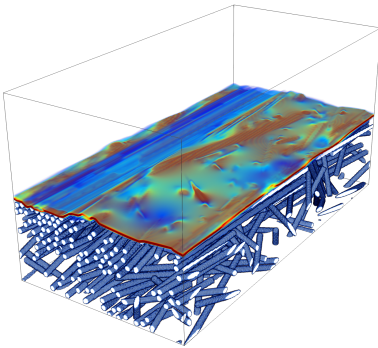
In this section, we investigate a carbon fiber reinforced composite. Carbon fibers are used due to their favorable strength-density ratio. The individual fibers have a strong anisotropy in both elastic and strength properties. As a result of the manufacturing process, they show higher Young's modulus and higher strength in fiber direction compared to the plane perpendicular to it. We use a crack resistance tensor for a fiber



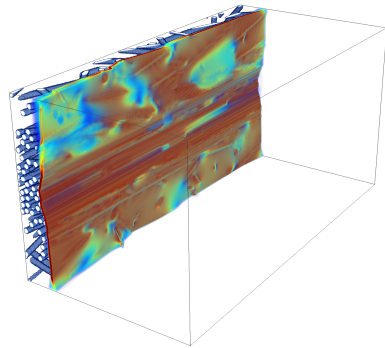
(a) Carbon fiber reinforced composite



(b) Crack surface for $\bar{\xi} = e_y, \gamma^{\text{eff}} = 1.82 \gamma$



(c) Crack surface for $\bar{\xi} = e_y, \gamma^{\text{eff}} = 0.85 \gamma$



(d) Crack surface for $\bar{\xi} = e_z, \gamma^{\text{eff}} = 0.87 \gamma$

Figure 5.8: Carbon fiber reinforced composite and crack surface for varying direction. (Ernesti and Schneider, 2022)

oriented in (unit) direction p as

$$\mathbf{G} = 25 \gamma p \otimes p + 0.5 \gamma (\text{Id} - p \otimes p),$$

assuming an internal contrast of 50 for the crack resistance, as suggested by Pillai et al. (2020). Furthermore, we model the matrix material in our composite with the isotropic crack resistance γ , assuming that the fibers transverse crack resistance is lower than that of the matrix material. The microstructure under consideration contains 290 fibers of $450\mu\text{m}$ length and $7\mu\text{m}$ diameter, oriented in an almost unidirectional manner in x -direction with second order orientation tensor $\text{diag}(0.9, 0.05, 0.05)$ and a total of filler content of 15%, see Fig. 5.8a. The structure was generated using sequential addition and migration (Schneider, 2017).

Fig. 5.8b shows the crack surface oriented in x -direction. We notice fiber pullout and matrix failure, as well as fiber damage that appears to be non-perpendicular to the fiber direction. The effective crack energy is increased by 50% compared to the matrix material. The crack surfaces in y - and z -direction are shown in Fig. 5.8c and Fig. 5.8d, respectively. Both crack surfaces look qualitatively similar. We notice both matrix failure and inter-fiber debonding, since we assumed the fibers perpendicular to their orientation to be weaker than the matrix material. For both cases, the effective properties are lower compared to the matrix material and almost equal.

5.5 Conclusion

In this chapter, we presented a numerical method for computing the effective crack energy of a heterogeneous medium with distinct anisotropy via weighted minimal surfaces. We derived the anisotropic maximum flow problem and discussed the implementation into an FFT-based homogenization tool for isotropic fracture. We saw that

both the solver framework and the discretization established for the isotropic case serves as a firm foundation for the anisotropic case. Indeed, the extension requires evaluating the projection onto ellipsoids in an efficient manner.

This anisotropic extension of the homogenization of the fracture energy enables the treatment of additional material classes compared to previous works. Applications were presented for polycrystalline ceramics and carbon-fiber reinforced composites.

In the literature on anisotropic phase-field fracture, 2D polycrystalline materials are often investigated in addition to the 3D case. The anisotropy may be encoded by the cleavage parameter β , which penalizes crack propagation in certain directions and forces the crack path to follow a weak plane. In our homogenization framework, we observed the behavior for the 2D case to fundamentally differ from the 3D case. In two dimensions, a crack is not geometrically restricted to follow the weakest plane through each grain. Therefore, the cleavage parameter β has no further meaning beyond a certain threshold. In the 3D case, on the other hand, neighborhood relations between different grains prohibit the crack to form freely in order to follow the weakest plane for each grain. Therefore, we observe a strong dependence of the effective crack energy on the cleavage parameter β , emphasizing its importance from the viewpoint of materials science.

Additionally, we saw that our framework allows us to investigate carbon fiber structures, which show distinct anisotropy within each fiber. This enables modeling additional effects compared to isotropic fibers, studied in chapter 4. With isotropic inclusions either weakening, similar to pores, or toughening with respect to the matrix material can be modeled. The inclusion of anisotropic fibers allows for toughening in one direction, for instance the fiber direction, and weakening in the transverse direction, broadening the spectrum for material design.

Chapter 6

Investigations on the influence of the boundary conditions when computing the effective crack energy of random heterogeneous materials using fast marching methods¹

6.1 Introduction

Nearly 25 years ago, Francfort and Marigo introduced a variational fracture model (Francfort and Marigo, 1998) based on Griffith's original energy criterion (Griffith, 1921). The model was formulated in terms of an energy functional to be minimized and added impetus to phase-field fracture mechanics (Bourdin et al., 2000; Wu et al., 2020). The latter is rather popular, as it permits to simulate both crack initiation and crack propagation in a common framework based on traditional

¹ This chapter is based on Ernesti et al. (2023) which was built on the results of the master thesis by Lendvai (2022) which was supervised by me. In order to include this paper into the structure of this work I shortened both the introduction and the second section. Furthermore, minor additional changes to the manuscript have been made. The results which were originally presented in Lendvai (2022) are found in section 6.4. Figures which are found in the master thesis are labeled accordingly.

finite element methods. The phase-field model may be interpreted as a regularization of the Francfort-Marigo model, inspired by the Ambrosio-Tortorelli approximation (Ambrosio and Tortorelli, 1990) of the Mumford-Shah functional (Mumford and Shah, 1989). Alternatively, the phase-field fracture model may be interpreted as a non-local damage model (Dimitrijevic and Hackl, 2008; Bažant, 1991).

Multi-scale methods (Milton, 2002) are used to predict the macroscopic behavior of microstructured materials, explicitly accounting for the material behavior of the constituents and their arrangement on the microscale. Homogenization theories serve as the mathematical underpinnings of modern multi-scale methods. Seminal contributions focus on periodic homogenization (De Giorgi and Spagnolo, 1973; Babuska, 1973; Larsen, 1975), where the underlying microstructure is given by a periodic cell. Since microstructured materials are often random due to their manufacturing process (Jeulin, 2021), stochastic homogenization results (Papanicolaou and Varadhan, 1981; Kozlov, 1978) have been established, where an infinitely large domain with a random microstructure is investigated. One method to evaluate effective properties based on stochastic homogenization results is by exploring *representative volume elements* (RVEs). For prescribed accuracy and fixed boundary condition type, a volume element is called representative provided it approximates the effective properties of the infinitely large domain up to this prescribed accuracy (Drugan and Willis, 1996). Since the size of the RVE is not known a priori and dependent on various factors, the RVE size is often found via computations on volume elements of increasing size (Gusev, 1997; Segurado and Llorca, 2002) until a desired degree of *representativity* is reached. For elliptic PDEs such as elasticity and conductivity problems, theoretical results show that for different boundary conditions applied to cells of finite size, i.e., periodic, Dirichlet or Neumann boundary conditions, the effective quantities evaluated on the cells share the same infinite-volume limit (Sab, 1992; Bourgeat and Piatnitski, 2004; Owhadi, 2003). Yet, it is well known that

the boundary conditions may have a strong influence on the necessary size of the RVE, see Kanit et al. (2003).

In the field of fracture mechanics, multi-scale approaches face additional difficulties compared to linear elastic or conductivity problems. One necessary ingredient for multi-scale methods is a distinct scale separation, allowing the quantities of interest, displacements, stresses or strains, to be separable into a large-scale and small-scale component. In an elastic material without a crack, for instance, this separation leads to a cell formula on the microscale, from which effective quantities may be derived. This approach does not work within a cracked microstructure, since this crack and the stress singularity resulting from it would be present on both the micro- and the macroscale. On the other hand, investigations on volume elements of finite size may be conducted with phase-field fracture models (Chen et al., 2019; Ernesti et al., 2020). However, it is well known (Gitman et al., 2007) that such a procedure will not, in general, lead to a macroscopic model for softening materials. Thus, special care is required.

Our strategy is based on a periodic homogenization result of Braides et al. (1996) for the Mumford-Shah functional (Mumford and Shah, 1989) and energetic minimization. This result covers the Francfort-Marigo model of brittle fracture (Francfort and Marigo, 1998) in the case of anti-plane shear when considering a fixed quasi-static time discretization and neglecting crack irreversibility (for instance in the very first load step on an un-cracked specimen). Within their result, Braides et al. (1996) show a decoupling of the volumetric part and the surface part of the Mumford-Shah functional. In the context of the Francfort-Marigo model this implies a decoupling of the effective stiffness and the effective crack energy in the anti-plane shear case. Furthermore, they provide specific formulas for both effective quantities. From their work the *effective crack energy* is defined as the area of the crack resistance-weighted minimal surface cutting through the microstructure. Numerical approaches to computing the *effective crack energy* have been proposed by Schneider

(2020), as well as Ernesti and Schneider (2021; 2022) using FFT-based algorithms and periodic boundary conditions, see also chapters 4 and 5. Recently, Michel-Suquet addressed the approach based on the homogenization result of Braides et al. (1996) using an alternative solution strategy by pointing out similarities with limit load analysis (Christiansen, 1981).

Contributions

The aim of this chapter is to investigate the effective crack energy of solids with random microstructures and the influence of the imposed boundary conditions. We give a brief summary on the cell formula for the effective crack energy based on the periodic (Braides et al., 1996) and stochastic (Cagnetti et al., 2019) homogenization results for the Mumford-Shah functional (Mumford and Shah, 1989) in section 6.2. For both the periodic and the stochastic setting, the effective crack energy is expressed in terms of a multi-cell formula on specifically notched cubes, which we call Dirichlet boundary conditions. For periodic homogenization, this multi-cell strategy is overly arduous, and a single-cell formula is sufficient, provided *periodic* boundary conditions are used, as well. Therefore, it makes sense to investigate periodic boundary conditions for random materials, as well. Indeed, for periodic boundary conditions, powerful numerical tools for computing the effective quantities based on the fast Fourier transform (FFT) are available (Schneider, 2020; Ernesti and Schneider, 2021; 2022), see also chapters 4 and 5. Dirichlet boundary conditions on the other hand are not easily integrated into this framework.

In a two-dimensional setting the problem of computing the effective crack energy reduces to finding weighted minimal paths. One prominent algorithm to compute such paths is the fast marching method introduced by Sethian (1996; 1999) where fast implementations are publicly

available². In the context of fracture mechanics, the fast marching method has already been used for fatigue fracture using stress intensity factors (Jovičić et al., 2005) and in combination with the extended finite element method (Stolarska et al., 2001; Sukumar et al., 2003; 2008). We discuss a straightforward way to compute the effective crack energy with the help of the fast marching method in section 6.3. One advantage of this method is that Dirichlet boundary conditions can easily be applied, since every point of a domain may be used as a starting or ending point. Section 6.4 comprises the numerical results. We first validate the fast marching method in terms of accuracy of the discretization and compare the results for periodic boundary conditions with established tools. Finally, we investigate the influence of the boundary condition on the approximated effective crack energy for microstructure samples of increasing cell size. We compare Dirichlet and periodic boundary conditions and study their necessary size of the computational cell.

6.2 The effective crack energy of heterogeneous random media³

Consider a domain $\Omega \subset \mathbb{R}^d$ and a heterogeneous field of crack resistances $\gamma : \Omega \rightarrow \mathbb{R}_{>0}$ which is periodic with periodicity η . Following the homogenization result of Braides et al. (1996) for the Mumford-Shah functional (Mumford and Shah, 1989) we define the effective crack energy as follows: Inside an infinite periodic continuation of our material with periodicity η we place a cube LQ_n of edge length L with its e_1 axis rotated onto the prescribed normal n . On such a cube, we compute a γ -weighted minimal surface S cutting the cube under the constraint

² <https://github.com/scikit-fmm/scikit-fmm>, accessed in November 2021

³ In this section we provide a brief summary of section 2.4.2 to enhance the readability of this chapter.

that the surface cuts the boundary of the cube at $x_1 = L/2$ within the coordinate system of the cube, see Fig. 2.10 in section 2.4.2 for a visual representation. The effective crack energy is given by the limit of these computed weighted minimal surfaces as the cube edge-length $L \rightarrow \infty$. In mathematical terms, the effective crack energy is defined via

$$\gamma_{\text{eff}}(n) = \lim_{L \rightarrow \infty} \inf_S \frac{1}{L^{d-1}} \int_S \gamma dA. \quad (6.1)$$

Let us take a closer look at the cell formula (6.1). From a computational point of view, the limit of $L \rightarrow \infty$ is not practicable, as we can only deal with finite computational domains. To overcome this issue, we may restrict to a single cell LQ and employ the boundary conditions used above, which we call *Dirichlet* boundary conditions. In this case, we fix the surface S on the boundary ∂LQ of the cube at $x_1 = L/2$ within the local coordinate system of the cube. Actually, any cut at $x_1 \in [0, L]$ could be chosen. We choose $x_1 = L/2$ for definiteness.

The approach by Braides et al. (1996) involves a multi-cell formula (6.1) although the homogenization problem is periodic. As the integrand in the problem (6.1) is convex, it is reasonable to hope that a single-cell formula may prove sufficient for computing the effective crack resistance γ_{eff} . This is indeed true, as shown by Braides and Piat (1995) and Chambolle and Thouroude (2009). More precisely, they showed that the effective crack energy $\gamma_{\text{eff}}(n)$ in equation (6.1) may be computed on a single cell Y_η with period η and for fields with periodic boundary conditions

$$\gamma_{\text{eff}}(n) = \inf_{\phi: Y_\eta \rightarrow \mathbb{R}, \text{ periodic}} \frac{1}{|Y_\eta|} \int_{Y_\eta} \gamma \|n + \nabla \phi\| dx. \quad (6.2)$$

Many materials of industrial relevance show a randomness in their microstructure composition, and periodic homogenization is not sufficient for describing those. Recently, Cagnetti et al. (2019) proved an extension

of the result of Braides et al. (1996) to stochastic homogenization for the Mumford-Shah functional. Remarkably, the result provides a true extension of the periodic case. The explicit formula they find is the same as in the periodic case, i.e., (6.1), but the infinite-volume limit is indispensable for stochastic homogenization.

The case of stochastic homogenization of elastic materials is well-studied. To compute effective quantities on cells of finite size, appropriate boundary conditions are required. Upon the infinite-volume limit the chosen boundary conditions do not affect the effective quantities (Sab, 1992; Bourgeat and Piatnitski, 2004; Owhadi, 2003). However, for cells of finite size, the boundary conditions have an influence on the approximation quality of the "true" effective stiffness, as shown by Sab (1992); Kanit et al. (2003). Typically, using periodic boundary conditions and periodized ensembles of random microstructures result in optimal convergence rates (Schneider et al., 2022).

In contrast to computing the effective stiffness or effective conductivity of a microstructured material, very little is known about the influence of the boundary conditions when computing the effective crack energy evaluated on cells of finite size. The aim of this chapter is to provide a first step in this direction. For the periodic boundary conditions and in three spatial dimensions, Schneider (2020) proposed an algorithm for computing the effective crack energy on cells on finite size. The approach relies on Strang's minimum cut/maximum flow duality (Strang, 1983), see also chapters 4 and 5.

Due to the tremendous computational effort involved, we restrict to two-dimensional microstructures. In this case, it is possible to compute shortest paths with fast marching, see section 6.3, which is well-known among experts.

6.3 Finding the minimum cut with the fast marching method

6.3.1 From minimum cut to shortest path problems

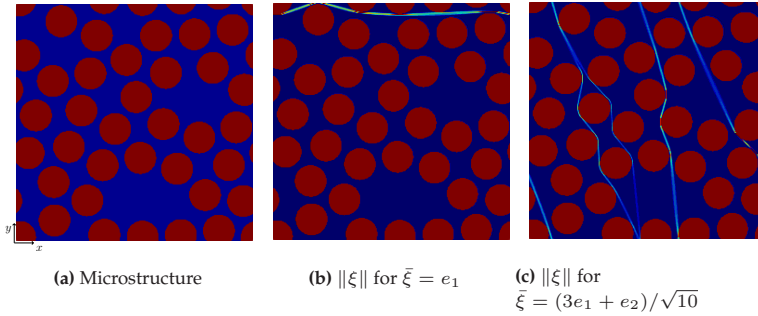


Figure 6.1: Microstructure and minimum cut field (ξ in eq. (2.32)) for an axis-aligned and a non-axis-aligned prescribed mean normal. (Ernesti et al., 2023)

To gain some intuition into minimum cut fields in two spatial dimensions, we consider a periodic microstructure of circular inclusions, shown in Fig. 6.1a. The structure contains 35 fillers, i.e., 50% area fraction. We consider tough inclusions, i.e., these have a (much) higher crack resistance than the matrix material. Fig. 6.1b and Fig. 6.1c show the minimum cut for mean crack normals $\bar{\xi} = e_1$ and $\bar{\xi} = (3e_1 + e_2)/\sqrt{10}$. In both cases, the minimum cut field localizes and takes the shape of a crack path that cuts through the microstructure. However, a distinct difference is present between the two cases. For the axis-aligned case, the cut field traverses the microstructure once, cutting from left to right. For the non-axis aligned case, the cut field wraps around the microstructure several times in order to both preserve the mean normal of the cut and to retain periodicity.

Thus, at least for the axis-aligned case, it appears reasonable the

one unit cell needs to be crossed. In the example shown, the green curve crosses the horizontal "boundary" twice. Such a curve may be represented by a shortest path algorithm if periodicity in y -direction is accounted for. Otherwise the red curve would arise as the shortest path from left to right.

Unfortunately, taking periodicity in y -direction into account does not always offer the proper strategy, as the microstructure in Fig. 6.2b shows. A straight "obstacle" with high crack resistance is placed along the diagonal. For prescribed normal $\bar{\xi} = e_1$, the minimum cut has to cross the obstacle. The shortest path strategy with periodic boundary conditions in y -direction, however, would give rise to the green path. Unfortunately, the shown path does not give rise to the correct path normal $\bar{\xi} = e_1$, but to the normal n pointing in diagonal direction! If, instead, no periodicity in y -direction is permitted, the correct crack path (in red) is computed.

To summarize, the charming idea of working with shortest path algorithms to compute the effective crack energy for axis-aligned crack normals may be unsuited to some microstructures. Therefore, it is unavoidable to perform a validation against minimum cut methods. For the microstructure models considered in this article, such a comparison is contained in section 6.4.3.

6.3.2 Finding shortest paths by the fast marching method

There is a deep connection between the eikonal equation and efficient path finding which led Sethian (1996; 1999) to devise computationally efficient algorithms for the latter. More precisely, consider a domain $\Omega \subset \mathbb{R}^d$ and suppose a wave propagates through our domain, starting from some point $x_0 \in \Omega$ at a given velocity $v : \Omega \rightarrow \mathbb{R}_{>0}$. Then, the time $T : \Omega \rightarrow \mathbb{R}_{\geq 0}$ this wave needs to arrive at point $x \in \Omega$ solves the

eikonal equation

$$\|\nabla T(x)\| = \frac{1}{v(x)}, \quad x \in \Omega, \quad (6.3)$$

with $T(x_0) = 0$. If the velocity v is spatially homogeneous, the level sets of the travel time T describe concentric spheres around the starting point x_0 . For a heterogeneous velocity, the wavefront is refracted. Sethian (1996; 1999) introduced the fast marching method as a fast algorithm for solving the eikonal equation. The fast marching method is an integrated strategy where the spatial discretization and the strategy for solving the eikonal equation are well orchestrated. More precisely, the solution strategy uses a modification of Dijkstra's algorithm (Dijkstra, 1959) well-known in graph theory (Gera et al., 2018). The fast marching method finds application in various fields ranging from shortest path finding (Kimmel and Sethian, 1996; Mirebeau, 2018; Garrido et al., 2006) to simulating wildfire spreading (Carballeira et al., 2021) and within the extended finite element method (Sukumar et al., 2003; 2008).

In d spatial dimensions and on a regular grid with N^d grid points, the fast marching method has the computational complexity $O(N^d \log N)$. In contrast, iterative procedures for solving the eikonal equation (6.3) typically have a complexity of $O(N^{d+1})$. This complexity reduction is partly caused by an underlying min-heap data structure (Williams, 1964). The problem of computing the effective crack energy on a microstructure involves finding a weighted minimal surface, as we pointed out in chapter 2. For the special case of two-dimensional structures, this problem simplifies to finding shortest paths in a given two-dimensional microstructure, for which various methods are available Willot (2015b; 2019). In particular, the fast marching method may be applied as follows.

1. The crack resistance $\gamma(x)$ serves as the weight in computing the weighted shortest path playing the role of a *resistance* for the crack to propagate. In contrast, for a propagating wave, the velocity $v(x)$

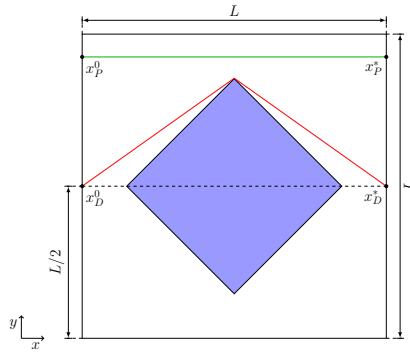


Figure 6.3: Example for (non-unique) shortest path with Dirichlet (index "D", red) and periodic (index "P", green) boundary conditions. (Ernesti et al., 2023)

enables the propagating wave to travel faster at a higher speed. Therefore we set the right hand side of the eikonal equation (6.3) to $\gamma(x)$ instead of $1/v(x)$ for computing the effective crack energy with fast marching⁴.

2. The solution field $T(x)$ embodies the γ -weighted distance from point x to the origin x^0 . We therefore call it the *distance field* throughout this work.
3. To compute the effective crack energy of a given microstructure cell $Y = [0, L]^2$ with crack normal $n = e_2$ and Dirichlet boundary conditions, we choose a starting point $x_0 = (0, L/2)^T$ and evaluate the distance field T in $x^* = (L, L/2)^T$. The effective crack energy is given by $T(x^*)/L$, see the red path in Fig. 6.3.

⁴ The crack resistance γ and the inverse velocity $1/v$ have different physical units. However, both the effective crack energy and the travel time field scale homogeneously under a rescaling of the crack resistance and the inverse velocity. Thus, upon introducing a conversion factor between crack resistance and the velocity in the beginning, the same conversion factor permits to recover the effective crack energy from the computed distance field. For simplicity of notation, we therefore suppress mentioning the conversion factor and tacitly assume it to be chosen appropriately.

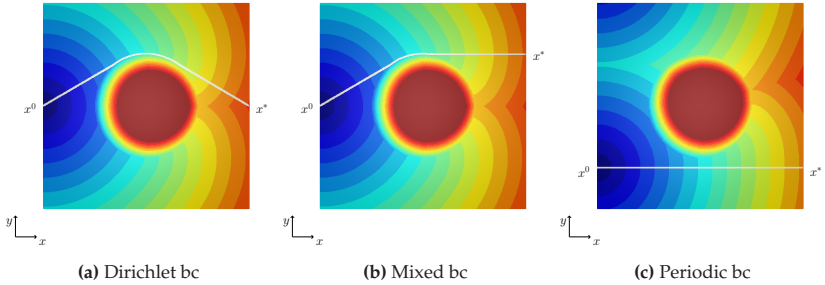


Figure 6.4: Distance field and crack path for different boundary conditions for a single circular inclusion microstructure. (Ernesti et al., 2023)

4. The solution for periodic boundary conditions with mean normal $n = e_y$ is given by the γ -weighted shortest periodic path from the left hand side to the right hand side. To find this shortest path with the fast marching approach, we consider all paths with the starting point $x^0 = (0, y)$ and end point $x^* = (L, y)$ for some $y \in [0, L]$, and select the starting point which returns the smallest crack energy, see the green path in Fig. 6.3. On a computational grid with $N \times N$ pixels, this process includes N fast marching computations, which increases the computational complexity to $O(N^3 \log N)$.
5. The fast marching method enables computing the minimum crack energy in a straightforward way. However, the involved crack path is not directly accessible. Rather, different approaches are available to obtain the crack in post processing, see for instance Noyel et al. (2011). Using the fact that the shortest crack path is perpendicular to the level sets of the distance field T , we rely on a gradient descent method to compute the crack path from any point x to the origin x^0 . To do so, we compute a spline interpolation on the numerically evaluated gradient of the distance field T .

One advantage of the fast marching method over the maximum flow approach discussed in chapters 4 and 5 is that additional boundary

conditions can easily be studied, as we can choose any point of Ω as our starting or ending point. We consider three different cases, illustrated in Fig. 6.4, which shows the level sets of the distance field and the resulting crack path for a structure containing a single circular inclusion of diameter $L/2$ positioned at the center of a square with edge length L . The inclusion has a much higher crack resistance than the embedding matrix, forcing the crack path to avoid the inclusion altogether. The distance field and the crack path for Dirichlet boundary conditions is shown in Fig. 6.4a. The distance field describes concentric circles starting from the left hand side until the inclusion is reached and a refraction occurs. To draw the crack path, we start on the right hand side at $y = L/2$ and follow the path perpendicular to the contour lines of the distance field. Notice that this path does not prescribe the shortest path from the right hand side of the structure to the origin on the left hand side. Indeed, Fig. 6.4b shows this shortest path originating in x^0 to the right-hand side. To draw this path we select x^* as the point on the right hand side with the minimum effective crack energy and draw the path perpendicular to the contour lines of the distance field. Since the mean crack normal may differ from the prescribed mean normal we do not focus on this case in this paper. For periodic boundary conditions the crack path is not unique for this example, as both above and below the inclusion straight paths are possible, see Fig. 6.4c for one possible option.

6.4 Numerical investigations

6.4.1 Setup⁵

The fast marching based algorithm for computing the effective crack energy was implemented in Python 3 based on the `scikit-fmm` module⁶, which provides both first-order and second-order fast marching methods. These differ in the convergence order of the underlying approximation of first derivatives. The first-order fast marching method uses classical forward and backward differences, whereas for the second-order method a three point stencil approximation of forward and backward differences is used Rickett and Fomel (1999). The crack paths were visualized by first computing the gradient of the resulting distance field by finite differences, interpolating this gradient field with bi-cubic splines and finally using gradient descent starting from the end point of the crack path.

For the computations based on the minimum cut/maximum flow approach, we relied on an in-house FFT-based code (Schneider, 2020; Ernesti and Schneider, 2021; 2022), see also chapters 4 and 5. The continuous equations were discretized with the CCMF discretization (Couprie et al., 2011) and solved by a damped version of the alternating direction method of multipliers (ADMM) (Glowinski and Marrocco, 1975; Gabay and Mercier, 1976) with adaptive choice for the penalty parameter, see Ernesti and Schneider (2021). We chose a relative tolerance of 10^{-4} .

All fast marching computations were run on an ARM-based SoC Apple M1 with 8 GB of RAM using a single thread. The minimum cut/maximum flow computations were performed on a desktop com-

⁵ The numerical investigations presented in this section are the result of the master thesis by Lendvai (2022) which was supervised by me. We reevaluated the findings of this thesis in a joint publication (Ernesti and Schneider, 2022) which forms the basis of this chapter.

⁶ <https://github.com/scikit-fmm/scikit-fmm>, accessed in November 2021

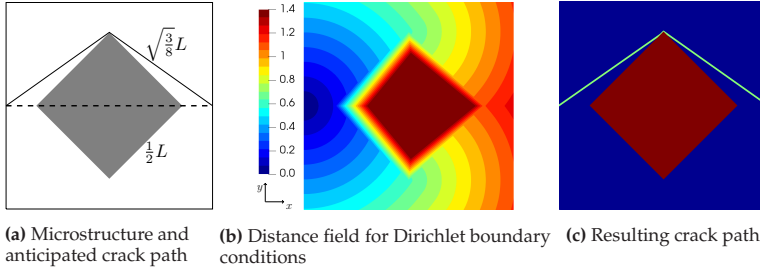


Figure 6.5: Microstructure of a rotated square with anticipated crack path, distance field and crack path for Dirichlet boundary conditions. (Lendvai, 2022; Ernesti et al., 2023)

puter with 32 GB of RAM and six 3.7 GHz cores.

6.4.2 A single rotated square inclusion

To investigate the accuracy of the fast-marching approach, we start with a structure containing a single square inclusion of edge length $L/2$, which is rotated at 45 degrees and positioned at the center of our computational domain of edge length L , see Fig. 6.5a. The crack resistance of the inclusion is given by $\gamma_{\text{fib}} = 10 \gamma_{\text{mat}}$. We consider an initial double notch crack at $y = 0.5 L$, i.e., Dirichlet boundary conditions. The analytical solution, which may be extracted from the structural measurements, see Fig. 6.5a, is $\gamma_{\text{eff}}/\gamma_{\text{mat}} = \sqrt{3/2} \approx 1.22247$, see Fig. 6.5a. Fig. 6.5b shows a contour plot of the distance field. Starting from the initial notch on the left hand side, the distance field initially shows a circular expanding front. Upon hitting the inclusion, the field is refracted and a new circular front with the top/bottom edge of the inclusion as origin continues to the other side. Since the distance field is symmetric with respect to the x -axis, we slightly perturb the starting point for our gradient descent method in y -direction to break this symmetry and enforce a unique crack path. The evaluated crack path is shown in Fig. 6.5c. We observe that it

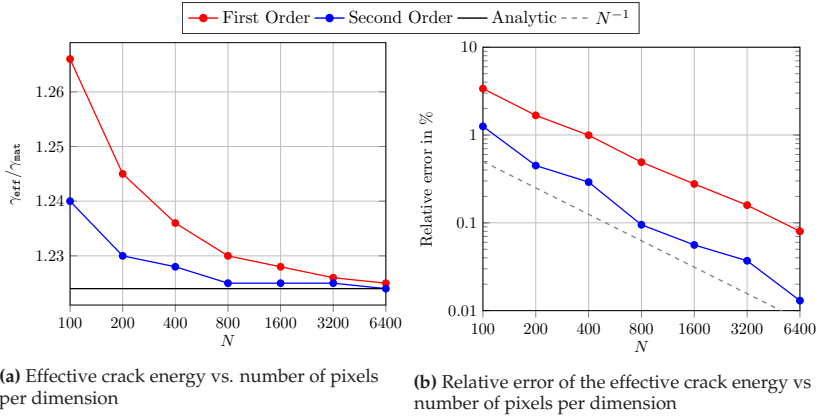


Figure 6.6: Effective crack energy and relative error for the rotated square microstructure. (Ernesti et al., 2023)

matches the geometrically anticipated path.

Next, we investigate the quality of the solution with respect to the grid size. We compute the effective crack energy for different resolutions ranging from 100 to 6400 pixels per side length of our computational domain. Furthermore, we investigate the performance of both first-order and second-order fast marching methods. The results are shown in Fig. 6.6a, where the absolute values of the crack energy are depicted, as well as in Fig. 6.6b, which shows the relative error compared to the analytical solution. Both the first and the second-order methods converge to the analytical solution with a linear rate of convergence. However, the second-order approach leads to a higher accuracy than the first-order approach, even on a coarser grid. To reach the accuracy of the second-order fast marching using first-order requires almost four times more pixels per edge length. Hence, we rely on the second-order fast marching method for the remainder of this chapter.

6.4.3 Comparison with minimum cut/maximum flow

In our next study, we investigate a periodic structure containing 32 unidirectional fibers and a filler fraction of 50%, which are represented as circular inclusions, see Fig 6.7. The structure was generated using a mechanical contraction algorithm (Williams and Philipse, 2003). The inclusions are considered tough, i.e., they have a higher crack resistance than the matrix and we set $\gamma_{\text{fib}} = 10 \gamma_{\text{mat}}$. We investigate various resolutions ranging from 128 to 4096 pixels per edge length.

In this section, we would like to investigate whether the results obtained with the fast-marching method and with the FFT-based technique give rise to similar results. Indeed, as discussed in section 6.3.1, it is necessary to exclude certain pathological situations in order to gain confidence into the results obtained with the fast marching method. We wish to emphasize that due to the lack of uniqueness of the solutions to the minimization problem (2.32), we may only expect the obtained effective crack energies to be close. However, a similar obtained minimum cracks are certainly a sufficient condition for the latter.

To enforce periodic boundary conditions in the fast-marching setting, we iterate over all pixels on the right hand side of the microstructure, evaluate the distance field at the same height on the other side and select the minimum. The distance field is shown in Fig. 6.7c. From the near center of the y -axis we observe a circular expanding front which is refracted at every inclusion. For both, the fast marching and the minimum cut/maximum flow formulation and the two considered resolutions, the crack paths are shown in Fig. 6.8. Notice that the way these two methods extract the crack path is very different. Whereas the crack path of the fast marching method is computed via gradient descent along the distance field, the crack path of the minimum cut/maximum flow approach is given by the total minimum cut through the microstructure with mean normal e_y , which is a field that localizes around the crack attaining large values whose magnitude has no physical meaning. This results from

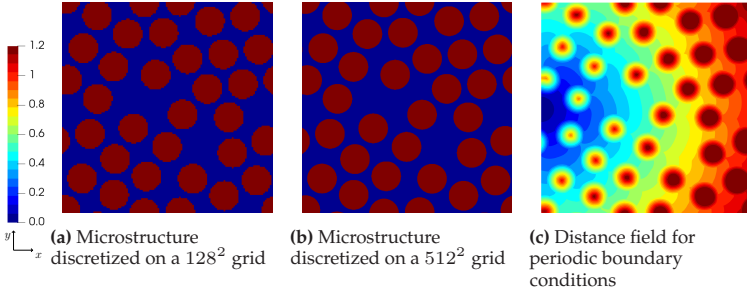


Figure 6.7: Microstructure containing 32 circular inclusions for different resolutions and distance field for periodic boundary conditions. (Lendvai, 2022; Ernesti et al., 2023)

the fact that the minimum cut is given by the gradient of the periodic field ϕ in equation(6.2) which has a jump discontinuity across the crack. Evaluating this quantity numerically results in large but finite values which tend to infinity as the pixel length goes to zero. Both methods find extremely similar crack paths. On a coarser grid of 128^2 pixels, the fast marching crack in Fig. 6.8b exhibits some small isolation distance to the inclusions, which is not the case for the minimum cut field. This isolation distance vanishes for higher resolutions, see Fig. 6.8d. These computational results resolve possible doubts about the expressivity of the fast marching results for the considered microstructures.

In Fig. 6.9, the effective crack energy for the two approaches under consideration is plotted against the resolution, together with the relative error, where we used the solution on the 4096^2 grid as the ground truth for each method. Both approaches show a linear rate of convergence with respect to the resolution per edge length. Furthermore, both approaches overestimate the effective crack energy on a coarser grid. However, in order to reach the accuracy of the minimum cut, the fast marching method requires between 1.5 and 2 times the resolution of the edge length. Notice the difference in the complexity of the two methods. The complexity of the minimum cut/maximum flow is mainly driven by the FFT, which has a complexity of $O(N^2 \log N)$, as well as the number of

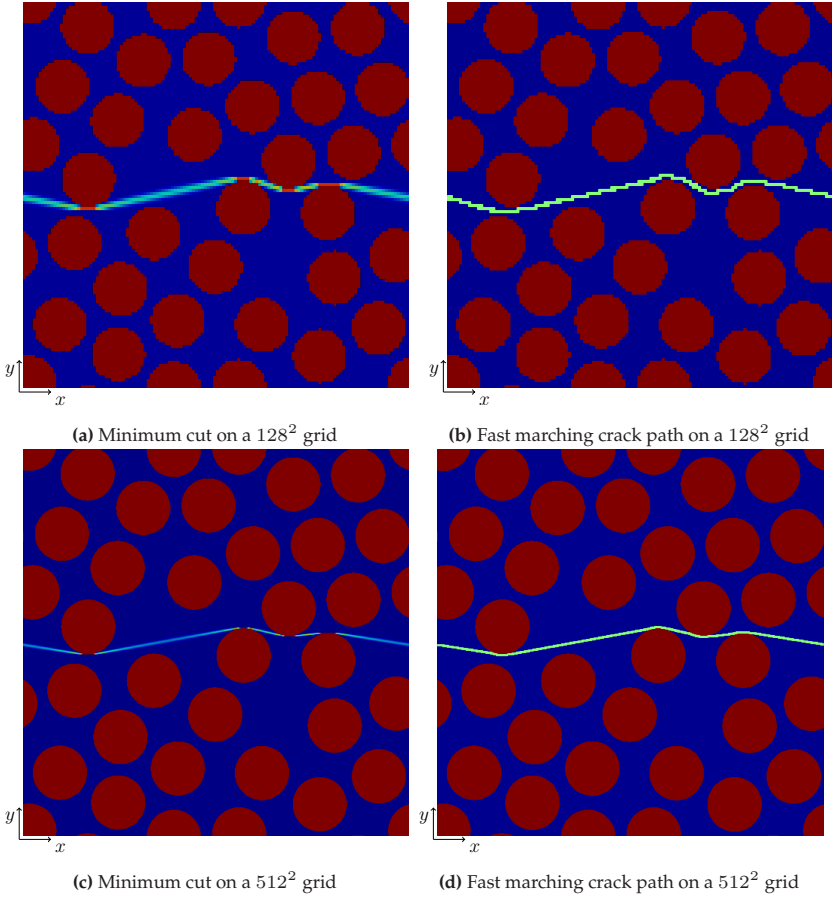


Figure 6.8: Periodic crack paths for minimum cut/maximum flow and fast marching method of a microstructure containing 32 circular inclusions for different grid sizes. (Lendvai, 2022; Ernesti et al., 2023)

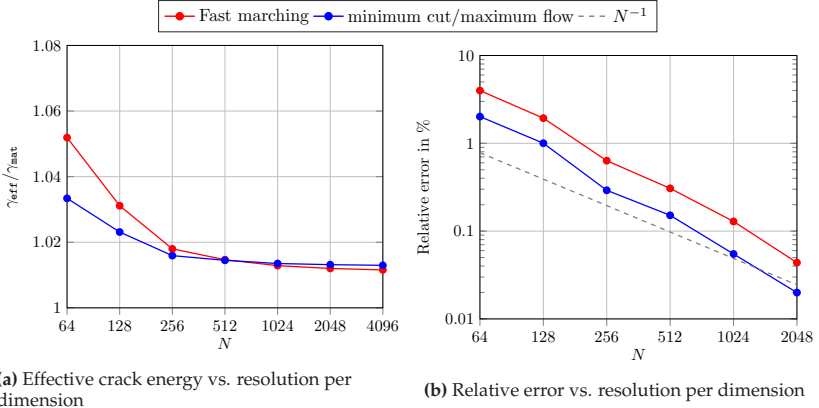


Figure 6.9: Effective crack energy and relative error comparing fast marching with minimum cut/maximum flow. (Ernesti et al., 2023)

required iterations, which range between 2000 and 7000 in order to reach the desired accuracy of 10^{-4} . The fast marching approach has a complexity of $O(N^3 \log N)$ for periodic boundary conditions. As a result we noticed for resolutions below $N = 2048$ that the fast marching method required less computational time than the minimum cut/maximum flow method, each running on a single thread. For $N = 4096$ the fast marching method required twice the computational time of minimum cut/maximum flow.

6.4.4 The influence of boundary conditions

In our next study we investigate the influence of the boundary conditions on the effective crack energy for computational cells of increasing size. We consider two types of boundary conditions, namely Dirichlet boundary conditions and periodic boundary conditions. For Dirichlet boundary conditions, we consider the crack propagating at $y = 0.5L$ to the other side of the domain at the same height. Fully periodic boundary conditions are attained by the minimum value when iterating over

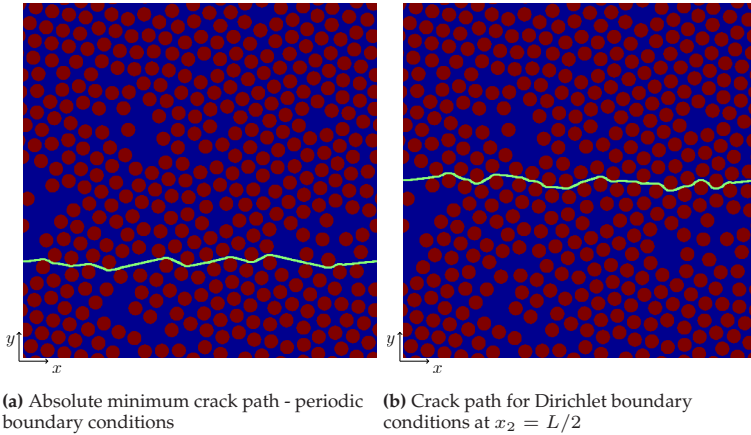
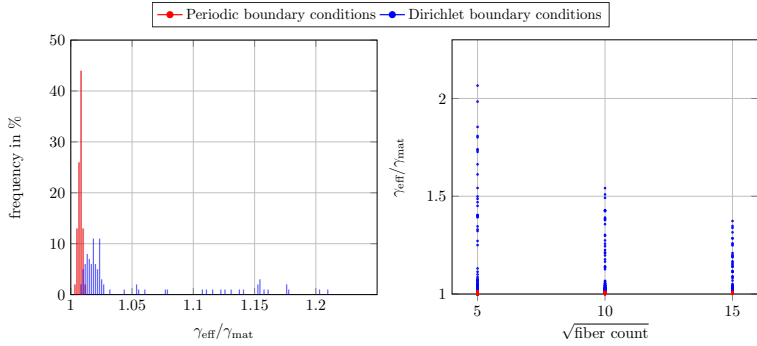


Figure 6.10: Crack paths for different boundary conditions. (Lendvai, 2022; Ernesti et al., 2023)

all pixels in y -direction using Dirichlet boundary conditions starting from each pixel. The material parameters are chosen as before, i.e., the inclusions are considered tough with a material contrast of 10.

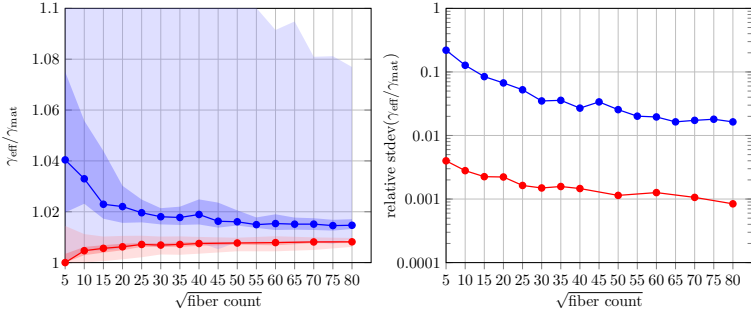
A comparison of the crack paths for different boundary conditions is shown in Fig. 6.10, where we consider a microstructure with 50% circular inclusions, i.e., unidirectional continuous fibers. The crack path for the periodic boundary conditions interacts with less inclusions, resulting in a path with more straight segments compared to the Dirichlet boundary conditions.

To further investigate the boundary conditions, we consider microstructures with 30% and 50% filler fraction and a varying number of inclusions ranging from 5^2 to 80^2 . For each number of inclusions we consider 100 microstructure realizations which were generated using mechanical contraction (Williams and Philipse, 2003). For the Dirichlet boundary conditions we consider all realizations. To reduce the computational costs for periodic boundary conditions we only take half of the realizations into account for a fiber count of 50^2 and higher. The results



(a) Histogram of the effective crack energy of 100 microstructures containing 25^2 inclusions

(b) Scatter plot of the effective crack energy vs. fiber count



(c) Median, 30 to 70 percentile range and total range for the effective crack energy vs. fiber count

(d) Relative standard deviation vs. fiber count

Figure 6.11: Comparison of the boundary conditions for 30% filler content. (Ernesti et al., 2023)

for volume fractions 30% and 50% are shown in Fig. 6.11 and Fig. 6.12, respectively. Fig. 6.11a and Fig. 6.12a show a histogram of the crack energy for 25^2 inclusions. On the y -axis, the number (in percent) of microstructures is shown whose effective crack energy corresponds to the x coordinate. We notice that the range of the periodic boundary condition is shifted to the lower values of the effective crack energy ranging, into the lower part of the Dirichlet boundary conditions. For the Dirichlet boundary conditions we notice some accumulation in the lower range up to $\gamma_{\text{eff}} = 1.025 \gamma_{\text{mat}}$ for 30% filler fraction and $\gamma_{\text{eff}} = 1.06 \gamma_{\text{mat}}$ for 50% filler fraction. Above these thresholds both histograms show some dispersion. These dispersions result from the fact that for some microstructures, the initial crack in the Dirichlet boundary conditions starts in an inclusion. Hence, the crack has to exit the inclusion first which causes an increase of the effective crack energy.

Fig. 6.11b and Fig. 6.12b show the scatter of the effective crack energy computed for all 100 microstructure realizations in the lower fiber count range. For both volume fractions, we observe that the Dirichlet boundary conditions result in a much wider range of possible values for the effective quantity γ_{eff} than the periodic boundary conditions. Furthermore, we observe a division of this wide range into wide scatter, about one third of the data for 30% filler fraction and on half of the data for a filler fraction of 50%. Furthermore, we see an accumulation of the remaining data around lower effective values. Additionally, we notice that the range of the outliers decreases for increasing fiber count since these effects result from initial cracks inside of inclusions.

To gain additional insight into the influence of the boundary conditions, we investigate the median as well as the upper and the lower percentile ranges in Fig. 6.11c and Fig. 6.12c. We observe that the range of effective crack energies for the two boundary conditions under consideration overlap for both volume fractions. Hence, for some microstructures, the Dirichlet boundary conditions result in the same effective crack energy as the periodic boundary condition for a possibly different microstructure

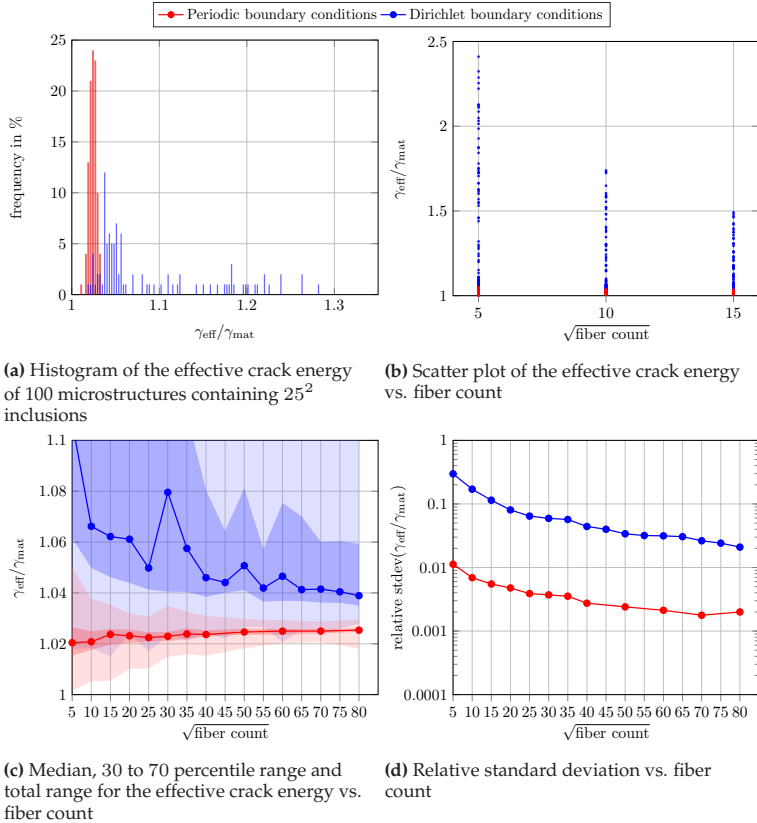


Figure 6.12: Comparison of the boundary conditions for 50% filler content. (Ernesti et al., 2023)

realization. Furthermore, we notice that for both boundary conditions the total range and the mid percentile range become smaller for an increasing fiber count. The median lines are approaching each other as the fiber count increases, however, at a very low rate. In general, the range of possible values for the effective crack energy for Dirichlet boundary conditions is much wider compared to periodic boundary conditions. Furthermore, the median for periodic boundary conditions is roughly placed in the center of the data set. In contrast, for Dirichlet boundary conditions the median and the mid percentile range are placed in the lower quarter of the data sets, reflecting the aforementioned outliers.

Last but not least, we investigate the relative standard deviation of the two data sets over the fiber count, see Fig. 6.11d and Fig. 6.12d. We observe a decrease of the standard deviation as the fiber count increases. Furthermore, we notice that the standard deviation for periodic boundary conditions is more than one magnitude lower than for Dirichlet boundary conditions. Specifically, for a volume fraction of 50%, we notice an increase of the standard deviation for the last microstructure sample with 80^2 fillers. A possible explanation for this effect may be found in Fig. 6.12c where we notice that the spread of the standard deviation is caused by some computations with lower effective crack energy compared to the median/mean value. These lower outliers are caused by sections of *straight* crack paths which are still possible and probable for very large microstructures.

To sum up, we strongly discourage using the Dirichlet boundary conditions. Rather, periodic boundary conditions should be preferred.

6.5 Conclusion

In this chapter we studied the influence of the boundary conditions on the effective crack energy of heterogeneous materials. Based on homoge-

nization result (Braides et al., 1996; Friedrich et al., 2022; Cagnetti et al., 2019) for the Francfort-Marigo model of brittle fracture (Francfort and Marigo, 1998) in a quasi-static setting and without crack irreversibility, we investigated a method for computing the effective crack energy using the fast marching method (Sethian, 1996). We validated our approach and compared it to the FFT-based methods using periodic boundary conditions discussed in chapters 4 and 5. In addition to periodic boundary conditions, the fast marching method provides additional freedom in the boundary condition choice. With this freedom at hand we compared periodic and Dirichlet boundary conditions for a continuously reinforced composite with tough inclusions, containing filler fractions of 30% and 50%. We noticed in a study with several realizations of volume elements of increasing size that the periodic boundary conditions result in a much lower spreading of the results compared to Dirichlet boundary conditions. This was reflected in the standard deviation, which was one magnitude lower for the periodic boundary conditions compared to Dirichlet boundary conditions. For an increasing size of the computational cell, we noticed that the medians approached each other. However, periodic boundary conditions should be preferred over Dirichlet boundary conditions due to the much lower standard deviation. This lower standard deviation indicates that the necessary computational cell for periodic boundary conditions is considerably smaller than for Dirichlet boundary conditions. Thus, we strongly recommend using periodic boundary conditions.

Applying periodic boundary conditions in the context of the fast marching method relied on an iterative process over one axis of the domain, i.e., increasing the complexity of the algorithm on an $N \times N$ grid from $O(N^2 \log N)$ for Dirichlet boundary conditions to $O(N^3 \log N)$. For microstructures of moderate size, i.e., up to $N = 2048$, the fast marching method is still competitive with an FFT-based solver for the minimum cut/maximum flow problem. However, for larger structures the higher complexity forms a strong argument against using fast marching for

periodic boundary conditions.

Classical fast marching algorithms are only applicable to isotropic crack resistances in the plane. To cover anisotropies in the crack resistance (Ernesti and Schneider, 2022), anisotropic fast marching methods Waheed (2020) may be explored.

Last but not least, let us mention that it would be desirable to have mathematical results at hand which concern the influence of boundary conditions on the effective crack energy. Indeed, for elastic solids, results (Sab, 1992; Bourgeat and Piatnitski, 2004; Owhadi, 2003) are available which provide a list of suitable boundary conditions whose influence becomes negligible when going to the infinite-volume limit. Previous work by Bouchitte and Suquet (1991; 1994) for limit-load problem suggests that Dirichlet boundary conditions may be used, whereas Neumann boundary conditions give rise to different results. Further research may be necessary to clarify this issue.

Chapter 7

Summary and conclusions

The two main goals of this thesis were to find suitable characterizers for microstructures applicable to a wide class of microstructures, and to establish computational tools for multi-scale brittle fracture.

Well established multi-scale homogenization methods for hardening type materials (Matouš et al., 2017) face difficulties when applied to softening type materials (Gitman et al., 2007). Therefore, a first attempt to simulate phase-field fracture on heterogeneous microstructures, discussed in section 2.3, provides only limited applicability for a multi-scale approach to fracture. This problem motivated us to pursue a different path.

In this work we focussed on the Francfort-Marigo model of brittle fracture (Francfort and Marigo, 1998). The Francfort-Marigo model provides a variational approach to fracture by subsequently solving free-discontinuity problems fulfilling an irreversibility constraint. Braides et al. (1996) provided a periodic homogenization result for a similar class of free-discontinuity problems, which is directly applicable to a single increment of the Francfort-Marigo model under specific loading conditions, namely anti-plane shear, while neglecting the irreversibility constraint. Furthermore, extensions lifting these requirements individually were established. Giacomini and Ponsiglione (2006) included the irreversibility constraint and Cagnetti et al. (2019) provided an extension to random, ergodic media, both within the anti-plane shear setting. Friedrich et al. (2022) lifted the restriction to anti-plane shear for periodic

microstructures and the two-dimensional case.

Motivated by the homogenization result of Braides et al. (1996), which gives specific formulas for the homogenized bulk and surface term in free-discontinuity problems, the effective crack energy is defined as the minimum cut through the microstructure of varying crack resistances. To solve this problem, Schneider (2020) proposed an FFT-based solution strategy for complex three dimensional microstructures based on the minimum cut/maximum flow duality shown by Strang (1983).

Chapter 3 was devoted to the characterization of digital microstructures. Microstructure characterization is concerned with finding simple quantitative expressions to classify microstructures and provides a crucial step before finding effective material parameters using homogenization approaches. By taking an approach based on Minkowski tensors which originate in stochastic geometry, we established the quadratic normal tensor as a suitable characterizer for microstructures which, due to local symmetries on the microscale, indicates a macroscopic anisotropy in the effective material behavior. Our main findings are listed below.

- We established the quadratic normal tensor as a robust characterizer of microstructures since it is translation invariant and does not scale with the size of the microstructure. Due to its tensorial form it naturally accounts for anisotropy.
- We provided a robust computational method to compute the quadratic normal tensor on large scale gray images of microstructures. We carefully validated our approach and investigated multi-grid convergence.
- We investigated complex microstructures of industrial interest. First, we compared the quadratic normal tensor with the fiber orientation tensor of second order for a fiber reinforced composite. We furthermore compared its accuracy with a well established method to compute fiber orientation tensors, namely a structure tensor approach. Finally, we investigated sand-binder structures used in casting appli-

cations, demonstrating the wide range of possible shapes for which the quadratic normal tensor may be computed.

In **chapter 4** we established a novel discretization and solver strategy for the cell formula for computing the effective crack energy. The approach of Schneider (2020) used trigonometric collocation (Moulinec and Suquet, 1994; 1998) and finite elements with reduced integration (Willot, 2015a) to discretize the cell formula. Furthermore, an FFT-based primal-dual hybrid gradient method (Chambolle and Pock, 2016) was used to solve the discretized equations. This initial work had two shortcomings. The involved discretizations showed checkerboard artifacts and non-smooth solution fields. Furthermore, the performance of the solver prevented finding high accuracy solutions. In (Ernesti et al., 2021) we found that higher accuracy and smoother solution fields may be established using a discretization presented by Couprie et al. (2011) based on a combinatorially consistent grid, namely the CCMF discretization. However, only computations using a small number of degrees of freedom were possible with this approach as only direct solvers were available. Our main findings in chapter 4 were the following.

- We provided an implementation of the CCMF discretization into a framework for FFT-based micromechanics. The implementation relies on a doubling of the degrees of freedom. The resulting solution fields exhibit far less artifacts than the discretizations previously investigated by Schneider (2020).
- To solve the discretized problem we relied on the alternating direction method of multipliers (ADMM) (Glowinski and Marrocco, 1975; Gabay and Mercier, 1976). In particular, augmenting the strategy with an adaptive parameter strategy (Schneider, 2021b) showed promising results.
- In a study on a continuous-fiber reinforced composite we found that for the CCMF discretization the residual correlates with the error compared to an accurate solution (Ernesti et al., 2021; Domahidi

et al., 2013) which was not the case for other discretizations (Willot, 2015a). The adaptive strategy showed a strong reduction of the iterations required to reach desired accuracies. In particular, we found the Barzilai-Borwein adaptive strategy (Xu et al., 2017) to be most promising.

- In subsequent numerical experiments we investigated complex microstructures ranging from fiber reinforced composites to structures with porous space.

We provided an extension of the approach presented in chapter 4 in **chapter 5** to account for locally anisotropic crack resistances. Our main findings are listed below.

- We considered an anisotropic minimum cut problem which includes the anisotropy via a tensorial crack resistance. For this case we derived an anisotropic maximum flow cell formula to compute the effective crack energy.
- In order to include this anisotropy into the framework presented in chapter 4 we established a projection operator, more precisely the projection onto an ellipsoid. To solve this projection problem we relied on Newton's method.
- This novel framework including anisotropy allows the study of additional classes of materials. We investigated polycrystalline brittle materials with a cleavage plane in each grain, as well as a carbon fiber reinforced composite with a transversely isotropic crack resistance in each fiber.

In **chapter 6** we focussed particularly on the case of stochastic homogenization where Cagnetti et al. (2019) provided the theoretical background. From a mathematical point of view, the qualitative theory of stochastic homogenization and (non-porous) linear elastic materials is well established (Papanicolaou and Varadhan, 1981; Kozlov, 1978; Sanchez-Palencia, 1980). Whereas the effective properties do not depend on the boundary conditions, apparent properties, i.e., those evaluated

on cells of finite size, are affected by the choice of boundary conditions. In particular, a higher accuracy of the apparent properties is typically achieved with periodic boundary conditions. In this chapter we investigated the influence of the boundary conditions on the apparent crack energy evaluated using the cell formula of Braides et al. (1996). Several remarks on our main findings are in order.

- Even before their established homogenization result, Braides and Piat (1995) showed that using periodic boundary conditions on a single periodic cell results in the same effective surface term for free-discontinuity problems than considering the infinite volume limit using Dirichlet boundary conditions.
- In order to compare the boundary conditions in the stochastic case we established the fast marching method (Sethian, 1996; 1999) as a tool to compute the effective crack energy on two dimensional microstructures. In particular, using fast marching methods provided additional freedom in the choice of the boundary conditions compared to the approach presented in chapters 4 and 5.
- After a validation of the fast marching approach we investigated the influence of the boundary conditions on various ensembles of cells and increasing cell size. Our investigations showed that for an increasing cell size the influence of the boundary condition decreases. However, Dirichlet boundary conditions resulted in a large scatter for different microstructure realizations compared to periodic boundary conditions and in particular a standard deviation of one magnitude higher. As a result we strongly recommend using periodic boundary conditions to compute the effective crack energy on heterogeneous microstructures.

Let us put our multi-scale approach for brittle fracture into perspective. The foundation for our approach is laid by a mathematical homogenization result for free discontinuity problems. Based on this result the effective crack energy is defined via a minimum cut problem.

We overcame numerical issues, namely checkerboard artifacts in the discretization and slow converging solvers, by introducing a novel solver and discretization strategy which allowed for higher accuracy solutions than previous work (Schneider, 2020). Anisotropic materials may be studied by computing the orthogonal projection on an ellipsoid. Investigations of the boundary conditions on 2D structures using fast marching methods indicated that using periodic boundary conditions results in a decrease of the necessary size of the computational domain compared to Dirichlet boundary conditions.

Nevertheless, the presented approach does have its limitations. First of all, the original homogenization result holds only for a restricted setup of the Francfort-Marigo model, i.e., neglecting irreversibility and assuming anti-plane shear loading. Subsequent work extending the original approach (Friedrich et al., 2022; Giacomini and Ponsiglione, 2006) only lifted these restrictions individually but not all at once.

A second issue lies in the Francfort-Marigo model itself and its mathematical roots in free-discontinuity problems. The homogenization result proves Γ -convergence of the functionals upon homogenization. By definition, Γ -convergence implies the convergence of global minimizers of the functionals but provides no statement on local minimizers. Following physical intuition, local minimizers may be more realistic but are excluded from the mathematical treatment. Consider for instance a crack propagating through a microstructure. As the crack hits an obstacle, it may change its direction based on what is *currently* energetically more favorable, but may not follow the globally minimal path.

A further consequence of the given homogenization result is the decoupling of the effective crack energy and the effective stiffness upon homogenization. This may indeed contrast with physical intuition as pointed out by Michel and Suquet (2022), who considered a two phase laminate material with different elastic properties in the phases but equal crack resistance γ . Michel and Suquet (2022) pointed out that the laminate material may in fact be toughened due to the presence of a

phase with a lower stiffness. In this case the effective crack resistance may exceed γ which is not possible with our approach.

An additional issue is caused by the presence of two small scales, i.e., the characteristic length of the microstructure, and the loading increment on the macro-scale, which is considered quasi-static. The ansatz proposed here considers a fixed discretization of the load into small increments and vanishing size of the microstructure in each step. Therefore, if a macroscopic crack propagates by a certain increment as a result of an increased load, the size of the microstructure upon homogenization is smaller than the crack increment. Hence, the macroscopic crack passes the microstructure cell within a single load increment. This point of view contrasts with other approaches from the literature on multi-scale fracture mechanics. For instance, Hossain et al. (2014) investigated quasi-static crack propagation on the microscale using a phase-field fracture model and identified the *effective crack resistance* as the maximum J-integral in time. However, their approach is not based on a mathematical homogenization result, and thus, a macroscopic model would have to be postulated. More to the point, the limit of vanishing time step size and the limit of vanishing microstructure size do not seem to commute. Hence, further investigations on this may be required.

Furthermore, investigations whether the quasi-static assumption holds may be of interest. In particular, quasi-static refers to a low velocity of an applied load which allows to neglect dynamical effects. It also assumes that the crack itself travels with a low velocity. If the crack passes the microstructure within a single load step its velocity may in fact be too large for this assumption. This would require a novel homogenization result which accounts for dynamic effects.

Lastly, let us point out that the Francfort-Marigo model does not distinguish tension and compression since the bulk energy of the Francfort-Marigo model is quadratic in the strain field. This contradicts physical intuition, see Fig. 2.2 when a compressive load causes the crack phases to close which may result in an interpenetration of the material with

itself and motivated energy splittings for phase-field fracture models (Amor et al., 2009; Miehe et al., 2010b). The model by Amor et al. (2009) converges to the Francfort-Marigo model with the additional constraint to non-interpenetrating crack faces for vanishing phase-field width (Chambolle et al., 2018). For this constraint to non-interpenetrating crack faces no homogenization result is yet available.

To conclude, the presented approach does have its limitations. On the one hand, the basis is laid by a proven homogenization result. But on the other hand, several assumptions for the homogenization result to hold may contradict with physical intuition. To overcome these issues, introducing these physical constraints into novel homogenization approaches may serve as a first step. From the application point of view, further investigations on the non-commuting small scales may be conducted. Michel and Suquet (2022) suggested for instance an additional time stepping on the microscale. However, caution has to be taken in order to stay on the trail provided by a well defined homogenization result. This distinguishes our approach from others who compute the effective crack resistance (Lebihain et al., 2021; Hossain et al., 2014). Furthermore, due to the global minimization involved, the established effective crack energy does form a lower bound to the *true* effective crack resistance. It is therefore suitable to model the *worst case scenario*, but may not incorporate certain toughening effects (Michel and Suquet, 2022).

Future work to continue our ansatz may discuss the up-scaling aspect of the presented homogenization approach. Using the presented tools one may compute the effective crack energy and use well known methods to compute the effective stiffness (Milton, 2002) of given microstructures. Using these effective quantities, simulations on the component scale may be conducted using phase-field methods. These face two main difficulties in the presence of anisotropy. First, the use of energy splittings to account for a tension-compression anisotropy faces difficulties if the stiffness is anisotropic. Due to the anisotropy, the eigensystems of local

strains and stresses do not align. In this case, an additive decomposition of the energy is not possible, in general. Furthermore, the question arises how to define tension or compression in the anisotropic setting. An initial contribution was proposed by van Dijk et al. (2020) who consider the elastic energy as an isotropic tensor function of a quantity Ψ via $\varepsilon : \mathbb{C} : \varepsilon = \Psi : \Psi$. For an energy decomposition expressed in Ψ , the well-established splittings of Miehe et al. (2010b) and Amor et al. (2009) are applicable.

Secondly, the phase-field model has to account for an anisotropic crack resistance. Several approaches have been proposed to incorporate tensorial crack resistances, we refer to section 6.1 for an overview. Following Focardi (2001) we may chose an approximation of the surface energy of the form

$$\int_{\Omega} \frac{\bar{\gamma}}{2} \left[\frac{d^2}{l} + l\varphi^2(\nabla d) \right] dx \quad (7.1)$$

within a phase field model for some anisotropic norm $\varphi : \mathbb{R}^d \rightarrow \mathbb{R}_{\geq 0}$ and mean crack resistance $\bar{\gamma}$. A common approach (Clayton and Knap, 2014) uses $\varphi^2(\nabla d) = \nabla d \cdot M \nabla d$ for some symmetric, positive definite matrix M . One question of particular interest is how to relate the anisotropic norm φ and the prefactor $\bar{\gamma}$ with the effective crack energy γ^{eff} .

Finally, a strategy for components with locally varying fibrous microstructure may be conducted. Here, the approach of fiber orientation interpolation proposed by Köbler et al. (2018) may be promising.

Appendix A

Minkowski tensors for specific shapes

A.1 Minkowski tensor of a ball

Consider the ball $B_R(0)$, parameterized by spherical coordinates (r, φ, θ) , with $r \in [0, R)$, $\varphi \in [0, 2\pi]$, and $\theta \in [0, \pi]$. The transformation to Cartesian coordinates reads

$$\mathbf{x}(r, \varphi, \theta) = \begin{pmatrix} r \sin(\theta) \cos(\varphi) \\ r \sin(\theta) \sin(\varphi) \\ r \cos(\theta) \end{pmatrix}.$$

The outward-pointing unit normal on $\partial B_R(0)$ is given by $\mathbf{n}(r, \varphi, \theta) = \mathbf{x}(1, \varphi, \theta)$ and is thus independent of r . With this parameterization at hand, the Minkowski tensor $W_1^{0,2}$ computes as

$$\begin{aligned} W_1^{0,2}(B_R(0)) &= \frac{R^2}{3} \int_0^{2\pi} \int_0^\pi \mathbf{n}(\varphi, \theta) \otimes \mathbf{n}(\varphi, \theta) \sin(\theta) d\theta d\varphi \\ &= \frac{4\pi R^2}{9} \text{Id}. \end{aligned}$$

A.2 Minkowski tensor of a cylinder

We consider a cylinder K in \mathbb{R}^3 , oriented in z -direction. We parameterize it by cylindrical coordinates (r, φ, z) with $r \in [0, R]$, $\varphi \in [0, 2\pi]$ and $z \in (0, L)$. The transformation to Cartesian coordinates reads

$$\mathbf{x}(r, \varphi, z) = \begin{pmatrix} r \cos(\varphi) \\ r \sin(\varphi) \\ z \end{pmatrix}.$$

We divide the boundary into three subsets, describing the side, top and bottom of the cylinder $\partial K = \partial K_s \cup \partial K_t \cup \partial K_b$. The side ∂K_s is parameterized by $r = R$, $\varphi \in (0, 2\pi]$, $z \in [0, L]$, the bottom ∂K_b by $r \in [0, R]$, $\varphi \in (0, 2\pi]$, $z = 0$ and the top ∂K_t by $r \in [0, R]$, $\varphi \in (0, 2\pi]$, $z = L$. The outward-pointing unit normals for the side, bottom and top boundary, respectively, read

$$\mathbf{n}_s = \begin{pmatrix} \cos(\varphi) \\ \sin(\varphi) \\ 0 \end{pmatrix}, \quad \mathbf{n}_t = \begin{pmatrix} 0 \\ 0 \\ 1 \end{pmatrix} \quad \text{and} \quad \mathbf{n}_b = \begin{pmatrix} 0 \\ 0 \\ -1 \end{pmatrix}.$$

With this parametrization at hand, we compute the Minkowski tensor $W_1^{0,2}$ of K by

$$\begin{aligned} W_1^{0,2}(K) &= \frac{1}{3} \int_0^{2\pi} \int_0^L \begin{pmatrix} \cos^2(\varphi) & \cos(\varphi) \sin(\varphi) & 0 \\ \cos(\varphi) \sin(\varphi) & \sin^2(\varphi) & 0 \\ 0 & 0 & 0 \end{pmatrix} R d\varphi dz \\ &\quad + \frac{2}{3} \int_0^R \int_0^{2\pi} \mathbf{e}_z \otimes \mathbf{e}_z r dr d\varphi \\ &= \frac{\pi}{3} LR (\mathbf{e}_x \otimes \mathbf{e}_x + \mathbf{e}_y \otimes \mathbf{e}_y) + \frac{2\pi}{3} R^2 \mathbf{e}_z \otimes \mathbf{e}_z \\ &= \frac{2\pi}{3} R^2 \left[\mathbf{e}_z \otimes \mathbf{e}_z + \frac{L}{2R} \left(\text{Id} - \mathbf{e}_z \otimes \mathbf{e}_z \right) \right]. \end{aligned}$$

Dividing $W_1^{0,2}(K)$ by its trace gives the quadratic normal tensor of K :

$$\text{QNT}(K) = \frac{R}{R+L} \mathbf{e}_z \otimes \mathbf{e}_z + \frac{L}{2(R+L)} \left(\text{Id} - \mathbf{e}_z \otimes \mathbf{e}_z \right).$$

If $R \ll L$ holds, then $R/(R+L)$ is the smallest eigenvalue, which indicates an extension in \mathbf{e}_z -direction. The larger eigenvalue $L/(2(R+L))$ has multiplicity 2, indicating some symmetry within the $\mathbf{e}_x - \mathbf{e}_y$ -plane. If $R \gg L$ holds, the smaller eigenvalue has multiplicity 2, indicating a disc-like shape within the $\mathbf{e}_x - \mathbf{e}_y$ -plane.

Appendix B

Performance of additional penalty factor choices for ADMM

In addition to the lower bound and the Barzilai-Borwein strategy for choosing the penalty factor ρ in combination with different damping parameters δ , see Section 4.4.3, we investigated two additional choices which are popular in the literature. More precisely, we consider residual balancing (He et al., 2000) and the averaging strategy proposed by Lorenz and Tran-Dinh (2019), which perform admirably for linear elastic and inelastic homogenization problems (Schneider, 2021b). The resulting residual and error plots are shown in Fig. B.1. For the CCMF-discretization and the damping parameter $\delta = 0.5$, the residual balancing strategy led to an unstable behavior. The choice $\delta = 0.25$ resolves this instability. However, this approach does not lead to a highly accurate solution. The averaging strategy by Lorenz and Tran-Dinh (2019) shows more promising results, reaching a tolerance of 10^{-4} in fewer than 2000 iterations and $\delta = 0.25$. However, this parameter choice turns out to be inferior to the Barzilai-Borwein approach. The relative error (4.36), shown in Fig. B.1b correlates with the residual in a similar way as for the choices considered in Section 4.4.3. For the rotated staggered grid discretization, the Lorenz-Tran-Dinh scaling with $\delta = 0.25$ shows the best performance. However, only low accuracy in terms of the relative error (4.36) may be reached.

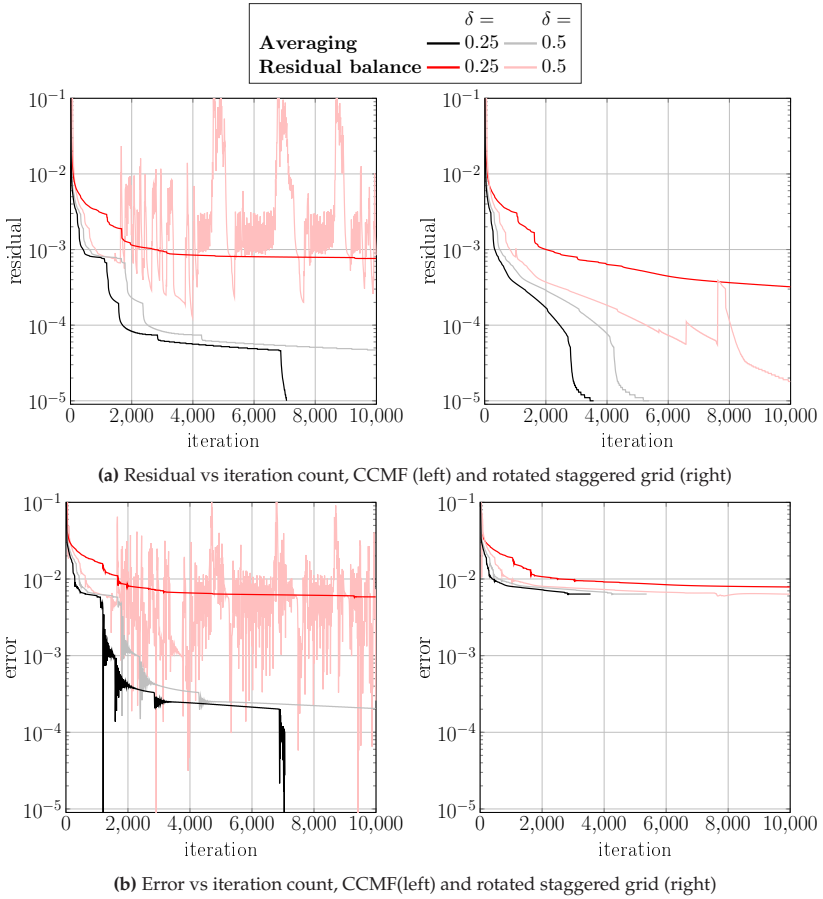


Figure B.1: Residual and error measure for CCMF and rotated staggered grid discretizations, comparing different solver parameters. (Ernesti and Schneider, 2021)

Bibliography

Adams, B., Olson, T., 1998. The mesostructure - property linkage in polycrystals. *Progress in Materials Science* 43 (1), 1–87.

Advani, S. G., Tucker, C. L., 1987. The Use of Tensors to Describe and Predict Fiber Orientation in Short Fiber Composites. *Journal of Rheology* 31, 751–784.

Alesker, S., 1999. Description of Continuous Isometry Covariant Valuations on Convex Sets. *Geometriae Dedicata* 74, 241–248.

Ambati, M., Gerasimov, T., De Lorenzis, L., 2015. A review on phase-field models of brittle fracture and a new fast hybrid formulation. *Computational Mechanics* 55, 383–405.

Ambati, M., Kruse, R., De Lorenzis, L., 2016. A phase-field model for ductile fracture at finite strains and its experimental verification. *Computational Mechanics* 57 (1), 149–167.

Ambrosio, L., Fusco, N., Pallara, D., 2000. *Functions of Bounded Variation and Free Discontinuity Problems*. Oxford University Press, Oxford.

Ambrosio, L., Tortorelli, V. M., 1990. Approximation of functionals depending on jumps by elliptic functionals via Γ -convergence. *Communications on Pure and Applied Mathematics* 43, 999–1036.

Amestoy, M., Leblond, J.-B., 1992. Crack paths in plane situation—II, detailed form of the expansion of the stress intensity factors. *International Journal of Solids and Structures* 29, 465–501.

Amidi, S., Wang, J., 2017. Direct Measurement of Traction–Separation Law of Concrete–Epoxy Interfaces Subjected to Moisture Attack under Mode-I Loading. *Journal of Composites for Construction* 21.

Amor, H., Marigo, J.-J., Maurini, C., 2009. Regularization formulation of the variational brittle fracture with unilateral contact: Numerical experiments. *Journal of the Mechanics and Physics of Solids* 57 (8), 1209–1229.

Anderson, E., Bai, Z., Bischof, C., Blackford, S., Demmel, J., Dongarra, J., Du Croz, J., Greenbaum, A., Hammarling, S., McKenney, A., Sorensen, D., 1999. *LAPACK Users' Guide*, 3rd Edition. Society for Industrial and Applied Mathematics, Philadelphia.

Babuska, I., 1973. Solution of interface problems by homogenization I. *SIAM Journal on Mathematical Analysis* 7, 603–634.

Bach, A., Marziani, R., Zeppieri, C. I., 2021. Γ -convergence and stochastic homogenization of singularly-perturbed elliptic functionals. *Calculus of Variations and Geometric Measure Theory at Pisa preprint* (5031), 1–48.

Bakhvalov, N., Panasenko, G., 1989. *Homogenisation: Averaging Processes in Periodic Media*. Mathematics and its Applications. Springer, Dordrecht.

Bansal, R. K., Kubis, A., Hull, R., Fitz-Gerald, J., 2006. High-resolution three-dimensional reconstruction: a combined scanning electron microscope and focused ion-beam approach. *Journal of Vacuum Science & Technology B* 24 (2), 554 – 561.

Barchiesi, M., Lazzaroni, G., Zeppieri, C. I., 2016. A bridging mechanism in the homogenisation of brittle composites with soft inclusions. *SIAM Journal on Mathematical Analysis* 48 (2), 1178–1209.

Barenblatt, G. I., 1962. The Mathematical Theory of Equilibrium Cracks in Brittle Fracture. *Advances in Applied Mechanics* 7, 55–129.

- Bažant, Z. P., 1991. Why continuum damage is nonlocal: Micromechanics argument. *Journal of Engineering Mechanics* 117, 1070–1087.
- Bay, R. S., Tucker III, C. L., 1992. Stereological measurement and error estimates for three-dimensional fiber orientation. *Polymer Engineering and Science* 32, 240–253.
- Behnel, S., Bradshaw, R., Citro, C., Dalcin, L., Seljebotn, D. S., Smith, K., 2011. Cython: The Best of Both Worlds. *Computing in Science Engineering* 13 (2), 31–39.
- Benveniste, Y., 1987. A new approach to the application of Mori-Tanaka's theory in composite materials. *Mechanics of Materials* 6, 147–157.
- Berthier, E., Ponson, L., Dascalu, C., 2014. Quasi-brittle Fracture of Heterogeneous Materials: A Nonlocal Damage Model. *Procedia Materials Science* 3, 1878–1883.
- Boeff, M., Gutknecht, F., Engels, P. S., Ma, A., Hartmaier, A., 2015. Formulation of nonlocal damage models based on spectral methods for application to complex microstructures. *Engineering Fracture Mechanics* 147, 373–387.
- Böhlke, T., 2006. Texture simulation based on tensorial Fourier coefficients. *Computers and Structures* 84, 1086–1094.
- Böhlke, T., Jöchen, K., Kraft, O., Löhe, D., Schulze, V., 2010. Elastic properties of polycrystalline microcomponents. *Mechanics of Materials* 42, 11–23.
- Böhlke, T., Lobos, M., 2014. Representation of Hashin-Shtrikman Bounds of cubic crystal aggregates in terms of texture coefficients with application in materials design. *Acta Materialia* 67, 324–334.
- Borden, M., Verhoosel, C., Scott, M., Hughes, T., Landis, C., 2012. A phase-field description of dynamic brittle fracture. *Computer Methods in Applied Mechanics and Engineering* 217, 77–95.

Bouchitte, G., Suquet, P., 1991. Homogenization, Plasticity and Yield design. In: Dal Maso, G., Dell'Antonio, G. F. (Eds.), *Composite Media and Homogenization Theory*. Birkhäuser, Boston.

Bouchitte, G., Suquet, P., 1994. Equi-coercivity of variational problems: the role of recession functions. In: Brézis, J.-L. L. H. (Ed.), *Nonlinear partial differential equations and their applications*. Vol. 12 of *College de France Seminar*. Longman, Harlow.

Bourdin, B., Francfort, G. A., Marigo, J.-J., 2000. Numerical experiments in revisited brittle fracture. *Journal of the Mechanics and Physics of Solids* 48, 797–826.

Bourgeat, A., Piatnitski, A., 2004. Approximations of effective coefficients in stochastic homogenization. *Annales de l'Institut H. Poincaré* 40, 153–165.

Bower, A. F., Ortiz, M., 1991. A three-dimensional analysis of crack trapping and bridging by tough particles. *Journal of the Mechanics and Physics of Solids* 39, 815–858.

Boyd, S., Vandenberghe, L., 2004. *Convex Optimization*. Cambridge University Press, Cambridge.

Brach, S., Hossain, M. Z., Bourdin, B., Bhattacharya, K., 2019. Anisotropy of the effective toughness of layered media. *Journal of the Mechanics and Physics of Solids* 131, 96–111.

Braides, A., 1998. *Approximation of Free-Discontinuity Problems*. Lecture Notes in Mathematics. Springer Berlin, Heidelberg.

Braides, A., Defranceschi, A., Vitali, E., 1996. Homogenization of Free Discontinuity Problems. *Archive for Rational Mechanics and Analysis* 135, 297–356.

- Braides, A., Piat, V. C., 1995. A Derivation Formula for Convex Integral Functionals Defined on $BV(\Omega)$. *Journal of Convex Analysis* 2 (1/2), 69–85.
- Bredies, K., Lorenz, D., 2018. *Mathematical Image Processing*. Springer, Cham, Switzerland.
- Brown, W. F., 1955. Solid Mixture Permittivities. *The Journal of Chemical Physics* 23, 1514–1517.
- Bryant, E. C., Sun, W. C., 2018. A mixed-mode phase field fracture model in anisotropic rocks with consistent kinematics. *Computer Methods in Applied Mechanics and Engineering* 342, 561–584.
- Bunge, H. J., 1982. *Texture Analysis in Materials Science: Mathematical Methods*. Butterworth & Co, London.
- Burke, S., Ortner, C., Süli, E., 2010. An adaptive finite element approximation of a variational model of brittle fracture. *SIAM Journal on Numerical Analysis* 48, 980–1012.
- Burke, S., Ortner, C., Süli, E., 2013. An Adaptive Finite Element Approximation Of a Generalized Ambrosio–Tortorelli Functional. *Mathematical Models and Methods in Applied Sciences* 23 (09), 1663–1697.
- Cagnetti, F., Dal Maso, G., Scardia, L., Zeppieri, C. I., 2019. Stochastic Homogenization of Free-Discontinuity Problems. *Archive for Rational Mechanics and Analysis* 233, 935–974.
- Carballeira, J., Nicolás, C., Garrido, S., Moreno, L., 2021. Wildfire Spreading Simulator Using Fast Marching Algorithm. *Simulation Notes Europe* 31, 159–167.
- Chambolle, A., 2004. An approximation result for special functions with bounded deformation. *Journal de Mathématiques Pures et Appliquées* 83, 929–954.

Chambolle, A., Conti, S., Francfort, G. A., 2018. Approximation of a brittle fracture energy with a constraint of non-interpenetration. *Archive for Rational Mechanics and Analysis* volume 228, 867–889.

Chambolle, A., Crismale, V., 2019. Existence of strong solutions to the Dirichlet problem for the Griffith energy. *Calculus of Variations and PDE* 58 (4), 136.

Chambolle, A., Crismale, V., 2021. Compactness and lower semicontinuity in GSB. *Journal of the European Mathematical Society* 23 (3), 701–719.

Chambolle, A., Francfort, G. A., Marigo, J.-J., 2009. When and how do cracks propagate? *Journal of the Mechanics and Physics of Solids* 57, 1614–1622.

Chambolle, A., Pock, T., 2016. An introduction to continuous optimization for imaging. *Acta Numerica* 25, 161–319.

Chambolle, A., Thouroude, G., 2009. Homogenization of interfacial energies and construction of plane-like minimizers in periodic media through a cell problem. *Networks & Heterogeneous Media* 4, 127–152.

Chan, S. K., Tuba, I. S., Wilson, W. K., 1970. On the finite element method in linear fracture mechanics. *Engineering Fracture Mechanics* 2, 1–17.

Chen, Y., Vasiukov, D., Gélébart, L., Park, C. H., 2019. A FFT solver for variational phase-field modeling of brittle fracture. *Computer Methods in Applied Mechanics and Engineering* 349, 167–190.

Cherepanov, G. P., 1967. The propagation of cracks in a continuous medium. *Journal of Applied Mathematics and Mechanics* 31 (3), 503–512.

Chowdhury, S. R., Narasimhan, R., 2000. A cohesive finite element formulation for modeling fracture and delamination in solids. *Sadhana* 25, 561–587.

- Christiansen, E., 1981. Computations of limit loads. *International Journal for Numerical Methods in Engineering* 17, 1547–1570.
- Chung, S. T., Kwon, T. H., 1995. Numerical Simulation of Fiber Orientation in Injection Molding of Short-Fiber-Reinforced Thermoplastics. *Polymer Engineering and Science* 35, 604–618.
- Clayton, J. D., Knap, J., 2014. A geometrically nonlinear phase field theory of brittle fracture. *International Journal of Fracture* 189, 139–148.
- Clayton, J. D., Knap, J., 2015. Phase field modeling of directional fracture in anisotropic polycrystals. *Computational Materials Science* 98, 158–169.
- Cnudde, V., Cwirzen, A., Massachaele, B., Jacobs, P. J. S., 2009. Porosity and microstructure characterization of building stones and concretes. *Engineering Geology* 103, 76–83.
- Cook, T. S., Erdogan, F., 1972. Stresses in bonded materials with a crack perpendicular to the interface. *International Journal of Engineering Science* 10, 677–697.
- Cooley, J. W., Turkey, J. W., 1965. An algorithm for the machine calculation of complex Fourier series. *Mathematics of Computation* 19, 297–301.
- Couprie, C., Grady, L., Talbot, H., Najman, L., 2011. Combinatorial Continuous Maximum Flow. *SIAM Journal on Imaging Sciences* 4 (3), 905–930.
- Dal Maso, G., 2013. Generalised functions of bounded deformation. *Journal of the European Mathematical Society* 15 (5), 1943–1997.
- Daniels, F., ter Haar Romenij, B. M., Rubbens, M. P., van Assen, H. C., 2007. Quantification of Collagen Orientation in 3D Engineered Tissue. In: 3rd Kuala Lumpur International Conference on Biomedical Engineering 2006. Springer, Berlin, Heidelberg.

Dastjerdi, A. K., Tan, E., Barthelat, F., 2013. Direct Measurement of the Cohesive Law of Adhesives Using a Rigid Double Cantilever Beam Technique. *Experimental Mechanics* 53, 1763–1772.

De Giorgi, E., Spagnolo, S., 1973. Sulla convergenza degli integrali dell'energia per operatori ellittici del secondo ordine. *Annali della Scuola Normale Superiore di Pisa* 8, 391 – 411.

De Lorenzis, L., Maurini, C., 2021. Nucleation under multi-axial loading in variational phase-field models of brittle fracture. *International Journal of Fracture* .

Démery, V., Rosso, A., Ponson, L., 2014. From microstructural features to effective toughness in disordered brittle solids. *EPL (Europhysics Letters)* 105, 34003.

Dijkstra, E. W., 1959. A note on two problems in connection with graphs. *Numerische Mathematik* 1, 269–271.

Dimitrijevic, B. J., Hackl, K., 2008. A Method for Gradient Enhancement of Continuum Damage Models. *Technische Mechanik* 28.

Dinic, E. A., 1970. Algorithm for solution of a problem of maximum flow in a network with power estimation. *Soviet Mathematics – Doklady* 11, 1277–1280.

Domahidi, A., Chu, E., Boyd, S., 2013. ECOS: An SOCP Solver for Embedded Systems. In: 2013 European Control Conference (ECC).

Dorn, C., Schneider, M., 2019. Lippmann-Schwinger solvers for the explicit jump discretization for thermal computational homogenization problems. *International Journal for Numerical Methods in Engineering* 118 (11), 631–653.

- Drugan, W., Willis, J. R., 1996. A micromechanics-based nonlocal constitutive equations and estimates of representative volume element size for elastic composites. *Journal of the Mechanics and Physics of Solids* 44, 497–524.
- Dugdale, D. S., 1960. Yielding of steel sheets containing slits. *Journal of the Mechanics and Physics of Solids* 8, 100–104.
- Döbrich, C. M., Rau, C., Krill III, C. E., 2004. Quantitative characterization of the three-dimensional microstructure of polycrystalline Al-Sn using X-ray microtomography. *Metallurgical and Materials Transactions A* 35 (7), 1953 – 1961.
- Edmonds, J., Karp, R. M., 1972. Theoretical improvements in algorithmic efficiency for network flow problems. *Journal of the ACM* 19 (2), 248–264.
- Elias, P., Feinstein, A., Shannon, C. E., 1956. A note on the maximum flow through a network. *IRE Transactions on Information Theory* 2 (4), 399–404.
- Elices, M., Guinea, G. V., Gomez, J., Planas, J., 2002. The cohesive zone model: advantages, limitations and challenges. *Engineering Fracture Mechanics* 69, 137–163.
- Erdogan, F., Biricikoglu, V., 1973. Two bonded half planes with a crack going through the interface. *International Journal of Engineering Science* 11, 745–766.
- Eriksen, H. K., Lilje, P. B., Branday, A. J., Górski, K. M., 2004. Estimating N-Point Correlation Functions from Pixelized Sky Maps. *The Astrophysical Journal Supplement Series* 151, 1–11.
- Ernesti, F., 2018. An FFT-based solver for brittle fracture on heterogeneous microstructures. Master thesis, Karlsruhe Institute of Technology (KIT), Department of Mathematics.

Ernesti, F., Lendvai, J., Schneider, M., 2023. Investigations on the influence of the boundary conditions when computing the effective crack energy of random heterogeneous materials using fast marching methods. *Computational Mechanics* 71, 277–293.

Ernesti, F., Schneider, M., 2021. A fast Fourier transform based method for computing the effective crack energy of a heterogeneous material on a combinatorially consistent grid. *International Journal for Numerical Methods in Engineering* 122, 6283–6307.

Ernesti, F., Schneider, M., 2022. Computing the effective crack energy of heterogeneous and anisotropic microstructures via anisotropic minimal surfaces. *Computational Mechanics* 69, 45–57.

Ernesti, F., Schneider, M., Böhlke, T., 2020. Fast implicit solvers for phase field fracture problems on heterogeneous microstructures. *Computer Methods in Applied Mechanics and Engineering* 363, 112793.

Ernesti, F., Schneider, M., Böhlke, T., 2021. Computing the effective crack energy of microstructures via quadratic cone solvers. *PAMM Proceedings in Applied Mathematics & Mechanics* 21, e202100100.

Ernesti, F., Schneider, M., Winter, S., Hug, D., Last, G., Böhlke, T., 2022. Characterizing digital microstructures by the Minkowski-based quadratic normal tensor. *Mathematical Methods in the Applied Sciences* 46, 961–985.

Esser, E., Zhang, X., Chan, T. F., 2010. A general framework for a class of first order primal-dual algorithms for convex optimization in imaging science. *SIAM Journal on Imaging Sciences* 3 (4), 1015–1046.

Ettmeyer, F., Lechner, P., Hofmann, T., Andrä, H., Schneider, M., Grund, D., Volk, W., Günther, D., 2020. Digital Sand Core Physics: Predicting physical properties of sand cores by simulations on digital microstructures. *International Journal of Solids and Structures* 188-189, 155–168.

- Focardi, M., 2001. On the variational approximation of free-discontinuity problems in the vectorial case. *Mathematical Models and Methods in Applied Sciences* 11, 663–684.
- Ford, L. R., Fulkerson, D. R., 1956. Maximal flow through a network. *Canadian Journal of Mathematics* 8, 399–404.
- Francfort, G. A., Marigo, J.-J., 1998. Revisiting brittle fracture as an energy minimization problem. *Journal of Mechanics Physics of Solids* 46, 1319–1342.
- Friedrich, M., Perugini, M., Solombrino, F., 2022. Γ -convergence for free-discontinuity problems in elasticity: Homogenization and relaxation. *Indiana University Mathematics Journal* accepted, 1–50.
- Fries, T.-P., Belytschko, T., 2010. The extended/generalized finite element method: An overview of the method and its applications. *International Journal for Numerical Methods in Engineering* 84 (3), 253–304.
- Gabay, D., Mercier, B., 1976. A dual algorithm for the solution of nonlinear variational problems via finite element approximations. *Computers and Mathematics with Applications* 2 (1), 17–40.
- Gajek, S., Schneider, M., Böhlke, T., 2021. An FE-DMN method for the multiscale analysis of short fiber reinforced plastic components. *Computer Methods in Applied Mechanics and Engineering* 384, 113952.
- Garrido, S., Moreno, L., Blanco, D., 2006. Voronoi diagram and fast marching applied to path planning. In: *Proceedings 2006 IEEE International Conference on Robotics and Automation, 2006. ICRA 2006*.
- Gera, R., Haynes, T. W., Hedetniemi, S. T. (Eds.), 2018. *Graph Theory. Problem Books in Mathematics*. Springer.
- Gerasimov, T., De Lorenzis, L., 2019. On penalization in variational phase-field models of brittle fracture. *Computer Methods in Applied Mechanics and Engineering* 354, 990–1026.

- Giacomini, A., Ponsiglione, M., 2003. A Discontinuous Finite Element Approximation of Quasi-static Growth of Brittle Fractures. *Numerical Functional Analysis and Optimization* 24 (7–8), 813–850.
- Giacomini, A., Ponsiglione, M., 2006. A Γ -convergence approach to stability of unilateral minimality properties in fracture mechanics and applications. *Archive for Rational Mechanics and Analysis* 180, 399–477.
- Gitman, I. M., Askes, H., Sluys, L., 2007. Representative volume: Existence and size determination. *Engineering Fracture Mechanics* 74, 2518–2534.
- Giusti, E., 1984. *Minimal Surfaces and Functions of Bounded Variation*. Vol. 80 of *Monographs in Mathematics*. Birkhäuser, Boston.
- Glowinski, R., Marrocco, A., 1975. Sur l'approximation, par éléments finis d'ordre un, et la résolution, par pénalisation-dualité d'une classe de problèmes de Dirichlet non linéaires. *ESAIM: Mathematical Modelling and Numerical Analysis - Modélisation Mathématique et Analyse Numérique* 9, 41–76.
- Gmati, H., Mareau, C., Ammar, A., El Arem, S., 2020. A phase-field model for brittle fracture of anisotropic materials. *International Journal for Numerical Methods in Engineering* 121 (15), 3362–3381.
- Goldberg, A. V., Rao, S., 1998. Beyond the flow decomposition barrier. *Journal of the ACM* 45 (5), 783–797.
- Gol'dstein, R. V., Salganik, R. L., 1974. Brittle fracture of solids with arbitrary cracks. *International Journal of Fracture* 10, 507–523.
- Goree, J. G., Venezia, W. A., 1977. Bonded elastic half-planes with an interface crack and a perpendicular intersecting crack that extends into the adjacent material. *International Journal of Engineering Science* 15, 1–17, 19–27.

- Göring, D., Klatt, M., Stegmann, C., Mecke, K., 2013. Morphometric analysis in gamma-ray astronomy using Minkowski functionals. *Astronomy & Astrophysics* 555 (A38), 1–7.
- Griffith, A. A., 1921. The phenomena of rupture and flow in solids. *Philosophical Transactions of the Royal Society of London. Series A* 221, 163–198.
- Groeber, M. A., Haley, B. K., Uchic, M. D., Dimiduk, D. M., Ghosh, S., 2006. 3D reconstruction and characterization of polycrystalline microstructures using a FIB-SEM system. *Materials Characterization* 57 (4), 259–273.
- Gross, D., Seelig, T., 2017. *Fracture Mechanics*, 3rd Edition. Springer, Heidelberg.
- Guderlei, R., Klenk, S., Mayer, J., Schmidt, V., Spodarev, E., 2007. Algorithms for the computation of the Minkowski functionals of deterministic and random polyconvex sets. *Image and Vision Computing* 25, 464–474.
- Gusev, A. A., 1997. Representative volume element size for elastic composites: A numerical study. *Journal of the Mechanics and Physics of Solids* 45 (9), 1449–1459.
- Hadwiger, H., 1951. Beweis eines Funktionalsatzes für konvexe Körper. *Abhandlungen aus dem Mathematischen Seminar der Universität Hamburg* 17, 69–76.
- He, B. S., Yang, H., Wang, S. L., 2000. Alternating Direction Method with Self-Adaptive Penalty Parameters for Monotone Variational Inequalities. *Journal of Optimization Theory and Applications* 106 (2), 337–356.
- He, M.-Y., Hutchinson, J. W., 1989. Crack deflection at an interface between dissimilar elastic materials. *International Journal of Solids and Structures* 25, 1053–1067.

Heinecke, F., Willberg, C., 2019. Manufacturing-Induced Imperfections in Composite Parts Manufactured via Automated Fiber Placement. *Journal of Composites Science* 3, 1–24.

Heister, T., Wheeler, M. F., Wick, T., 2015. A primal-dual active set method and predictor-corrector mesh adaptivity for computing fracture propagation using a phase field approach. *Computer Methods in Applied Mechanics and Engineering* 290, 466–495.

Hesch, C., Weinberg, K., 2014. Thermodynamically consistent algorithms for a finite-deformation phase-field approach to fracture. *International Journal for Numerical Methods in Engineering* 99, 906–924.

Hessman, P. A., Riedel, T., Welschinger, F., Hornberger, K., Böhlke, T., 2019. Microstructural analysis of short glass fiber reinforced thermoplastics based on x-ray micro-computed tomography. *Composites Science and Technology* 183, 1–10.

Hintermüller, M., Holler, M., Papafitsoros, K., 2018. A function space framework for structural total variation regularization with applications in inverse problems. *Inverse Problems* 34 (6), 1–39.

Hofacker, M., Miehe, C., 2012. Continuum phase field modeling of dynamic fracture: variational principles and staggered FE implementation. *International Journal of Fracture* 178, 113–129.

Hollstein, T., Kienzler, R., 1988. Fracture mechanics characterisation of crack growth under creep conditions. *The Journal of Strain Analysis for Engineering Design* 23, 87–96.

Hossain, M. Z., Hsueh, C.-J., Bourdin, B., Bhattacharya, K., 2014. Effective toughness of heterogeneous media. *Journal of the Mechanics and Physics of Solids* 71 (15), 15–32.

- Hug, D., Kiderlen, M., Svane, A. M., 2017. Voronoi-based estimation of Minkowski tensors from finite point samples. *Discrete & Computational Geometry* 57, 545–570.
- Hug, D., Schneider, R., 2015. Hölder continuity for support measures of convex bodies. *Archiv der Mathematik* 104 (1), 83–92.
- Hug, D., Schneider, R., Schuster, R., 2008a. Integral geometry of tensor valuations. *Advances in Applied Mathematics* 41, 482–509.
- Hug, D., Schneider, R., Schuster, R., 2008b. The space of isometry covariant tensor valuations. *St. Petersburg Mathematical Journal* 19, 137–158.
- Hussain, M. A., Pu, S., Underwood, J., 1974. Strain energy release rate for a crack under combined mode I and mode II. In: *Fracture Analysis: Proceedings of the 1973 National Symposium on Fracture Mechanics, Part II*.
- Inceoglu, F., Ville, J., Ghamri, N., Pradel, J. L., Druin, A., Valette, R., Vergnes, B., 2011. Correlation Between Processing Conditions and Fiber Breakage During Compounding of Glass Fiber-Reinforced Polyamide. *Polymer Composites* 32, 1842–1850.
- Irwin, G. R., 1957. Analysis of Stresses and Strains Near the End of a Crack Transversing a Plate. *Journal of Applied Mechanics* 24, 361–364.
- Irwin, G. R., 1962. Crack-extension force for a part-through crack in a plate. *Journal of Applied Mechanics* 29, 2281–2291.
- Irwin, G. R., 1968. Linear fracture mechanics, fracture transition, and fracture control. *Engineering Fracture Mechanics* 1, 241–257.
- Jensen, E. B. V., Kiderlen, M. (Eds.), 2017. *Tensor Valuations and Their Applications in Stochastic Geometry and Imaging*. Vol. 2177 of *Lecture Notes in Mathematics*. Springer, Cham.

- Jeulin, D., 1988. On image analysis and micromechanics. *Revue de Physique Appliquée* 23 (4), 549–556.
- Jeulin, D., 1994a. Fracture Statistics Models and Crack Propagation in Random Media. *Applied Mechanics Reviews* 47 (1S), S141–S150.
- Jeulin, D., 1994b. Random structure models for composite media and fracture statistics. *Advances in Mathematical Modelling of Composite Materials* 15, 239–289.
- Jeulin, D., 2021. *Morphological Models of Random Structures*. Springer, Cham.
- Jikov, V., Kozlov, S., Oleinik, O., 1994. *Homogenization of Differential Operators and Integral Functionals*. Springer, Berlin.
- Jin, C., Netrapalli, P., Jordan, M. I., 2018. Accelerated gradient descent escapes saddle points faster than gradient descent. In: Bubeck, S., Perchet, V., Rigollet, P. (Eds.), *Proceedings of the 31st Conference On Learning Theory*. Vol. 75 of *Proceedings of Machine Learning Research*.
- Jirasek, M., 1998. Nonlocal Models for Damage And Fracture: Comparison of Approaches. *International Journal of Solids and Structures* 35, 4133–4145.
- Jones, R. M., 1998. *Mechanics of Composite Materials*, 2nd Edition. Taylor & Francis, Boca Raton, USA.
- Jovičić, G., Živković, M., Jovičić, N., 2005. Numerical modeling of crack growth using the level set fast marching method . *FME Transactions* 33, 11–19.
- Junk, M., Budday, J., Böhlke, T., 2012. On the solvability of maximum entropy moment problems in texture analysis. *Mathematical Models and Methods in Applied Sciences* 12, 1250043.

- Kakouris, E. G., Triantafyllou, S. P., 2019. Phase-Field Material Point Method for dynamic brittle fracture with isotropic and anisotropic surface energy. *Computer Methods in Applied Mechanics and Engineering* 357, 112503.
- Kanatani, K., 1984. Distribution of directional data and fabric tensors. *International Journal of Engineering Science* 22, 149–164.
- Kanit, T., Forest, S., Galliet, I., Mounoury, V., Jeulin, D., 2003. Determination of the size of the representative volume element for random composites: statistical and numerical approach. *Journal of the Mechanics and Physics of Solids* 40 (13–14), 3647–3679.
- Kate, J. M., Gokhale, C. S., 2006. A simple method to estimate complete pore size distribution of rocks. *Engineering Geology* 84, 48–69.
- Katzav, E., Adda-Bedia, M., Arias, R., 2007. Theory of dynamic crack branching in brittle materials. *Journal of Fracture* 143, 245–271.
- Kehrer, L., Wicht, D., Wood, J. T., Böhlke, T., 2018. Dynamic mechanical analysis of pure and fiber-reinforced thermoset- and thermoplastic-based polymers and free volume-based viscoelastic modeling. *GAMM-Mitteilungen* 48, 1–16.
- Kimmel, R., Sethian, J. A., 1996. Fast Marching Methods for Computing Distance Maps and Shortest Paths.
- Kiseliou, Y. N., 1994. Algorithms of Projection of a Point onto an Ellipsoid. *Lithuanian Mathematical Journal* 34, 141–159.
- Klatt, M., Schröder-Turk, G. E., Mecke, K., 2017. Mean-intercept anisotropy analysis of porous media. II. Conceptual shortcomings of the MIL tensor definition and Minkowski tensors as an alternative. *Medical Physics* 44, 3663–3675.
- Klatt, M. A., Göring, D., Stegmann, C., Mecke, K., 2012. Shape analysis of counts maps. *AIP Conference Proceedings* 1505 (1), 737–740.

Klenk, S., Schmidt, V., Spodarev, E., 2006. A new algorithmic approach to the computation of Minkowski functionals of polyconvex sets. *Computational Geometry* 34, 127–148.

Klusemann, B., Svendsen, B., 2010. Homogenization methods for multi-phase elastic composites: Comparisons and benchmarks. *Technische Mechanik* 4, 374–386.

Köbler, J., Schneider, M., Ospald, F., Andrä, H., Müller, R., 2018. Fiber orientation interpolation for the multiscale analysis of short fiber reinforced composite parts. *Computational Mechanics* 61 (6), 729–750.

Kolmogorov, V., Zabin, R., 2004. What energy functions can be minimized via graph cuts? *IEEE Transactions on Pattern Analysis and Machine Intelligence* 26, 147–159.

Korte, S., Ritter, J., Jiao, C., Midgley, P. A., Clegg, W. J., 2011. Three-dimensional electron backscattered diffraction analysis of deformation in MgO micropillars. *Acta Materialia* 59 (19), 7241–7254.

Kozlov, S., 1979. The averaging of random operators. *Mat. Sb. (N.S.)* 109 (2), 188–202.

Kozlov, S. M., 1978. Averaging of differential operators with almost periodic rapidly oscillating coefficients. *Mathematics of the USSR-Sbornik* 107 (149) (2 (10)), 199–217.

Krause, M., Hausherr, J. M., Burgeth, B., Herrmann, C., Krenkel, W., 2010. Determination of the fibre orientation in composites using the structure tensor and local X-ray transform. *Journal of Materials Science* 45, 888–896.

Kuhn, C., 2013. Numerical and Analytical Investigation of a Phase Field Model for Fracture. Doctoral thesis (Dr.-Ing), TU Kaiserslautern.

Kuhn, C., Müller, R., 2016. A discussion of fracture mechanisms in heterogeneous materials by means of configurational forces in a phase field fracture model. *Computer Methods in Applied Mechanics and Engineering* 312, 95–116.

Kuhn, C., Noll, T., Müller, R., 2016. On phase field modeling of ductile fracture. *GAMM-Mitteilungen* 39 (1), 35–54.

Kuhn, C., Schlüter, A., Müller, R., 2015. On degradation functions in phase field fracture models. *Computational Materials Science* 108 (part B), 374–384.

Kuhn, J., Schneider, M., Sonnweber-Ribic, P., Böhlke, T., 2020. Fast methods for computing centroidal Laguerre tessellations for prescribed volume fractions with applications to microstructure generation of polycrystalline materials. *Computer Methods in Applied Mechanics and Engineering* 369, 113175.

Larsen, B. C., Yang, W., Ice, G. E., Budai, J. D., Tischler, J. Z., 2002. Three-dimensional X-ray structural microscopy with submicrometre resolution. *Nature* 415 (6874), 887–890.

Larsen, E., 1975. Neutron transport and diffusion in inhomogeneous media. *Journal of Mathematical Physics* 16, 1421–1427.

Laubie, H. H., 2013. Linear elastic fracture mechanics in anisotropic solids: Application to fluid-driven crack propagation. Ph.D. thesis, Massachusetts Institute of Technology.

Lebichain, M., 2019. Large-scale crack propagation in heterogeneous materials : an insight into the homogenization of brittle fracture properties. PhD dissertation, Sorbonne Université.

Lebichain, M., Ponson, L., Kondo, D., Leblond, J.-B., 2021. Effective toughness of disordered brittle solids: a homogenization framework. *Journal of the Mechanics and Physics of Solids* 153, 104463.

Lendvai, J., 2022. On the influence of the boundary conditions for computing the effective crack energy of heterogeneous materials. Master thesis, Karlsruhe Institute of Technology (KIT), Department of Mechanical Engineering.

Lenoir, A., 1997. Fast Estimation of Mean Curvature on the Surface of a 3D Discrete Object. *Discrete Geometry for Computer Imagery* 1347, 175–186.

Li, B., Peco, C., Millán, D., Arias, I., Arroyo, M., 2015. Phase-field modeling and simulation of fracture in brittle materials with strongly anisotropic surface energy. *International Journal for Numerical Methods in Engineering* 102, 711–727.

Lorenz, D. A., Tran-Dinh, Q., 2019. Non-stationary Douglas–Rachford and alternating direction method of multipliers: adaptive step-sizes and convergence. *Computational Optimization and Applications* 74, 67–92.

Ma, R., Sun, W. C., 2020. FFT-based solver for higher-order and multi-phase-field fracture models applied to strongly anisotropic brittle materials. *Computer Methods in Applied Mechanics and Engineering* 362, 112781.

Maggi, F., 2012. *Sets of Finite Perimeter and Geometric Variational Problems: An Introduction to Geometric Measure Theory*. Cambridge University Press.

Mandal, T. K., Nguyen, V. P., Wu, J.-Y., 2020. Evaluation of variational phase-field models for dynamic brittle fracture. *Engineering Fracture Mechanics* 235, 107169.

Mantz, H., Jacobs, K., Mecke, K., 2008. Utilizing Minkowski functionals for image analysis: A marching square algorithm. *Journal of Statistical Mechanics: Theory and Experiment* 2008, 1–29.

- Matheron, G., 1975. *Random Sets and Integral Geometry*. John Wiley & Sons, New York.
- Matouš, K., Geers, M. G. D., Kouznetsova, V. G., Gillman, A., 2017. A review of predictive nonlinear theories for multiscale modeling of heterogeneous materials. *Journal of Computational Physics* 330, 192–220.
- Michel, J. C., Moulinec, H., Suquet, P., 2000. A computational method based on augmented Lagrangians and fast Fourier transforms for composites with high contrast. *Computer Modelling in Engineering and Sciences* 1 (2), 79–88.
- Michel, J. C., Moulinec, H., Suquet, P., 2001. A computational scheme for linear and non-linear composites with arbitrary phase contrast. *International Journal for Numerical Methods in Engineering* 52, 139–160.
- Michel, J.-C., Suquet, P., 2022. Merits and limits of a variational definition of the effective toughness of heterogeneous materials. *Journal of the Mechanics and Physics of Solids* 164, 104889.
- Mickel, W., Kapfer, S. C., Schröder-Turk, G. E., Mecke, K., 2013. Shortcomings of the bond orientational order parameters for the analysis of disordered particulate matter. *Journal of Chemical Physics* 138, 44501.
- Miehe, C., Aldakheel, F., Raina, A., 2016. Phase field modeling of ductile fracture at finite strains: A variational gradient-extended plasticity-damage theory. *International Journal of Plasticity* 84, 1–32.
- Miehe, C., Hofacker, M., Welschinger, F., 2010a. A phase field model for rate-independent crack propagation: Robust algorithmic implementation based on operator splits. *Computer Methods in Applied Mechanics and Engineering* 199, 2765–2778.

- Miehe, C., Welschinger, F., Hofacker, M., 2010b. Thermodynamically consistent phase-field models of fracture: Variational principles and multi-field FE implementations. *International Journal for Numerical Methods in Engineering* 83, 1273–1311.
- Milton, G. W., 2002. *The Theory of Composites*. Cambridge University Press, Cambridge.
- Mirebeau, J.-M., 2018. Fast-Marching Methods for Curvature Penalized Shortest Paths. *Journal of Mathematical Imaging and Vision* 60, 784–815.
- Moës, N., Dolbow, J., Belytschko, T., 1999. A finite element method for crack growth without remeshing. *International Journal for Numerical Methods in Engineering* 46, 131–150.
- Monchiet, V., Bonnet, G., 2012. A polarization-based FFT iterative scheme for computing the effective properties of elastic composites with arbitrary contrast. *International Journal for Numerical Methods in Engineering* 89, 1419–1436.
- Monga, O., Ayache, N., Sander, P. T., 1991. From voxel to curvature. In: *Geometric Methods in Computer Vision*. Vol. 1570. SPIE.
- Montgomery-Smith, S., Jack, D., Smith, D. E., 2011. The Fast Exact Closure for Jeffery’s equation with diffusion. *Journal of Non-Newtonian Fluid Mechanics* 166, 343–353.
- Moulinec, H., Silva, F., 2014. Comparison of three accelerated FFT-based schemes for computing the mechanical response of composite materials. *International Journal for Numerical Methods in Engineering* 97, 960–985.
- Moulinec, H., Suquet, P., 1994. A fast numerical method for computing the linear and nonlinear mechanical properties of composites. *Comptes Rendus de l’Académie des Sciences. Série II* 318 (11), 1417–1423.

- Moulinec, H., Suquet, P., 1998. A numerical method for computing the overall response of nonlinear composites with complex microstructure. *Computer Methods in Applied Mechanics and Engineering* 157, 69–94.
- Müller, V., Böhlke, T., 2016. Prediction of effective elastic properties of fiber reinforced composites using fiber orientation tensors. *Composite Science and Technology* 130, 36–45.
- Mumford, D., Shah, J., 1989. Optimal Approximations by Piecewise Smooth Functions and Associated Variational Problems. *Communications on Pure and Applied Mathematics* 42, 577–685.
- Na, S. H., Sun, W. C., 2018. Computational thermomechanics of crystalline rock, Part I: A combined multi-phase-field/crystal plasticity approach for single crystal simulations. *Computer Methods in Applied Mechanics and Engineering* 338, 657–691.
- Neumann, M., Hirsch, C., Stanek, J., Benes, V., Schmidt, V., 2019. Estimation of geodesic tortuosity and constrictivity in stationary random closed sets. *Scandinavian Journal of Statistics* 46, 848–884.
- Nguyen, T. T., Réthoré, J., Yvonnet, J., Baietto, M. C., 2017. Multi-phase-field modeling of anisotropic crack propagation for polycrystalline materials. *Computational Mechanics* 60, 289–314.
- Nocedal, J., Wright, S. J., 1999. *Numerical Optimization*. Springer, New York.
- Noyel, G., Angulo, J., Jeulin, D., 2011. Fast computation of all pairs of geodesic distances. *Image Analysis & Stereology* 30, 101–109.
- Nozawa, R., 1994. Examples of max-flow and min-cut problems with duality gaps in continuous networks. *Mathematical Programming* 63, 213–234.
- Olver, P. J., 2014. *Introduction to Partial Differential Equations*. Springer, Cham, Switzerland.

- Osher, S. J., Fedkiw, R., 2002. *Level Set Methods and Dynamic Implicit Surfaces*. Springer, New York.
- Owhadi, H., 2003. Approximation of the effective conductivity of ergodic media by periodization. *Probability Theory and Related Fields* 125, 225–258.
- Pandolfi, A., Li, B., Ortiz, M., 2013. Modeling fracture by material-point erosion. *International Journal of Fracture* 184, 3–16.
- Papanicolaou, G. C., Varadhan, S. R. S., 1981. Boundary value problems with rapidly oscillating random coefficients. In: *Random fields, Vol. I, II* (Esztergom, 1979). Vol. 27 of *Colloq. Math. Soc. János Bolyai*. North-Holland, Amsterdam-New York, pp. 835–873.
- Pellet, X., Scardia, L., Zeppieri, C. I., 2019. Homogenisation of high-contrast Mumford-Shah energies. *SIAM Journal on Mathematical Analysis* 51 (3), 1035–1079.
- Pham, K., Amor, H., Marigo, J. J., Maurini, C., 2011. Gradient damage models and their use to approximate brittle fracture. *International Journal of Damage Mechanics* 20 (4), 618–652.
- Pillai, U., Triantafyllou, S. P., Essa, Y., de la Escalera, F. M., 2020. An anisotropic cohesive phase field model for quasi-brittle fractures in thin fibre-reinforced composites. *Composite Structures* 252, 112635.
- Pinter, P., Dietrich, S., Bertram, B., Kehrer, L., Elsner, P., Weidenmann, K., 2018. Comparison and error estimation of 3D fibre orientation analysis of computed tomography image data for fibre reinforced composites. *NDT and E International* , 26–35.
- Pock, T., Cremers, D., Bischof, H., Chambolle, A., 2009. An algorithm for minimizing the Mumford-Shah functional. In: *ICCV Proceedings*. Vol. LNCS. Springer.

- Polyak, B. T., 1964. Some methods of speeding up the convergence of iteration methods. *USSR Computational Mathematics and Mathematical Physics* 4 (5), 1–17.
- Prajapati, N., Herrmann, C., Späth, M., Schneider, D., Selzer, M., Nestler, B., 2020. Brittle anisotropic fracture propagation in quartz sandstone: insights from phase-field simulations. *Computational Geosciences* 24, 1361–1376.
- Rao, T. V., 2003. *Metal Casting: Principles and Practice*. New Age International, New Delhi, Switzerland.
- Rataj, J., 2006. Estimation of intrinsic volumes from parallel neighbourhoods. *Rendiconti del Circolo Matematico di Palermo Series 2 Supplemento (77)*, 553–563.
- Ren, H., Thuang, X., Anitescu, C., Rabczuk, T., 2019. An explicit phase field method for brittle dynamic fracture. *Computers & Structures* 217, 45–56.
- Reuss, A., 1929. Berechnung der Fließgrenze von Mischkristallen auf Grund der Plastizitätsbedingung für Einkristalle. *ZAMM - Zeitschrift für Angewandte Mathematik und Mechanik* , 49–58.
- Rezaei, S., Mianroodi, J. R., Brepols, T., Reese, S., 2021. Direction-dependent fracture in solids: Atomistically calibrated phase-field and cohesive zone model. *Journal of the Mechanics and Physics of Solids* 147, 104253.
- Rice, J., 1967. Mechanics of Crack Tip Deformation and Extension by Fatigue. In: *Fatigue Crack Propagation*. American society for testing and materials.
- Rice, J., 1985. First-order variation in elastic fields due to variation in location of a planar crack front. *Journal of Applied Mechanics* 52, 571–579.

Rice, J. R., 1968. A Path Independent Integral and the Approximate Analysis of Strain Concentration by Notches and Cracks. *Journal of Applied Mechanics* 35, 379–386.

Rice, J. R., Tracey, D. M., 1973. Computational Fracture Mechanics. In: et al, S. J. F. (Ed.), *Numerical and Computer Methods in Structural Mechanics*. Academic Press.

Rickett, J., Fomel, S., 1999. A second-order fast marching eikonal solver. SEP Report 100, 287–292.

Rimoli, J. J., Rojas, J. J., 2015. Meshing strategies for the alleviation of mesh-induced effects in cohesive element models. *International Journal of Fracture* 193, 29–42.

Robb, K., Wirjadi, O., Schladitz, K., 2007. Fiber orientation estimation from 3d image data: Practical algorithms, visualization, and interpretation. In: *7th International Conference on Hybrid Intelligent Systems (HIS 2007)*.

Roux, S., Vandembroucq, D., Hild, F., 2003. Effective toughness of heterogeneous brittle materials. *European Journal of Mechanics A/Solids* 22, 743–749.

Sab, K., 1992. On the homogenization and the simulation of random materials. *European Journal of Mechanics - A/Solids* 11, 585–607.

Saenger, E. H., Bohlen, T., 2004. Finite-difference modeling of viscoelastic and anisotropic wave propagation using the rotated staggered grid. *Geophysics* 69, 583–591.

Saenger, E. H., Gold, N., Shapiro, S. A., 2000. Modeling the propagation of elastic waves using a modified finite-difference grid. *Wave Motion* 31, 77–92.

Sanchez-Palencia, E., 1980. *Non-Homogeneous Media and Vibration Theory*. Springer, Berlin.

- Saouma, V. E., Ayari, M. L., Leavell, D. A., 1987. Mixed mode crack propagation in homogeneous anisotropic solids. *Engineering Fracture Mechanics* 27 (2), 171–184.
- Schladitz, K., Büter, A., Godehardt, M., Wirjadi, O., Fleckenstein, J., Gerster, T., Hassler, U., Jaschek, K., Maisl, M., Maisl, U., Mohr, S., Netzelmann, U., Potyra, T., Steinhauser, M. O., 2017. Non-destructive characterization of fiber orientation in reinforced SMC as input for simulation based design. *Composite Structures* 160, 195–203.
- Schmidt, B., Fraternali, F., Ortiz, M., 2009. Eigenfracture: an eigen-deformation approach to variational fracture. *Multiscale Modeling and Simulation* 7 (3), 1237–1266.
- Schneider, M., 2017. The Sequential Addition and Migration method to generate representative volume elements for the homogenization of short fiber reinforced plastics. *Computational Mechanics* 59, 247–263.
- Schneider, M., 2020. An FFT-based method for computing weighted minimal surfaces in microstructures with applications to the computational homogenization of brittle fracture. *International Journal for Numerical Methods in Engineering* 121 (7), 1367–1387.
- Schneider, M., 2021a. A review of non-linear FFT-based computational homogenization methods. *Acta Mechanica* 232, 2051–210.
- Schneider, M., 2021b. Non-stationary polarization methods in FFT-based computational micromechanics. *International Journal for Numerical Methods in Engineering* 122, 6800–6821.
- Schneider, M., Hofmann, T., Andrä, H., Lechner, P., Etemeyer, F., Volk, W., Steeb, H., 2018. Modelling the microstructure and computing effective elastic properties of sand core materials. *International Journal of Solids and Structures* 143, 1–17.

- Schneider, M., Josien, M., Otto, F., 2022. Representative volume elements for matrix-inclusion composites - a computational study on the effects of an improper treatment of particles intersecting the boundary and the benefits of periodizing the ensemble. *Journal of the Mechanics and Physics of Solids* 158, 104652.
- Schneider, M., Ospald, F., Kabel, M., 2016. Computational homogenization of elasticity on a staggered grid. *International Journal for Numerical Methods in Engineering* 105 (9), 693–720.
- Schneider, R., 2000. Tensor valuations on convex bodies and integral geometry. *Rendiconti del Circolo Matematico di Palermo Series II* 65, 295–316.
- Schneider, R., 2014. *Convex Bodies: The Brunn-Minkowski theory*, expanded Edition. Vol. 151 of *Encyclopedia of Mathematics and its Applications*. Cambridge University Press, Cambridge.
- Schneider, R., Weil, W., 2008. *Stochastic and Integral Geometry*. Springer, Berlin Heidelberg.
- Schreiber, C., Etrich, T., Kuhn, C., Müller, R., 2009. A Phase Field Modeling Approach of Crack Growth in Materials with Anisotropic Fracture Toughness. In: Garth, C., Aurich, J. C., Linke, B., Müller, R., Ravani, B., Weber, G. H., Kirsch, B. (Eds.), *2nd International Conference of the DFG International Research Training Group 2057 – Physical Modeling for Virtual Manufacturing (iPMVM 2020)*. Vol. 89 of *Open Access Series in Informatics (OASIs)*. Schloss Dagstuhl – Leibniz-Zentrum für Informatik, Dagstuhl, Germany.
- Schröder-Turk, G. E., Mickel, W., Kapfer, S. C., Klatt, M. A., Schaller, F. M., Hoffmann, M. J., Kleppmann, N., Armstrong, P., Inayat, A., Hug, D., Reichelsdorfer, M., Peukert, W., Schwieger, W., Mecke, K., 2011. Minkowski Tensor Shape Analysis of Cellular, Granular and Porous Structures. *Advanced Materials* 23, 2535–2553.

Schröder-Turk, G. E., Mickel, W., Kapfer, S. C., Schaller, F. M., Breidenbach, B., Hug, D., Mecke, K., 2013. Minkowski tensors of anisotropic spatial structure. *New Journal of Physics* 15, 1–38.

Sedmak, A., 2018. Computational fracture mechanics: An overview from early efforts to recent achievements. *Fatigue & Fracture of Engineering Materials & Structures* 41, 2438–2474.

Segurado, J., Llorca, J., 2002. A numerical approximation to the elastic properties of sphere-reinforced composites. *Journal of the Mechanics and Physics of Solids* 50 (10), 2107–2121.

Sethian, J., 1996. A fast marching level set method for monotonically advancing fronts. *Proceedings of the National Academy of Sciences of the United States of America* 93, 1591–1595.

Sethian, J. A., 1999. *Level Set Methods and Fast Marching Methods*. Cambridge University Press, Cambridge.

Shanthraj, P., Svendsen, B., Sharma, L., Roters, F., Raabe, D., 2017. Elasto-viscoplastic phase field modelling of anisotropic cleavage fracture. *Journal of the Mechanics and Physics of Solids* 99, 19–34.

Sih, G. C., Paris, P. C., Irwin, G. R., 1965. On cracks in rectilinearly anisotropic bodies. *International Journal of Fracture Mechanics* 1, 189–203.

Stolarska, M., Chopp, D. L., Moës, N., Belytschko, T., 2001. Modelling crack growth by level sets in the extended finite element method. *International Journal for Numerical Methods in Engineering* 51, 943–960.

Strang, G., 1983. Maximal flow through a domain. *Mathematical Programming* 26, 123–143.

- Sukumar, N., Chopp, D. L., Béchet, E., Moës, N., 2008. Three-dimensional non-planar crack growth by a coupled extended finite element and fast marching method . *International Journal for Numerical Methods in Engineering* 76, 727–748.
- Sukumar, N., Chopp, D. L., Moran, B., 2003. Extended finite element method and fast marching method for three-dimensional fatigue crack propagation. *Engineering Fracture Mechanics* 70, 29–48.
- Sun, Y., Edwards, M. G., Chen, B., Li, C., 2021. A state-of-the-art review of crack branching. *Engineering Fracture Mechanics* 257, 108036.
- Svane, A. M., 2014. Estimation of Intrinsic Volumes from Digital Grey-Scale Images. *Journal of Mathematical Imaging and Vision* 49, 352–376.
- Svane, A. M., 2015. Estimation of Minkowski tensors from digital grey-scale images. *Image Analysis and Stereology* 34, 51–61.
- Teichtmeister, S., Kienle, D., Aldakheel, F., Keip, M.-A., 2017. Phase field modeling of fracture in anisotropic brittle solids. *International Journal of Non-Linear Mechanics* 97, 1–21.
- Torquato, S., 2002. *Random Heterogeneous Materials*. Vol. 16. Springer, New York.
- Torquato, S., Jiao, Y., 2010. Robust algorithm to generate a diverse class of dense disordered and ordered sphere packings via linear programming. *Phys. Rev. E* 82, 061302.
- Torquato, S., Stell, G., 1982. Microstructure of two-phase random media. I. The n-point probability functions. *The Journal of Chemical Physics* 77, 2071–2077.
- Tyler, D. E., 1987. Statistical Analysis for the Angular Central Gaussian Distribution on the Sphere. *Biometrika* 74 (3), 579–589.

- van Dijk, N. P., Espadas-Escalante, J. J., Isaksson, P., 2020. Strain energy density decompositions in phase-field fracture theories for orthotropy and anisotropy. *International Journal of Solids and Structures* 196-197, 140–153.
- Voigt, W., 1889. Ueber die Beziehung zwischen den beiden Elasticitätsconstanten isotroper Körper. *Annalen der Physik* 274, 573–587.
- Waheed, U., 2020. A fast-marching eikonal solver for tilted transversely isotropic media. *Geophysics* 85, 385–393.
- Weinberg, K., Wieners, C., 2022. Dynamic phase-field fracture with a first-order discontinuous Galerkin method for elastic waves. *Computer Methods in Applied Mechanics and Engineering* 389, 114330.
- Wheeler, M. F., Wick, T., Wollner, W., 2014. An augmented-Lagrangian method for the phase-field approach for pressurized fractures. *Computer Methods in Applied Mechanics and Engineering* 271, 69–85.
- Wiegmann, A., Zemitis, A., 2006. EJ-HEAT: A fast explicit jump harmonic averaging solver for the effective heat conductivity of composite materials. *Berichte des Fraunhofer ITWM* 94, 1–21.
- Williams, J. G., 1989. Chapter 1 - fracture mechanics of anisotropic materials. In: Friedrich, K. (Ed.), *Application of Fracture Mechanics to Composite Materials*. Vol. 6 of Composite Materials Series. Elsevier, pp. 3–38.
- Williams, J. W. J., 1964. Algorithm 232 - heapsort. *Communications of the ACM* 7, 347–348.
- Williams, S., Philipse, A., 2003. Random packings of spheres and spherocylinders simulated by mechanical contraction. *Physical Reviews E* 67, 1–9.

Willot, F., 2015a. Fourier-based schemes for computing the mechanical response of composites with accurate local fields. *Comptes Rendus Mécanique* 343, 232–245.

Willot, F., 2015b. The power laws of geodesics in some random sets with dilute concentration of inclusions. In: *Mathematical Morphology and Its Applications to Signal and Image Processing*. Springer International Publishing, pp. 535–546.

Willot, F., 2019. Localization in random media and its effect on the homogenized behavior of materials. habilitation, Université Paris Sorbonne.

Willot, F., 2020. The effective conductivity of strongly nonlinear media: The dilute limit. *International Journal of Solids and Structures* 184, 287–295.

Willot, F., Abdallah, B., Pellegrini, Y.-P., 2014. Fourier-based schemes with modified Green operator for computing the electrical response of heterogeneous media with accurate local fields. *International Journal for Numerical Methods in Engineering* 98, 518–533.

Wimmer, G., Schuecker, C., Pettersmann, H. E., 2009. Numerical simulation of delamination in laminated composite components – A combination of a strength criterion and fracture mechanics. *Composites: Part B* 40, 158–165.

Wirjadi, O., Schladitz, K., Rack, A., Breuel, T., 2009. Applications of anisotropic image filters for computing 2D and 3D-fiber orientations. In: *Proceedings of the 10th European Congress of ISS*.

Wu, E. M., 1967. Application of Fracture Mechanics to Anisotropic Plates. *Journal of Applied Mechanics* 34 (4), 967–974.

Wu, J.-Y., Nguyen, V. P., 2018. A length scale insensitive phase-field damage model for brittle fracture. *Journal of the Mechanics and Physics of Solids* 119, 20–42.

Wu, J.-Y., Nguyen, V. P., Nguyen, C. T., Sutula, D., Sinaie, S., Bordas, S. P. A., 2020. Phase-field modeling of fracture. In: Bordas, S. P. A., Balint, D. S. (Eds.), *Advances in Applied Mechanics*. Vol. 53. Elsevier, Ch. 1, pp. 1–183.

Xu, Z., Figueiredo, M. A. T., Goldstein, T., 2017. Adaptive ADMM with Spectral Penalty Parameter Selection. In: Singh, A., Zhu, J. (Eds.), *Proceedings of the 20th International Conference on Artificial Intelligence and Statistics*. Vol. 54 of *Proceedings of Machine Learning Research*. PMLR, Fort Lauderdale.

Zaefferer, S., Wright, S. I., Raabe, D., 2008. Three-dimensional orientation microscopy in a focused ion beam-scanning electron microscope: a new dimension of microstructure characterization. *Metallurgical and Materials Transactions A* 39 (2), 374–389.

Zähle, M., 1986. Integral and current representation of Federer's curvature measures. *Archiv der Mathematik* 46 (6), 557–567.

**Schriftenreihe Kontinuumsmechanik im Maschinenbau
Karlsruher Institut für Technologie (KIT)
(ISSN 2192-693X)**

- Band 1** Felix Fritzen
Microstructural modeling and computational homogenization of the physically linear and nonlinear constitutive behavior of micro-heterogeneous materials.
ISBN 978-3-86644-699-1
- Band 2** Rumena Tsotsova
Texturbasierte Modellierung anisotroper Fließpotentiale.
ISBN 978-3-86644-764-6
- Band 3** Johannes Wippler
Micromechanical finite element simulations of crack propagation in silicon nitride.
ISBN 978-3-86644-818-6
- Band 4** Katja Jöchen
Homogenization of the linear and non-linear mechanical behavior of polycrystals.
ISBN 978-3-86644-971-8
- Band 5** Stephan Wulfinghoff
Numerically Efficient Gradient Crystal Plasticity with a Grain Boundary Yield Criterion and Dislocation-based Work-Hardening.
ISBN 978-3-7315-0245-6
- Band 6** Viktor Müller
Micromechanical modeling of short-fiber reinforced composites.
ISBN 978-3-7315-0454-2

- Band 7** Florian Rieger
Work-hardening of dual-phase steel.
ISBN 978-3-7315-0513-6
- Band 8** Vedran Glavas
Micromechanical Modeling and Simulation of Forming Processes.
ISBN 978-3-7315-0602-7
- Band 9** Eric Bayerschen
Single-crystal gradient plasticity with an accumulated plastic slip: Theory and applications.
ISBN 978-3-7315-0606-5
- Band 10** Bartholomäus Brylka
Charakterisierung und Modellierung der Steifigkeit von langfaserverstärktem Polypropylen.
ISBN 978-3-7315-0680-5
- Band 11** Rudolf Neumann
Two-Scale Thermomechanical Simulation of Hot Stamping.
ISBN 978-3-7315-0714-7
- Band 12** Mauricio Lobos Fernández
Homogenization and materials design of mechanical properties of textured materials based on zeroth-, first- and second-order bounds of linear behavior.
ISBN 978-3-7315-0770-3
- Band 13** Malte Schemmann
Biaxial Characterization and Mean-field Based Damage Modeling of Sheet Molding Compound Composites.
ISBN 978-3-7315-0818-2
- Band 14** Jürgen Albiez
Finite element simulation of dislocation based plasticity and diffusion in multiphase materials at high temperature.
ISBN 978-3-7315-0918-9

- Band 15** Maria Loredana Kehrer
Thermomechanical Mean-Field Modeling and Experimental Characterization of Long Fiber-Reinforced Sheet Molding Compound Composites.
ISBN 978-3-7315-0924-0
- Band 16** Peter Hölz
A dynamic and statistical analysis of the temperature- and fatigue behavior of a race power unit – The effect of different thermodynamic states.
ISBN 978-3-7315-0988-2
- Band 17** Andreas Prahs
A Gradient Crystal Plasticity Theory Based on an Extended Energy Balance.
ISBN 978-3-7315-1025-3
- Band 18** Johannes Ruck
Modeling martensitic phase transformation in dual phase steels based on a sharp interface theory.
ISBN 978-3-7315-1072-7
- Band 19** Hannes Erdle
Modeling of Dislocation - Grain Boundary Interactions in Gradient Crystal Plasticity Theories.
ISBN 978-3-7315-1196-0
- Band 20** Johannes Görthofer
Microstructure generation and micromechanical modeling of sheet molding compound composites.
ISBN 978-3-7315-1205-9
- Band 21** Daniel Wicht
Efficient fast Fourier transform-based solvers for computing the thermomechanical behavior of applied materials.
ISBN 978-3-7315-1220-2
- Band 22** Juliane Lang
Thermomechanical Modeling and Experimental Characterization of Sheet Molding Compound Composites.
ISBN 978-3-7315-1232-5

- Band 23** Julian Karl Bauer
**Fiber Orientation Tensors and Mean Field Homogenization:
Application to Sheet Molding Compound.**
ISBN 978-3-7315-1262-2
- Band 24** Sebastian Gajek
**Deep material networks for efficient scale-bridging in
thermomechanical simulations of solids.**
ISBN 978-3-7315-1278-3
- Band 25** Jannick Kuhn
**Microstructure modeling and crystal plasticity parameter
identification for predicting the cyclic mechanical behavior
of polycrystalline metals.**
ISBN 978-3-7315-1272-1
- Band 26** Felix Ernesti
A computational multi-scale approach for brittle materials.
ISBN 978-3-7315-1285-1

Materials of industrial interest often show a complex microstructure. This microstructure directly influences their macroscopic material behavior. For simulations on the component scale, multi-scale methods may exploit this microstructural information.

This work is devoted to a multi-scale approach for brittle materials. The mathematical foundation of this work is laid by a homogenization result for free discontinuity problems. This homogenization result includes specific cell formulas for the effective crack energy and the effective stiffness of heterogeneous materials which decouple upon homogenization. We investigate novel discretization methods and FFT-based solvers to efficiently compute the effective crack energy. Furthermore, we provide extensions to locally anisotropic materials and investigate the influence of the boundary conditions on apparent properties.

ISSN 2192-693X
ISBN 978-3-7315-1285-1

Gedruckt auf FSC-zertifiziertem Papier

